

DOCTORAL DISSERTATION

博士論文

**Development of Eddy Current Probes Based on Various
Core Shapes and Materials**

様々なコア形状と材料に基づく渦電流プローブの開発

21TG902

LE QUANG TRUNG

(レ クアン チュン)

Supervisor

Assoc. Prof. NAOYA KASAI

**Department of Artificial Environment
Graduate School of Environment and Information Sciences
Yokohama National University**

March 2024

DOCTORAL DISSERTATION



**Development of Eddy Current Probes Based on Various
Core Shapes and Materials**

Submitted by

LE QUANG TRUNG

Supervised by

Assoc. Prof. NAOYA KASAI

**Department of Artificial Environment
Graduate School of Environment and Information Sciences
Yokohama National University**

March 2024

DOCTORAL DISSERTATION

Development of Eddy Current Probes Based on Various Core Shapes and Materials

Dissertation approved:

1. Assoc. Prof. Naoya KASAI
Academic Supervisor
2. Prof. Tadahiro SHIBUTANI
Committee Member
3. Assoc. Prof. Takeshi KOBAYASHI
Committee Member
4. Prof. Shinji OKAZAKI
Committee Member
5. Assoc. Prof. Mieko KUMASAKI
Committee Member

Abstract

In this study, a novel EC probe was developed utilizing a copper core known for its high electrical conductivity and non-magnetic characteristics, featuring slits and a conical structure for controlled EC flow. The probe demonstrated effective crack detection on aluminum plates. To address sensitivity to lift-off distance, a differential signal approach was employed, and a novel EC convergence probe with two copper cores and a UEC component, aligning with self-differential and self-nulling characteristics, was introduced. Challenges arose with the ECC probe, as crack signal amplitude diminished when EC lines were parallel to the crack. To overcome this, a rotating uniform eddy current convergence (RUECC) probe was introduced with a specially designed copper core, generating a robust rotating EC on the specimen's surface. The RUECC probe effectively detected small defects in all directions, overcoming limitations of previous ECC probes. Additionally, the study presents a rotating uniform eddy current (RUEC) probe with four rectangular excitation coils aligned on a single plane, ensuring uniform eddy current amplitudes across the test specimen's surface. The proposed novel film EC probe, inspired by FAEC sensors, adopts a square configuration with an interwoven detection coil and excitation coil, creating four distinct interaction zones for comprehensive crack detection in all orientations. Non-electrical conductivity and magnetic properties are leveraged by incorporating four ferrite cores into all excitation coils of the RUEC probe. Furthermore, ferromagnetic amorphous alloy particles (FAAP) are strategically added to the film EC probe to enhance the magnetic field amplitude and optimize crack signals. Finally, an analysis was conducted on three distinct configurations of EC probes characterized by similar excitation and detection coil dimensions. These configurations had orientations either pancake-like or tangential to the surface of the test specimen. The primary objective was to assess the ECs generated on the test specimen and evaluate the magnitude of the resultant crack signals. To achieve this, finite element analysis was employed to compare and appraise the efficiency of EC generation on the surface among these three configurations. Following this, experimental trials were conducted using the three EC probes to validate the simulation findings and assess their efficacy in detecting artificial cracks on an aluminum plate.

Acknowledgement

I would like to express my deepest appreciation and heartfelt gratitude to my advisor, Associate Professor Naoya KASAI, for his unwavering belief in my abilities and for guiding me through the process of exploring my potential. Without his continuous motivation, valuable input, and guidance, this research would not have been possible to complete.

My sincere thanks also go to my committee members, Professor Tadahiro SHIBUTANI and Professor Takeshi KOBAYASHI, for their constructive encouragement, valuable guidance, and suggestions. They served as important members of my committee, and their feedback has helped me to refine my research.

I am grateful to all my doctoral dissertation committees, including Professor Shinji OKAZAKI, and Associate Professor Mieko KUMASAKI, for their comments and suggestions, which have helped me to sharpen my writing skills and to develop future research ideas.

I would like to extend my special thanks to Associate Professor Kazumi MATSUI for his valuable comments on my doctoral dissertation, which have contributed to its improvement.

I would like to express my special thanks to Dr. Kouichi SEKINO, whose technical assistance was crucial in procuring test materials and equipment for collecting experimental data. His support has been invaluable and has helped me to achieve excellence in my research.

I want to convey my sincere gratitude to the research team, which includes Mr. Seishu MIYAZAKI and Mr. Atsushi KASHAHARA. Their indispensable technical support in conducting simulations and gathering experimental data has been instrumental in enhancing the quality of my research. Their assistance has been invaluable and has significantly contributed to the excellence achieved in my work.

Finally, I would like to acknowledge the support of the scholarship of the Foundation for Dietary Scientific Research from Nisshin Seifun Group (2021-2022 period), and the scholarship of JEES Mitsui Fudosan No. MITSUI2204 (2022-2024 period) for funding my research.

Statement of Originality

I certify that this dissertation and the research supporting this study represent solely my own work. While I may have referenced the work of other research groups and individuals, I acknowledge and give full credit to them as appropriate throughout this dissertation.

Le Quang Trung

March 2024

Table of content

Abstract.....	I
Acknowledgement	II
Statement of Originality.....	III
Table of content.....	IV
List of tables.....	IX
List of figures.....	XI
Nomenclature.....	XIX
Chapter 1 :Introduction.....	1
1.1. Background.....	1
1.2. Motivation.....	6
1.3. Objectives	6
1.4. The outline of dissertation	7
1.5. Eddy Current Testing in Non-destructive Testing.....	9
1.5.1. Eddy current testing probes.....	9
1.5.2. The theory of eddy current testing	11
Chapter 2 : Utilizing copper core with special design to generate strongly convergence eddy current	18
2.1. Introduction.....	18
2.2. Study on an eddy current convergence probe using special design copper core and single detection coil to detect flaws on aluminum plates	18
2.2.1. Materials and Methods.....	18
2.2.1.1. Design of ECC probe with copper core (Type 1).....	18

2.2.1.2.	Design of ECC probe with hollows and plate under the excitation coil (Type 2).....	19
2.2.1.3.	Finite element simulation with ECC probe	20
2.2.1.4.	Principle of output signal with a single detection coil.....	24
2.2.2.	Experiment with ECC probe	24
2.2.3.	Experimental results and discussion	27
2.2.3.1.	Measurement results with Scanning #1 and Scanning #2	28
2.2.3.2.	Measurement results of path #1 and path #2	30
2.3.	Uniform eddy current convergence probes exhibiting self-differential and self-nulling attributes for the purpose of detecting cracks within conductive materials.....	32
2.3.1.1.	Design of ECC probe with copper core (Type 1)	32
2.3.1.2.	Design of UECC probe with a pair of copper cores (Type 2)	33
2.3.2.1.	3D FEM model	33
2.3.2.2.	Results of FEM simulation for both UECC probes.....	35
2.3.3.1.	Test piece with artificial cracks	38
2.3.3.2.	Experimental setup	39
2.3.4.1.	Measurement results with Scanning #1 and Scanning #2	41
2.3.4.2.	Measurement results of Path #A.....	42
2.3.4.3.	Experiment with small flaws on an aluminum plate	45
2.4.	Summary	46
Chapter 3: Rotating eddy current convergence probe with a sophisticated copper core design for crack detection		48
3.1.	Introduction.....	48
3.2.	Probe design and methods	48
3.2.1.	Structure of the RUECC probe.....	48

3.2.2.	Method of generating an RUEC on the surface of the test piece	49
3.2.3.	3D-Finite element simulation results	51
3.2.4.	Principle of the output detection signal.....	53
3.3.	Experimental setup.....	54
3.4.	Experimental results and discussions.....	57
3.4.1.	Authenticating the small crack detection ability of the RUECC probe	57
3.4.2.	Validating the crack detection ability of the RUECC probe through six paths.....	58
3.5.	Summary	61

Chapter 4: Enhancing excitation magnetic field intensity with support materials (FAAP and ferrite)
..... 63

4.1.	Introduction.....	63
4.2.	Enhanced crack detection in conductive materials using a rotating uniform eddy current probe with four rectangular excitation coils and ferrite cores	64
4.2.1.	Design and methods of RUEC probe	64
4.2.1.1.	Design of RUEC probe using four rectangular excitation coils	64
4.2.1.2.	Methods and 3D-FEA simulations	65
4.2.1.3.	Principle of crack output signal	69
4.2.2.	Experimental setup.....	73
4.2.3.	Experimental results and discussions.....	75
4.2.3.1.	Measurement obtains of scanning directions with RUEC probe.....	76
4.2.3.2.	Measurement obtains along two paths.....	78
4.3.	Enhancing Crack Detection in Low Carbon Steel using a Rotating Uniform Eddy Current Probe and Noise Signal Filtering through Multivariate Singular Spectral Analysis	79
4.3.1.	Exploring the principles of the RUEC probe and the significant advantages of ferrite cores for enhancing crack detection capabilities.....	79

4.3.1.1.	Exploring the structure of the RUEC probe	79
4.3.1.2.	Simulation results	80
4.3.1.3.	Crack signal detection	83
4.3.2.	Signal Processing Methods	85
4.3.2.1.	Wavelet Filter.....	85
4.3.2.2.	Multivariate Singular Spectral Analysis (MSSA) Filter.....	85
4.3.3.	Experimental setup.....	87
4.3.4.	Experimental results and discussions	89
4.3.5.	MSSA results and discussions.....	91
4.4.	Enhanced Film Eddy Current Probe with Interleaved Detection Coil and Amplification by Ferromagnetic Amorphous Alloy Particles	95
4.4.1.	Methods and film EC probe design.....	95
4.4.2.	Experimental implementation	98
4.4.3.	Experimental results and discussion	102
4.5.	Summary	110
Chapter 5: Influence of eddy current probe configurations on crack signal amplitude: exploring the impact of excitation coil orientation		111
5.1.	Introduction.....	111
5.2.	The performance of previous EC probe.....	111
5.3.	Materials and models for this study	113
5.3.1.	Materials.....	113
5.3.2.	Finite element method (FEM) simulation	113
5.3.3.	The principle of formation of EMFs in the detection coil and the crack signal.....	116
5.3.3.1.	The principle of crack detection signal with Type 1.....	117

5.3.3.2. The principle of crack detection signal with Type 2 and Type 3	120
5.4. Experimental setup.....	122
5.5. Results and discussions.....	124
5.5.1. Measurement results of three EC probe models.....	124
5.5.2. Measurement results of path #1 and path #2.....	126
5.6. Summary	129
Chapter 6: Conclusions	131
• International Journal Publication (7 Published)	143
• Technical Report (1)	144
• Domestic Conference (4)	144
• International Conference (2)	144
• Best Paper Award (1)	145
• Awards (1)	145

List of tables

Table 2.1 Electromagnetic parameters of the ECC probes utilized in the analysis.	21
Table 2.2 Dimensions of four artificial flaws in the aluminum plate	25
Table 2.3 The specifications of the ECC probes.....	25
Table 2.4 Electromagnetic parameters used in the analysis for UECC probes.....	34
Table 2.5 Parameters of the 3D FEM model with UECC probes	35
Table 2.6 Dimensions of artificial cracks on the 5052-aluminum alloy surface	38
Table 2.7 Specifications of the excitation and detection coils in each UECC probe.....	39
Table 3.1. Electromagnetic parameters used in the analysis for RUECC probe.....	49
Table 3.2. Sizes of artificial cracks in two aluminum plates using for experiments with RUECC probe.	55
Table 3.3. Specifications of each excitation coil and the circular detection coil for the RUECC probe.	56
Table 4.1 The parameters of RUEC probe’s material used for the simulation.	66
Table 4.2: Simulation results for the output signal of the single detection coil in cases of cracks (Unit: mV).....	72
Table 4.3 Dimensions of cracks used for RUEC probe (Unit: mm)	74
Table 4.4 The information of the exciting and detecting coils of RUEC probe.	74
Table 4.5 Electromagnetic parameters of the RUEC probe for simulation.	80
Table 4.6 Electromagnetic parameters used in analysis for Film EC probe.	96
Table 4.7 Sizes of the four artificial cracks on the aluminum plate.....	99
Table 4.8 Specifications of the Film EC probe’s excitation and detection coils.....	100
Table 4.9 Amount of crack peak signals amplitude increasing due to FAAP of the film EC probe (unit: mV).....	106
Table 5.1 Electromagnetic parameters used in analysis for EC probe models.	114
Table 5.2 The sizes of four artificial cracks in the aluminum plate used for EC probe models.	122

Table 5.3 The parameters of each excitation coil and the detection coil used for EC probe models.
..... 124

List of figures

Figure 1.1. Flowchart of eddy current probe investigation in the dissertation	8
Figure 1.2. The principle of ECT sensor:	11
Figure 1.3. The equivalent model diagram of ECT	16
Figure 2.1. Structure of ECC probe (Unit in mm): (a) Top view, (b) Section view of A-A', (c) Section view of B-B'.	19
Figure 2.2. Structure of ECC probe with hollows and a plate under the excitation coil. (Unit in mm): (a) Top view, (b) Section view of A-A', (c) Section view of B-B'	20
Figure 2.3. Structure of ECC probe with hollows and a plate under the excitation coil. (Unit in mm): (a) Top view, (b) Section view of A-A', (c) Section view of B-B'	21
Figure 2.4. Contour and arrow plots of the EC distribution on the surface of the copper core of EC probe: (a) Without slit, (b) With slits, (c) With hollows and a plate under the excitation coil.	22
Figure 2.5. Contour and arrow plots of the EC distribution on cross-section B-B' of the probe: (a) Without slit, (b) With slits, (c) With hollows and a plate under the excitation coil.....	23
Figure 2.6. Contour plot of the EC distribution on the surface of the test piece: (a) Without slit, (b) With slits, (c) With hollows and a plate under the excitation coil.	23
Figure 2.7. Structure of a detection coil: (a) Top view, (b) Section view of A-A', (c) The placement of the detection coil.....	24
Figure 2.8. Specifications of aluminum plate using for experiment with the ECC probes (Unit in mm).....	25
Figure 2.9. Experimental setup with ECC probes.....	26
Figure 2.10. Shapes of ECC probe: (a) Without slit (Type 0), (b) With slits (Type 1), (c) With hollows and a plate under the excitation coil (Type 2)	27
Figure 2.11. Shape of the detection coil using for ECC probes.....	27
Figure 2.12. Scanning direction and paths on test piece with ECC probes: (a) Scanning #1, (b) Scanning #2.....	28
Figure 2.13. Measurement results of EC convergence probe: (a) Scanning #1 of type 0, (b)	

Scanning #1 of type 1, (c) Scanning #1 of type 2, (d) Scanning #2 of type 0, (e) Scanning #2 of type 1, (f) Scanning #2 of type 2.....	29
Figure 2.14. Principle of the output signal with a detection coil: (a) Without flaw, (b) With a flaw.	30
Figure 2.15. Measurement results of ECC probe with a detection coil with scanning #1: (a) Path #1, (b) Path #2.....	30
Figure 2.16. Measurement results of ECC probe with a detection coil with scanning #2: (a) Path #1, (b) Path #2.....	31
Figure 2.17 Structure of EC convergence probe with hollows and a plate under the excitation coil (units in mm): (a) top view, (b) section view of A-A', (c) section view of B-B', and (d) structure of a pair of circular detection coils.....	32
Figure 2.18 Structure of EC convergence probe with a pair of copper cores (units in mm): (a) top view, (b) section view of A-A', (c) section view of B-B', and (d) structure of a single detection coil	33
Figure 2.19 3D FEM model of the EC probe: (a) Type 1 and (b) Type 2.....	34
Figure 2.20 Contour and arrow plots of the EC distribution on the surface of the copper core of EC convergence probe: (a) Type 1 and (b) Type 2.....	35
Figure 2.21 Contour and arrow plots of the EC distribution on cross-section B-B' of the probe: (a) Type 1 and (b) Type 2	36
Figure 2.22 Contour plot of the EC distribution on the surface of the test piece: (a) Type 1 and (b) Type 2.....	37
Figure 2.23 EC amplitude on the surface of the test piece along Path #A: (a) Type 1 and (b) Type 2.....	38
Figure 2.24 Aluminum alloy plate specifications (units in mm): (a) Test piece #1 and (b) Test.. piece #2	38
Figure 2.25 Experimental setup and the UECC probes: (b) Type 1 and (c) Type 2	40
Figure 2.26 Scanning direction and paths on the test piece with UECC probes: (a) Scanning #1 and	

(b) Scanning #2	41
Figure 2.27 Experimental results of the UECC probe: (a) Scanning #1 of Type 1, (b) Scanning #1 of Type 2, (c) Scanning #2 of Type 1, and (d) Scanning #2 of Type 2. The unit of the signal is mV.	42
Figure 2.28 Measurement results of UECC probe with Path #A: (a) Scanning #1 of Type 1, (b) Scanning #1 of Type 2, (c) Scanning #2 of Type 1, and (d) Scanning #2 of Type 2	43
Figure 2.29 Crack signal explanation for measurement results of Type 1: (a) without crack, (b) position ①, and (c) position ②	44
Figure 2.30 Crack signal explanation for measurement results of Type 2: (a) without crack, (b) position ③, and (c) position ④	44
Figure 2.31 Measurement results of UECC probe on test piece #2: (a) scanning direction, (b) result of Type 1, and (c) result of Type 2	45
Figure 2.32 Measurement results of UECC probe on test piece #2: (a) Type 1 with 32.2 mA of excitation current and (b) Type 2 with 253 mA of excitation current.....	46
Figure 3.1 Structure of the RUECC probe (unit in mm): (a) Copper core, (b) EC convergence controller, (c) Two pairs of double excitation coils, (d) and (e) Top view and section view along A-A' of the detection coil, (f) Overall RUECC probe.....	48
Figure 3.3 Simulation results of RUEC distribution patterns with the RUECC probe: (a) At 0 degrees, (b) At 45 degrees ($\pi/4$), (c) At 90 degrees ($\pi/2$), (d) At 135 degrees ($3\pi/4$), (e) At 180 degrees (π), (f) At 225 degrees ($5\pi/4$), (g) At 270 degrees ($3\pi/2$), (h) At 315 degrees ($7\pi/4$).....	52
Figure 3.4 Principle of the output detection signal with the circular detection coil: (a) Without a crack, (b) With a crack under the left side of the detection coil, (c) With a crack under the right side of the detection coil.	53
Figure 3.5 Specifications of aluminum alloy plates for RUECC probe (units in mm): (a) Test piece #1 and (b) Test piece #2.	54
Figure 3.6 Experimental implementation: (a) Experimental setup, (b) RUECC probe, (c) Actual shape of the copper core, (d) Actual shape of the excitation coils, (e) Actual shape of the circular detection coil.....	56

Figure 3.7 Experimental results with RUECC probe: (a) Test piece 1, (b) Test piece 2.	57
Figure 3.8 Measurement results of six paths obtained with the RUECC probe: (a) Path #1 (the length of cracks 4 mm deep in test specimen 1 was perpendicular to the x-axis), (b) Path #2 (the length of cracks 2 mm deep in test specimen 1 was perpendicular to the x-axis), (c) Path #3 (the crack length in test specimen 1 was inclined 45 degrees from the x-axis), (d) Path #4 (the crack length in test specimen 1 was parallel to the x-axis), (e) Path #5 (the length of cracks 2 mm deep in test specimen 2 was perpendicular to the x-axis), (f) Path #6 (the length of cracks 4 mm deep in test specimen 2 was perpendicular to the x-axis).....	59
Figure 4.1. The structure of RUEC probe using four rectangular coils as two pairs of excitation coils (all units: mm): (a) top view, (b) front view.	64
Figure 4.2. Applied alternating current for two pairs of excitation coils with phase difference 90 degrees.	65
Figure 4.3. 3D-FEA simulation RUEC probe models: (a) without ferrite core, (b) with ferrite cores put inside all exciting coils.	66
Figure 4.4. Shaded and arrow plots of concentrated magnetic fluxes in the excitation coils: (a) without ferrite core, (b) with ferrite cores put inside each exciting coil.....	67
Figure 4.5. Distribution plots of the UEC on the test specimen surface: (a) without ferrite core, (b) with ferrite cores put inside each exciting coil.	68
Figure 4.6. 3D-FEM results of RUEC distribution patterns using RUEC probe: (a) RUEC at 0 degrees, (b) RUEC at 45 degrees, (c) RUEC at 90 degrees, (d) RUEC at 135 degrees, (e) RUEC at 180 degrees, (f) RUEC at 225 degrees, (g) RUEC at 270 degrees, (h) RUEC at 315 degrees, (h) RUEC at 360 degrees.....	69
Figure 4.7. Illustration of self-nulling and self-differential properties.	70
Figure 4.8. Theory of crack signal output with a circular detecting coil: (a) balanced condition without crack, (b) balanced condition with a crack, (c) unbalanced condition.	71
Figure 4.9. Specifications of aluminum plate using for RUEC probe	73
Figure 4.10. Experimental setup for RUEC probe.....	74
Figure 4.11. Scanning directions and the paths with RUEC probe: (a) scanning #1, (b) scanning	

#2.....	76
Figure 4.12. Measurement obtained in scanning #1 with RUEC probe: (a) without ferrite core, (b) with ferrite cores.	77
Figure 4.13. Measurement obtained in scanning #2 with RUEC probe: (a) without ferrite core, (b) with ferrite cores.	77
Figure 4.14. Measurement obtained in scanning #1 of two paths with RUEC probe: (a) path #A, (b) path #B.	78
Figure 4.15. Measurement obtained in scanning #2 of two paths with RUEC probe: (a) path #A, (b) path #B.	78
Figure 4.16. The schematic structure of the RUEC probe with ferrite cores.....	79
Figure 4.17. The simulation results of UEC distribution on the surface of low carbon steel: (a) RUEC probe without ferrite core and (b) with ferrite cores, (c) The value of RMS $ J $ smoothed obtained by line A-A' from RUEC probe without ferrite core and (d) with ferrite cores.	81
Figure 4.18. The simulation results of magnitude and direction of EC generated on the surface of low carbon steel by two sources of excitation current.	82
Figure 4.19. The principle of crack signal detection with circular detection core: Balanced condition (a) without crack and (b) with a crack at the center of detection core, Unbalanced condition (c) with a crack at the left side of detection core and (d) with a crack at the right side of detection core.	83
Figure 4.20. Specifications of low carbon steel plate with cracks (Unit in mm).....	88
Figure 4.21. The prototype of the RUEC probe systems	89
Figure 4.22. The measurement results of two scanning with RUEC probe: (a) Scanning #A without ferrite core, (b) Scanning #B without ferrite core, (c) Scanning #A with ferrite cores, (d) Scanning #B with ferrite cores.....	90
Figure 4.23. Eigenvalues distribution of the ECT scan results.....	92
Figure 4.24. ECT scan signal reconstructed by MSSA method with different groups of submatrices.	93

Figure 4.25. ECT scan signal filtered by wavelet-PCA, Denoise, and MSSA methods.....	94
Figure 4.26 Structure of film EC probe (units are in mm). (a) structure of film EC probe, (b) actual film EC probe, and (c) FAAP.....	95
Figure 4.27 (a) Film EC probe models without FAAP and (b) with FAAP.	96
Figure 4.28 Contour plot of the EC distribution on the surface of the test piece with different excitation frequencies. (a) 300 kHz of frequency without FAAP, (b) 500 kHz of frequency without FAAP, (c) 1 MHz of frequency without FAAP, (d) 300 kHz of frequency with FAAP, (e) 500 kHz of frequency with FAAP, and (f) 1 MHz of frequency with FAAP.....	97
Figure 4.29 Shaded plot of magnetic flux distribution along the section A-A' (See Fig. 1(a)). (a) without FAAP, and (b) with FAAP	98
Figure 4.30 Four artificial cracks on the aluminum plate used for Film EC probe.	99
Figure 4.31. Experimental setup with the film EC probe. (a) experimental setup, (b) film EC probe, and (c) FAAP in a plastic bag.	101
Figure 4.32. Scanning direction and a path on the test piece with Film EC probe.....	102
Figure 4.33. Measurement results of film EC probe. (a) 300 kHz of frequency without FAAP, (b) 500 kHz of frequency without FAAP, (c) 1 MHz of frequency without FAAP, (d) 300 kHz of frequency with FAAP, (e) 500 kHz of frequency with FAAP, and (f) 1 MHz of frequency with FAAP.	103
Figure 4.34 Measurement results of film EC probe along Path #A: (a) 300 kHz of frequency, (b) 500 kHz of frequency, and (c) 1 MHz of frequency.	105
Figure 4.35 Principle of crack detection signal of the film EC probe: (a) the crack with 20 mm length under the center of the interaction zone; (b) crack with 20 mm length under the center of the film EC probe; and (c) crack with 40 mm length under the center of the film EC probe.....	106
Figure 4.36 Principle of film EC probe: (a) without FAAP, (b) with FAAP	107
Figure 4.37 The relationship between the full width at half maximum value of the crack signals and the length of cracks. (a) without FAAP, (b) with FAAP	109
Figure 4.38 The relationship between the maximum value of V_0 and the depth of cracks. (a) without FAAP, (b) with FAAP	109

Figure 5.1 The principle of previous EC probe: (a) The structure of EC probe, (b) EC intensity along A-A' direction on the test specimen surface, (c) EC distribution on the test specimen surface, (d) Principle of EMFs generated on the circular detection coil.	112
Figure 5.2 Structure of EC probe components (units in mm): (a) Each rectangular excitation coil, (b) Circular detection coil.	113
Figure 5.3 EC probe models for FEM simulation: (a) Three excitation coils in pancake direction (Type 1), (b) A double excitation coils in pancake and tangential directions (Type 2), (c) Four excitation coils in tangential direction (Type 3).	114
Figure 5.4 FEM simulation results with three EC probe models: (a) EC intensity distributed on the test specimen surface with Type 1, (b) EC intensity distributed on the test specimen surface with Type 2, (c) EC intensity distributed on the test specimen surface with Type 3, (d) EC intensity obtained along B-B' path of Type 1, (d) EC intensity obtained along B-B' path of Type 2, (d) EC intensity obtained along B-B' path of Type 3.	115
Figure 5.5 Region of EC on the test specimen used for generating EMFs ε_1 and ε_2 in the detection coil.....	117
Figure 5.6 Principle of electromotive forces generated on detection coil for Type 1: (a) The signal generated on the detection coil, (b) The direction of EMFs on the detection coil.....	118
Figure 5.7 Principle of the output detection signal with the circular detection coil of Type 1: (a) Without a crack, (b) With a crack under the left side of the detection coil, (c) With a crack under the center of the detection coil.	119
Figure 5.8 Principle of electromotive forces generated on detection coil for Type 2 and Type 3: (a) The signal generated on the detection coil of Type 2, (b) The signal generated on the detection coil of Type 3, (c) The direction of EMFs on the detection coil.....	120
Figure 5.9 Principle of the output detection signal with the circular detection coil of Type 2 and Type 3: (a) Without a crack, (b) With a crack under the left side of the detection coil, (c) With a crack under the center of the detection coil.	121
Figure 5.10 Diagram of the experimental setup.....	122
Figure 5.11. Specifications of aluminum plate	123

Figure 5.12. Experimental implementation: (a) Experimental setup, (b) Actual shape of Type 1, (c) Actual shape of Type 2, (d) Actual shape of Type 3 123

Figure 5.13. Measurement results of three EC probe Types through the scanning process: (a) Scanning direction and Paths of EC probes for experiments, (b) Measurement result of Type 1, (c) Measurement result of Type 2, (d) Measurement result of Type 3. 125

Figure 5.14. Measurement results of three EC probe Types through two Paths: (a) Path #1 of Type 1, (b) Path #2 of Type 1, (c) Path #1 of Type 2, (d) Path #2 of Type 2, (e) Path #1 of Type 3, (d) Path #2 of Type 3. 128

Nomenclature

H : magnetic field intensity (A/m)

H_1 : alternating magnetic field surrounding the coil (A/m)

T : current vector potential (Vs/m)

\mathcal{A} : magnetic scalar potential (A)

B : magnetic flux density (T)

I_1 : alternating current applying in the coil (A)

H_2 : induced magnetic field in the test specimen (A/m)

I_2 : induced eddy current in the test specimen (A)

E : electric field intensity (V/m)

σ : electrical conductivity (S/m)

ε : electric permittivity (F/m)

ω : angular frequency of the excitation current (rad/s)

f : frequency of the excitation current (Hz)

T : period of the excitation current (s)

μ_0 : permeability of free space (H/m)

μ_r : relative permeability (H/m)

μ : magnetic permeability of the test specimen's material (H/m)

J : current density (A/m²)

J_s : current density induced by the excitation current coil (A/m²)

J_e : eddy current density within the test specimen (A/m²)

J_l : eddy current density at specific point (A/m²)

J_0 : eddy current density at the surface of the test specimen (A/m²)

I_t : eddy current within the test specimen (A)

I_e : current applied to the excitation coil (A)

U : voltage applied to the excitation coil (V)

Z : impedance of the excitation coil (Ω)

R_e : resistance of the excitation coil (Ω)

R_t : resistance of the test specimen (Ω)

R : resistance of the real part of the excitation coil (Ω)
 L_e : inductive components of the EC probe coil (H)
 L_t : inductance components of the test specimen (H)
 L : equivalent self-inductance of the imaginary part of the excitation coil (H)
 ρ : charge density (C/m^3)
 δ : skin depth (m)
 M : mutual inductance (H)
 D : electric displacement field (C/m^2)
 N : number of turns of detection coils (turn)
 Z_l : the distance from the specimen's surface to the specific point (m)
 θ : phase of the eddy current (degree)
 EC_1 : eddy current induced on the copper core by Pair #1 (A)
 EC_2 : eddy current induced on the copper core by Pair #2 (A)
 $RUEC$: rotating uniform eddy current induced on test specimen (A)
 A : amplitude of the current density (A/m^2)
 $\psi(t)$: mother wavelet
 $v(t)$: input signal of wavelet filter
 V_l : scan line signal from the RUEC probe
 S : represents the scan length of RUEC probe
 N : a length of each embedding matrix segment of MSSA
 M : number of stacking times creating the embedding matrix of MSSA
 H_l : embedding matrix of MSSA
 A : covariance matrix of MSSA
 λ_i : eigenvalues of embedding matrix of MSSA
 U, V : left and right eigenvectors of covariance matrix (C)
 $M^* = \min(M, N)$
 $N^* = \max(M, N)$
 \tilde{V}_l : reconstructed signal of MSSA

Chapter 1 :Introduction

1.1. Background

In industries such as aviation, automotive, petroleum, and bridge construction, various components like pipelines, machine parts, and conductive materials play pivotal roles in the structural integrity of these systems. Ensuring the quality and integrity of these structural components is of paramount importance to guarantee the safety and reliability of these complex systems. Tragic incidents, such as plant facility collapses resulting from gas pipeline explosions, structural failures in aircraft due to initial cracks, or bridge collapses caused by the rupture of main load-bearing cables, have inflicted substantial human and economic losses. The root cause of many of these disasters is the gradual development of cracks in structural components subjected to tensile or compressive forces, leading to a significant reduction in their fracture strength. While it is impossible to predict precisely when cracks may form in structural components, it remains essential to conduct regular inspections to identify existing cracks and potentially forecast their behavior, including location and size. This proactive approach is critical for maintaining product quality and the stability of structural components in accordance with industry standards. Nondestructive testing (NDT) stands as a cornerstone technique in various industries, encompassing both production and maintenance systems [1]–[4]. NDT allows for the examination of materials or products without causing damage, resulting in significant time and cost savings in production, maintenance, and repair processes.

The occurrence of defects during their usage poses safety risks and escalates repair costs, underscoring the necessity for reliable and efficient detection methods. Eddy current (EC) testing has emerged as one such method and has been employed for several decades [1], [5]–[9]. EC testing operates on the principle of electromagnetic induction and finds wide applications in industries like aerospace, automotive, and manufacturing [5], [8]–[16]. By inducing a magnetic field in the material under examination, EC testing generates eddy currents within the conductive material. The resultant alterations in the magnetic field can be detected and utilized to identify potential defects, including cracks or corrosion. To enhance the efficacy of EC testing, researchers have devoted their efforts to developing novel types of EC probes that enhance detection signals and mitigate noise [17]–[19]. These probes are meticulously designed to augment the sensitivity and precision of EC testing, enabling the early identification of potential defects and more accurate determination of their location and magnitude.

There exist two strategies for enhancing the effectiveness of crack detection using EC probes. The first strategy revolves around optimizing the design of both the excitation and detection coils, taking their shapes and configurations into account. An exemplary implementation of the UEC methodology is embodied by the Hoshi probe, pioneered by Hoshikawa and extensively studied [20]–[29]. By detecting these variations, the probe can identify and assess any defects or irregularities in the material. One of Hoshikawa's remarkable discoveries was related to the circular detection element. When designed with a helical pattern and equipped to be self-nulling and self-discriminating, it can effectively filter out noise signals resulting from the lifting, lowering, or scanning motions of the eddy current probe [20], [26]. Notably, this probe is designed with a self-nulling characteristic [30] and boasts a high signal-to-noise (S/N) ratio. Its purpose is to identify flaws such as weld zone cracks, surface irregularities, and discontinuities within non-magnetic stainless steel test specimens. Furthermore, it effectively mitigates the interference of lift-off noise, contributing to more accurate flaw detection outcomes. Another notable development involves an EC probe equipped with two pancake-shaped rectangular excitation coils, engineered for robust induction, owing to its self-nulling attribute and elevated S/N ratio [31], [32]. This novel EC probe is configured with a pair of rectangular excitation coils and a circular detection coil, all aligned in a pancake orientation. This deliberate design aims to optimize the probe's sensitivity to flaws while maintaining an efficient and reliable flaw detection process. In efforts to mitigate the impact of lift-off variations on measurement signals, Hoshikawa et al. [20] introduced a novel approach involving the Uniform Eddy Current (UEC) probe for detecting cracks in test pieces. The UEC concept entails a unidirectional eddy current flow following a linear trajectory across the test piece, achieved through the specialized design of the probe's excitation coil. Notably, the UEC probe exhibits intrinsic self-differential and self-nulling attributes. Probes possessing self-differential characteristics exhibit high sensitivity to localized changes in the test piece, such as the presence of cracks, while displaying lower susceptibility to lift-off fluctuations. The self-nulling aspect implies that the detection coil's output signal remains null due to a balanced state when a crack is not situated beneath the detection coil. Consequently, this feature serves to minimize the influence of lift-off variations on measurement signals, thereby bolstering the signal-to-noise (S/N) ratio of the crack signal. Numerous researchers have delved into the investigation of UECs [3], [4], [26], [30], [31], [33], [34]. A prototypical UEC probe configuration encompasses a rectangular excitation coil oriented tangentially, thus generating a UEC distribution on the test

piece, coupled with a circular detection coil characterized by self-differential and self-nulling functionalities. Nevertheless, the UEC probe generated unidirectional eddy currents in the test piece, which excelled when the UEC orientation was perpendicular to the cracks but exhibited weaker performance when the induced current was parallel to the cracks [30], [31]. To address this limitation, a Rotation Uniform Eddy Current (RUEC) probe [35], [36] was introduced, comprised of double rectangular excitation coils generating a rotating uniform eddy current on the test piece along with a circular detection coil [34]. Experimental outcomes demonstrated that the RUEC probe adeptly detected flaws in all directions.

Eddy Current Testing (ECT) applied across various industrial sectors, offers a potent means of examining residual strain [37] and residual stress [38] within low carbon steel. Nonetheless, a noticeable gap in research lies in the application of the ECT approach to detect cracks within this material. This gap can be attributed to the material's structural diversity and compositional variability, which exposes it to susceptibility to noise interference during ECT measurements. The EC probe is an indispensable instrument utilized for the assessment of conductive materials, particularly metals, while preserving their integrity [17], [39], [40]. Functioning on the principle of electromagnetic induction, the EC probe discerns defects such as cracks and anomalies on or beneath the surface [1], [41]. When performing ECT on low carbon steel, a common challenge arises from the susceptibility to noise. The relatively low electrical conductivity of low carbon steel can contribute to significant noise levels within the eddy current signals. This noise can emanate from diverse sources, encompassing electromagnetic interference, surface irregularities, and material non-uniformities. The presence of such noise has the potential to compromise the precision and dependability of defect detection and characterization when utilizing ECT on low carbon steel. To tackle this challenge, adopting an optimal probe design alongside the incorporation of ferrite cores emerges as a viable strategy for noise mitigation and enhancement of the signal-to-noise (S/N) ratio. This dual approach serves to ameliorate noise-related issues and concurrently augment the efficacy of eddy current testing on low carbon steel. Furthermore, the implementation of signal filtering techniques assumes paramount importance in this context. Employing sophisticated digital filters and adaptive algorithms, for instance, can effectively suppress undesired signals while extracting the desired crack signals with heightened efficiency [42]–[45]. By amalgamating these strategies, the integrity of defect detection and characterization on low carbon steel can be significantly elevated, surmounting the noise-related hindrances

inherent in the process.

The other strategy involves amplifying the magnetic field's intensity (applied to the test piece) through the utilization of ferrite material, a high-permeability substance, as the core material within the excitation coil [46]–[50]. In a previous investigation [51], an eddy current sensor was implemented, employing an E-shaped ferrite core. Positioned on the central leg of the E-core was the excitation coil, while two pick-up coils were anti-serially interconnected on the side legs. Another research endeavor concentrated on optimizing the design of a pulsed EC probe, encompassing various configurations: a ferrite-cored absolute probe, a ferrite-cored mutual-induction-type probe, and a ferrite-cored mutual-induction-type probe with outer shielding. This study highlighted the probe's capability to detect flaws situated more than 4 mm beneath the surface of an 8 mm thick austenite stainless steel plate [52]. A coaxial probe featuring a ferrite core brings about enhancements in the signal-to-noise ratio, sensitivity to lift-off effects, and dynamic range. Consequently, this advancement yields an improved measurement resolution [53]. This innovative design choice, integrating ferrite material into the core, not only elevates the overall performance of the EC probe but also extends its application to the detection of deeper-seated defects within challenging materials, thereby augmenting the effectiveness of flaw detection techniques. In our earlier investigation, a ferrite core was similarly incorporated into the design of the detection coil to amplify the signal-to-noise ratios within a remote field EC probe [54]–[57]. Another distinct research effort focused on augmenting the excitation capability by employing a probe featuring a C-shaped core constructed from laminated silicon steel. This specialized probe demonstrated its efficacy by successfully detecting the carburized layer through a magnetic layer positioned on the external surface of ethylene pyrolysis furnace tubes [58], [59]. The utilization of a C-shaped core, composed of laminated silicon steel, facilitated enhanced excitation performance, thereby enabling the probe to effectively penetrate through the magnetic layer and discern subsurface features, such as the carburized layer. This inventive application showcases the versatility of core materials and their strategic deployment to optimize the functionality of EC probes across diverse inspection scenarios. Analytical models have been developed to study EC probes with ferrite cores [60]–[63]. They derived the reflection coefficient for a conductor with multiple uniform layers and predicted probe impedance for a single ferrite core probe situated over the layered conductor.

In recent times, the adoption of flexible array Eddy Current (FAEC) sensors has gained

significant traction due to their remarkable capability to inspect components with intricate geometries, thus enhancing defect detection particularly in scenarios with minimal lift-off gaps [64]–[70]. A notable contribution to the advancement of FAEC sensors is the introduction of a model centered around rectangular coplanar spiral coils. This model facilitates the calculation of mutual inductance for such coils positioned above a conductive plate, significantly informing the design of these innovative probes [67]. Furthermore, the integration of Tunnel Magnetoresistance (TMR) sensors into FAEC setups has emerged as a noteworthy approach. TMR sensors play a pivotal role in quantitatively monitoring crack propagation, with their feedback sequences contributing to comprehensive defect assessment [68]. Zhang and colleagues introduced a versatile FAEC sensor capable of bending and even folding, particularly valuable for steel ball surface quality inspection [69]. Employing rectangular planar coils, this sensor demonstrated a heightened sensitivity to shallow defects, intricate surfaces, and scratches. Experimentally validating its efficacy, various defects – linear, cross, and arc cracks – were prepared on steel ball surfaces. The sensor exhibited an impressive surface defect inspection accuracy of 95.52%, coupled with a minimal false inspection rate below 0.7%. Extending the application scope, Zhang et al. ventured into the development of an FAEC sensor geared towards the detection of defects on curved surfaces of end-stage turbine blades [70]. Comprising a probe holder, flexible substrate, and an array probe, this sensor configuration showcased the alignment of defect size, position, and shape with reality. While FAEC sensors have demonstrated remarkable benefits in the realm of ECT, it's essential to acknowledge a drawback – the correlation between the number of turns and the induced EC amplitude on the sample surface. Despite this limitation, FAEC sensors continue to drive advancements in defect detection, enabling efficient evaluation of complex geometries and enhancing the precision of nondestructive evaluation.

In a different domain of research, scientists have undertaken investigations into amorphous and nanomagnetic materials, which encompass attributes like high permeability and a substantial saturation magnetic flux density (B_s) [71]. Notably, the saturation magnetic flux density (B_s) within iron-based amorphous alloys has been enhanced to 1.64 T, thereby manifesting a significant performance enhancement in magnetic devices, including sensors and transformers [72]. Furthermore, a comparative study has indicated that the magnetic softness exhibited by Fe–Si–B-based alloys surpasses that of Fe–Zr–B-based alloys by approximately 5–10 times [73]. This signifies a crucial advancement, as materials with higher magnetic softness tend to display superior

magnetic performance, making them particularly valuable for various applications in the field of electromagnetics and magnetic devices.

1.2. Motivation

The primary objective of this study is to explore methods for improving the effectiveness of eddy current (EC) probes in the detection of cracks by varying core shapes and materials. Specifically, a core constructed from copper, known for its elevated electrical conductivity and absence of magnetic properties, is applied to generate converging eddy currents. Conversely, a core comprising a blend of ferrite and ferromagnetic amorphous alloy particles, possessing characteristics of non-electrical conductivity and magnetic properties, are utilized to amplify the excitation magnetic field.

This study underscores the aim of attaining two pivotal benefits: heightened sensitivity and enhanced reliability in predicting crack depths. These advantages stem from the strategic amalgamation of traits inherent in traditional EC probes. The incorporation of a copper core alongside magnetic alloy particles results in a distinctive combination, augmenting the discriminatory capabilities and precision of the probe's measurements. As a consequence, the intent of this study is to contribute to the advancement of EC technology for widespread implementation in the examination and surveillance of material structures, particularly in achieving accurate and efficient crack detection.

1.3. Objectives

Based on *Notice No.93 of the Office of Hazardous Materials Regulation* [74], cracks in the welded joint between the side plate and the annular plate, experiencing severe stress conditions, should not surpass 1.5 mm in depth and 4.0 mm in length. Therefore, within the scope of our study, we created artificial cracks with dimensions spanning lengths from 1mm to 40mm and depths from 1mm to 4mm. The width of these artificially induced cracks was precisely maintained at 0.5mm.

Initially, emphasis was placed on crafting an inventive EC probe distinguished by a copper core, incorporating distinctive features like horizontal and vertical slits, along with a conical structure. This probe demonstrated remarkable crack detection capabilities on aluminum plates, employing a singular circular detection coil. Challenges related to sensitivity to lift-off distance prompted the enhancement of the signal-to-noise (S/N) ratio through two approaches: a differential signal method utilizing two detection coils and the introduction of a groundbreaking EC convergence probe with paired copper cores and a unidirectional EC (UEC) component.

In addressing a specific ECC probe challenge, where crack signal amplitude varied with EC line orientation, a rotating uniform eddy current convergence (RUECC) probe was introduced. This intricately designed probe, featuring a specialized copper core, successfully generated rotating ECs on the specimen's surface, surmounting limitations faced by previous ECC probes and significantly improving crack detection capabilities in all orientations.

Furthermore, exploration extended to the development of a rotating uniform eddy current (RUEC) probe for artificial crack identification in conductive materials. This probe, equipped with four coils and ferrite cores, demonstrated uniform RUEC distribution across all directions on the test specimen's surface, as validated through finite element method simulations and practical experiments.

The study also introduced a square-film EC probe tailored for surface crack detection on aluminum. This probe, incorporating iron-based ferromagnetic amorphous alloy particles (FAAP), demonstrated improved magnetic flux density and enhanced crack detection capabilities, validated through finite element simulations and practical experiments on aluminum plates.

Finally, the configuration of EC probes was explored, examining three distinct orientations relative to the test specimen's surface. Finite element analysis and experimental trials were employed to assess EC generation efficiency and crack detection efficacy for each configuration.

In summary, the objectives of this study encompassed the development of novel EC probes, the enhancement of S/N ratios, the introduction of innovative RUECC and RUEC probes, and the exploration of a square-film EC probe, contributing significantly to the advancement of eddy current inspection technology across various applications.

1.4. The outline of dissertation

This dissertation comprises 6 chapters, each serving a distinct purpose. In **Chapter 1**, a succinct overview is presented, encompassing the Background, Eddy Current Testing in Non-destructive Testing, Motivation, Objectives, and the overall structure of the dissertation. The primary goal of this chapter is to delve into methodologies aimed at augmenting the efficacy of eddy current (EC) probes in the detection of cracks, employing varied core shapes and materials. Specifically, a copper core, recognized for its elevated electrical conductivity and non-magnetic characteristics, is harnessed to generate converging eddy currents. In contrast, a core composed of a blend of non-oriented copper and iron alloy particles, possessing both electrical conductivity and magnetic attributes, is deployed to amplify the excitation magnetic field. The utilization of these

diverse core materials and shapes is central to the investigation's objective of refining crack detection capabilities.

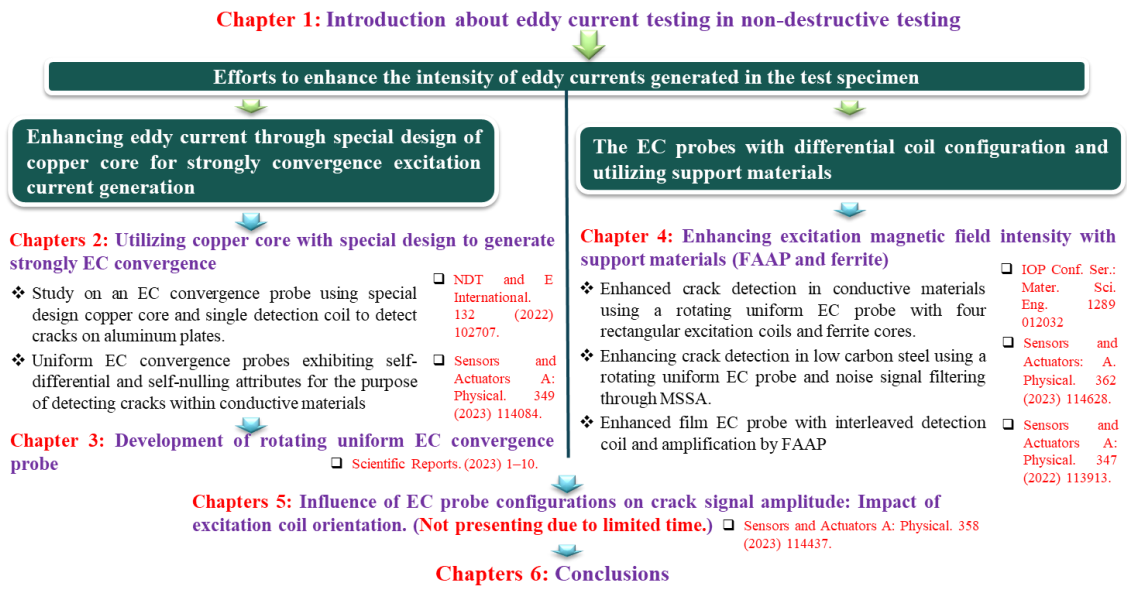


Figure 1.1 Flowchart of eddy current probe investigation in the dissertation

Chapter 2 initiates the discussion by detailing the creation of an unconventional EC probe, deviating from the conventional use of ferrite cores. Instead, a copper core with high electrical conductivity and non-magnetic properties is employed. The copper core is meticulously designed with horizontal and vertical slits, complemented by a conical structure, aiming to regulate the EC flow. This innovative design concentrates EC convergence at the tip of the copper core, resulting in strong induction effects on the test specimen. Further augmentation of its capabilities involves the incorporation of a single circular detection coil at the core's center, enabling effective crack detection on aluminum plates, as validated by the remarkable outcomes in experimental trials. However, a sensitivity challenge arises with the EC convergence probe, particularly regarding variations in lift-off distance, impacting the signal-to-noise ratio (S/N). To address this challenge, two approaches are introduced to enhance the S/N ratio. Firstly, a differential signal approach is implemented using two detection coils. Additionally, a novel EC convergence probe, featuring paired copper cores and a unidirectional EC (UEC) component, is introduced. This design produces an output signal with a single circular detection, aligning with self-differential and self-nulling characteristics.

Chapter 3 introduced the Uniform Rotating Eddy Current Convergence (RUECC) probe that can address the limitations of ECC probe in Chapter 2. The probe not only inherited the

strengths of its predecessors, such as the capability to converge eddy currents and manifest self-nulling and self-differencing characteristics found in earlier ECC probes, but also, through enhanced design, engendered rotating uniform eddy currents. This innovation significantly bolstered the adaptability of the RUECC probe in identifying cracks of all sizes and directions. This represents a substantial stride forward in enhancing crack detection sensitivity, positioning the RUECC probe as a promising instrument in the continuous evolution of non-destructive testing methodologies.

Chapter 4 introduces a novel RUEC probe engineered for the identification of artificial cracks in conductive materials. This probe, constructed with four rectangular coils and ferrite cores, achieves a uniform RUEC distribution across all directions on the test specimen's surface. FEM simulations and experimental trials validate the probe's successful crack detection capabilities. Moreover, to refine the measurement outcomes, we subjected them to multivariate singular spectral analysis (MSSA) for noise reduction. Subsequently, we conducted a comparative analysis between the denoised results obtained through MSSA and those derived from wavelet-based principal component analysis (wavelet-PCA) and a Denoise Filter. Additionally, the chapter explores a square-film EC probe designed for the detection of surface cracks on aluminum. This probe features a detection coil interleaved with the excitation coil, and iron-based ferromagnetic amorphous alloy particles (FAAP) are incorporated to enhance magnetic flux density. Finite element simulations and practical experiments confirm the substantial enhancement in crack-detection capabilities attributed to the integration of FAAP.

Chapter 5 shifts the focus to the configuration analysis of UEC probes, scrutinizing three distinct EC probe configurations with orientations either pancake-like or tangential to the test specimen's surface. Finite element analysis and experimental trials are employed to assess EC generation efficiency and crack detection efficacy for each configuration.

Chapter 6, the concluding chapter, encapsulates the comprehensive results derived from the exploration of advancements in eddy current (EC) probe technology for crack detection in conductive materials. A synthesis of the various studies presented in preceding chapters leads to several key conclusions.

1.5. Eddy Current Testing in Non-destructive Testing

1.5.1. Eddy current testing probes

The eddy current testing probe was introduced as a single-coil type, featuring only one coil

that served dual purposes as both the excitation and detection coil. Its operating principle involves measuring the change in impedance that occurs within the probe when a phenomenon alters the characteristics of the test object [75]. This probe model is simple, easy to use, and generates a robust detection signal, making it suitable for defect detection and predicting the length of defects. However, it is important to note that this type of probe has a limitation - it cannot predict the depth of a defect. The impedance is significantly affected by the lift-off of the coil from the test object, leading to inaccuracies in the measurement results. This means that even though the probe is effective in detecting defects and assessing their length, it falls short when it comes to providing information about the depth of the defects. Consequently, when depth measurement is crucial, this probe model may not be the most suitable choice.

Researchers have developed the transmit-received probe model, which includes two coils: the excitation coil and the detection coil. The main purpose of separating the functions of these coils is to minimize the negative impact of lift-off on the excitation coil during measurements. This approach has been successful in reducing the lift-off effect, which is a significant improvement. However, there is a downside to this advancement. Because of the separation, the detection signal tends to become weaker. To overcome this issue and maintain an acceptable level of detection signal strength, more excitation power is now required. This additional power helps boost the detection signal, compensating for the weakened output due to coil function separation. Despite these improvements, there is still a challenge when it comes to defect depth measurement. The confidence in the measurement results remains relatively low. This is because even though the lift-off effect has been minimized, it still has a considerable influence on the signal-to-noise ratio. As a result, the detection signal, being weaker, gets buried in noise, making it challenging to obtain accurate depth measurements [76], [77].

With the demand for advanced testing capabilities on the rise, which necessitates strict adherence to standard criteria and the ability to scan a wide variety of material properties, researchers are continuously conducting studies to develop new and improved probe models. Currently, NDT equipment market, including eddy current probes, is shifting towards more mobile, energy-efficient devices with extended battery life, heightened sensitivity, and the capacity to detect even smaller and buried defects. To meet this evolving industry demand and address the challenges, the research team has focused on creating innovative ECT probes. The primary aim of this advanced design is to cater to the dynamic needs of the industry and enhance the capabilities

of defect detection.

1.5.2. The theory of eddy current testing

One significant application of the EC effect is ECT. The underlying principle of ECT is illustrated in Figure 1.1. When an alternating current (I_1) with a specific frequency is applied to both ends of the coil depicted in the diagram, it generates an alternating magnetic field (H_1) surrounding the coil. As the coil is brought close to a conductive test specimen, the alternating magnetic field interacts with the specimen, inducing a secondary current (I_2) within the test piece. This induced current flows in a circular pattern inside the test specimen, creating a loop known as the "eddy current." Based on the principle of electromagnetic induction, the induced current (I_2) also generates another induced magnetic field (H_2). Due to Lenz's law, the direction of the original magnetic field (H_1) and the induced magnetic field (H_2) is opposite, leading to the opposition of the induced magnetic field to the original magnetic field. This phenomenon is referred to as the electromagnetic induction effect. The change in the coil impedance signal reflects this phenomenon. By measuring the coil impedance, it becomes possible to detect defects within the test specimen, allowing for the evaluation of its performance.

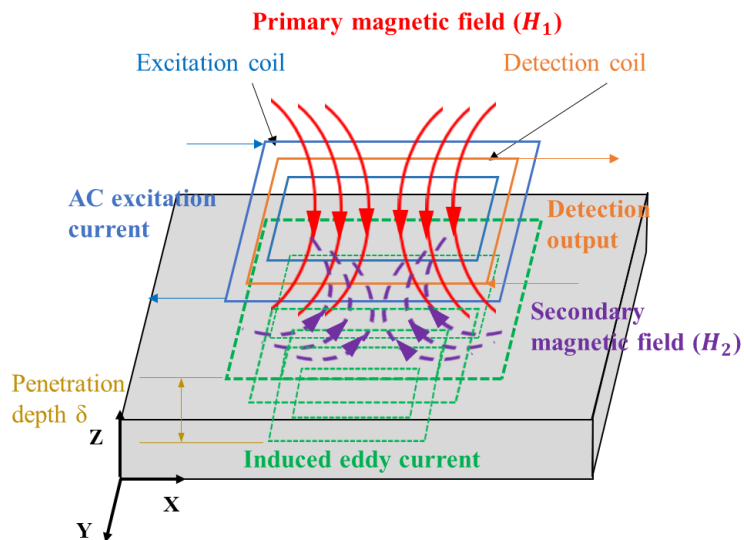


Figure 1.2. The principle of ECT sensor.

The intricate interaction of electromagnetic phenomena within a specimen under examination, exemplified in the context of material assessment using ECT sensors, follows the principles established by Maxwell's equation [78]. This relationship is further explained through Equation 1.1:

$$\nabla \times B = \mu_r \mu_0 (J_s + J_e + \frac{\partial D}{\partial t}) \quad (1.1)$$

On the left side of the equation, the symbol $\nabla \times B$ denotes the rotational behavior of the combined primary and secondary magnetic fields, collectively represented as B , within a defined spatial context. It illustrates how B evolves and spreads throughout the specified space. The terms on the right side of the equation account for the sources responsible for generating the magnetic field and inducing modifications to it. J_s represents the current induced by the excitation current coil when an alternating current is applied to the sensor. $J_e = \sigma E$ signifies the occurrence of ECs within the test specimen, a phenomenon directly proportional to the electric field intensity (E) at the specimen's surface. Here, σ denotes the surface electrical conductivity of the test specimen, a crucial factor determining its electrical conductivity. Additionally, μ_r and μ_0 respectively stand for the relative permeability and vacuum permeability of the test specimen. Lastly, $\partial D/\partial t$ indicates the temporal change in displacement current density, which can be disregarded at low frequencies in the ECT sensor.

The electrical conductivity (σ) exhibits notable variations between regions with and without cracks. For example, when examining an aluminum sample, it may range from 38.0 S/m to as low as 0 S/m. Consequently, the value of J_e in Equation (1.1) decreases to zero, causing changes in both magnetic and voltage detection. It's noteworthy that cracks don't disrupt the primary magnetic field; instead, they modify the secondary magnetic field within the test specimen. In this context, the output signal of the detection coil depends on several factors: the number of detection coils within the ECT sensor, changes in the magnetic field (B) across a surface area (S) [66], and it is computed using Equation (1.2):

$$V_{out} = -N \frac{d}{dt} \int_S B dS \quad (1.2)$$

ECs, emerging at various depths within the test specimen, can be calculated using Equation (1.3) [79]. It becomes apparent upon examination that the amplitude of the induced EC experiences an exponential decrease, while the phase of the EC undergoes a linear delay with increasing depth.

$$J_l = J_0 e^{-\frac{Z_l}{\delta}} \quad (1.3)$$

In this equation, J represents the EC density at depth l , and I_0 denotes the EC density at the surface of the test specimen. Z_l is determined as the distance from the specimen's surface to the specific point of interest beneath it, indicating the depth of the skin layer. When the EC density at

a particular depth within the experimental specimen decreases to 1/e of the EC density generated at the specimen's surface, this depth is referred to as the penetration depth. It is calculated using Equation (1.4):

$$\delta = \frac{1}{\sqrt{\pi f \mu \sigma}} \quad (1.4)$$

The equation governing the determination of the phase (θ) of the EC at a specific location beneath the surface, induced by a nearby source of EC, is an integral component of Equation (1.3) and is derived through the following expression:

$$\theta = \frac{Z_l}{\delta} \quad (1.5)$$

ECT is an NDT technique used to inspect and evaluate the integrity of conductive materials, such as metals. It relies on the principle of electromagnetic induction, where a time-varying magnetic field induces eddy currents in the conductive material. Maxwell's equations govern the behavior of electromagnetic fields in conductive materials. Four Maxwell's equations for ECT can be written as follows:

- The connection between the change in magnetic field intensity H (on the left-hand side) and the combined effect of the surface current density contribution (σE) along with the surface current density resulting from the interplay between the electric field and the medium ($j\omega \epsilon E$, on the right-hand side):

$$\nabla \times H = (\sigma + j\omega \epsilon)E \quad (1.6)$$

In this equation:

$\nabla \times H$ is the curl of the magnetic field intensity vector H , as explained before.

σ is the electrical conductivity of the medium, indicating the medium's ability to conduct electricity.

$j\omega \epsilon$ represents the product of surface current density and the electric permittivity ϵ of the medium.

E is the electric field.

- Ampère's law with Maxwell's addition asserts that the curl of the electric field is proportionally linked to the negation of the current density-magnetic field intensity product. This correlation underscores the interplay between evolving electric fields and the generation of

magnetic fields:

$$\nabla \times E = -j\omega\mu H \quad (1.7)$$

In this equation:

$\nabla \times E$: represents the curl of the electric field vector E . The curl measures the rotation or circulation of a vector field in space.

$j\omega\mu$: This term consists of the current density vector j multiplied by the angular frequency (ω) and the magnetic permeability (μ) of the medium, ω is the angular frequency of the excitation current, and μ is the magnetic permeability of the medium.

- Gauss's law for magnetism asserts that the divergence of the magnetic field intensity is null. Put more simply, this signifies that magnetic field lines neither initiate nor converge at any point (origins or endpoints). Instead, the magnetic field is characterized as being solenoidal or devoid of divergence, implying the formation of closed loops:

$$\nabla \cdot H = 0 \quad (1.8)$$

In this equation:

$\nabla \cdot H$: represents the divergence of the magnetic field intensity vector H . Divergence measures the rate at which a vector field "spreads out" from a point.

- Gauss's law for electric fields asserts that the divergence of the electric field at any given point within space is equivalent to the electric charge density at that precise location, divided by the electric permittivity of the medium. In simpler terms, this equation indicates that the electric flux (the movement of electric field lines) departing from an enclosed surface corresponds to the total charge enclosed by that surface, with the proportionality constant being contingent upon the electric permittivity of the material where the charges reside. This equation holds as a foundational tenet in electromagnetism and contributes to elucidating the generation of electric fields by electric charges. It elucidates the way electric charges give rise to electric fields that emanate outward, with the degree of field expansion being determined by the charge density and the attributes of the surrounding medium:

$$\nabla \cdot E = \frac{\rho}{\epsilon} \quad (1.9)$$

In this equation:

$\nabla \cdot E$: represents the divergence of the electric field vector E . Divergence measures how much the electric field "spreads out" from a point.

ρ : symbolizes the charge density, which indicates the amount of electric charge per unit volume.

ϵ : represents the electric permittivity of the medium, which characterizes the ability of the medium to store electrical energy.

However, in the case of eddy currents, it is common to neglect the contribution of the free charge's density (ρ) in conductive materials, considering it to be nearly zero due to the rapid motion of these free charges. As a result, the divergence of the electric field (E) is approximately zero in the quasistatic approximation, leading to the transformation of equation (1.10) to:

$$\nabla \cdot E = 0 \quad (1.10)$$

By multiplying both sides of equation (1.6) with the Nabla operator, we undergo a transformation, resulting in:

$$\nabla \times \nabla \times H = (\sigma + j\omega\epsilon)\nabla \times E \quad (1.11)$$

Expanding the Nabla operator using the operation $\nabla \times \nabla \times H = \nabla(\nabla \cdot H) - \nabla^2 H$, where $\nabla \cdot H = 0$ according to equation (1.8), yields equation (1.12):

$$-\nabla^2 H = (\sigma + j\omega\epsilon)\nabla \times E \quad (1.12)$$

By substituting the value $\nabla \times E = -j\omega\mu H$ from equation (1.7) into equation (1.12), we arrive at equation (1.13) and (1.14):

$$-\nabla^2 H = (\sigma + j\omega\epsilon)j\omega\mu H \quad (1.13)$$

$$-\nabla^2 H - (j\omega\mu\sigma - \omega^2\mu\epsilon)H = 0 \quad (1.14)$$

From equations (1.13) and (1.14), it becomes evident that the medium's electromagnetic field assumes a wave-like behavior. In practical calculations, it's observed that the value of σ within the parentheses of equation (1.8) significantly surpasses the $\omega\epsilon$ value. This is due to the high electrical conductivity of metals (σ), approximately 10^7 (S/m), in contrast to the vacuum's electric constant $\epsilon = 8.85 \times 10^{-12}$ (F/m). As a result, the $\omega\epsilon$ term becomes minuscule, thus rationalizing its omission. Consequently, equation (1.14) can be elegantly simplified to:

$$-\nabla^2 H - j\omega\mu\sigma H = 0 \quad (1.15)$$

Utilizing a methodology akin to the calculation, we derive the subsequent equations:

$$-\nabla^2 E - j\omega\mu\sigma E = 0 \quad (1.16)$$

$$-\nabla^2 J - j\omega\mu\sigma J = 0 \quad (1.17)$$

These equations serve to depict the operational mechanisms of electromagnetic fields, magnetic field intensity (H), electric field intensity (E), and current density (J) within conductive materials during eddy current testing. They enable an understanding of how eddy currents are induced within conductive materials when exposed to a varying magnetic field. These eddy currents can be attenuated or influenced by defects or alterations in the material's physical properties. Through the analysis of these equations, we can anticipate the response of eddy currents to such changes and thereby ascertain the presence of defects.

To confirm the EC flow of copper core and induction EC to the surface of the test piece, a time-harmonic analysis was carried out by employing finite element analysis software (Magnet 7.9). The eddy current problem is solved by Magnet 7.9 software using the $T-\Omega$ method through the following the equations:

$$\text{rot}\left(\frac{1}{\sigma}\text{rot}\mathbf{T}\right) = -\frac{\partial}{\partial t}\{\mu(H_1 + T - \text{grad}\Omega)\} \quad (1.18)$$

$$\text{div}\{\mu(H_1 + T - \text{grad}\Omega)\} = 0 \quad (1.19)$$

By simultaneously solving equations (1.18) and (1.19), it is possible to analyze the magnetic field and eddy current on the test specimen.

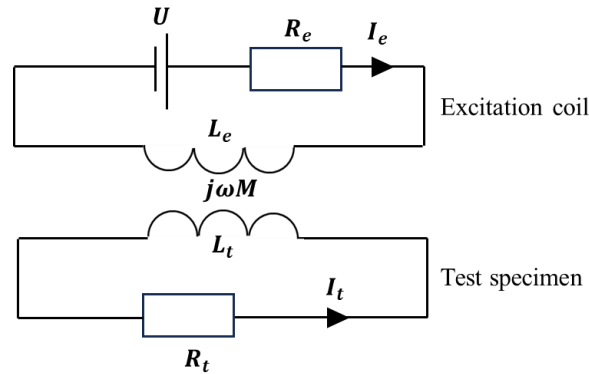


Figure 1.3. The equivalent model diagram of ECT

To comprehend the relationship between the parameters of the excitation coil and the characteristics of the test specimen, a proposed equivalent model features two mutually coupled AC circuits, as illustrated in Figure 1.2. This facilitates the implementation of impedance analysis, a widely employed technique in ECT.

To comprehend the interaction between the excitation coil and the test specimen, we employ an equivalent transformer circuit to model this scenario. The primary circuit is composed

of elements R_e , which represent the resistance of the excitation coil, along with a closed circuit incorporating inductive components L_e of the EC probe coil. Similarly, the secondary circuit includes elements R_t , representing the resistance of the test specimen, and a closed circuit featuring inductive components L_t of the test specimen. Here, U represents the excitation voltage across the excitation coil's terminals, and M signifies the mutual inductance shared between the excitation coil and the test specimen. The voltage equations within the primary and secondary circuits conform to Kirchhoff's laws:

$$(R_e + j\omega L_e)I_e - j\omega MI_t = U \quad (1.20)$$

$$(R_t + j\omega L_t)I_t - j\omega MI_e = 0 \quad (1.21)$$

By transforming equations (1.20) and (1.21), the equivalent impedance of the excitation coil is derived and expressed in equation (1.22):

$$Z = \frac{U}{I_e} = R_e + \frac{(2\pi f)^2 M^2}{R_t^2 + (2\pi f)^2 L_t^2} R_t + j \left(2\pi f L_e - \frac{(2\pi f)^3 M^2 L_t}{R_t^2 + (2\pi f)^2 L_t^2} \right) \quad (1.22)$$

From the equations, the equivalent resistance of the real part (R) and the equivalent self-inductance of the imaginary part (L) of the excitation coil can be computed through equations (1.23 and 1.24):

$$R = R_e + \frac{(2\pi f)^2 M^2}{R_t^2 + (2\pi f)^2 L_t^2} R_t \quad (1.23)$$

$$L = 2\pi f L_e - \frac{(2\pi f)^3 M^2 L_t}{R_t^2 + (2\pi f)^2 L_t^2} \quad (1.24)$$

Upon analyzing equation (1.22), a clear pattern emerges: the mutual inductance (M) amplifies as the distance between the excitation coil and the test specimen diminishes, irrespective of the test specimen's magnetic properties. The influences impacting the equivalent self-inductance (L) encompass dual factors: the magnetic effect (linked to the specimen's magnetic attributes) affecting L_e , and the eddy current effect affecting L_t , collectively yielding a counteractive influence on the equivalent self-inductance due to these two effects. When the EC probe is situated close to the test object, the equivalent self-inductance of the EC probe experiences an upsurge, and conversely, a reduction occurs (referred to as the lift-off effect). In contrast, when the test specimen is either non-magnetic or magnetic, the primary driver of the equivalent self-inductance (L) within the excitation coil is the eddy current effect engendered within the test specimen, culminating in a reduction of the EC probe's equivalent self-inductance.

Chapter 2 : Utilizing copper core with special design to generate strongly convergence eddy current

2.1. Introduction

In this chapter, a novel approach was pursued, diverging from the conventional development of EC probes utilizing ferrite cores. Instead, a copper core endowed with high electrical conductivity and non-magnetic attributes was harnessed as the foundational element for the creation of the innovative EC convergence (ECC) probe. The distinctive design of the copper core encompasses two slits, oriented both horizontally and vertically, coupled with a conical shape positioned at the lower portion. These intricate structural features were strategically engineered to regulate the flow of eddy currents within the core. The resulting outcome is the emergence of a concentrated eddy current at the apex of the copper core, generating robust induction within the test piece. To complement this, a singular circular detection coil was thoughtfully integrated at the bottom and center of the copper core to facilitate flaw detection. The induction effect of the ECC probe, featuring the copper core, on the test piece was meticulously evaluated through finite element simulations. Subsequently, a series of experimental trials were conducted using the developed probe, affirming its exceptional capabilities in flaw detection. The amalgamation of theoretical analysis and empirical experimentation underscores the potency of the novel ECC probe with a copper core, positioning it as a promising advancement in NDT methodologies.

As previously delineated, the fundamental objective of this chapter revolved around the development of UECC probes. These probes were equipped with either two detection coils or a singular detection coil, both of which were endowed with self-differential and self-nulling attributes. The primary target of these probes was the detection of surface cracks in aluminum. To fulfill this objective, an intricate analysis of the EC induced on the aluminum test piece surface by the EC convergence probes with either two detection coils or a singular detection coil was executed utilizing finite element method (FEM) simulations. Subsequently, empirical tests were conducted to assess the efficacy of crack detection on the aluminum surface using the UECC probes configurations.

2.2. Study on an eddy current convergence probe using special design copper core and single detection coil to detect flaws on aluminum plates

2.2.1. Materials and Methods

2.2.1.1. Design of ECC probe with copper core (Type 1)

Illustrated in Figure 2.1 is the schematic representation of an ECC probe (referred to as Type 1) configuration. This advanced design comprises an excitation coil interplaying with a copper core. The copper core is thoughtfully engineered with two strategic slits, oriented both horizontally and vertically, in conjunction with a conically shaped lower segment. This intricately crafted structure serves to adeptly govern the flow of eddy currents generated by the excitation coil. The outcome of this meticulous design is the convergence of eddy currents at the apex of the copper core, thereby yielding a potent induction effect upon the test piece. It's noteworthy that the core structure is conceptually aligned with the framework elucidated in a prior investigation [80]. The excitation coil is composed of 700 turns, wound using copper wire featuring a diameter of 0.2 mm. This specific configuration and winding technique contribute to the excitation coil's ability to generate a robust electromagnetic field within the ECC probe. The synergy between the excitation coil and the intricately designed copper core establishes the foundation for the ECC probe's efficacy in flaw detection and evaluation.

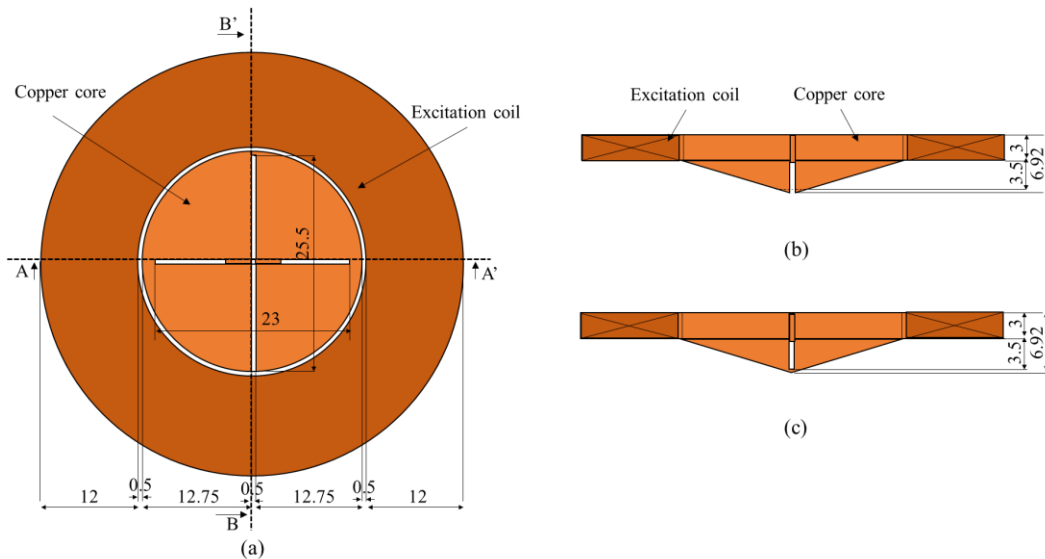


Figure 2.1. Structure of ECC probe (Unit in mm): (a) Top view, (b) Section view of A-A', (c) Section view of B-B'.

2.2.1.2. Design of ECC probe with hollows and plate under the excitation coil (Type 2)

Depicted in Figure 2.2 is the configuration of an ECC probe distinguished by its incorporation of hollows and a plate beneath the excitation coil (referred to as Type 2). The underlying structural blueprint of Type 2 mirrors that of Type 1. However, in this variant, strategic modifications have been introduced. Specifically, the traditional slits in the copper core have been

replaced with a plate positioned beneath the excitation coil, and a hollow feature has been introduced within the core itself. These meticulous adjustments collectively facilitate the convergence of a more robust EC at the tip of the copper core. Akin to Type 1, the excitation coil of Type 2 comprises the same number of turns, reinforcing the comparability of the ensuing results. The utilization of identical excitation coil parameters between the two types enables a direct comparison of the EC induction effects achieved at the tip of the copper core. This comparative approach aims to provide valuable insights into the impact of the introduced modifications on the EC behavior within the probe's configuration.

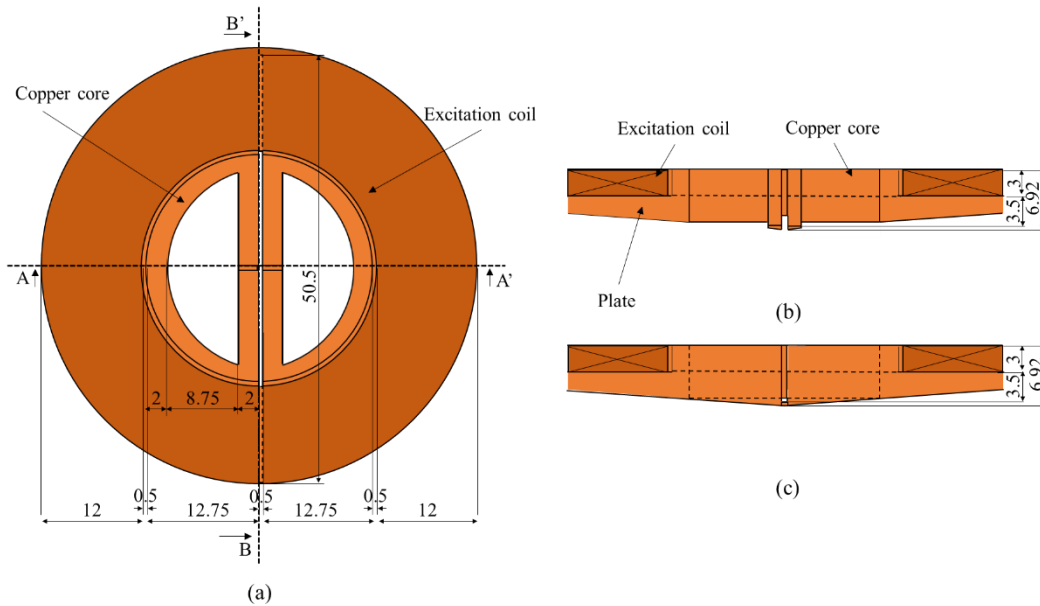


Figure 2.2. Structure of ECC probe with hollows and a plate under the excitation coil. (Unit in mm): (a) Top view, (b) Section view of A-A', (c) Section view of B-B'.

2.2.1.3. Finite element simulation with ECC probe

To validate the trajectory of EC within the copper core, as illustrated in both Figures. 2.1 and 2.2, and to ascertain the resultant EC induction on the test piece's surface, a meticulous time-harmonic analysis was conducted employing finite element analysis software (Magnet 7 version 7.9.0.18, Mentor Graphics Corporation). The analytical representation of the ECC probe, featuring a copper core, is depicted in Figure 2.3.

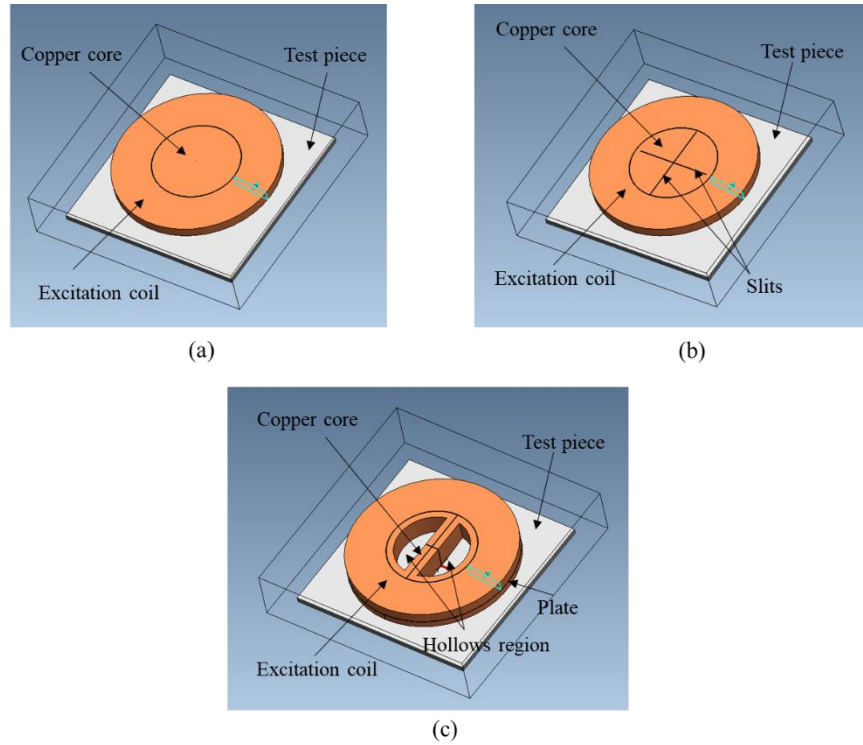


Figure 2.3. Structure of ECC probe with hollows and a plate under the excitation coil. (Unit in mm): (a) Top view, (b) Section view of A-A', (c) Section view of B-B'.

Figure 2.3(a) serves as a reference, depicting an EC probe equipped with a copper core devoid of any slits, thereby facilitating a direct comparison with the ECC probes outfitted with slits, hollows, and a plate. This juxtaposition allows for a comprehensive assessment of the influence of these structural alterations on the EC behavior, aiding in drawing insightful conclusions about their respective impacts on the induction and convergence of EC within the probe's configuration.

Table 2.1 Electromagnetic parameters of the ECC probes utilized in the analysis.

	Material	Electrical conductivity, σ (MS/m)	Relative permeability, μ_r
Wire of Excitation coil			
Wire of Detection coil	Copper	57.7	1.0
Core of coil			
Test piece	Aluminum	38.0	

The analysis employed ECC probes with specifications consistent with those illustrated in Figures 2.1 and 2.2. These specific probe configurations were chosen for the purpose of conducting a thorough investigation into their performance characteristics. To simulate real-world conditions, an aluminum plate measuring 70 mm in length, 70 mm in width, and 10 mm in thickness was selected as the test specimen. The electromagnetic parameters integral to this analysis are comprehensively outlined in Table 2.1. During the simulation, the ECC probes were subjected to an excitation frequency of 10 kHz, while an excitation current of 10 mA was applied. These specific values were thoughtfully chosen to provide a controlled environment for assessing the probes' interactions with the aluminum plate test piece.

Figure 2.4 illustrates arrow and contour plots depicting the distribution of ECs across the surface of the copper core within the EC convergence probe. In Figure 2.5, similar arrow and contour plots showcase the EC distribution along the B-B section of the copper core within the ECC probe.

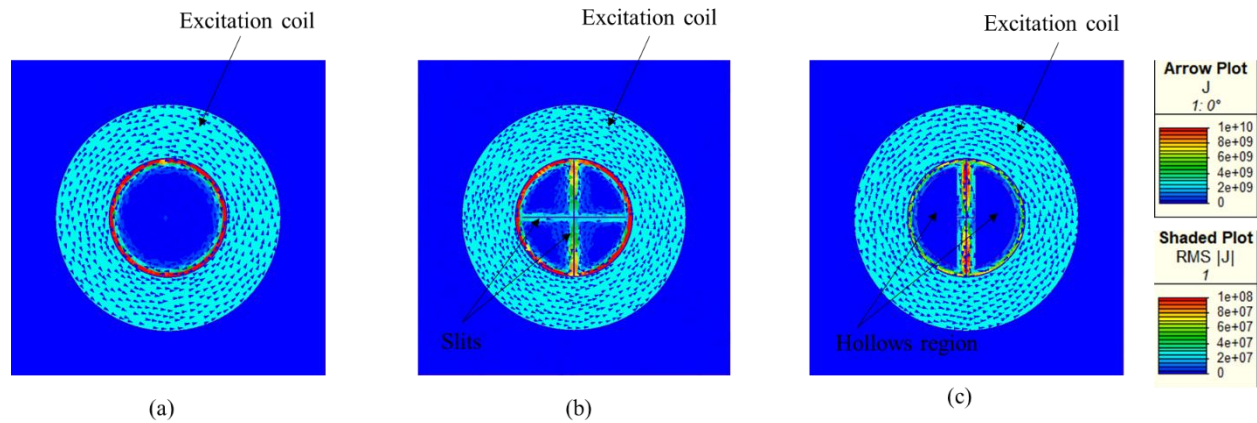


Figure 2.4. Contour and arrow plots of the EC distribution on the surface of the copper core of EC probe: (a) Without slit, (b) With slits, (c) With hollows and a plate under the excitation coil.

As depicted in Figure 2.4(a), the analytical outcomes indicate that the EC generated within the copper core predominantly circulates along the outer periphery of the copper core. However, these currents do not exhibit convergence towards the tip of the copper core, as observed in Figure 2.5(a). Consequently, the resultant induced EC on the test piece appears to be minimal, as illustrated in Figure 2.6(a). In the context of the modified EC convergence probe, the incorporation of slits, hollows, and a plate within the copper core initiates a significant transformation in the distribution of eddy currents (EC), a phenomenon visually captured in Figures 2.4(b) and 2.4(c). This structural adjustment introduces distinctive pathways for the flow of EC, particularly

accentuated along the introduced slits. Consequently, these architectural enhancements engender a directed movement of EC towards the terminus of the copper core, propelled by the influence of the slits and hollows. This convergence is vividly depicted in Figures 2.5(b) and 2.5(c), where the EC congregates at the tip of the copper core.

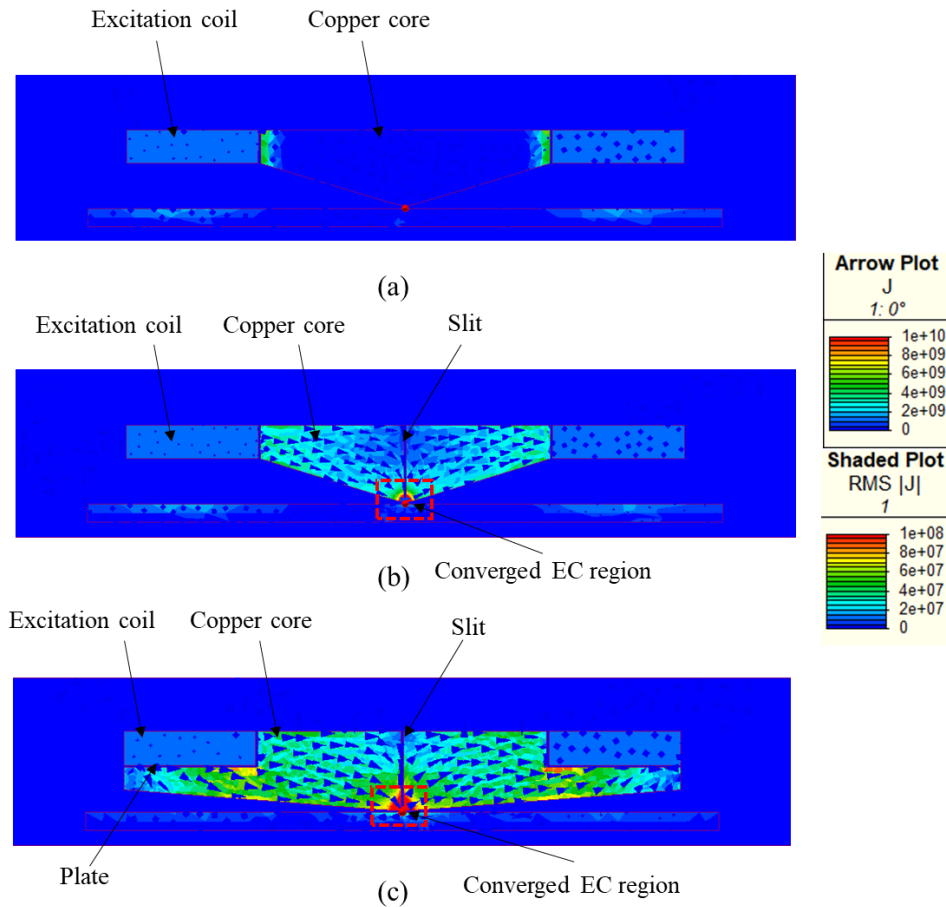


Figure 2.5. Contour and arrow plots of the EC distribution on cross-section B-B' of the probe: (a) Without slit, (b) With slits, (c) With hollows and a plate under the excitation coil.

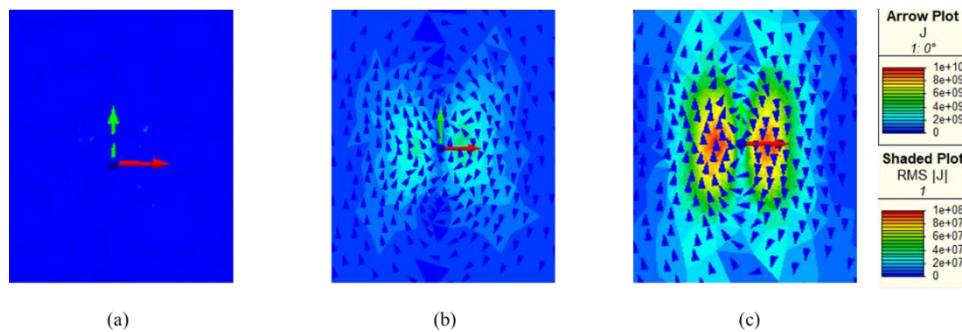


Figure 2.6. Contour plot of the EC distribution on the surface of the test piece: (a) Without slit,

(b) With slits, (c) With hollows and a plate under the excitation coil.

This orchestrated shift in the flow of EC culminates in the induction of significant EC effects onto the test piece. This induction is primarily attributed to the orchestrated convergence of eddy currents at the tip of the copper core, generating a strong EC upon the test piece's surface. This transformative process is thoughtfully captured in Figures 2.6(b) and 2.6(c).

2.2.1.4. Principle of output signal with a single detection coil

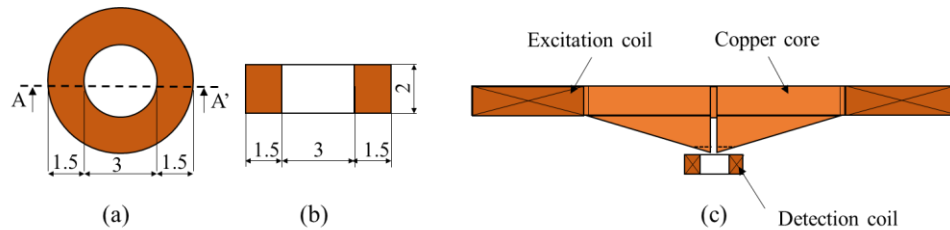


Figure 2.7. Structure of a detection coil: (a) Top view, (b) Section view of A-A', (c) The placement of the detection coil.

Figure 2.7 provides an insight into the configuration of the detection coil employed in the study. Elaborating on the characteristics of the circular detection coil, Figures 2.7(a) and 2.7(b) meticulously outline its specifications. With a total of 854 turns, the detection coil is meticulously constructed using copper wire of 0.02 mm diameter. This coil is strategically positioned at the central and lower segment of the copper core, a placement thoughtfully depicted in Figure 2.7(c).

2.2.2. Experiment with ECC probe

For the experimental evaluation, an aluminum plate was chosen as the test specimen, with its particulars presented in Figure 2.8. To emulate real-world scenarios, four artificial flaws, varying in lengths and depths, were meticulously crafted within the aluminum plate through the utilization of electrical discharge machining. The exact dimensions of these simulated flaws are meticulously documented in Table 2.2 for reference. Furthermore, essential details regarding the excitation and detection coils can be found in Table 2.3, offering a comprehensive overview of the experimental setup.

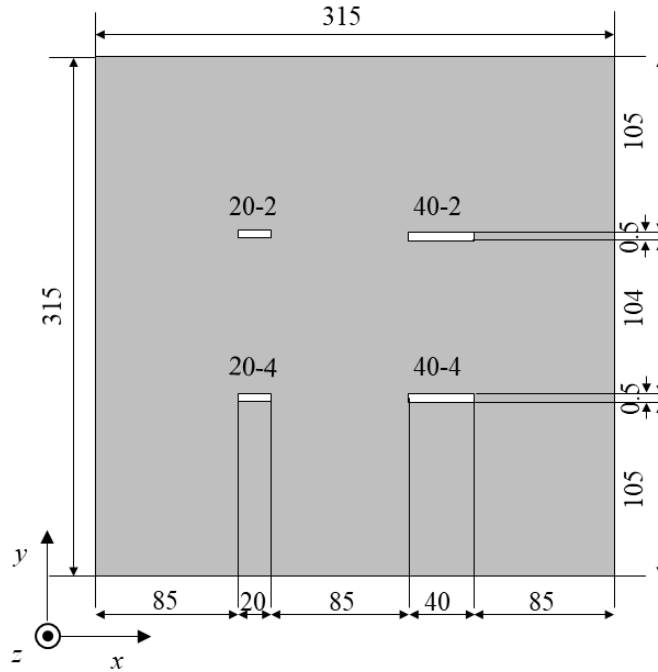


Figure 2.8. Specifications of aluminum plate using for experiment with the ECC probes (Unit in mm)

Table 2.2 Dimensions of four artificial flaws in the aluminum plate

Symbol of flaw	Width (mm)	Length (mm)	Depth (mm)
20-2	0.5	20	2
20-4			4
40-2		40	2
40-4			4

Table 2.3 The specifications of the ECC probes

Excitation coil	Turns	700
	Wire diameter (mm)	0.2
	Resistance (Ω)	49
	Impedance (Ω)	160
	Inductance (mH)	24
Detection coil	Turns	854

Wire diameter (mm)	0.02
Resistance (Ω)	103
Impedance (Ω)	105
Inductance (mH)	2.5

The output signal from the singular detection coil underwent processing through a two-phase lock-in amplifier (NF 5601 B) before being recorded onto a digital oscilloscope (Graphtec GL7000), which boasted a data sampling rate of 4 Hz. The coordination of the EC convergence probe's movements across the test specimen's scanning surface was orchestrated by a computer-controlled positioning robot module. The probe traversed the surface at a consistent speed of 10 mm/s. Notably, the scanning was conducted in both the x and y directions, each with a step size of 1 mm, thereby ensuring comprehensive coverage of the test area.

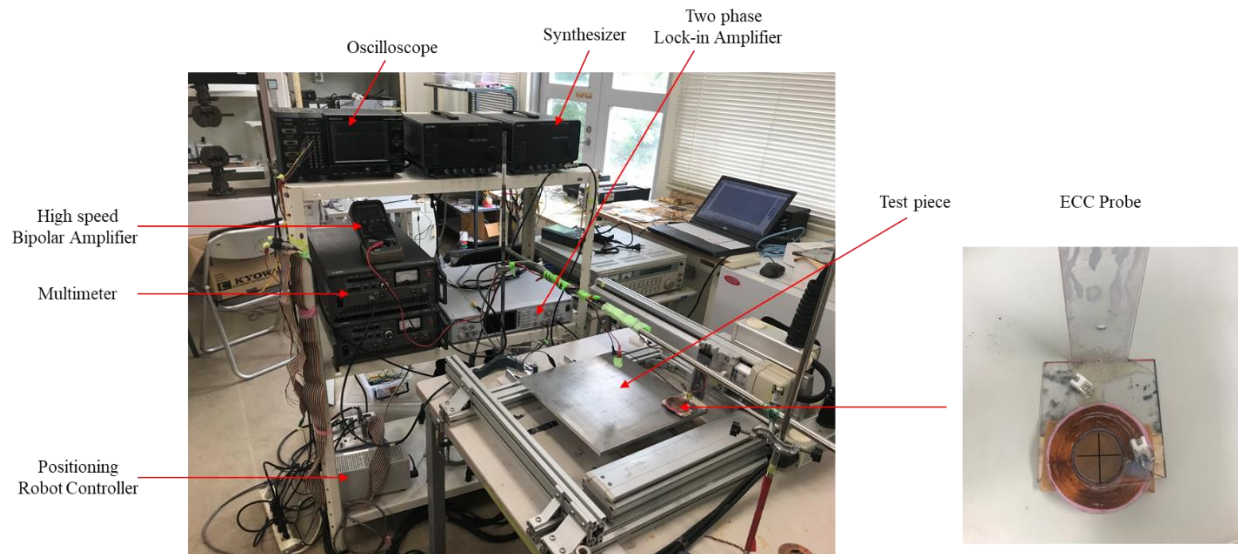


Figure 2.9. Experimental setup with ECC probes

Illustrated in Figure 2.9 is the configuration of the experimental setup. The excitation coil was driven by an electrical current with a frequency of 10 kHz and a magnitude of 10 mA. To generate this current, a combination of a function generator (WAVE FACTORY WF1946B, NF Co., Yokohama, Japan) and a high-speed bipolar amplifier (NF HAS 4012, NF Co., Yokohama, Japan) was employed.

During this experiment, three variations of the copper core configuration were examined:

one with a solid copper core, lacking any slits (Figure 2.10(a)), another with two slits, oriented both horizontally and vertically (Figure 2.10(b)), and a third incorporating hollows and a plate beneath the excitation coil (Figure 2.10(c)). For each experimental setup, a single circular detection coil was consistently employed, as depicted in Figure 2.11.

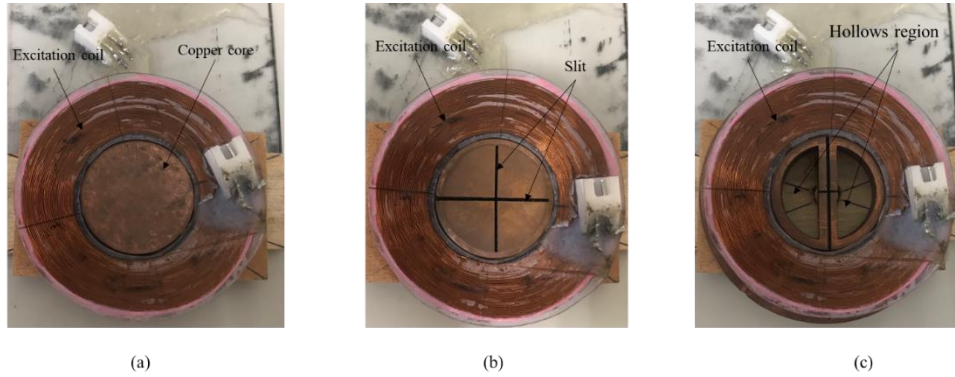


Figure 2.10. Shapes of EEC probe: (a) Without slit (Type 0), (b) With slits (Type 1), (c) With hollows and a plate under the excitation coil (Type 2)

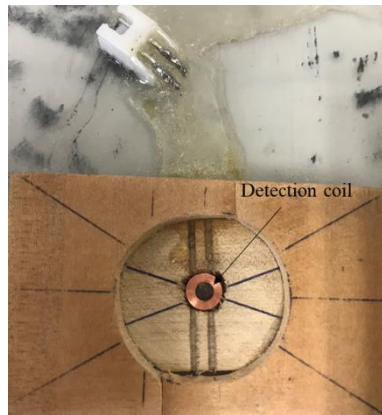


Figure 2.11. Shape of the detection coil using for ECC probes

2.2.3. Experimental results and discussion

Figure 2.12 illustrates the scanning trajectory of the ECC probe across the test piece. The two distinct scanning patterns are presented in Figures 2.12(a) and 2.12(b). In the first scanning pattern (Scanning #1), the EC convergence probe traversed along the x-axis, with subsequent repetitions involving shifts along the y-axis direction. The second scanning pattern (Scanning #2) involved a 90° rotation of the test piece's position compared to Scanning #1. During Scanning #2, the probe moved along the y-axis, with further repetitions involving shifts along the x-axis direction.

In Scanning #1, the EC generated within the test piece by the probe was oriented

perpendicular to the length of the flaw under investigation. Conversely, in Scanning #2, the EC generated because of the copper core in the test piece ran parallel to the length of the flaw.

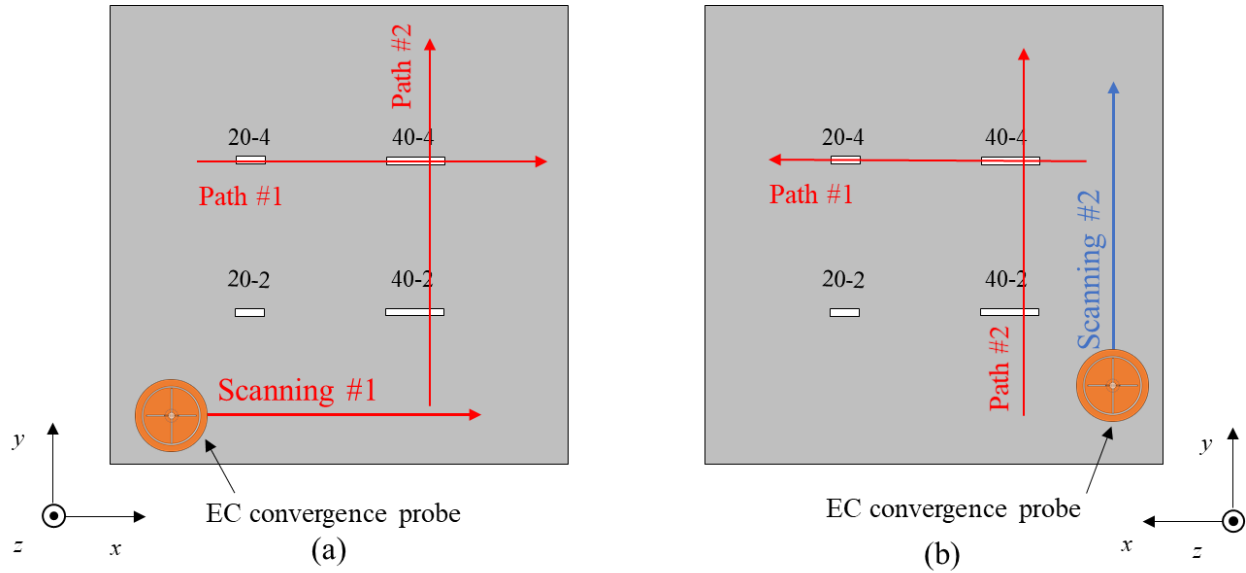


Figure 2.12. Scanning direction and paths on test piece with ECC probes: (a) Scanning #1, (b) Scanning #2

2.2.3.1. Measurement results with Scanning #1 and Scanning #2

The measurement outcomes for the three distinct sample configurations, employing a detection coil and subjected to Scanning #1, are presented in Figures 2.13(a), 2.13(b), and 2.13(c) correspondingly. Likewise, for Scanning #2, which involves a 90° rotation of the test piece from its original position in Scanning #1, the measurement results are depicted in Figures 2.13(d), 2.13(e), and 2.13(f), respectively.

Based on the measurement outcomes, it is evident that all four flaws are distinctly detectable in both Type 1 and Type 2 configurations. Notably, when the flaw region is positioned outside the detection coil's coverage, the signal amplitude for Type 2 is the most pronounced, ranging from 111 to 113 mV. This observation implies that the converging current at the tip of the copper core in Type 2 is the most robust. In contrast, Type 0 exhibits the smallest signal response, measuring between 0.5 and 1 mV. Despite the finite element simulation results indicating a lack of convergence of eddy currents at the tip of the copper core in Type 0, there is still a minimal induction of eddy currents on the test piece. This accounts for the extremely faint signals of 40-4 and 20-4, as illustrated in Figures 2.13(a) and 2.13(d).

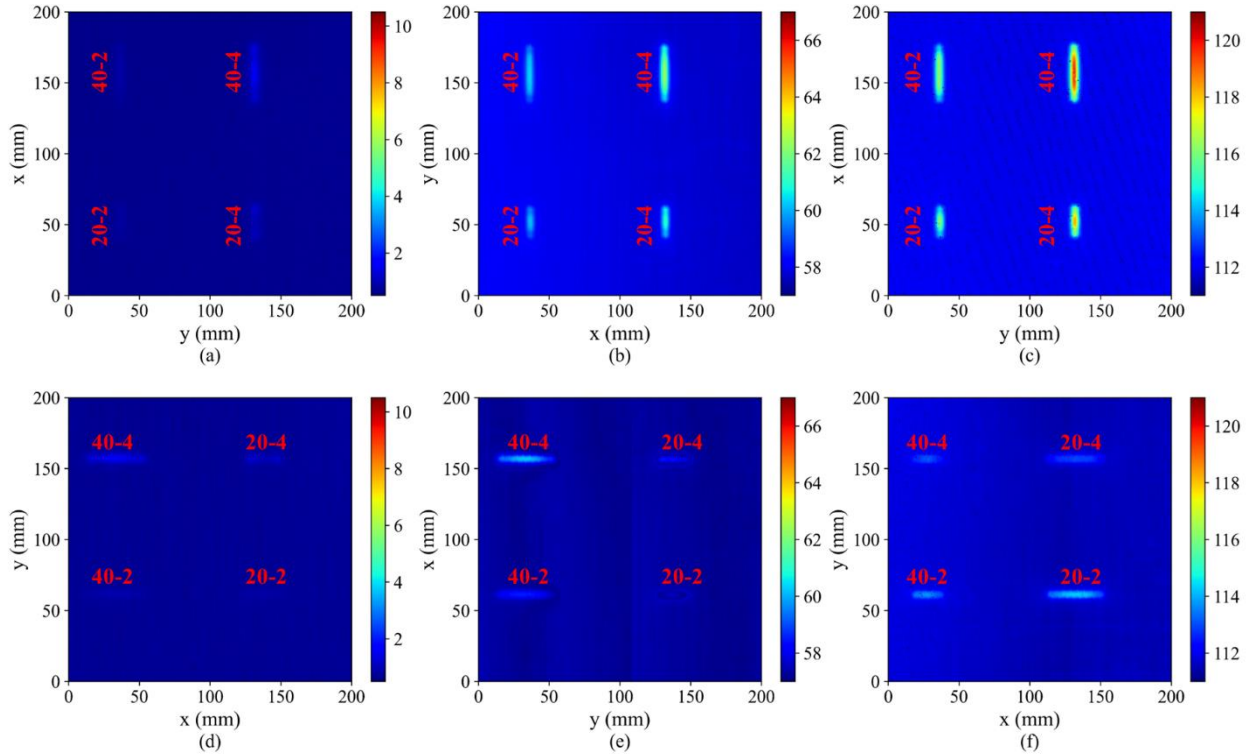


Figure 2.13. Measurement results of EC convergence probe: (a) Scanning #1 of type 0, (b) Scanning #1 of type 1, (c) Scanning #1 of type 2, (d) Scanning #2 of type 0, (e) Scanning #2 of type 1, (f) Scanning #2 of type 2.

In scenarios where the test piece lacks any flaws, the eddy currents (EC) induced within the test piece interact in a way that the magnetic flux originating from the EC within the copper core undergoes a cancellation process, as depicted in Figure 2.14(a). Consequently, the signal detected at the coil is diminished due to a reduced magnetic flux traversing through the detection coil. However, in the presence of a flaw within the test piece, a relatively weaker EC is generated on the flaw-affected area due to the compromised electromagnetic characteristics. This alteration leads to a reduction in the effectiveness of canceling out the magnetic flux generated by the EC in the copper core, as illustrated in Figure 2.14(b). Subsequently, a larger magnetic flux passes through the detection coil, amplifying the signal measured by the detection coil.

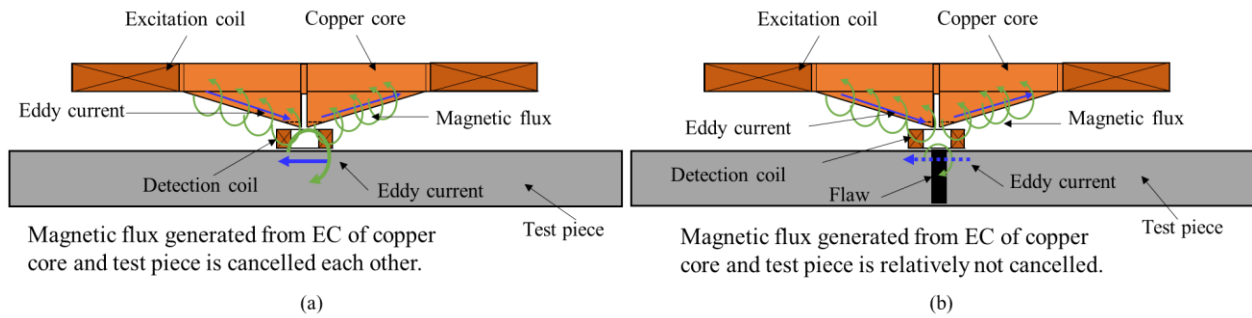


Figure 2.14. Principle of the output signal with a detection coil: (a) Without flaw, (b) With a flaw.

2.2.3.2. Measurement results of path #1 and path #2

To assess the flaw detection capability of the EC convergence probe, two scanning patterns, denoted as #1 and #2, were employed. The probe traversed along path #1, encompassing two distinct flaw regions (40-4 and 20-4), before proceeding to path #2, which covered two additional flaw regions (40-2 and 40-4). The outcomes of these experiments are visually presented in Figures 2.15 and 2.16.

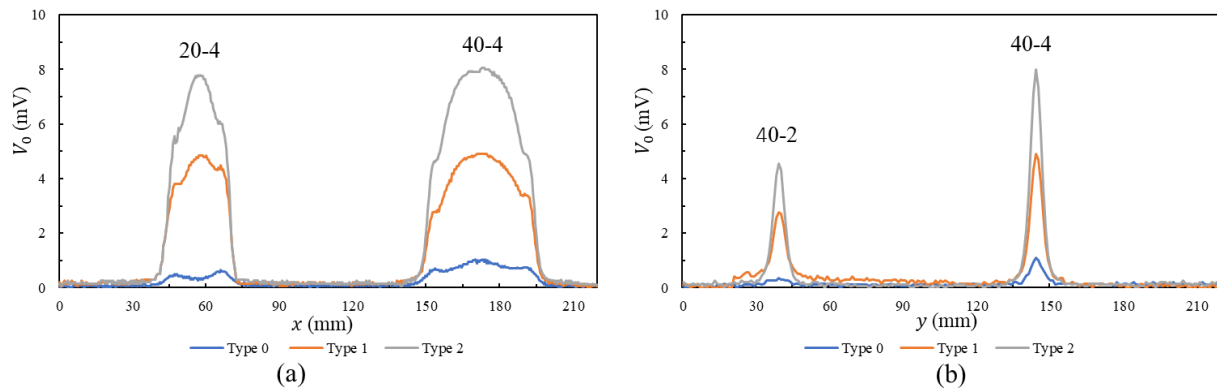


Figure 2.15. Measurement results of ECC probe with a detection coil with scanning #1: (a) Path #1, (b) Path #2

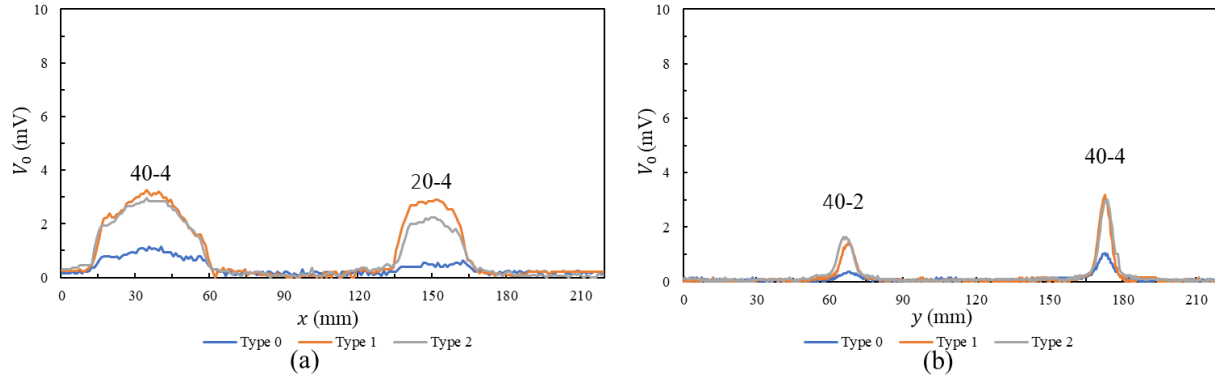


Figure 2.16. Measurement results of ECC probe with a detection coil with scanning #2: (a) Path #1, (b) Path #2

In Figures 2.15 and 2.16, each signal has been normalized by subtracting the signal obtained from the flaw-free region. Notably, Type 2 exhibits the highest peak magnitude, signifying a robust EC convergence effect. During traversal along path #1, the peak signal magnitude for Type 2 registers around 8 mV. Conversely, for path #2, this peak magnitude is approximately 5 mV for the flaw denoted as 40-2, and 8 mV for the flaw marked as 40-4. This variation can be attributed to greater disruption caused by increased flaw depth. The magnitude of the peak is indicative of the flaw depth in measurements conducted using the same probe type. Furthermore, a distinct flaw signal becomes apparent as the probe's detection coil interacts with the flaw region. Consequently, the signal amplitude provides insight into the flaw's length.

Moreover, upon comparing the signals obtained from scanning #1 and #2, a noticeable distinction arises: the peak detection signal of scanning #1 surpasses that of scanning #2. This divergence stems from the more pronounced disruption condition exhibited by the EC generated during scanning #1, attributable to its perpendicular alignment with the flaw's length. Conversely, during scanning #2, a lesser disruption condition arises as the EC aligns parallel to the flaw's length.

However, the flaw detection capability along the flaw direction remains relatively unaffected. The EC convergence probe retains its ability to detect all flaws, as depicted in Figure 2.13. This persistence in detectability arises from the EC convergence probe's capacity to generate a substantial EC across a confined area on the sample's surface.

2.3. Uniform eddy current convergence probes exhibiting self-differential and self-nulling attributes for the purpose of detecting cracks within conductive materials.

2.3.1. Probe design and methods

The core of the excitation coil featured a uniquely crafted copper core, which incorporated strategically placed slits, a concave surface, and an underlying plate. This intricate configuration, illustrated in Figures 2.17 and 2.18, was meticulously designed to facilitate the confluence of the electrical current at the tip of the copper core and to channel a substantial excitation current onto the surface of the test piece.

2.3.1.1. Design of ECC probe with copper core (Type 1)

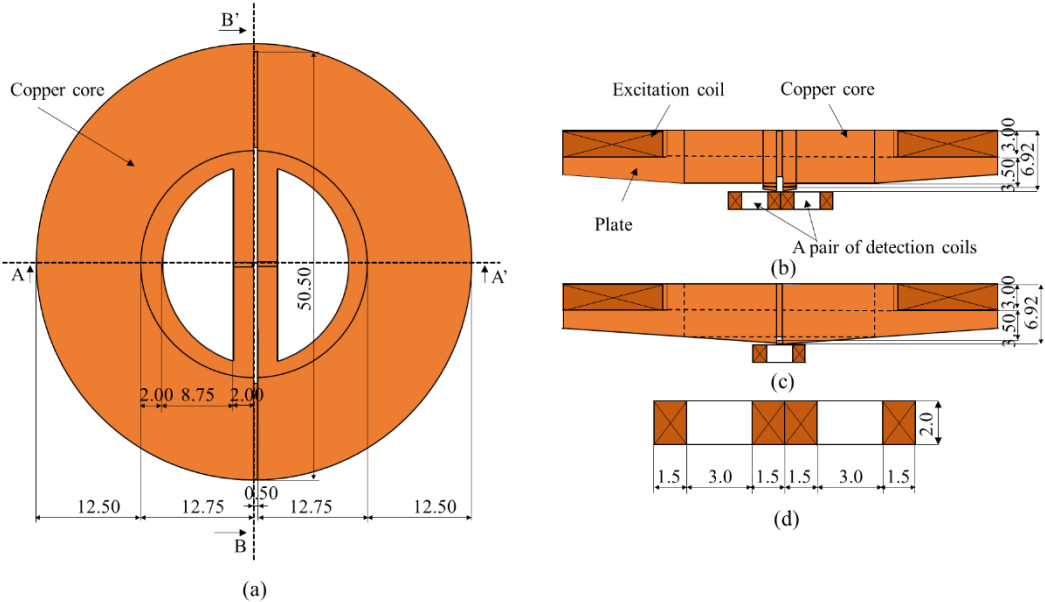


Figure 2.17 Structure of EC convergence probe with hollows and a plate under the excitation coil (units in mm): (a) top view, (b) section view of A-A', (c) section view of B-B', and (d) structure of a pair of circular detection coils

The specifications of the EC convergence probe denoted as Type 1, featuring a copper core, are meticulously outlined in Figure 2.17. This probe configuration encompasses an excitation coil, a hollowed copper core, and a plate thoughtfully positioned beneath the excitation coil, akin to the design previously detailed in [81], as visually represented in Figure 2.17(a). The excitation coil boasts a total of 700 turns, employing a copper wire with a diameter measuring 0.2 mm.

Positioned at the lowermost and central regions of the copper core, the detection coils find their place, as elegantly portrayed in Figures 2.17(b) and 2.17(c). These components are further

expounded upon in Figure 2.17(d), elucidating the specifics of the paired circular detection coils. Each of these coils comprises an impressive 854 turns, with the copper wire employed for their construction sporting a diameter of 0.05 mm.

2.3.1.2. Design of UECC probe with a pair of copper cores (Type 2)

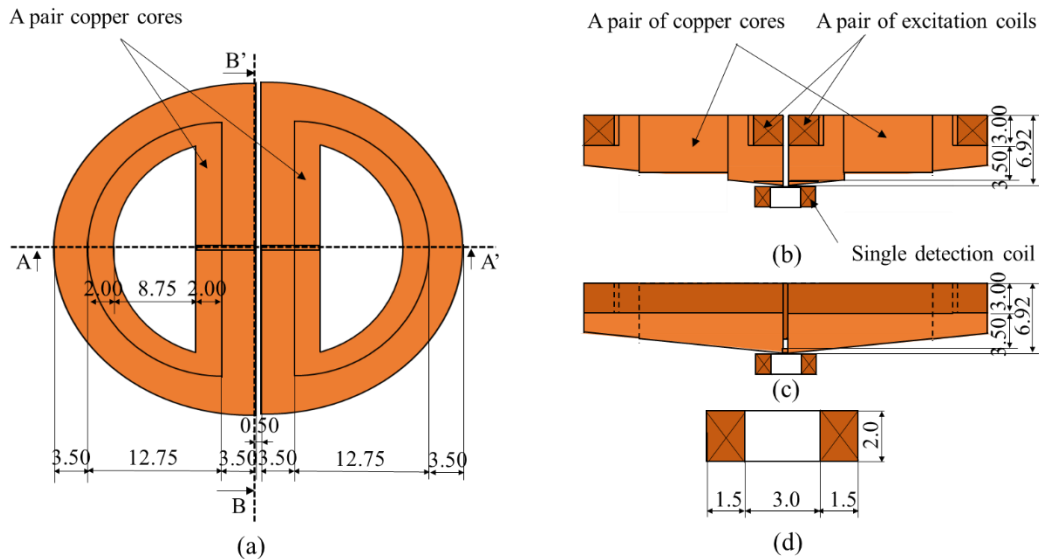


Figure 2.18 Structure of EC convergence probe with a pair of copper cores (units in mm): (a) top view, (b) section view of A-A', (c) section view of B-B', and (d) structure of a single detection coil

Figure 2.18 presents the detailed specifications of the UECC probe, designated as Type 2. This variant of the probe introduces a distinctive configuration, employing a pair of copper cores, and is meticulously described below. The UECC probe, or Type 2, showcases a distinct composition, featuring a pair of copper cores ingeniously positioned within individual excitation coils, as visually depicted in Figure 2.18(a). The excitation coils are meticulously wound, each encompassing 180 turns, utilizing a 0.2-mm-diameter copper wire for their construction. Furthermore, the detection coil is meticulously integrated, residing at both the lowermost and central regions of the copper core, thoughtfully illustrated in Figures 2.18(b) and 2.18(c) respectively. A comprehensive breakdown of the circular detection coil's attributes is provided in Figure 2.18(d). Specifically, the detection coil is crafted with an impressive 854 turns, employing a copper wire with a diameter of 0.05 mm.

2.3.2. Finite element simulation of Types 1 and 2

2.3.2.1. 3D FEM model

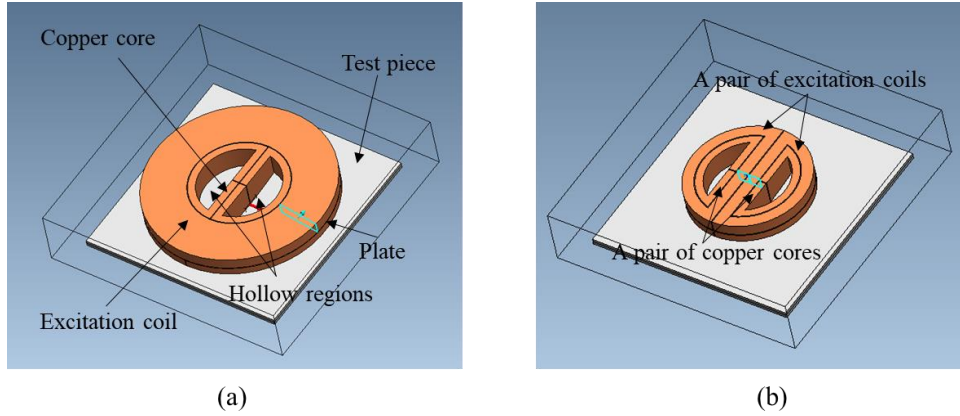


Figure 2.19 3D FEM model of the EC probe: (a) Type 1 and (b) Type 2

To validate the characteristics of EC flow across the copper core and the induction of EC on the test piece's surface, a comprehensive time-harmonic analysis of the EC convergence models was meticulously carried out. This analysis was facilitated through the utilization of advanced finite element analysis software, specifically Magnet 7 version 7.9.0.18, developed by Mentor Graphics Corporation. The results from this meticulous analysis are visually represented in Figures 2.19(a) and 2.19(b), providing a comprehensive depiction of the EC flow within the copper core and the consequential induction of EC on the test piece's surface. This thorough examination serves to confirm the anticipated behaviors and phenomena within the EC convergence probe system.

Table 2.4 outlines the essential electromagnetic parameters that played a pivotal role in our comprehensive analysis. The test piece employed for the investigation was an aluminum plate characterized by dimensions of $70 \times 70 \times 10$ mm. In our analytical endeavors, Types 1 and 2, as illustrated in Figures 2.17 and 2.18, respectively, were meticulously examined. The specifications of these probe types remained consistent with those visually depicted in the respective figures.

Table 2.4 Electromagnetic parameters used in the analysis for UECC probes.

	Material	Electrical conductivity, σ (MS/m)	Relative permeability, μ_r
Wire of excitation coil			
Wire of detection coil	Copper	57.7	1.0
Core of coil			
Test piece	Aluminum	38.0	

For Type 1, the analysis involved an excitation current of 7 mA and a frequency of 10 kHz. Meanwhile, Type 2 underwent scrutiny with an excitation current of 55 mA and the same frequency of 10 kHz. The selection of excitation current amplitudes for both types was informed by preliminary FEM analyses, ensuring the effective induction of EC on the test piece's surfaces. This methodical approach ensured a coherent and systematic evaluation of the two probe types, fostering reliable and insightful outcomes for our study.

Table 2.5 presents a comprehensive compilation of the key parameters employed in our finite element simulations. For the 3D FEM analysis for each probe type, a mesh featuring a tetrahedral shape was meticulously adopted across all elements. Delaunay triangulation was the selected mode of triangulation, systematically employed to facilitate an accurate and robust analysis. This careful and systematic approach to meshing and triangulation ensured the integrity and reliability of our simulations, further solidifying the validity of our study's results.

Table 2.5 Parameters of the 3D FEM model with UECC probes

Parameters	Type 1	Type 2
Total number of nodes	34708	19263
Total number of tetrahedra	193186	106787

2.3.2.2. Results of FEM simulation for both UECC probes

Figures 2.20 and 2.21 show the contour and arrow plots of the EC distribution on the surface of the copper core and cross-section B-B' of the EC convergence probe, respectively.

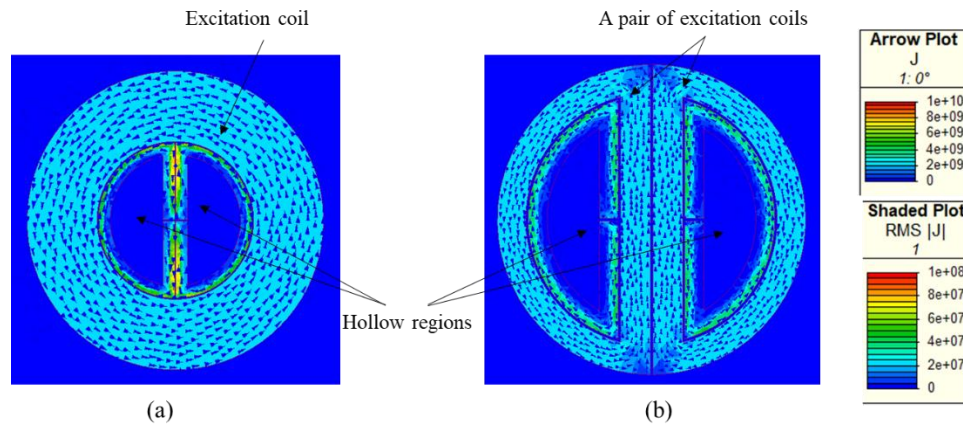


Figure 2.20 Contour and arrow plots of the EC distribution on the surface of the copper core of

EC convergence probe: (a) Type 1 and (b) Type 2

Illustrated in Figures 2.20(a) and 2.20(b) are the compelling effects of incorporating slits, hollows, and plates within the copper core. These structural features play a pivotal role in orchestrating the circulation of eddy currents along the designated slits and hollows. Consequently, the eddy currents exhibit a directed flow, converging resolutely towards the tip of the copper core, an intricate phenomenon adeptly captured in Figures 2.21(a) and 2.21(b). Notably, it is imperative to acknowledge that a conspicuous dichotomy exists in the eddy current patterns generated at the respective tips of the dual segments constituting the copper core (as depicted in Figure 2.20(a)). This intrinsic divergence in eddy current behavior engenders opposing manifestations on the test piece, a manifestation elegantly depicted in Figure 2.22(a).

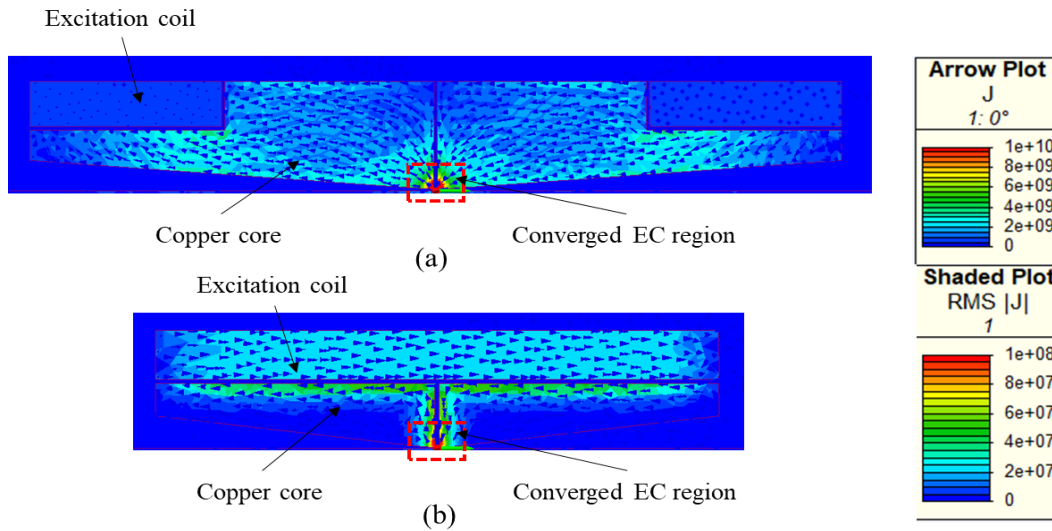


Figure 2.21 Contour and arrow plots of the EC distribution on cross-section B-B' of the probe:
(a) Type 1 and (b) Type 2

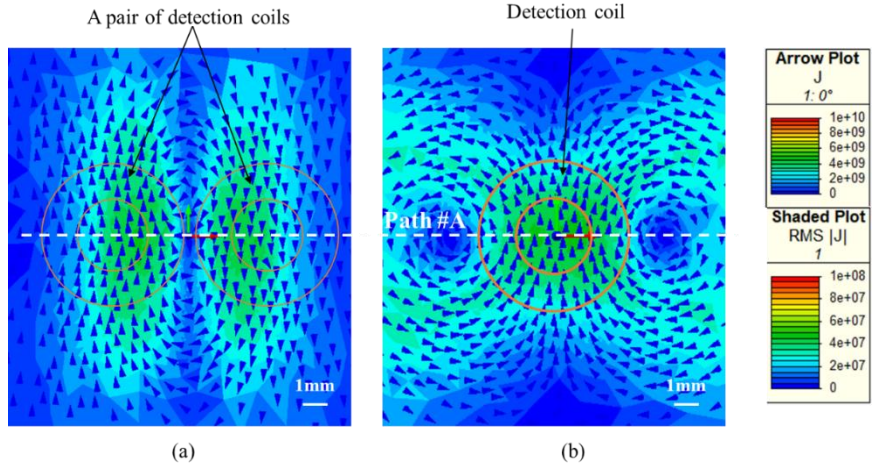


Figure 2.22 Contour plot of the EC distribution on the surface of the test piece: (a) Type 1 and (b) Type 2

In parallel, a unidirectional EC emerges upon the activation of a paired arrangement of copper cores, a phenomenon vividly depicted in Figure 2.22 (a). This orchestration precipitates an EC distribution akin to the uniform eddy current (UEC) paradigm, thereby engendering a semblance of UEC dynamics across the test piece. The impetus behind this occurrence stems from the concerted convergence of eddy currents at the juncture of the paired copper cores, a visual portrayal skillfully encapsulated in Figure 2.22(b).

The subsequent exploration, as showcased in Figure 2.23, endeavors to shed light on the EC amplitude profiling across the test piece's surface along Path #A, employing both probe variants. Evidently, while the amplitudes of the excitation current exhibit discernible dissimilarity, a notable congruence manifests in the amplitudes of the EC generated on the test piece's surface using both probe configurations. Hence, during the experimental phase, excitation currents with amplitudes of 7 mA and 55 mA were meticulously chosen for Type 1 and Type 2 respectively.

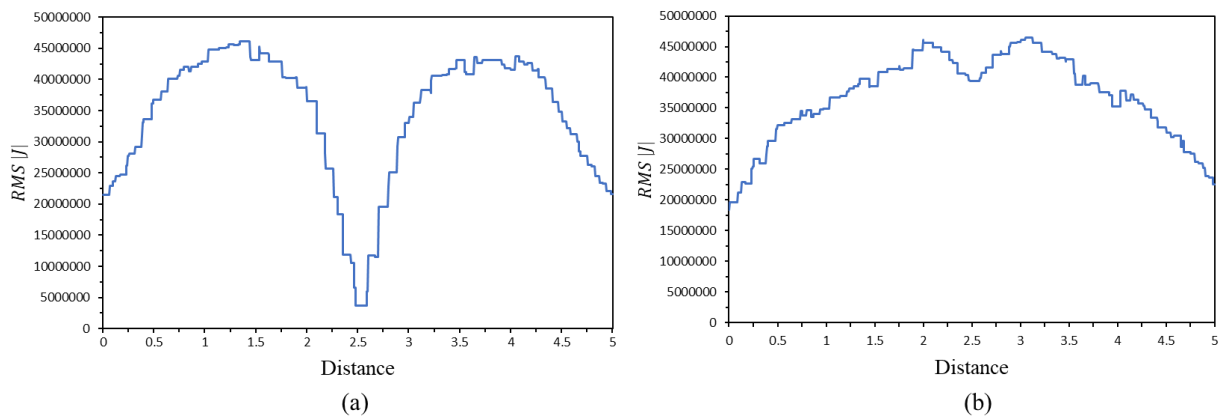


Figure 2.23 EC amplitude on the surface of the test piece along Path #A: (a) Type 1 and (b) Type 2

2

2.3.3. Experimental setup

2.3.3.1. Test piece with artificial cracks

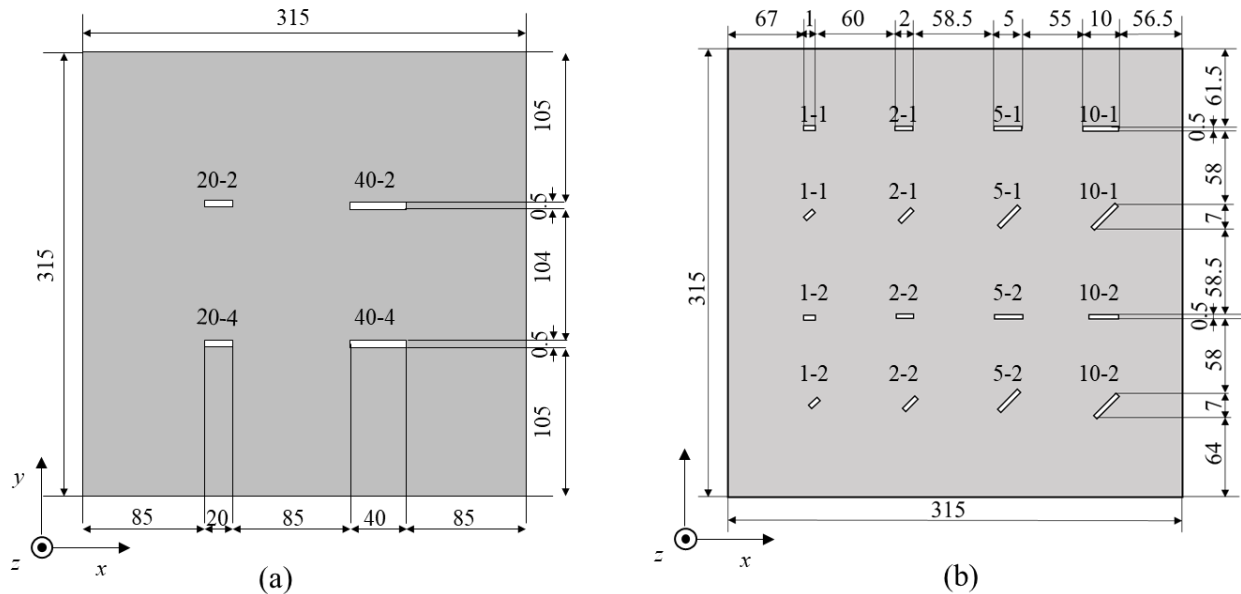


Figure 2.24 Aluminum alloy plate specifications (units in mm): (a) Test piece #1 and (b) Test piece #2

The details of the test piece, composed of 5052 aluminum alloy, along with its artificial cracks, are depicted in Figure 2.24. These simulated cracks were meticulously created through the process of electrical discharge machining. In Figure 2.24(a), we observe larger cracks, while Figure 2.24(b) illustrates comparatively smaller cracks. The specific measurements for each of these cracks are diligently outlined in Table 2.6.

Table 2.6 Dimensions of artificial cracks on the 5052-aluminum alloy surface

Test piece	Symbol of crack	Width (mm)	Length (mm)	Depth (mm)
1	20-2	0.5	20	2
	20-4			4
	40-2		40	2
	40-4			4
2	1-1	0.5	1	1
	1-2			2

	2-1		2	1
	2-2			2
	5-1		5	1
	5-2			2
	10-1		10	1

2.3.3.2. Experimental setup

The detailed specifications for each excitation coil, encompassing a pair of detection coils for Type 1 and a single detection coil for Type 2, have been meticulously documented in Table 2.7.

Table 2.7 Specifications of the excitation and detection coils in each UECC probe

The Type of UECC probe		Type 1	Type 2
Excitation coil	Turns	700	180
	Wire diameter (mm)	0.2	0.2
	Resistance (Ω)	49	6
	Impedance (Ω)	160	6.5
	Inductance (mH)	24	0.4
Detection coil	Turns	854	854
	Wire diameter (mm)	0.02	0.02
	Resistance (Ω)	103	103
	Impedance (Ω)	105	105
	Inductance (mH)	2.5	2.5

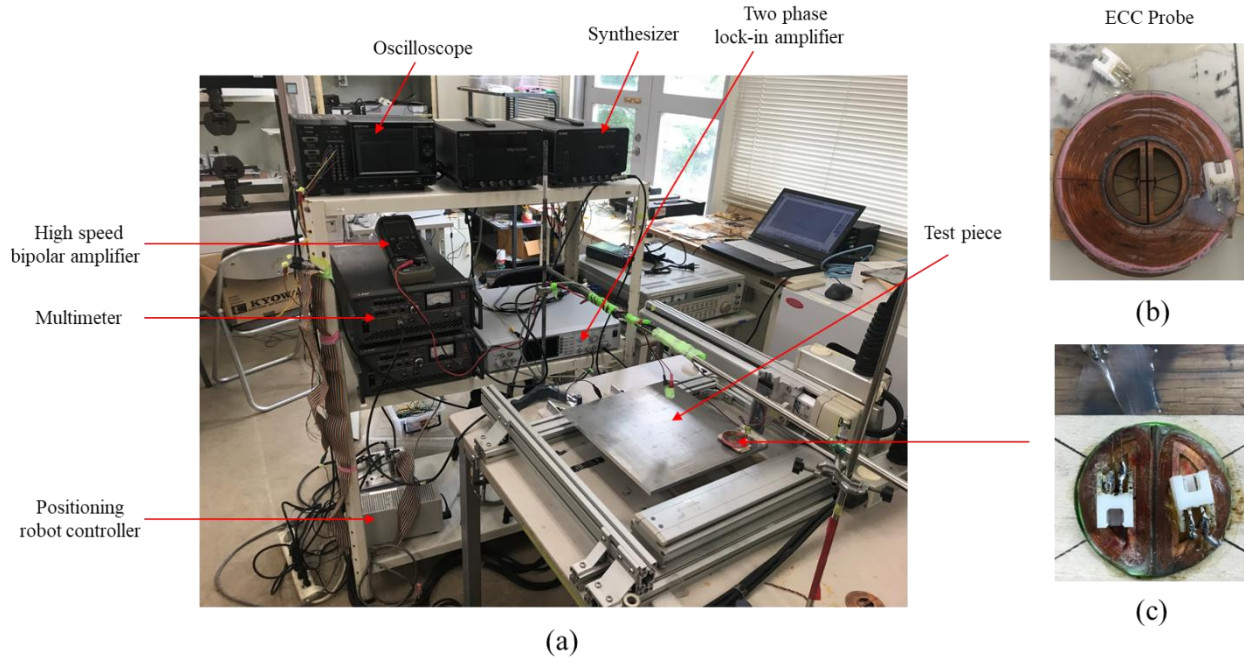


Figure 2.25 Experimental setup and the UECC probes: (b) Type 1 and (c) Type 2

Figure 2.25(a) illustrates the setup configuration of the experimental apparatus. The utilization of two distinct probe types in each experiment is visually depicted in Figures. 2.25(b) and 2.25(c). To facilitate the generation of the excitation current, a signal generator (WAVE FACTORY WF1946B, NF Co., Yokohama, Japan) coupled with a high-speed bipolar amplifier (NF HAS 4012, NF Co., Yokohama, Japan) was employed. The excitation parameters were set at a frequency of 10 kHz and an amplitude of 7 mA for Type 1, while for Type 2, they were maintained at a frequency of 10 kHz and an amplitude of 55 mA.

Subsequently, the signal retrieved from the detection coil was subject to processing through a two-phase lock-in amplifier (LI 5660, NF Co., Japan) before being stored within a digital oscilloscope (DATA PLATFORM GL7000, GRAPHTEC Co., Japan). To facilitate the movement of the EC convergence probe across the scanning surface of the test piece, a computer-controlled positioning robot module was deployed, functioning at a consistent speed of 10 mm/s. The scanning process was orchestrated with precision, featuring intervals of 1 mm in both the x and y directions. Importantly, during the scanning procedure, a protective measure was adopted by placing a 0.2 mm-thick plastic sheet beneath the detection coil, thereby preventing direct contact with the test piece, and safeguarding against potential damage.

2.3.4. Experimental results and discussion

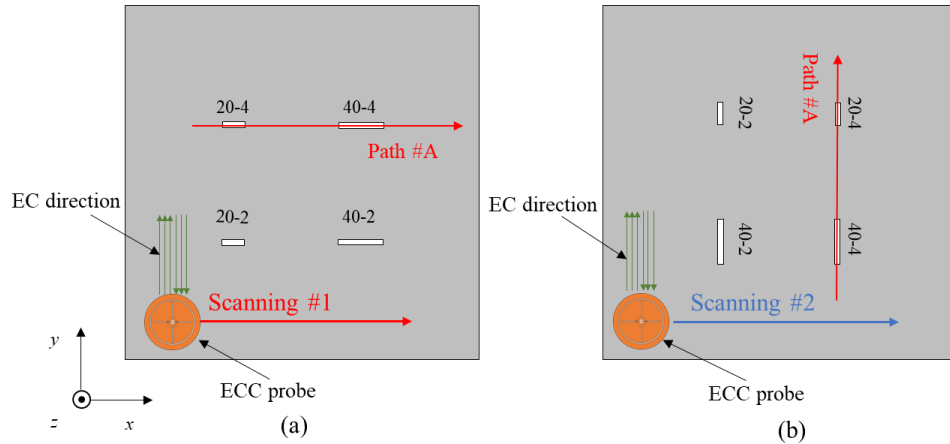


Figure 2.26 Scanning direction and paths on the test piece with UECC probes: (a) Scanning #1 and (b) Scanning #2

To validate the proposed methodology, a series of dual experiments were meticulously conducted on test piece #1 for each distinct probe type. The experimental protocol encompassed two distinctive scanning maneuvers, namely scanning #1 and scanning #2, both of which were executed to provide a comprehensive assessment.

Scanning #1, depicted in Figure 2.26(a), involved the systematic movement of the UECC probe along the x-axis, with subsequent shifts executed along the y-axis. This strategic maneuvering established a configuration in which the EC induced by the copper core within the test piece maintained a perpendicular orientation relative to the crack's longitudinal axis. In contrast, scanning #2, as illustrated in Figure 2.26(b), entailed the rotation of the test piece by 90° in relation to its initial orientation during Scanning #1. Within this framework, the UECC probe continued to traverse the x-axis, supplemented by incremental shifts along the y-axis. Consequently, the resultant arrangement ensured that the EC generated by the copper core within the test piece assumed a parallel alignment with the crack's length.

2.3.4.1. Measurement results with Scanning #1 and Scanning #2

The outcomes of the measurements conducted with Type 1 employing a pair of detection coils, as well as those obtained from Type 2 utilizing a single detection coil, during Scanning #1, are effectively portrayed in Figures 2.27(a) and 2.27(b), respectively. Similarly, the depiction of measurement results under identical conditions but during Scanning #2 can be observed in Figures 2.27(c) and 2.27(d) correspondingly.

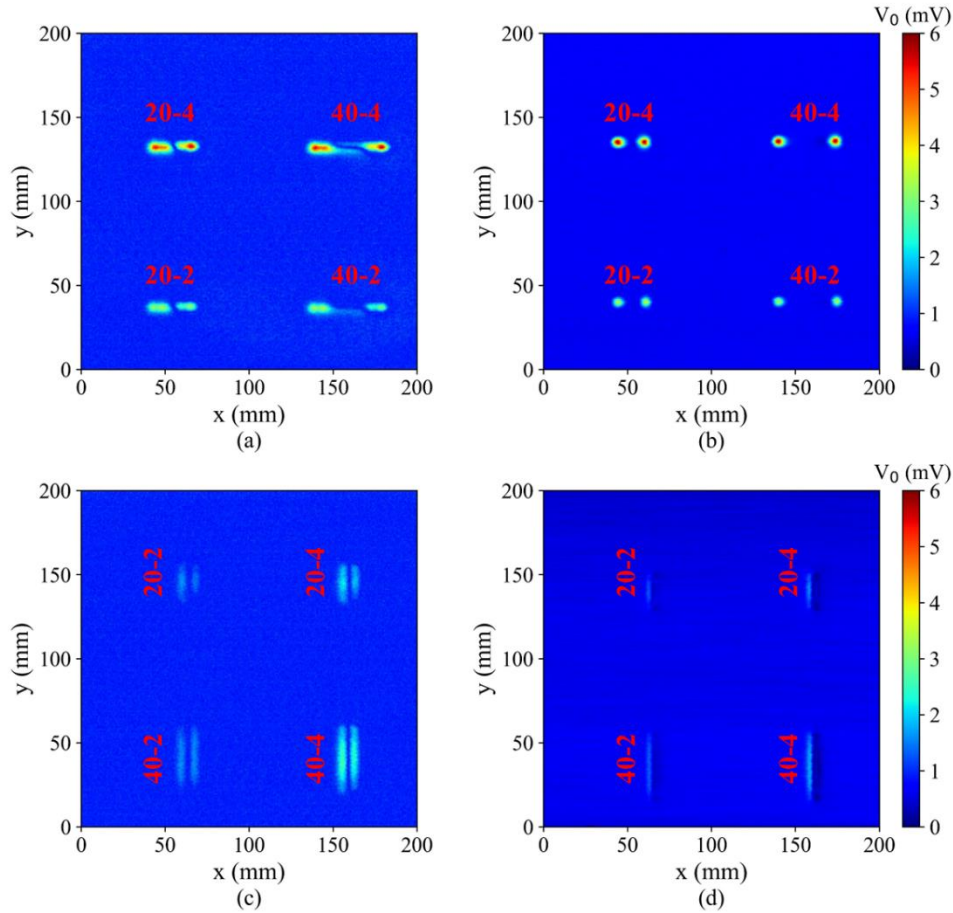


Figure 2.27 Experimental results of the UECC probe: (a) Scanning #1 of Type 1, (b) Scanning #1 of Type 2, (c) Scanning #2 of Type 1, and (d) Scanning #2 of Type 2. The unit of the signal is mV.

The measurement results provide conclusive evidence that all cracks can be reliably detected using both Type 1 and Type 2 probes. When a crack is positioned outside the detection coil range of the two probes, the signal from both probes registers as zero. This observation reaffirms the adherence of the two probe models to their self-nulling and self-differential attributes.

In Scanning #1, employing the pair of detection coils in the Type 1 probe yields two distinct signal magnitude peaks for each crack, whereas the use of the single detection coil in the Type 2 probe also generates two signal magnitude peaks for each crack. Notably, valley values are evident at the centers of the cracks for both the Type 1 and Type 2 probes. During Scanning #2, a conspicuous reduction in the signal magnitude peaks becomes apparent when the test piece is rotated by 90°.

2.3.4.2. Measurement results of Path #A

Measurements were conducted for both probe types using scanning #1 and scanning #2, following the trajectory of path #A as illustrated in Figure 2.26. This approach allowed us to assess the detection capability under conditions where the EC induced in the test piece by the copper core of the probes was either parallel or perpendicular to the length of the crack. The outcomes of these measurements are visually presented in Figure 2.28.

As depicted in Figure 2.28, it is evident that the signal peaks at the crack edge exhibit significant similarity. In the case of Scanning #1, Figure 2.28(a) displays two distinct broad peaks within each crack signal, while Figure 2.28(b) illustrates the presence of two peaks within each crack signal for Scanning #2. This disparity can be attributed to the differential characteristics of the pickup system, where the pair of detection coils employed in Type 1 possesses a longer effective length compared to the single detection coil utilized in Type 2.

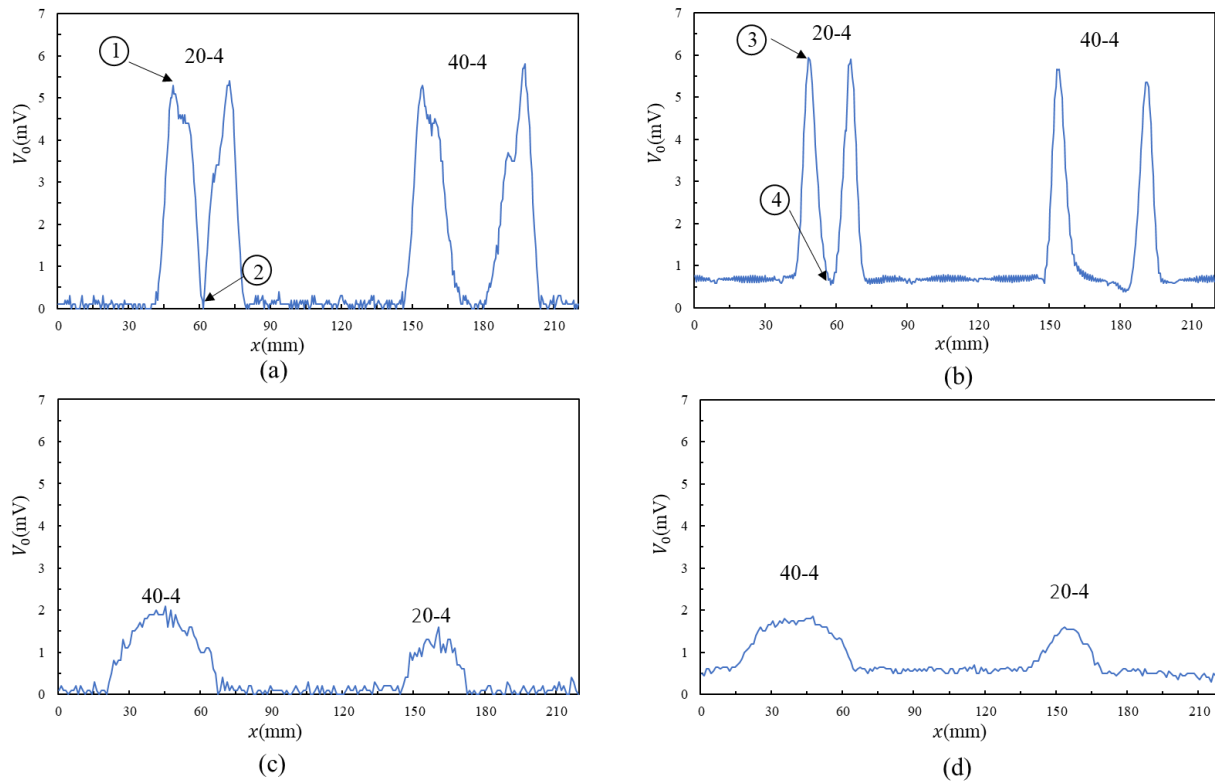


Figure 2.28 Measurement results of UECC probe with Path #A: (a) Scanning #1 of Type 1, (b) Scanning #1 of Type 2, (c) Scanning #2 of Type 1, and (d) Scanning #2 of Type 2

Nevertheless, the examination of Scanning #2 for both probe types reveals an interesting pattern where each crack is represented by a single peak. This phenomenon is attributed to the absence of simultaneous emf discontinuity within the detection coil when the ECs are aligned

parallel to the crack length. In the case of Scanning #2, the amplitude of the peak within the crack signal experiences a notable reduction. This reduction can be attributed to the fact that the parallel orientation of ECs along the crack length leads to a relatively minor disruption in the generated EC field.

Figures 2.29 and 2.30 provide a detailed illustration of the crack signal interpretation within the measurement results of Scanning #1. These results are obtained using a pair of detection coils (Figure 2.28(a)) and a single detection coil (Figure 2.28(b)), respectively.

When the test piece is free of cracks, the output signal from the detection coil remains close to zero, as depicted in both Figure 2.29(a) and 2.30(a). This phenomenon is a consequence of the EC distribution generated by the probes. This distribution exhibits uniform amplitudes at the tip of the two segments of the copper core for Type 1, and it maintains symmetry in relation to the detection coil for Type 2.

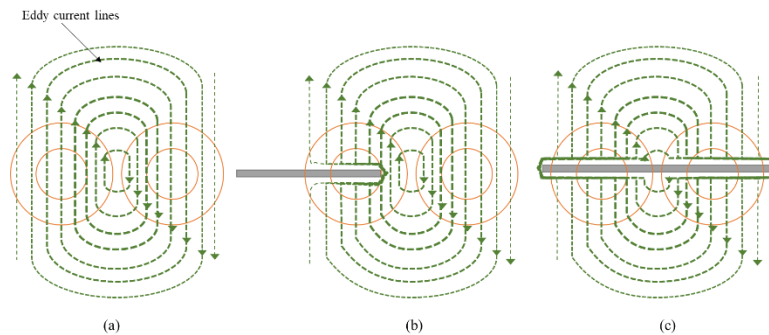


Figure 2.29 Crack signal explanation for measurement results of Type 1: (a) without crack, (b) position ①, and (c) position ②

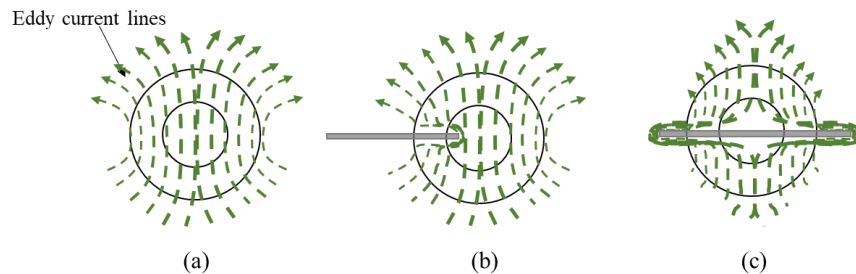


Figure 2.30 Crack signal explanation for measurement results of Type 2: (a) without crack, (b) position ③, and (c) position ④

At position ① in Figure 2.28(a), a deviation in the EC distribution is observed on the test piece. This discrepancy arises when the presence of a crack causes the EC to divert, resulting in a concentration of EC density within one of the detection coils (Figure 2.29(b)). A similar scenario

is observed for Type 2, where peak signals emerge at positions ③ due to the diversion of the EC caused by the crack, resulting in an asymmetrical EC distribution in relation to the detection coil (Figure 2.30(b)). Moreover, the output signal of the detection coil remains at zero for positions ② and ④ when the crack is centered within the probe, as evident in Figures 2.29(c) and 2.30(c). In such cases, the symmetrical nature of the probe design ensures that the EC distribution remains balanced and does not induce a signal within the detection coil.

2.3.4.3. Experiment with small flaws on an aluminum plate

To assess the crack detection capability of the Type 2 probe, an experiment involving both probe types was conducted on test piece #2. This evaluation, known as Scanning #3, entailed the movement of both probes along the x-axis, followed by a shift along the y-axis, as illustrated in Figure 2.31(a). Additionally, it is worth noting that the EC generated by the probe within the test piece is oriented perpendicular to the length of the crack.

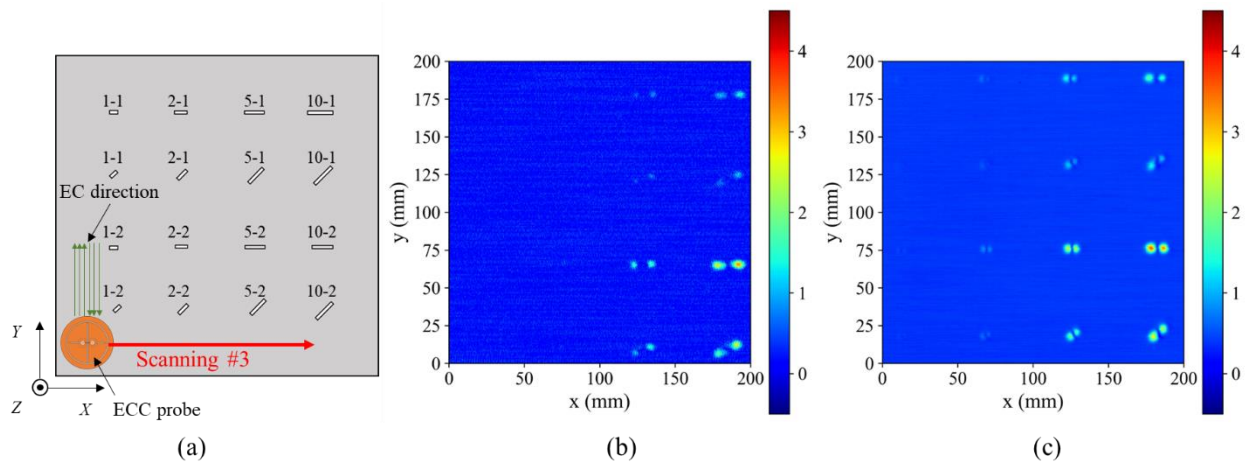


Figure 2.31 Measurement results of UECC probe on test piece #2: (a) scanning direction, (b) result of Type 1, and (c) result of Type 2

Figures 2.31(b) and 2.31(c) illustrate the measurement outcomes for the Type 1 and Type 2 probes, respectively. The results suggest that neither probe can detect a 1 mm length crack. However, when it comes to detecting cracks with a length of 2 mm, the Type 2 probe demonstrates superior detection prowess compared to its Type 1 counterpart. This enhanced performance of the Type 2 probe can be attributed to its EC distribution, akin to the UEC induced on the test piece, which contributes to a more sensitive crack-detection capability. This improvement is primarily due to the elevated S/N ratio of the Type 2 probe compared to the Type 1 probe, resulting in an increased ability to identify cracks.

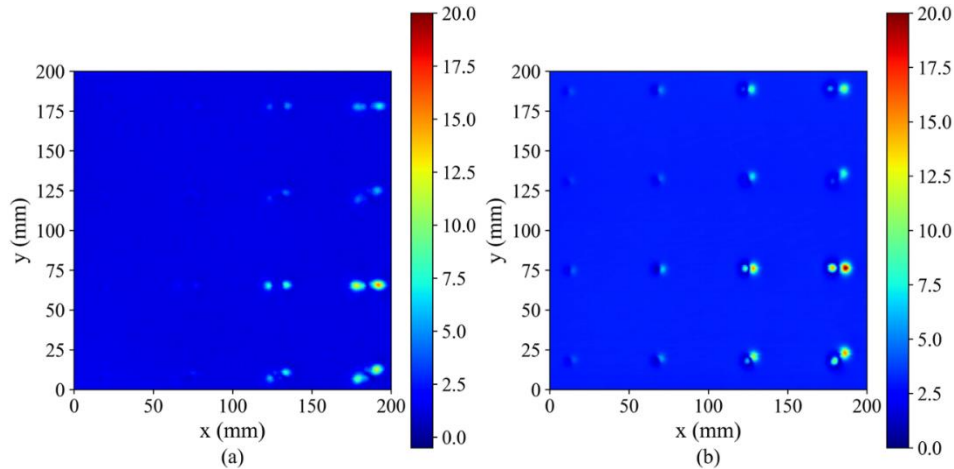


Figure 2.32 Measurement results of UECC probe on test piece #2: (a) Type 1 with 32.2 mA of excitation current and (b) Type 2 with 253 mA of excitation current

To ascertain the highest achievable detection capability of both probe types for a 1 mm crack length, the excitation current for each type was amplified by a factor of 4.6 at a frequency of 10 kHz. The outcomes of these measurements are displayed in Figure 2.32.

In the measurement results, it was evident that the Type 1 probe failed to detect cracks with a length of 1 mm (depicted in Figure 2.32(a)). However, the data demonstrated that the Type 2 probe succeeded in effectively detecting cracks of 1 mm length with varying depths (as depicted in Figure 2.32(b)).

2.4. Summary

In this chapter, an eddy current convergence (ECC) probe with a copper core was developed and analyzed for flaw detection. The incorporation of slits, hollows, and a plate in the copper core directed the flow of eddy currents (EC), resulting in enhanced convergence at the core's tip. Experimental investigations using different scanning patterns confirmed the probe's effectiveness in crack detection, even in scenarios where flaws were oriented parallel to the EC flow.

Signal analysis and comparison between scanning patterns demonstrated the probe's capability to discern flaws of varying depths and lengths. The peak detection signal was particularly pronounced when the EC flow was perpendicular to the length of the flaw, showcasing the probe's versatility in detecting flaws with different orientations.

The proposed ECC probe design, optimized for enhanced EC convergence with a copper core, shows promise for non-destructive testing applications. The study highlights significant

improvement in flaw detection, especially in scenarios favorably oriented to the EC flow, emphasizing the practical relevance of the research. Future studies could explore further refinements to the probe's design and its application in a broader range of materials and testing conditions.

The chapter introduced two probe types: a uniform eddy current convergence (UECC) probe with a pair of copper cores and a single detection coil, and an ECC probe with a pair of detection coils. Finite Element Analysis (FEA) validated EC distribution on the test piece's surface, and experimental validations using these probes revealed key findings:

- Both probe types effectively achieved EC convergence at the copper core's tip, yielding an output signal of 0 mV when defects were outside the detection coils. Type 2 successfully emulated UEC distribution, indicating self-nulling and self-differential properties.
- Both probe types identified flaws in aluminum plates, but a lack of simultaneous emf changes occurred when ECs were aligned parallel to the crack's length, leading to a minor disruption in the generated EC and reduced crack signal.
- Type 2, with elevated excitation current, successfully detected cracks with a 1 mm length and varying depths, a task challenging for Type 1.
- UECC probes showed potential for inspecting subsurface cracks within thinly structured conductive materials, but probe misalignment during measurements could introduce noise signals affecting the detection signal.

In conclusion, this chapter highlights the promising utility of the developed ECC probes for inspecting conductive materials, including subsurface cracks. However, precautions should be taken to mitigate adverse effects from probe misalignment during measurements.

Chapter 3: Rotating eddy current convergence probe with a sophisticated copper core design for crack detection

3.1. Introduction

In pursuit of empirical validation, finite element analysis was employed to corroborate the convergence of eddy currents at the core's tip. Subsequently, by meticulously crafting the copper core based on these analysis outcomes, we achieved successful realization of the RUECC at the core's tip. The profound efficacy of this design became evident through the RUECC probe's exceptional defect detection ability, surpassing the benchmarks set by existing literature. This pioneering approach holds immense promise in revolutionizing defect detection methodologies for diverse applications.

3.2. Probe design and methods

3.2.1. Structure of the RUECC probe

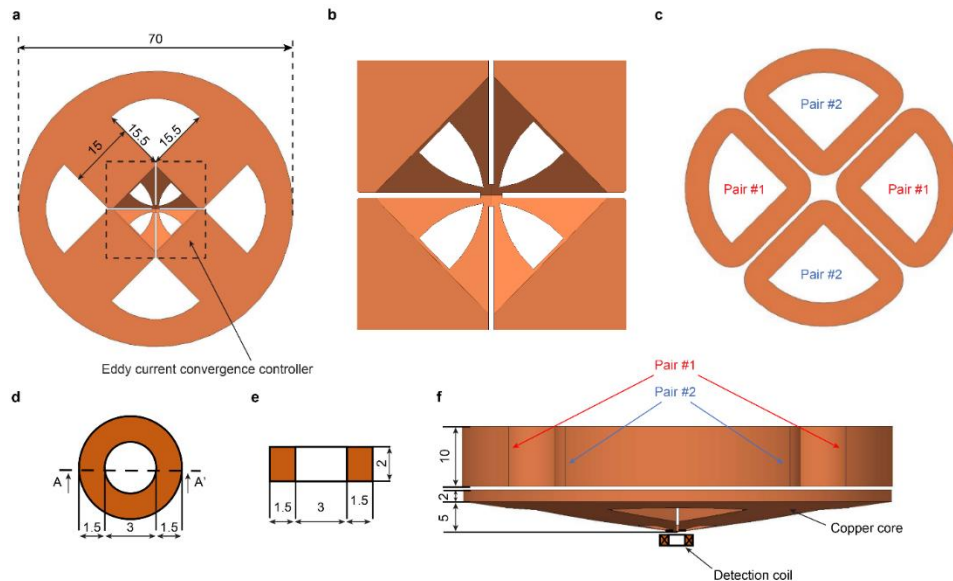


Figure 3.1 Structure of the RUECC probe (unit in mm): (a) Copper core, (b) EC convergence controller, (c) Two pairs of double excitation coils, (d) and (e) Top view and section view along A-A' of the detection coil, (f) Overall RUECC probe.

The structural components comprising the RUECC probe are depicted in Figure 3.1. A meticulously engineered copper core design, capable of inducing rotating ECs that converge at the core's tip, is vividly showcased in Figure 3.1(a) and 3.1(b). Positioned atop the copper core (as

illustrated in Figure 3.1(f)) were two pairs of double excitation coils, aligned within the same plane and dimensions (as depicted in Figure 3.1(c)). This strategic arrangement ensured that the ECs, which converged at the copper core's tip due to the influence of these dual pairs of excitation coils, orchestrated a synchronized rotation of equal amplitude across all directions. Each excitation coil was meticulously wound with 1000 turns of a 0.2 mm diameter copper wire.

The circular detection coil, a pivotal component, boasted dimensions outlined in Figure 3.1(d) and 3.1(e). This detection coil was meticulously situated at both the bottom and the center of the copper core (as demonstrated in Figure 3.1(f)). With precision, the detection coil consisted of 854 turns, meticulously wound using a 0.05 mm diameter copper wire. This intricate configuration and meticulous assembly underpin the RUECC probe's ability to generate and harness the desired rotating ECs for the optimal detection of defects.

3.2.2. Method of generating an RUEC on the surface of the test piece

To validate the proficiency of the copper core's intricate design in facilitating the convergence of ECs at the core's tip and the subsequent generation of a RUEC on the test piece surface, a simulation of the RUECC probe model was conducted. The dimensions of this model mirrored those illustrated in Figure 3.1. This simulation was executed utilizing the Magnet software (version 7.9.0.18, Mentor Graphics Corporation) through a time-harmonic 3D analysis approach. The goal was to ascertain the practicality and efficacy of the proposed design in inducing the desired EC convergence and RUEC pattern, thus laying the foundation for the subsequent experimental phase.

The electromagnetic parameters utilized in this analytical investigation have been outlined in Table 3.1. For the simulation, an aluminum plate measuring $70 \times 70 \times 10$ mm was employed. The RUECC probe operated with an excitation current of 10 mA and a frequency of 10 kHz.

Table 3.1. Electromagnetic parameters used in the analysis for RUECC probe.

	Material	Electrical conductivity, σ (MS/m)	Relative permeability, μ_r
Wire of excitation coil			
Wire of detection coil	Copper	57.7	1.0
Core of coil			

Figure 3.2 Principle of generating an RUEC with the RUECC probe, (a) Graph of two alternating current sources 90 degrees out of phase with each other, (b) ECs converging at the tip of the copper core, (c) Contour and arrow plots of the EC distribution on the excitation coil and RUEC generated on the test piece, (d) EC convergence controller, (e) Contour and arrow plots of the RUEC distribution on the test specimen.

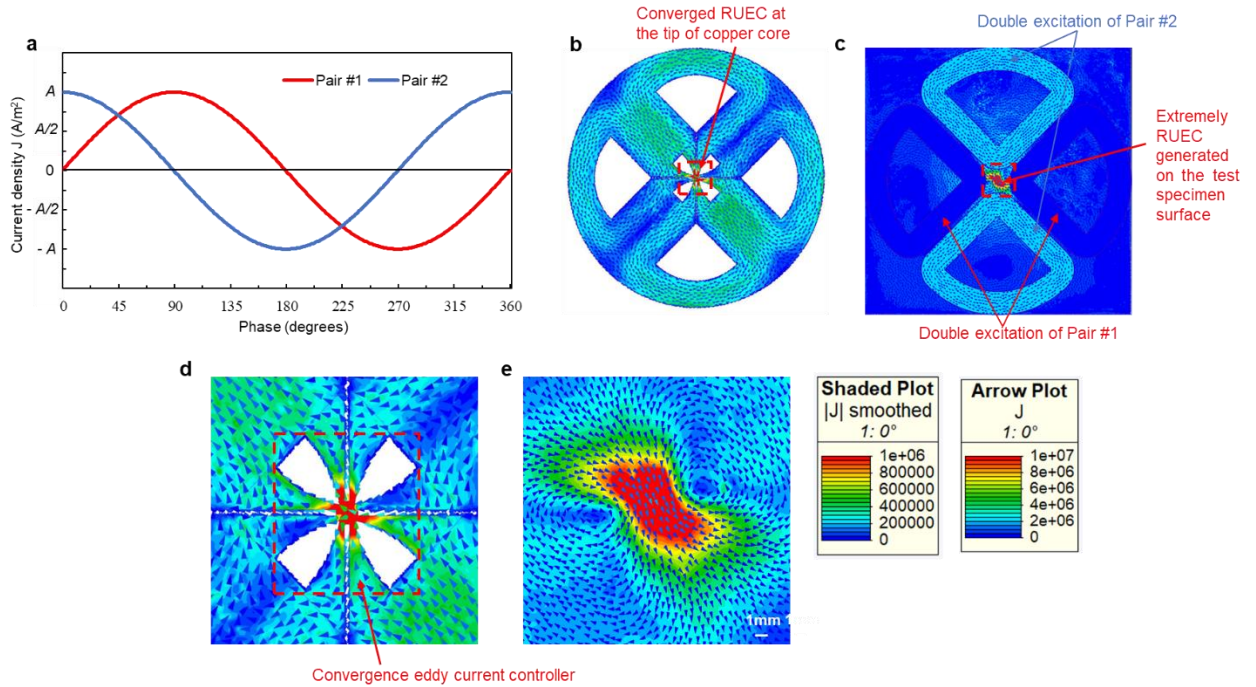


Figure 3.2 illustrates the underlying principle behind the creation of the RUEC pattern on the test piece surface, a result of the convergence of ECs at the tip of the copper core. The method employed here involves the application of two alternating excitation current sources, each exhibiting a phase difference of 90 degrees, to the two pairs of double excitation coils (as depicted in Figure 3.2(a)). Due to this phase difference, the ECs induced on the copper core by Pair #1 and Pair #2 can be described as follows:

$$EC_1 = A \cos(\omega t + \varphi) \quad (3.1)$$

$$EC_2 = A \cos\left(\omega t + \varphi + \frac{\pi}{2}\right) = A \sin(\omega t + \varphi) \quad (3.2)$$

Therefore, the total EC induced on the copper core is calculated by the equation:

$$EC_{total} = \sqrt{(EC_1)^2 + (EC_2)^2} = \sqrt{[A\cos(\omega t + \varphi)]^2 + [A\sin(\omega t + \varphi)]^2} = |A| \quad (3.3)$$

Here, EC_{total} represents the cumulative EC resulting from the combined effects of EC_1 and EC_2 , which are the ECs generated on the copper core through the action of double excitation coil Pairs #1 and #2. In this context, A and φ denote the amplitude of the current density and its respective phase, while $\omega = 2\pi f = 2\pi/T$, with f representing the frequency and T denoting the period. Equation (4.3) reveals that the total EC induced on the copper core undergoes continuous rotation with a fixed period $T = 1/f$, maintaining a consistent amplitude throughout.

In Figure 3.2(b), it observes both contour and arrow plots that provide a detailed representation of the distribution of EC across the surface of the copper core within the EC convergence probe. These plots help visualize how the ECs are distributed and how they interact within the core. Figure 3.2(c) presents contour and arrow plots that illustrate the distribution of eddy currents not only on the excitation coil but also on the test piece itself. These plots provide a comprehensive view of how the ECs are generated by the probe's excitation coil and how they manifest as a RUEC on the surface of the test piece. Additionally, Figure 3.2(e) presents contour and arrow plots that focus exclusively on the distribution of the RUEC on the test specimen. This visualization allows you to see how the RUEC spreads and converges across the test piece, highlighting the rotational and converging nature of the eddy currents as they interact with the material.

Let's consider a specific scenario at time $t = 0$, where the amplitude of Pair #1 is set to zero, while that of Pair #2 is at its maximum value, as depicted in Figures 3.2(a) and 3.2(c). Thanks to the intricate design of the copper core, this configuration leads to the convergence of the induced rotating ECs at the apex of the copper core, as visually represented in Figures 3.2(b) and 3.2(d). Consequently, an exceptionally potent RUEC is generated on the surface of the test piece, as depicted in Figures 3.2(c) and 3.2(e). Figure 3.2(c) provides a clear illustration of the resulting RUEC, showcasing a notably higher amplitude compared to the excitation current applied to the excitation coils. This outcome underscores the effectiveness of the proposed design in generating a robust RUEC that exhibits significantly enhanced magnitudes on the test piece's surface.

3.2.3. 3D-Finite element simulation results

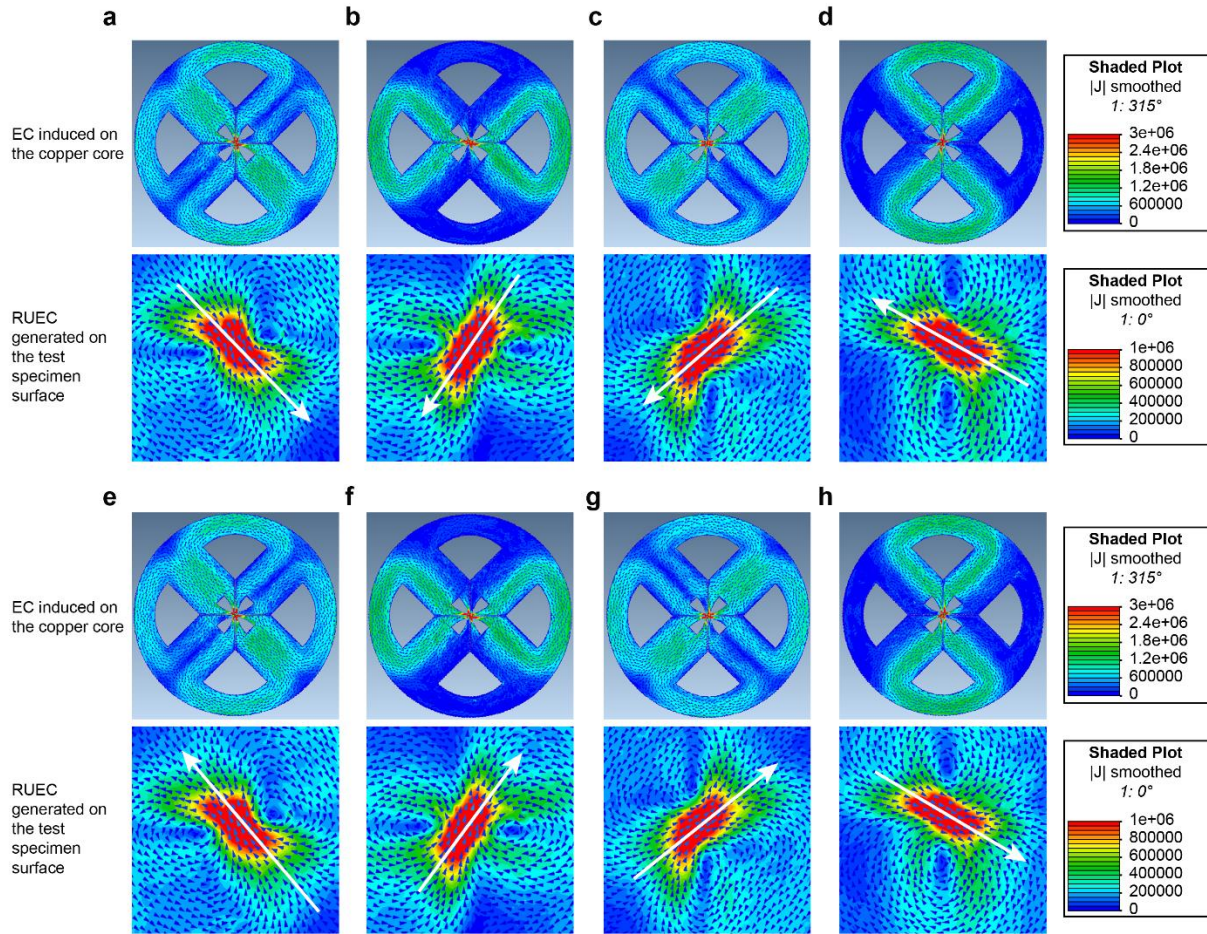


Figure 3.3 Simulation results of RUEC distribution patterns with the RUECC probe: (a) At 0 degrees, (b) At 45 degrees ($\pi/4$), (c) At 90 degrees ($\pi/2$), (d) At 135 degrees ($3\pi/4$), (e) At 180 degrees (π), (f) At 225 degrees ($5\pi/4$), (g) At 270 degrees ($3\pi/2$), (h) At 315 degrees ($7\pi/4$).

Figure 3.3 portrays the contour and arrow plots illustrating the distribution of ECs on both the copper core and the test piece surfaces. The simulation outcomes reveal a phenomenon wherein the converging ECs undergo rotation at the apex of the copper core, ultimately resulting in the creation of a RUEC on the surface of the test piece.

In cases where the phases are set at 0 and 180 degrees, the amplitude of Pair #1 is rendered negligible, while Pair #2 attains its maximum magnitude, albeit with an opposing polarity (as depicted in Figure 3.2(a)). This configuration leads to the emergence of Uniform Eddy Currents (UECs) on the test piece's surface, characterized by opposing directions (as illustrated in Figures 3.3(a) and 3.3(e)). Conversely, when the phases are configured at 90 and 270 degrees, the amplitude of Pair #2 is reduced to zero, while Pair #1 assumes its maximal amplitude with an

opposing polarity (as represented in Figure 3.2(a)). Consequently, UECs are again generated on the test piece's surface, also exhibiting opposing directions (as shown in Figures 3.3(c) and 3.3(e)). This pattern of opposing UECs persists for phase settings of 45 and 225 degrees (as observed in Figures 3.3(b) and 3.3(f)), as well as 135 and 315 degrees (as evident in Figures 3.3(d) and 3.3(h)).

As a result of these coherent phase relationships, a remarkable outcome ensues—the constant-intensity converging UECs on the test piece's surface undergo continuous rotation with a consistent period denoted as T . This rotational behavior is mirrored in the EMF generated across the circular detection coil, further enhancing the probe's capability to detect cracks spanning all possible directions. This characteristic represents a significant advancement, offering a substantial improvement in the detection capability of cracks within the test piece.

3.2.4. Principle of the output detection signal

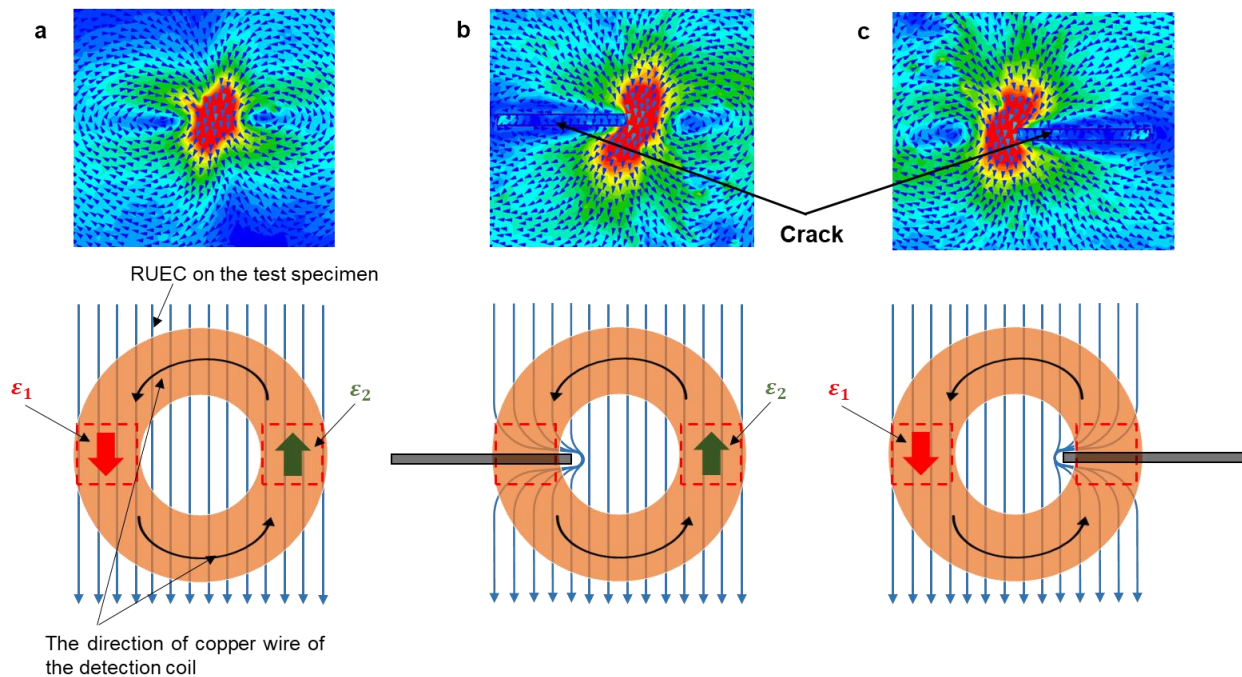


Figure 3.4 Principle of the output detection signal with the circular detection coil: (a) Without a crack, (b) With a crack under the left side of the detection coil, (c) With a crack under the right side of the detection coil.

The state of balance is achieved when EMFs ε_1 and ε_2 , generated within the detection coil, possess equal magnitudes but opposite polarities (Figure 3.4(a)). This equilibrium results in their mutual annulment, a phenomenon referred to as the self-differential characteristic. Consequently, the resultant output detection signal becomes null, giving rise to the self-nulling property.

Conversely, an unbalanced state arises when a crack exists beneath the detection coil of the RUECC probe. This crack disturbs the normal behavior of the RUECC, leading to a modification in the magnitude of either ε_1 (Figure 3.4(b)) or ε_2 (Figure 3.4(c)). This alteration disrupts the self-nulling equilibrium, thereby triggering the generation of a signal indicative of the presence of a crack.

3.3. Experimental setup

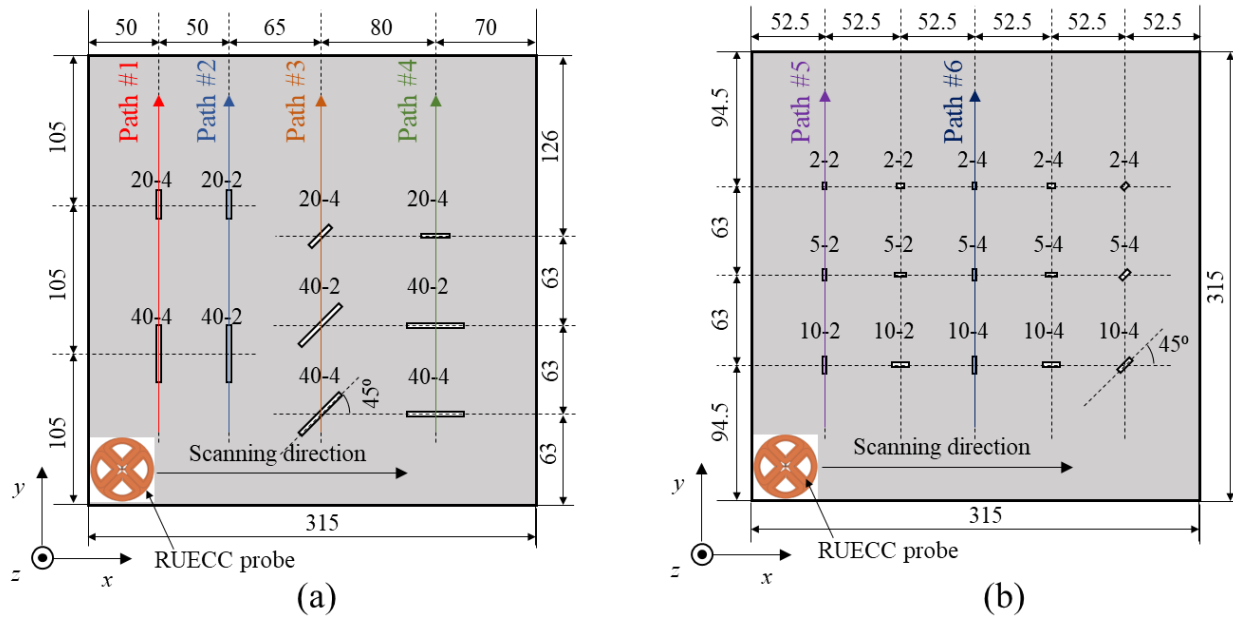


Figure 3.5 Specifications of aluminum alloy plates for RUECC probe (units in mm): (a) Test piece #1 and (b) Test piece #2.

For the experimental scanning procedure using the RUECC probe, the probe was systematically moved along the x-axis and then replicated by shifting it incrementally along the y-axis. This allowed for comprehensive coverage of the specimen's surface. To validate the efficacy of detecting cracks utilizing the approach involving rotating ECs converging at the tip of the copper core, two distinct 5052 aluminum plates were prepared as test specimens. These plates contained cracks of varying dimensions (denoted by L-D symbol: L representing the crack length in millimeters, and D indicating the crack depth in millimeters; all crack widths were standardized to 0.5 mm). Additionally, these plates exhibited different orientations, as illustrated in Figure 3.5(a) and 4.5(b).

Experimental trials were conducted on the first test specimen (Figure 3.5(a)) featuring

cracks with lengths of 40 and 20 mm and depths of 2 and 4 mm. This was aimed at assessing the performance of the RUECC probe, as well as evaluating its effectiveness in rejecting noise signals through the application of self-nulling and self-differential characteristics. Subsequently, another experiment was conducted on the second test specimen (Figure 3.5(b)), which encompassed small cracks situated near one another. The purpose of this trial was to gauge the RUECC probe's capability in detecting minute cracks effectively. It's important to note that these artificial cracks were fabricated using electrical discharge machining techniques. Throughout the scanning process, intervals of 1 mm were maintained in both the x and y directions. The dimensions of each crack are presented in Supplementary Table 3.2.

Table 3.2. Sizes of artificial cracks in two aluminum plates using for experiments with RUECC probe.

Test piece	Symbol of crack	Width (mm)	Length (mm)	Depth (mm)
1	20-2	0.5	20	2
	20-4			4
	40-2		40	2
	40-4			4
2	2-2		2	2
	2-4			4
	5-2	5	5	2
	5-4			4
	10-2	10	10	2
	10-4			4

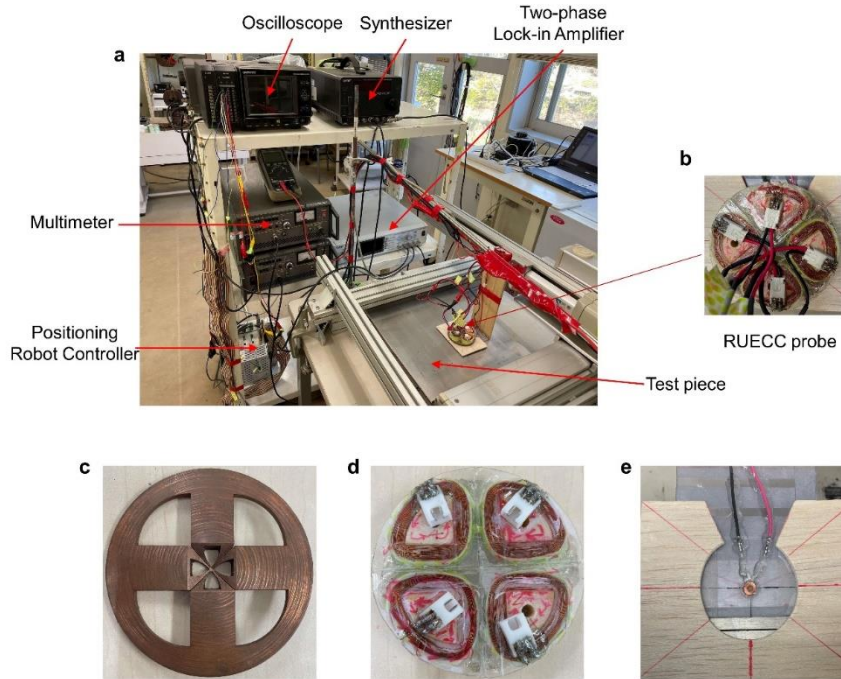


Figure 3.6 Experimental implementation: (a) Experimental setup, (b) RUECC probe, (c) Actual shape of the copper core, (d) Actual shape of the excitation coils, (e) Actual shape of the circular detection coil.

The experimental setup is depicted in Figure 3.6. Two sine wave excitation currents were employed, operating with a frequency of 10 kHz and a magnitude of 10 mA. These currents were precisely generated using a function generator (WAVE FACTORY WF1946B, NF Co., Yokohama, Japan) in conjunction with two high-speed bipolar amplifiers (NF HAS 4012, NF Co., Yokohama, Japan). To facilitate controlled movement, a computer-controlled positioning robot module orchestrated the motion of the RUECC probe across the scanning surface of the test specimen, maintaining a constant speed of 10 mm/s.

After the scanning process, the resulting output amplitude signals were captured by the single detection coil. These signals were then subjected to processing utilizing a two-phase lock-in amplifier (NF 5601B) before being stored within a digital oscilloscope (Graphtec GL7000). Detailed specifications of both the excitation coils and the circular detection coil pertaining to the RUECC probe can be found in Table 3.3.

Table 3.3. Specifications of each excitation coil and the circular detection coil for the RUECC probe.

Each excitation coil	Turns	1000
	Wire diameter (mm)	0.2
	Resistance (Ω)	38
	Impedance (Ω)	104
	Inductance (mH)	15
Detection coil	Turns	854
	Wire diameter (mm)	0.05
	Resistance (Ω)	103
	Impedance (Ω)	105
	Inductance (mH)	2.5

3.4. Experimental results and discussions

3.4.1. Authenticating the small crack detection ability of the RUECC probe

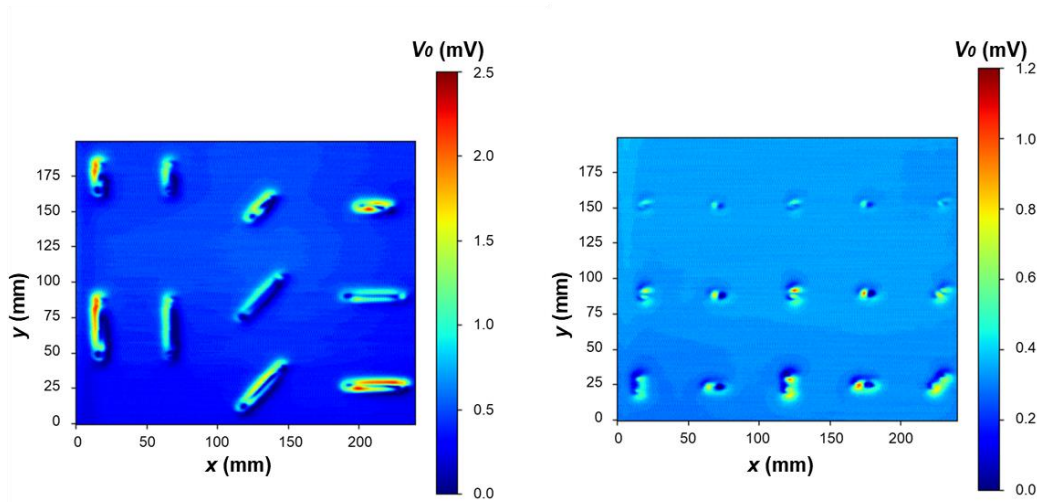


Figure 3.7 Experimental results with RUECC probe: (a) Test piece 1, (b) Test piece 2.

The experimental results obtained using the RUECC probe on test pieces 1 and 2 are illustrated in Figure 3.7. In general, the measurement outcomes effectively differentiate between signals emanating from cracks characterized by distinct dimensions and orientations. Nevertheless, a minor influence on the amplitude of the crack signal was observed for cracks inclined at 45 degrees (along Path #3) relative to the x-axis, in comparison to cracks with other orientations.

Evidently, the peak signal magnitudes along Paths #1, #2, and #4 for the cracks denoted as 40-4, 40-2, and 20-4 respectively, exhibit substantial similarity. However, the peak signal

magnitude along Path #3 demonstrates a reduction. This phenomenon arises from the challenge in adjusting the output signal amplitude to zero mV (approximately 0.3 mV in experimental execution) when the RUECC probe is placed over an area devoid of cracks. This difficulty arises due to the smaller area encompassing the strongly induced EC and the reduced dimensions of the circular detection coil, thereby complicating manual calibration in experimental implementation.

Furthermore, it's important to note that RUECs do not possess identical amplitudes in all directions. Specifically, the RUECC at a 45-degree angle represents a composite of RUECs at 0 and 90 degrees. Consequently, the EMFs generated within the detection coil experience a minor alteration when the cracks are inclined at 45 degrees, in comparison to the scanning directions parallel or perpendicular to the cracks. This phenomenon is vividly demonstrated through the dissimilarity in amplitude between the two peaks of the crack signal (as depicted in Figure 3.7(a)).

Hence, it becomes evident that the RUECC probe necessitates the possession of self-nulling and self-differential characteristics, as previously elucidated [30], [31]. Such attributes are imperative to amplify sensitivity to the maximum extent possible and to ensure precise evaluation of the physical attributes of cracks, especially when dealing with small cracks. However, an intriguing observation emerges in the context of small cracks in specimen 2 (Figure 3.7(b)), wherein two distinct crack signal peaks manifest. This peculiar occurrence can be attributed to the marginal disturbance caused by the formidable EC intensity on the surface of the test specimen, thereby having a negligible effect on the signals originating from small cracks. This observation underscores the remarkable sensitivity of the RUECC probe when detecting small cracks.

3.4.2. Validating the crack detection ability of the RUECC probe through six paths

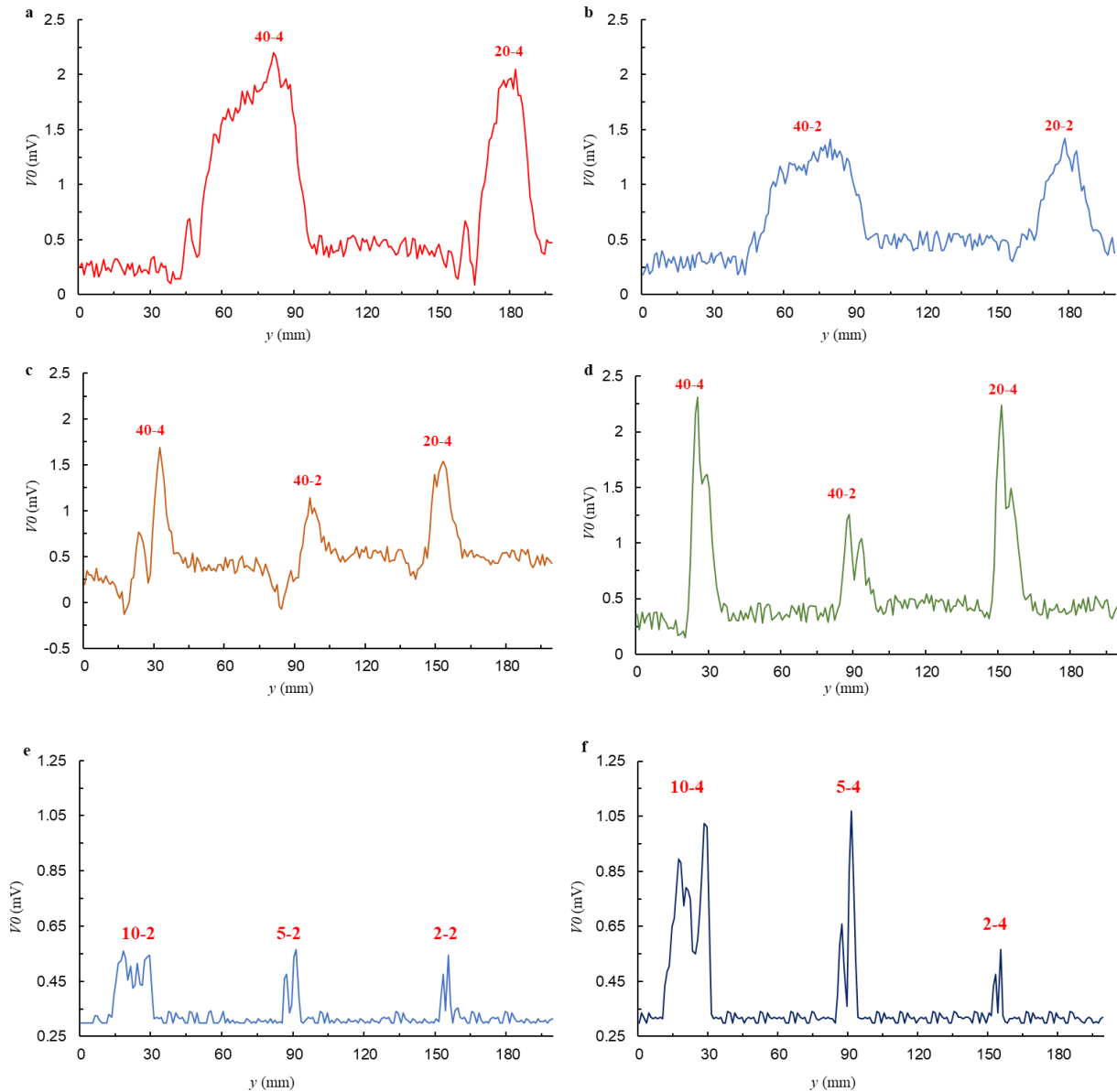


Figure 3.8 Measurement results of six paths obtained with the RUECC probe: (a) Path #1 (the length of cracks 4 mm deep in test specimen 1 was perpendicular to the x-axis), (b) Path #2 (the length of cracks 2 mm deep in test specimen 1 was perpendicular to the x-axis), (c) Path #3 (the crack length in test specimen 1 was inclined 45 degrees from the x-axis), (d) Path #4 (the crack length in test specimen 1 was parallel to the x-axis), (e) Path #5 (the length of cracks 2 mm deep in test specimen 2 was perpendicular to the x-axis), (f) Path #6 (the length of cracks 4 mm deep in test specimen 2 was perpendicular to the x-axis).

To authenticate the crack detection capability of the RUECC probe in all directions and to validate the induction of rotating ECs on the surface of the test specimen by the RUECC probe, an

array of measurements was performed. These measurements encompassed various scanning paths on test piece 1, including Path #1 (where the length of 4 mm deep cracks was perpendicular to the x-axis), Path #2 (with 2 mm deep cracks perpendicular to the x-axis), Path #3 (involving cracks inclined at a 45-degree angle from the x-axis), and Path #4 (with cracks parallel to the x-axis). The obtained measurement results for these paths are depicted in Figures 3.8(a-d), respectively. Moreover, the crack detection capability of the RUECC probe was further evaluated on test piece 2 along Path #5 (with 2 mm deep cracks perpendicular to the x-axis) and Path #6 (featuring 4 mm deep cracks also perpendicular to the x-axis). The measurement outcomes for these specific paths are illustrated in Figures 3.8(e) and 3.8(f), respectively.

The comprehensive measurement results validate the RUECC probe's efficacy in successfully detecting cracks present in both test specimens. Analyzing the data from Paths #1 to #4 in test piece 1 reveals noteworthy insights. It becomes evident that the peak signal amplitude for cracks with a depth of 4 mm (labeled as 40-4 and 20-4) is consistently twice that of cracks with a depth of 2 mm (denoted as 40-2 and 20-2). Similarly, a similar amplitude pattern emerges from the measurement results of paths #5 and #6 in test piece 2, where the maximum signal amplitude for cracks with a depth of 4 mm (referred to as 10-4 and 5-4) is twice that of cracks with a depth of 2 mm (labeled as 10-2 and 5-2). In the case of 2 mm length cracks, due to the propensity of UECs to deviate around cracks rather than propagate underneath, the maximum signal amplitude remains consistent between cracks with a length of 2 mm and depths of 2 mm and 4 mm. This observation underscores that the peak signal amplitude is indicative of the crack's depth. Furthermore, examining the measurement results in test specimen 1, it's evident that the distance between the two corner edges of the crack signal for a crack with a length of 40 mm (40-4 and 40-2) is twice that of a crack with a length of 20 mm (20-4 and 20-2). Similarly, this relationship holds in test piece 2, where the distance between the corner edges of the signal for a crack with a length of 10 mm (10-4 and 20-2) is double that of a crack with a length of 5 mm (5-4 and 5-2). Hence, the gap between the corner edges of the crack signal serves as an indicator of the crack's length.

Moreover, the distances between the corner edges of the crack signals obtained along Path #4 (perpendicular to the crack length) exhibit uniformity, attributable to the consistent crack width of 0.5 mm across all instances. Therefore, when measurement results are obtained perpendicular to the crack length, the separation between the corner edges of the crack signal provides insight into the crack's width. Although the output signal amplitude does not precisely reach zero,

registering at 0.3 mV (attributable to self-nulling and self-differential characteristics), distinguishing the crack signal, particularly the small crack in Figure 3.7(b), is easily feasible when the measured signal deviates from a finite baseline—0.3 mV as illustrated in Figure 3.8.

Analyzing the measurement outcomes of Path #3 and Path #4 reveals a dissimilarity in the dual peaks of the crack signals (depicted in Fig. 3c and d). Notably, the crack signal amplitudes observed along Path #3 (Figure 3.8(c)), corresponding to a crack length inclined at a 45-degree angle from the x-axis, were marginally diminished when contrasted with those observed along the other paths. This phenomenon can be attributed to the output signal amplitude of around 0.3 mV when the RUECC probe is devoid of any crack underneath, which marginally disrupts the balanced condition [30]. This underscores the pivotal role of self-nulling and self-differential characteristics [30], [31] in augmenting the RUECC probe's crack detection prowess. The impact on crack detection ability is marginal when the crack length is approximately at a 45-degree angle from the x-axis, whereas it remains unaffected for crack lengths in other orientations. This crucially addresses the principal drawback encountered in prior studies [17], [81]. Additionally, it's noteworthy that the separation between the corner edges of the crack signal obtained along Path #3 distinctly differs from that of the other paths. This is attributed to the 45-degree inclination of the measurement result concerning the crack length or width. In simpler terms, the separation between the corner edges of the crack signal along Path #3 does not provide an accurate indication of the crack's length or width.

Analyzing the crack signal within test piece 2 based on the measurements along Paths #5 and #6, it is evident from Figure 3.8(e) that the peak signal amplitudes for cracks with a depth of 2 mm (10-2, 5-2, 2-2) are relatively consistent. However, a notable reduction is observed in the peak signal amplitude for the crack with a depth of 4 mm and a length of 2 mm (2-4) when compared to those of lengths 10 mm and 5 mm (10-4, 5-4), as depicted in Figure 3.8(f). This discrepancy implies that the generated RUEC intensity within the test piece is insufficient to detect defects smaller than the 2-4 crack configuration. In such instances, potential solutions may involve adjusting the magnitude of the excitation current as well as the frequency of the excitation coils to enhance the RUEC intensity produced within the test specimen, a strategy elucidated in Ref. [17].

3.5. Summary

In summary, the new rotating uniform eddy current convergence (RUECC) probe represents a significant advancement in the realm of crack detection and nondestructive testing.

Through a meticulously designed copper core and a unique excitation coil configuration, the RUECC probe successfully demonstrates its capability to generate rotating eddy currents that converge at the tip of the copper core. This innovative design enables the probe to exhibit self-nulling and self-differential characteristics, which are crucial for enhancing crack detection sensitivity.

Experimental validation using two different test specimens showcases the remarkable performance of the RUECC probe. The probe effectively detects cracks of varying dimensions and orientations, thereby exhibiting its versatility and potential applicability across different scenarios. The ability to discern crack characteristics based on peak signal amplitudes and the distance between corner edges of crack signals underscores the probe's accuracy in assessing crack depth, length, and width.

However, the study also highlights certain limitations, particularly regarding cracks oriented at approximately 45 degrees from the scanning direction. These cases show a reduced peak signal amplitude because on the balanced condition, emphasizing the importance of maintaining self-nulling and self-differential properties to ensure consistent crack detection ability.

To overcome challenges related to detecting smaller defects, the study suggests potential solutions involving adjustments to the excitation current magnitude and frequency. This approach aligns with previous findings and provides a pathway for further refinement and optimization of the RUECC probe's performance.

In summary, the RUECC probe's innovative design, coupled with its ability to generate rotating eddy currents and exhibit self-nulling and self-differential characteristics, marks a significant advancement in crack detection technology. The experimental results underscore its efficacy in detecting cracks of varying dimensions and orientations, while also identifying areas for potential improvement. As a versatile and promising tool in the realm of nondestructive testing, the RUECC probe holds the potential to contribute substantially to the field's continuous evolution and enhancement.

Chapter 4: Enhancing excitation magnetic field intensity with support materials (FAAP and ferrite)

4.1. Introduction

This chapter presents a pioneering RUEC probe, employs a configuration of four rectangular excitation coils aligned on a single plane, resulting in the generation of eddy currents with uniform amplitudes across the surface of the test specimen when utilizing a pair of duple excitation coils. To further heighten the amplitude of the magnetic field and optimize the crack signal, the design is enhanced by incorporating four ferrite cores within all the excitation coils. The resultant effect of the RUEC induced on the test specimen surface and the efficacy of the ferrite cores in amplifying the magnetic field amplitude were confirmed through rigorous 3D-FEA simulations. Subsequently, experimental assessments were conducted on aluminum plates, utilizing both probes with and without ferrite cores. These experimental validations affirm the RUEC probe's proficiency in effectively detecting cracks across various orientations and dimensions. Moreover, to refine the measurement outcomes, we subjected them to multivariate singular spectral analysis (MSSA) for noise reduction. MSSA is a robust technique employed to extract the fundamental signal from noisy data by decomposing it into a set of orthogonal components. By effectively removing the noise-related components, the denoised signal was extracted, significantly enhancing the clarity and dependability of the measurement results. Subsequently, we conducted a comparative analysis between the denoised results obtained through MSSA and those derived from wavelet-based principal component analysis (wavelet-PCA) and a Denoise Filter. This comprehensive evaluation enabled us to ascertain the effectiveness of the applied noise reduction methods in improving the precision and reliability of crack detection using the RUEC probe model.

In addition, this chapter introduces a novel film EC probe, drawing inspiration from the merits of FAEC sensors that exhibit a strong crack-detection capacity due to their negligible lift-off gap. The proposed probe features a square configuration, with the detection coil interwoven with the excitation coil to establish four distinct interaction zones of EC on the test piece's surface, facilitating comprehensive crack detection in all orientations. The excitation and detection coils are meticulously arranged in a mutually alternating pattern within the same layer, yielding heightened sensitivity. Furthermore, an iron-based ferromagnetic amorphous alloy particle, referred to as FAAP, was strategically incorporated into the film EC probe. This addition, despite

lacking conductivity, contributes to elevating the magnetic flux density, thereby amplifying the probe's defect detection capability. In the initial phase, a FEM analysis was executed to ascertain the effectiveness of the FAAP in augmenting magnetic flux density and enhancing the induced EC on the test piece. Subsequently, experimental trials were conducted using four artificially induced cracks on an aluminum surface to validate the exceptional performance of the film EC probe. Through this dual approach of computational simulation and practical experimentation, the study establishes the probe's effectiveness in crack detection across varying scenarios.

4.2. Enhanced crack detection in conductive materials using a rotating uniform eddy current probe with four rectangular excitation coils and ferrite cores

4.2.1. Design and methods of RUEC probe

4.2.1.1. Design of RUEC probe using four rectangular excitation coils

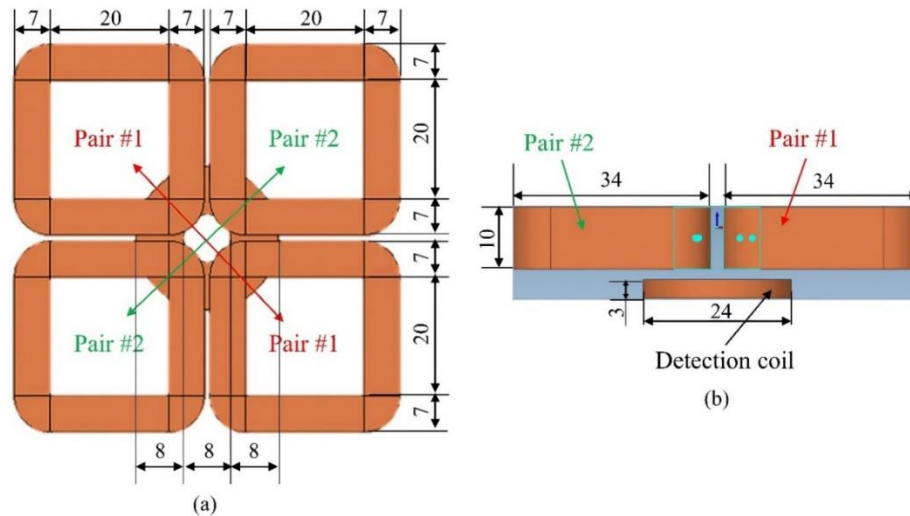


Figure 4.1. The structure of RUEC probe using four rectangular coils as two pairs of excitation coils (all units: mm): (a) top view, (b) front view.

Figure 4.1 illustrates the architecture of the RUEC probe, integrating several crucial attributes to heighten its sensitivity for defect detection across all orientations. A pivotal feature of the probe lies in the uniform dispersion of eddy currents produced by the excitation coils. This uniformity guarantees accurate defect detection throughout the test specimen, regardless of their spatial distribution. The RUEC probe comprises a pair of duple excitation coils, both positioned on the same plane and featuring identical dimensions. This design facet is pivotal in ensuring equivalence in the eddy currents generated by the two pairs of excitation coils, a phenomenon well-documented in prior research.

Each excitation coil is composed of 1000 turns of 0.2 mm diameter copper wire, facilitating the essential magnetic field generation required to induce eddy currents within the test specimen. Alongside the excitation coils, the RUEC probe integrates a circular detecting coil, strategically placed at the center and lower region of the excitation coils, as depicted in Figure 4.1(b). Constructed with 330 turns of 0.2 mm diameter copper wire, this configuration empowers the detecting coil to gauge the magnetic field engendered by the eddy currents in the test specimen. This resultant measurement forms the basis for defect detection capabilities.

4.2.1.2. Methods and 3D-FEA simulations

The diagram in Figure 4.2 portrays the application of alternating current to the two sets of duple excitation coils. It's of significance to observe that the phase of pair #1 lags 90° behind that of pair #2. As indicated in reference [34], the cumulative UEC induced on the test specimen's surface by these dual sets of excitation coils can be computed using equations (4.1.1) and (4.1.2). These equations respectively represent the UEC generated by pair #1 and pair #2, as established in the reference.

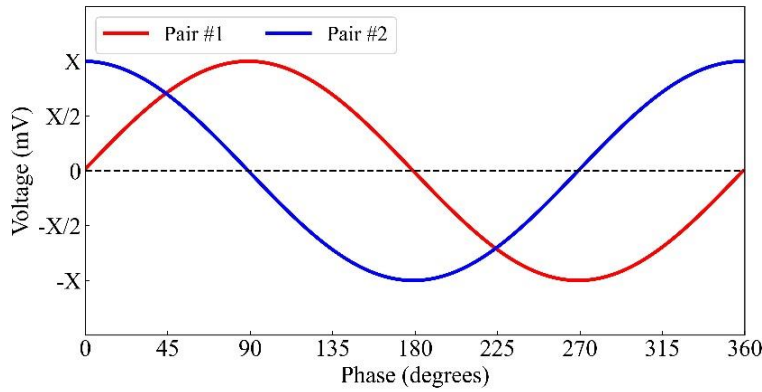


Figure 4.2. Applied alternating current for two pairs of excitation coils with phase difference 90 degrees.

$$EC_1 = A \sin(\omega t) \quad (4.1.1)$$

$$EC_2 = A \sin\left(\omega t + \frac{\pi}{2}\right) = A \cos(\omega t) \quad (4.1.2)$$

$$RUEC = \sqrt{(EC_1)^2 + (EC_2)^2} = A \quad (4.1.3)$$

The collective EC, referred to as RUEC, created on the surface of the test specimen is defined by equation (4.1.3). In this equation, A stands for the current amplitude, ω equals $2\pi/T$ where T symbolizes the period, and EC_1 and EC_2 represent the EC generated on the specimen's surface by

pair #1 and pair #2 of duple exciting coils, respectively. Equation (4.1.3) establishes that the RUEC generated on the test specimen through the utilization of two sets of duple exciting coils consistently remains equal to X across all phases.

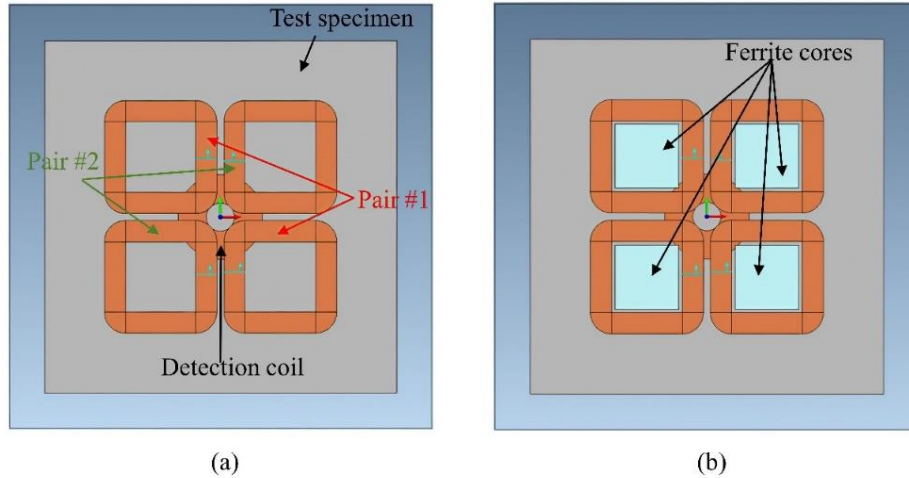


Figure 4.3. 3D-FEA simulation RUEC probe models: (a) without ferrite core, (b) with ferrite cores put inside all exciting coils.

The simulation of the RUEC probe was executed utilizing the models depicted in Figure 4.3, configured in a manner akin to the presentations in Figure 4.1. The simulated test specimen was an aluminum plate, measuring 100 mm in width, 100 mm in length, and 10 mm in depth.

The simulation involved the employment of two sets of duple exciting coils. These coils were operated with a current amplitude of 6 mA and a frequency of 10 kHz. Notably, a differential phase of 90° was maintained between the exciting currents of these two pairs of coils. Additionally, to augment the magnetic field amplitude, four ferrite cores were incorporated into the excitation coils of the RUEC probe. These ferrite cores measured 20 mm in length, 20 mm in width, and 10 mm in thickness. Their positioning within the excitation coils is demonstrated in Figure 4.3(b). The primary objective of this simulation was to contrast the amplified effect produced by the presence of ferrite cores with the RUEC model that lacked such cores. This assessment was carried out through time-harmonic 3D analysis, employing the Magnet software. A comprehensive overview of simulation parameters, including material properties, is provided in Table 4.1.

Table 4.1 The parameters of RUEC probe's material used for the simulation.

Material	Electrical conductivity, σ (MS/m)	Relative permeability, μ_r
----------	---	--------------------------------

Wire of Exciting coil	Copper	57	1
Wire of Detecting coil			
Test specimen	Aluminum	38	
Ferrite core	Ferrite	0	1000

Figure 4.4 provides a visual representation of the magnetic flux distribution across pair #2 of the duple exciting coil. The intent of this analysis is to examine the influence of the ferrite core on the magnetic flux distribution. The specific focus lies in comparing the magnetic flux distribution in cases where the ferrite core is either absent or present within the exciting coils.

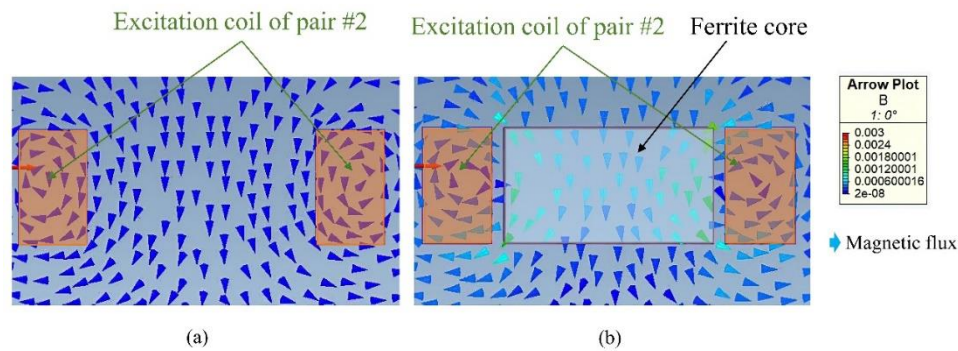


Figure 4.4. Shaded and arrow plots of concentrated magnetic fluxes in the excitation coils: (a) without ferrite core, (b) with ferrite cores put inside each exciting coil.

At the commencement of the analysis (0°), the magnetic flux distribution on Pair #2 of the duple exciting coils conforms to the conventional pattern and serves as our baseline for investigation. As demonstrated in Figure 4.4(a), the absence of ferrite cores within the exciting coils results in a relatively subdued concentration of magnetic flux. This observation, corroborated by the simulation outcomes, indicates a correspondingly limited induction of RUEC on the surface of the test specimen, as evidenced in Figure 4.5(a).

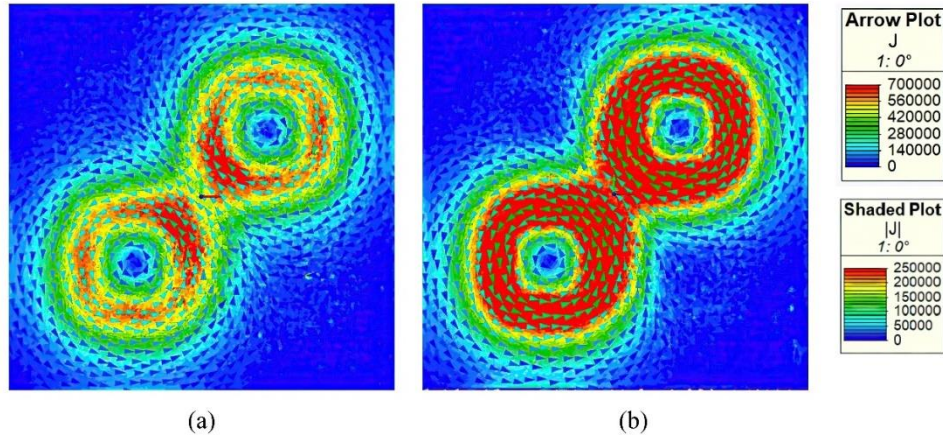


Figure 4.5. Distribution plots of the UEC on the test specimen surface: (a) without ferrite core, (b) with ferrite cores put inside each exciting coil.

In contrast, employing ferrite cores within the exciting coils leads to a marked augmentation in the magnetic flux traversing these coils [Figure 4.4(b)]. Consequently, this amplification translates to a more potent generation of RUEC on the test specimen surface, as illustrated in Figure 4.5(b). This outcome underscores the fact that the inclusion of ferrite cores can intensify the concentration of magnetic flux, thereby enhancing the overall effectiveness of the RUEC system.

Figure 4.6 illustrates the distribution of RUEC across the test specimen's surface, showcasing the comparison between the RUEC probe configurations with and without a ferrite core. The analysis encompassed measurements of the UEC values at different phases (0, 90, 180, 270, and 360 degrees) relative to the positioning of the excitation coils.

An in-depth examination of the UEC values unveils intriguing patterns. Firstly, the UEC values originating from pair #1 of the duple exciting coils exhibited a zero reading at phases 0, 180, and 360 degrees. In stark contrast, pair #2 registered its peak UEC values, culminating in the formation of UEC at a 45-degree angle along the y-direction [depicted in Figures 4.6(a), 4.6(e), and 6.6(i)]. This phenomenon was consistent at phases 90 and 270 degrees, wherein pair #1's UEC values reached their zenith, while pair #2's values plummeted to zero. Consequently, this yielded the development of UEC once again at a 45-degree angle along the y-direction, as portrayed in Figures 4.6(c) and 4.6(g).

Moreover, when phases were at 45, 135, 225, and 315 degrees, both pairs of the duple exciting coils produced UEC values of identical amplitudes. This resulted in the emergence of

UEC vectors extending along both the x- and y-directions [depicted in Figures 4.6(b), 4.6(d), 4.6(f), and 4.6(h)].

Overall, the figures underscore the intricate interplay between the excitation coils' arrangement, phases, and the resultant UEC distribution, elucidating the nuanced behavior of the RUEC probe.

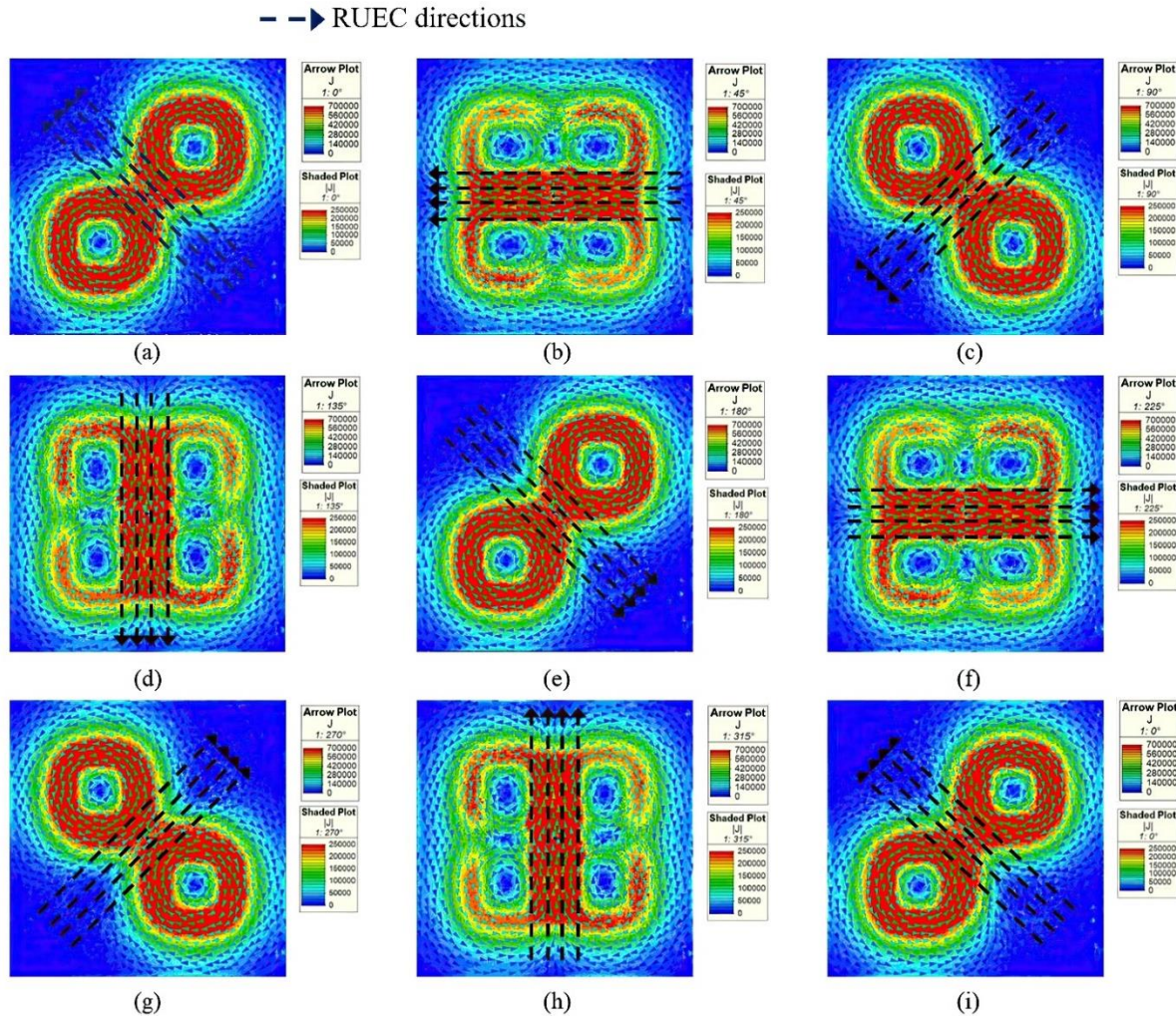


Figure 4.6. 3D-FEM results of RUEC distribution patterns using RUEC probe: (a) RUEC at 0 degrees, (b) RUEC at 45 degrees, (c) RUEC at 90 degrees, (d) RUEC at 135 degrees, (e) RUEC at 180 degrees, (f) RUEC at 225 degrees, (g) RUEC at 270 degrees, (h) RUEC at 315 degrees, (h) RUEC at 360 degrees.

4.2.1.3. Principle of crack output signal

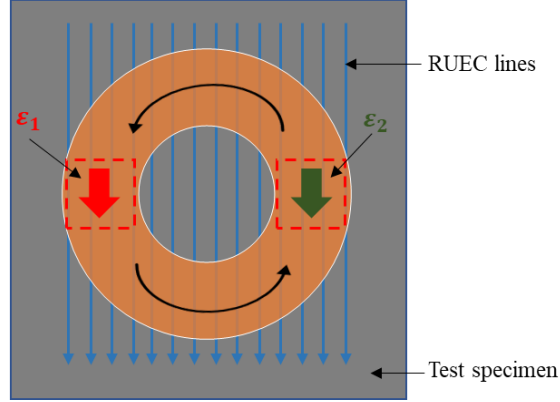


Figure 4.7. Illustration of self-nulling and self-differential properties.

As described in reference [30], the RUEC probe exhibits distinct self-nulling and self-differential characteristics. Notably, the detecting coil, visually depicted by the delineated red areas in Figure 4.7, is strategically positioned above the UEC flow. The objective is to generate EMF denoted as ε_1 and ε_2 , each with opposite polarities. This is achieved by inducing the UEC onto the surface of the test specimen within the designated red dotted box region as illustrated in Figure 4.7.

The cumulative EMF of the detecting coil, represented by the symbol ε , is mathematically formulated in equation (4.4):

$$\varepsilon = \varepsilon_1 - \varepsilon_2 \quad (4.4)$$

In this context, the symbols ε_1 and ε_2 denote the electromotive forces generated on opposite sides of the excitation coil. This fundamental arrangement is pivotal in realizing the self-differential trait inherent to the RUEC probe. The distinct polarities of ε_1 and ε_2 play a crucial role in this property, ensuring their mutual cancellation. Furthermore, the self-nulling attribute emerges when the cumulative EMF denoted by ε attains a value of zero, a condition facilitated by the equitable magnitudes of ε_1 and ε_2 .

Figure 4.8 illustrates the fundamental concept of crack signal detection utilizing a circular coil. This mechanism operates based on two distinct conditions: balanced and unbalanced. In the balanced state, the detecting coil remains inert, producing no discernible output signal in scenarios where no crack is present [depicted in Figures 4.8(a) and 4.8(d)] or when the crack aligns with the coil's center [as depicted in Figures 4.8(b), 4.8(e) and 4.8(g)]. This outcome emerges due to the near equivalence of the two EMFs, ε_1 and ε_2 , within the detecting coil. Although these forces exhibit opposite polarities, their magnitudes nullify each other, thereby resulting in a resultant

output amplitude signal of zero.

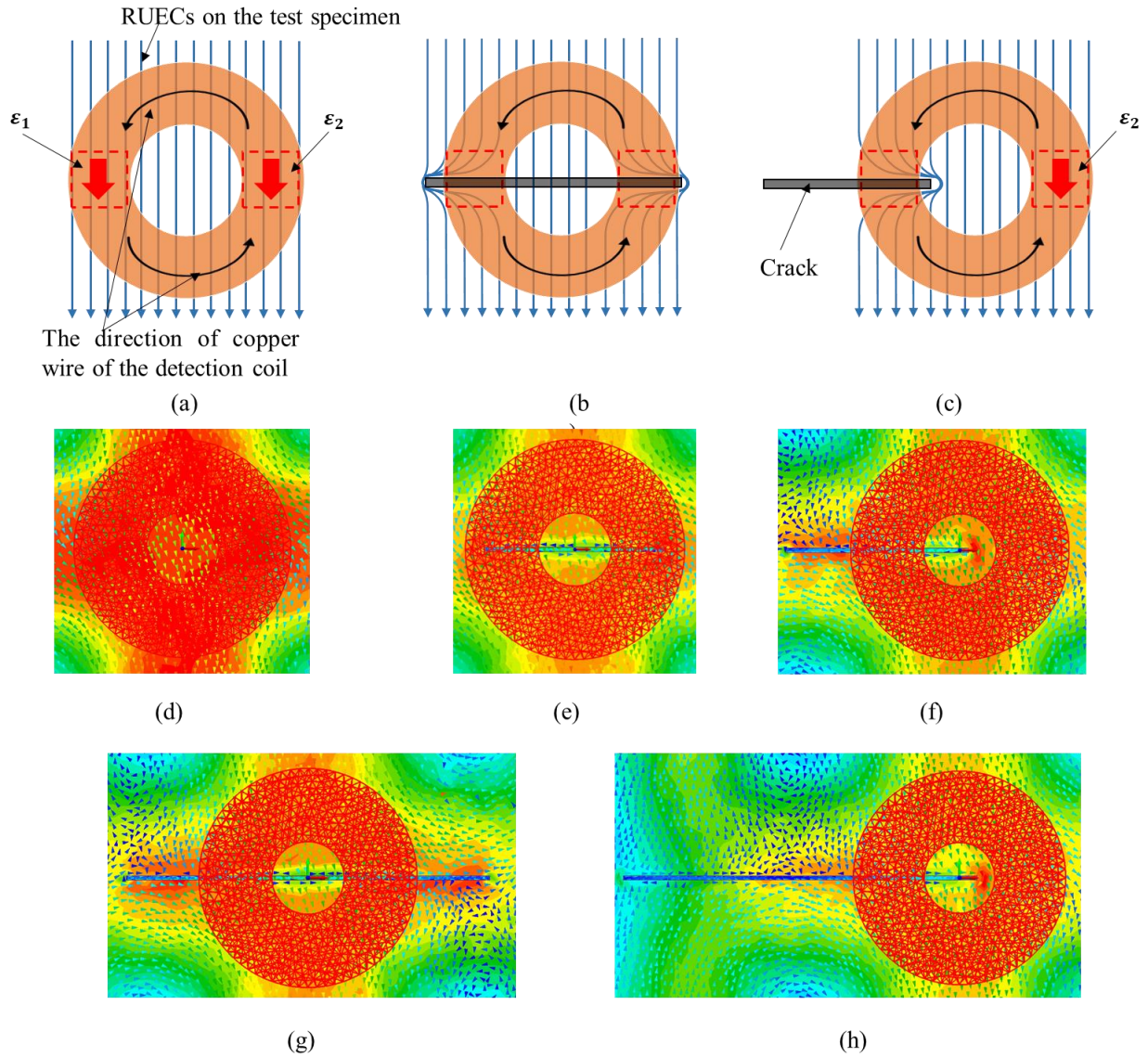


Figure 4.8. Theory of crack signal output with a circular detecting coil: (a) Balanced condition without cracks, (b) Balanced condition with a crack, (c) Unbalanced condition, (d) Simulation results for balanced conditions without cracks, (e) Simulation results for a balanced condition with a 20mm crack length, (f) Simulation results for a unbalanced condition with a 20mm crack length, (g) Simulation results for a balanced condition with a 40mm crack length, (f) Simulation results for a unbalanced condition with a 40mm crack length.

Conversely, the unbalanced condition arises when a crack exists, as demonstrated in Figures 4.8(c), 4.8(f), and 4.8(h). Here, the EMFs ε_1 or ε_2 change, giving rise to an output signal. The crack's presence disrupts the EC distribution, prompting an alteration in the induced voltage

within the detecting coil. Consequently, an output signal emerges, its magnitude correlating with the size of the crack. This output can be harnessed to ascertain both the precise location and extent of the crack.

Table 4.2: Simulation results for the output signal of the single detection coil in cases of cracks
(Unit: mV).

Symbol of cracks	Without cracks	With a crack in the left (peak)	With a crack in the center	With a crack in the right (peak)
20-2	1.77	4.21	2.73	4.21
20-4	1.77	7.45	0.85	7.45
40-2	1.77	4.27	2.5	4.27
40-4	1.77	7.84	1.23	7.84

The simulation results for the output signal of the single detection coil in cases where cracks are present are displayed in Table 4.2. From the simulation results, we can observe a significant change in the output signal of the single detection coil when cracks are present. Specifically, when comparing the cases of "Without cracks", "With a crack in the center" to "With a crack on the left", and "With a crack on the right", that presented to the peaks of crack output signals at points where cracks exist, as listed in Table 4.2. For example, at data point 20-2, the output signal increases from 1.77 mV to 4.21 mV with a crack on the left, decreases from 4.21 mV to 2.73 mV with a crack in the center, and increases from 1.77 mV to 4.21 mV with a crack on the right. Similarly, at data point 20-4, the output signal increases from 1.77 mV to 7.45 mV with a crack on the left, decreases from 7.45 mV to 0.85 mV with a crack in the center, and increases from 1.77 mV to 7.45 mV with a crack on the right.

Moreover, the peaks are almost the same with a depth of 2 mm for cracks (4.21 mV and 4.27 mV for 20-2 and 40-2, respectively), and a depth of 4 mm for cracks (7.45 mV and 7.84 mV for 20-4 and 40-4, respectively). Therefore, we can evaluate the crack depth through the peak of the output crack signal.

From the simulation results in Table 4.2, we can see that two peaks of crack signals represent two edges of the cracks, as shown in Figures 4.8(f) and 4.8(h). Consequently, we can evaluate the crack length through the two peaks of the output crack signal obtained by the detection coil.

4.2.2. Experimental setup

To conduct the experimental investigation, a test specimen composed of 5052 aluminum was meticulously fabricated for the purpose of testing and analysis. To replicate typical crack scenarios, four artificial cracks were deliberately introduced onto the test specimen's surface, with their dimensions precisely outlined in Table 4.3. The positions of these deliberately formed cracks were carefully identified and are visually depicted in Figure 4.9.

The experimental arrangement employed throughout the study is visually represented in Figure 4.10, while comprehensive information regarding the specific configurations of the probe coils can be found in Table 4.4. To stimulate the coil system and generate the required signals, a high-speed bipolar amplifier was employed. This amplifier effectively amplified two sine waves, each operating at a frequency of 10 kHz and sustaining a 90-degree phase disparity. These waves originated from a function generator. Once amplified, the resultant signal was directed towards the coil pairs within the excitation coils. Subsequently, the amplified signal flowed through these coil pairs, each maintained at a current intensity of 6 mA.

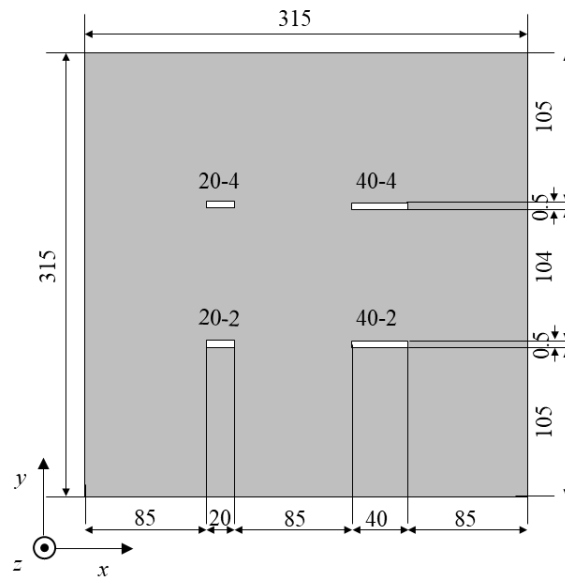


Figure 4.9. Specifications of aluminum plate using for RUEC probe

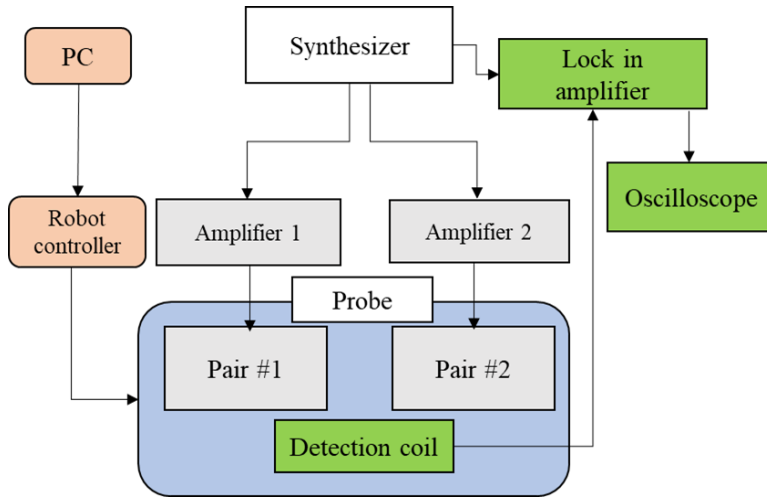


Figure 4.10. Experimental setup for RUEC probe.

Table 4.3 Dimensions of cracks used for RUEC probe (Unit: mm)

Crack symbol	Width	Length	Depth
20-2	0.5	20	2
20-4			4
40-2		40	2
40-4			4

Table 4.4 The information of the exciting and detecting coils of RUEC probe.

Each exciting coil	Turns	1000
	Wire diameter (mm)	0.2
	Resistance (Ω)	58.2
	Impedance (Ω)	212.2
	Inductance (mH)	32.49
Detecting coil	Turns	330
	Wire diameter (mm)	0.2
	Resistance (Ω)	16.2
	Impedance (Ω)	91.0

4.2.3. Experimental results and discussions

The primary objective of the experiments was to substantiate the RUEC probe's efficacy in detecting cracks across diverse orientations and conditions. To achieve this, two distinct scanning directions were meticulously employed to traverse the test specimen's surface, as visually depicted in Figure 4.11.

The first scanning approach, denoted as Scanning #1 (indicated by the violet line), encompassed guiding the RUEC probe along the x-axis, followed by its traversal along the y-axis, as depicted in Figure 4.11(a). This scanning direction aligned with the length of the cracks, essentially facilitating the detection of cracks when the scanning trajectory paralleled the crack length. On the other hand, scanning #2 (designated by the green line) involved maneuvering the RUEC probe along the y-axis and subsequently along the x-axis, as illustrated in Figure 4.11(b). This mode of scanning was perpendicular to the crack length, confirming the probe's ability to accurately detect cracks when its trajectory was orthogonal to the crack length.

Furthermore, measurements were meticulously gathered along paths #A (represented by the blue line) and #B (indicated by the red line) to enable a comparative analysis of the crack signal's amplitude. This comparison sought to elucidate how the crack depth and the integration of ferrite cores within the coils influenced the crack signal's magnitude. The presence of ferrite cores has the potential to influence the coils' sensitivity to crack detection. Through a juxtaposition of the outcomes obtained from these two paths, valuable insights can be gleaned into the impact of ferrite cores on the detection of cracks at varying depths.

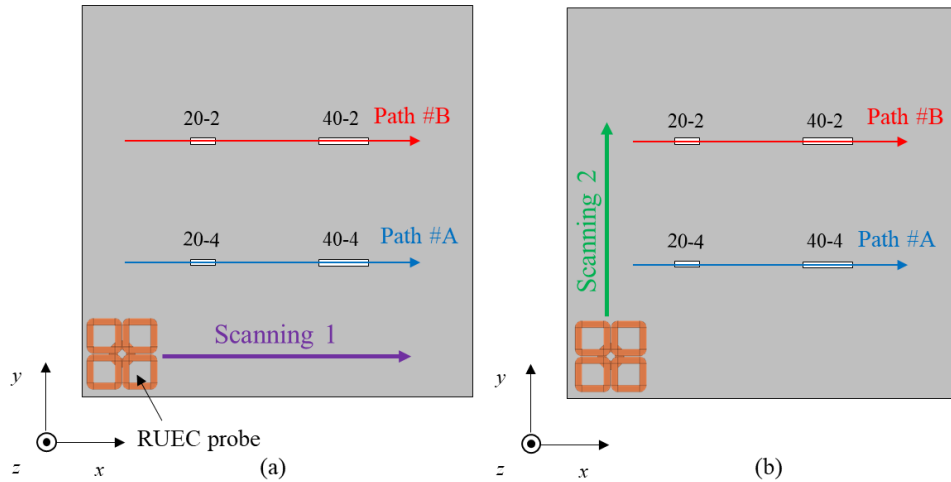


Figure 4.11. Scanning directions and the paths with RUEC probe: (a) scanning #1, (b) scanning #2.

4.2.3.1. Measurement obtains of scanning directions with RUEC probe

Figures 4.12 and 4.13 provide a comprehensive visual representation of the measurement outcomes yielded by the RUEC probe, both in the presence and absence of ferrite cores, for both scanning orientations - scanning #1 and scanning #2. These figures effectively encapsulate the experimental results of the crack detection process.

The results substantiate the RUEC probe's robust capability in detecting cracks characterized by distinct lengths and depths. This is discernible through the manifestation of two distinct amplitude peaks for each crack instance. Notably, when the detecting coil was situated at the midpoint of the crack's length (as illustrated in Figure 4.8(b)), the coil attained a state of equilibrium, thus resulting in a lack of discernible signals being generated. Furthermore, a noteworthy observation was made regarding the amplitude and peak values derived from cracks detected during scanning #1 and scanning #2. These values exhibited a striking similarity between the two scanning approaches. This synchronicity in values underscored the precision and dependability of the RUEC system in generating signals on the test specimen's surface, thereby affirming its efficacy in consistently identifying cracks of varying characteristics.

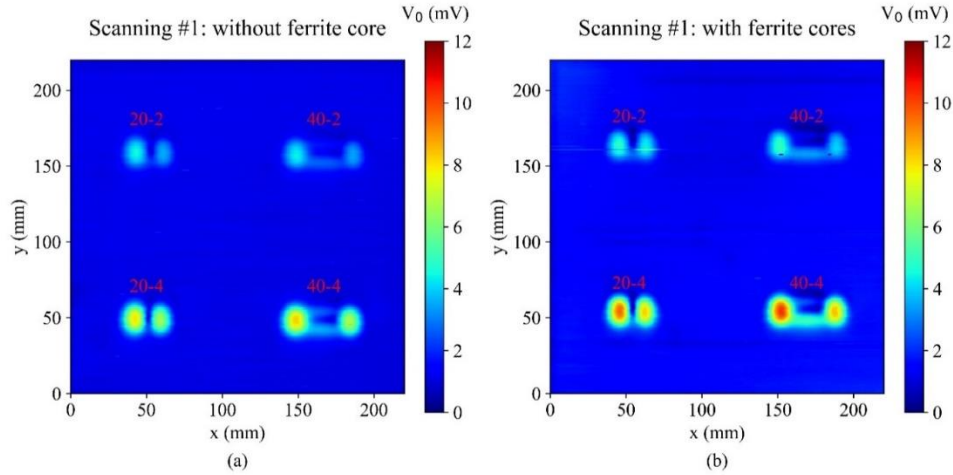


Figure 4.12. Measurement obtained in scanning #1 with RUEC probe: (a) without ferrite core, (b) with ferrite cores.

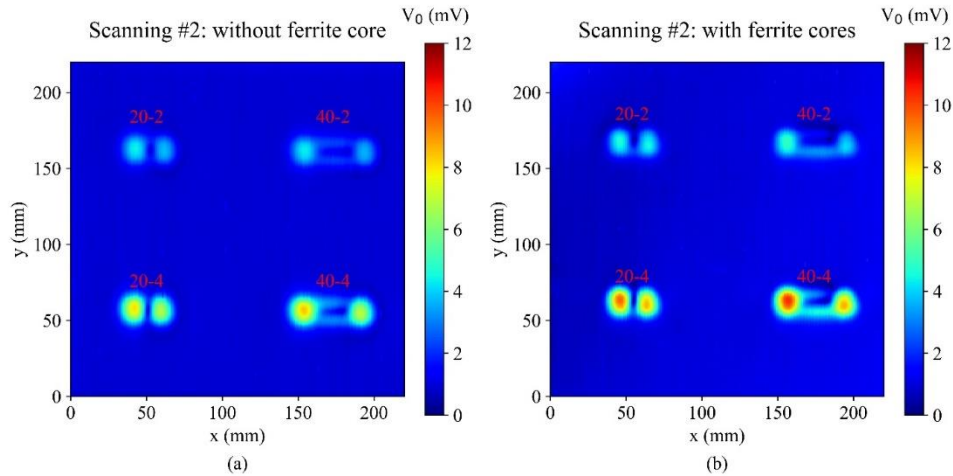


Figure 4.13. Measurement obtained in scanning #2 with RUEC probe: (a) without ferrite core, (b) with ferrite cores.

Furthermore, a notable enhancement in the crack signal amplitude was observed when the RUEC probe was augmented with ferrite cores, as opposed to its performance without such cores. This observation serves to underscore the pivotal role of ferrite cores in amplifying the sensitivity of the RUEC probe, rendering it more adept in the accurate detection of cracks. The investigation along paths #A and #B yielded insightful results indicating that the crack signal amplitude is indeed influenced by both the depth of the crack and the presence of ferrite cores within the coils. These results align with the anticipated effects of varying factors on the RUEC system's performance. Collectively, the comprehensive results garnered from the measurement process stand as a validation of the RUEC probe's efficacy. It effectively demonstrates the probe's proficiency in

discerning cracks across diverse orientations, depths, and lengths - a testament to its robustness and adaptability in the realm of crack detection.

4.2.3.2. Measurement obtains along two paths

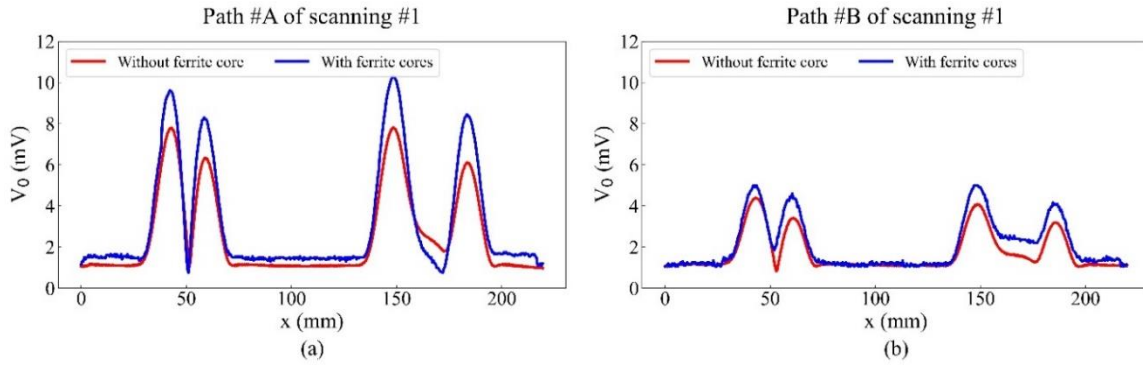


Figure 4.14. Measurement obtained in scanning #1 of two paths with RUEC probe: (a) path #A, (b) path #B.

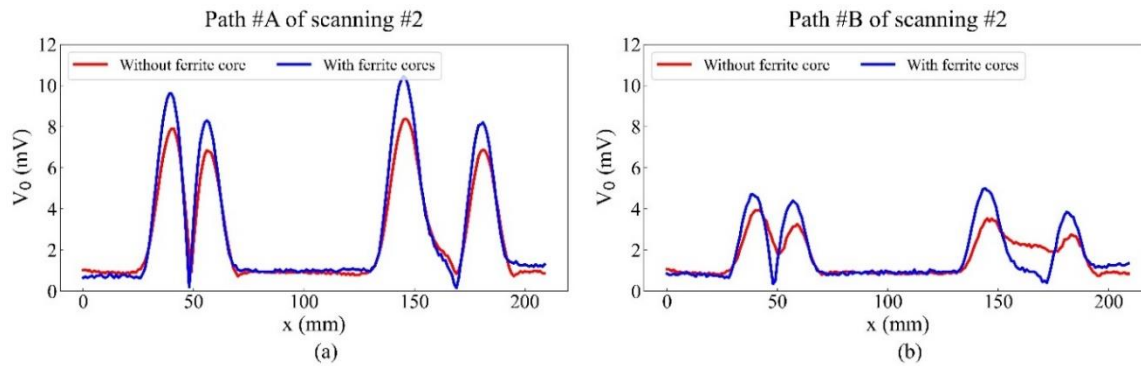


Figure 4.15. Measurement obtained in scanning #2 of two paths with RUEC probe: (a) path #A, (b) path #B.

The measurement results obtained using the RUEC probe along paths #1 and #2 (as illustrated in Figure 4.11) are presented in Figures 4.14 and 4.15, respectively. The incorporation of ferrite cores within each excitation coil emerged as a pivotal factor in significantly augmenting the signal amplitudes, thereby catering to cracks of varying dimensions. Notably, the signal peaks corresponding to a 40 mm crack length (40-4, 40-2) exhibited double the amplitude of those pertaining to a 20 mm crack length (20-4, 20-2). This trend suggests a proportional correlation between the distance separating the two signal peaks and the crack length. Equally illuminating, the crack signal amplitude for a 4 mm depth (40-4, 20-4) mirrored twice that of a 2 mm depth (40-2, 20-2), implying the potential to infer crack depth from the crack signal amplitude.

The outcomes yielded by the RUEC probe with and without the integration of ferrite cores

demonstrated striking parity across both scanning #1 and scanning #2. This convergence underscores the proficiency of the rotating eddy currents engendered on the test specimen's surface, extending its utility for adept crack detection across all orientations. Nevertheless, a noticeable divergence was discerned in the amplitudes of the two peaks comprising the crack signal. This deviation arises from the challenge of ensuring the self-nulling characteristic condition, mandating the attainment of uniform ε_1 and ε_2 values. Notably, in the absence of a crack under the RUEC probe, an approximate 1 mV output signal amplitude was recorded, as evident in Figures 4.14 and 4.15. To heighten the precision of crack detection and refine crack depth estimation, meticulous attention is required to calibrate the RUEC probes, aligning with the prerequisites of self-nulling and self-differential characteristics. This calibration procedure assumes paramount significance in fine-tuning the RUEC probe's performance.

4.3. Enhancing Crack Detection in Low Carbon Steel using a Rotating Uniform Eddy Current Probe and Noise Signal Filtering through Multivariate Singular Spectral Analysis

4.3.1. Exploring the principles of the RUEC probe and the significant advantages of ferrite cores for enhancing crack detection capabilities

4.3.1.1. Exploring the structure of the RUEC probe

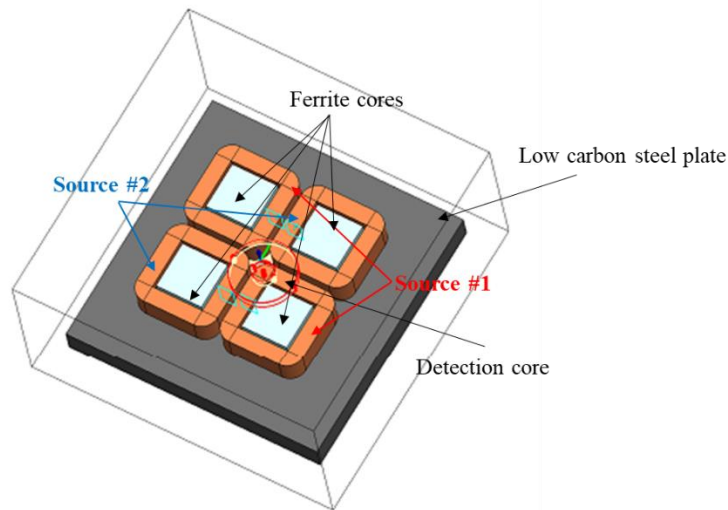


Figure 4.16. The schematic structure of the RUEC probe with ferrite cores

The structure of the RUEC probe, illustrated in Figure 4.16, is composed of four square-

shaped excitation cores, segregated into two orthogonal sources. By employing two out-of-phase alternating currents, the RUEC probe generates RUECs on the surface of a low carbon steel plate, enabling the detection of cracks regardless of their orientations, as referenced in [34].

Each excitation core is meticulously crafted using 1000 turns of 0.2mm diameter copper wire, thereby generating the requisite magnetic field necessary for inducing eddy currents within the test specimen. Furthermore, the RUEC probe is equipped with a circular detection core, strategically positioned at the center and situated beneath the excitation cores. This detection core constructed using 300 turns of 0.2mm diameter copper wire, effectively captures the variations in the eddy currents generated within the test specimen. This functionality enables the detection core to identify existing cracks within the material.

To further optimize the probe's performance, we have integrated ferrite cores within the excitation cores. These ferrite cores play an integral role in amplifying the magnetic field generated by the probe. This augmentation in the magnetic field's strength significantly enhances the probe's sensitivity to cracks, ultimately reinforcing its ability to detect and assess fractures with greater precision and reliability.

4.3.1.2. Simulation results

The examination of the magnetic field was conducted using a time-harmonic 3D solver embedded within the Magnet 7 version 7.9.0.18 software, a creation of Mentor Graphics Corporation. For the simulation of the excitation cores, a current of 10 mA at a frequency of 10 kHz was introduced to both source #1 and source #2. To establish the desired phase difference, the excitation currents for source #2 were set at a 90° disparity in comparison to source #1. The electromagnetic parameters employed for the simulation of the RUEC probe are meticulously outlined in Table 4.5.

Table 4.5 Electromagnetic parameters of the RUEC probe for simulation.

Object	Material	Electrical conductivity, σ (MS/m)	Relative permeability, μ_r
Core wire	Copper	57.7	1.0
Ferrite core	Ferrite	0	1000
Test specimen	Low carbon steel	6.99	200

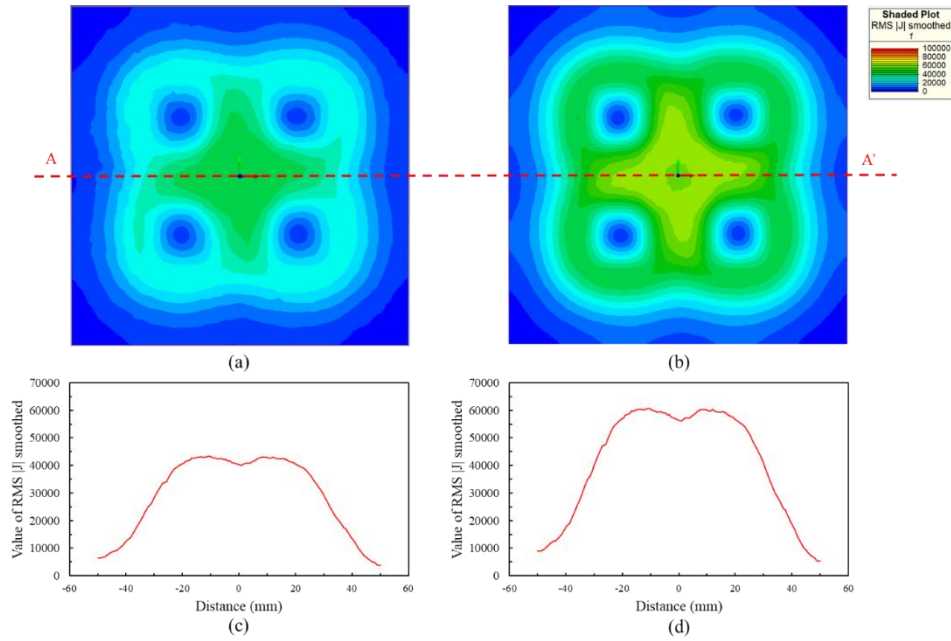


Figure 4.17. The simulation results of UEC distribution on the surface of low carbon steel: (a) RUEC probe without ferrite core and (b) with ferrite cores, (c) The value of RMS $|J|$ smoothed obtained by line A-A' from RUEC probe without ferrite core and (d) with ferrite cores.

Figure 4.17 portrays the outcomes of simulations, presenting the distribution of UEC across the surface of low carbon steel. In Figure 4.17(a), the UEC distribution is visualized when the RUEC probe is employed without a ferrite core. In contrast, Figure 4.17(b) exhibits the UEC distribution on the same surface utilizing the RUEC probe integrated with ferrite cores. A meticulous comparison between Figures 4.17(a) and 4.17(b) distinctly showcases the profound influence of ferrite cores on enhancing the UEC distribution on the low carbon steel surface. This enhancement results in more potent and concentrated eddy currents.

Additionally, Figures 4.17(c) and 4.17(d) depict the Root Mean Square (RMS) $|J|$ values, obtained by smoothing the current density along the line A-A', for the scenarios without ferrite core and with ferrite cores in the RUEC probe, respectively. The contrast between these figures is conspicuous. Figure 4.17(d) presents a substantial enhancement in the RMS $|J|$ value when the RUEC probe is equipped with ferrite cores. This improvement signifies a more robust and evenly distributed current density compared to the situation without ferrite cores, as evident in Figure 4.17(c). These simulation results robustly substantiate the prowess of ferrite cores in augmenting the generation and dispersion of eddy currents across the surface of low carbon steel. Consequently, this advancement translates into an elevated performance in inspections for the purpose of

detecting and evaluating defects.

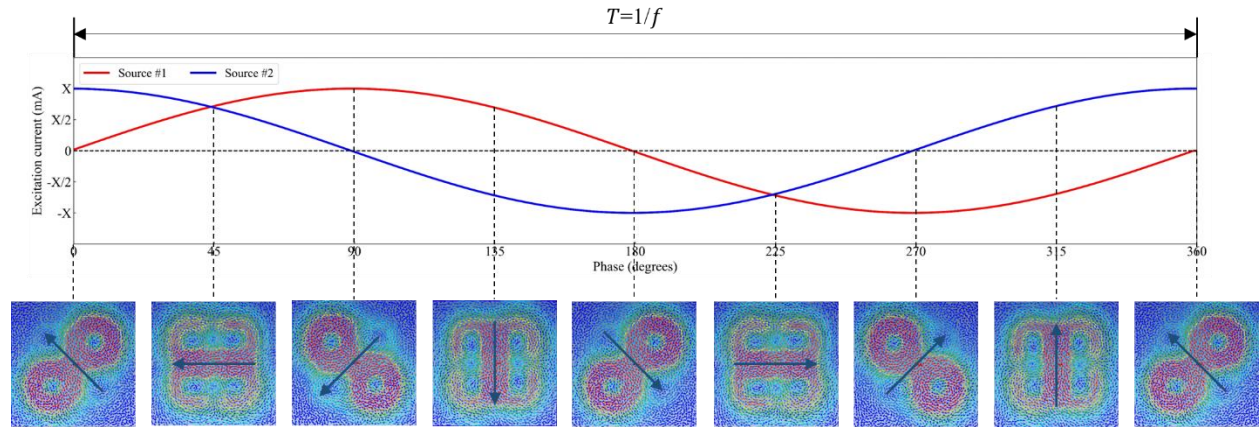


Figure 4.18. The simulation results of magnitude and direction of EC generated on the surface of low carbon steel by two sources of excitation current.

When the RUEC probe is equipped with two sources, each receiving an equal current amplitude but differing by a 90-degree phase, a distinctive eddy current pattern emerges on the surface of the low carbon steel. This pattern closely mirrors the configuration of the excitation cores. The introduction of these two phase-shifted sources plays a pivotal role in shaping the distribution of the eddy currents.

Upon activating a single current source, a corresponding magnetic field is generated around its associated excitation core. This magnetic field interacts with the surface of the low carbon steel, inducing eddy currents within the material. However, with the application of two current sources, both possessing equal amplitudes but existing in a 90-degree phase discrepancy, the result is the generation of two distinct magnetic fields surrounding the pairs of excitation cores. The interaction between these magnetic fields gives rise to a complex composite magnetic field on the surface of the low carbon steel. Consequently, this composite magnetic field engenders a total eddy current magnitude across the low carbon steel's surface. The quantification of this total eddy current magnitude can be accomplished using the provided formula:

$$RUEC = \sqrt{(EC_1)^2 + (EC_2)^2} = \sqrt{[A \cos(\omega t + \varphi)]^2 + [A \cos(\omega t + \{\varphi + \frac{\pi}{2}\})]^2} = |A| \quad (4.2.1)$$

In the provided equation, RUEC represents the eddy current magnitude generated on the surface of the low carbon steel plate. EC_1 and EC_2 correspond to the magnitudes of the excitation currents originating from source #1 and source #2, respectively. The variable ω is defined as $2\pi f$, where f

signifies the exciting frequency, and φ represents the phase difference of the excitation currents. The rotational behavior exhibited by eddy currents stems directly from the interplay between the magnetic fields and the directional attributes of the excitation cores. When these two magnetic fields interact, they amalgamate to form a synthesized magnetic field that subsequently undergoes circular rotation across the surface of the low carbon steel. This rotational phenomenon is clearly illustrated in Figure 4.18. Consequently, the resulting eddy currents adopt a consistent rotational pattern around the central axis of the RUEC probe, retaining an unchanging magnitude designated as $|A|$. The rotational characteristic of eddy currents facilitates the identification of cracks in all possible orientations on the surface of the low carbon steel. By meticulously analyzing and evaluating the alterations within these rotating eddy currents, we gain the capability to not only ascertain the presence of cracks within the low carbon steel but also to precisely determine their locations.

4.3.1.3. Crack signal detection

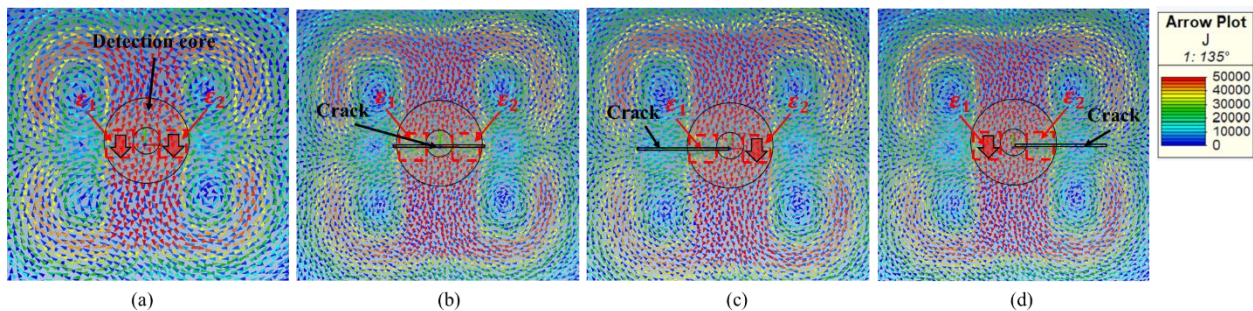


Figure 4.19. The principle of crack signal detection with circular detection core: Balanced condition (a) without crack and (b) with a crack at the center of detection core, Unbalanced condition (c) with a crack at the left side of detection core and (d) with a crack at the right side of detection core.

To begin with, the excitation current supplied to the excitation cores of the RUEC probe initiates the generation of a magnetic field encompassing the wire. This magnetic field interacts with the low carbon steel material, resulting in the emergence of an EC region. These ECs, induced by the magnetic field, subsequently give rise to a secondary magnetic field. Notably, this secondary magnetic field counteracts the initial magnetic field produced by the excitation current. As a result, the regions of the copper wire forming the detection core are aligned parallel to the direction of the ECs generated within the low carbon steel plate.

In this configuration, these detection core regions engage with the secondary magnetic field, thereby producing EMFs ε_1 and ε_2 within the detection core. This phenomenon is vividly illustrated by the red dashed lines in Figure 4.19. These EMFs represent voltage signals brought about by the interaction between the detection core and the secondary magnetic field. The crack signal arises through a process that involves the careful observation and analysis of fluctuations in the EMF values due to the interaction between ECs within the low carbon steel. When a crack is present within the low carbon steel, it disrupts the flow of ECs within the material. This disruption manifests as variations in the EMF values. A particularly noteworthy aspect is the rotational movement of the ECs within the low carbon steel, as depicted in Figure 4.18. As these ECs rotate, the corresponding EMF values exhibit corresponding rotational changes. This pivotal rotational behavior becomes instrumental in facilitating the detection of cracks in a comprehensive range of orientations. Be it a crack oriented horizontally, vertically, or at an angle, the inherent rotational motion of the ECs ensures the detectability of variations in EMF values, irrespective of the specific orientation of the crack.

The signal generated by the detection core can be categorized into two distinct conditions: balanced and unbalanced, as referenced in [34]. The balanced condition corresponds to the absence of cracks within the low carbon steel. In this state, the EMF values within the detection core possess equivalent magnitudes but exhibit opposite directions relative to the core's orientation. This characteristic, referred to as self-discrimination, leads to a mutual cancellation of the EMF values, resulting in an overall output signal of zero, as illustrated in Figure 4.19(a). However, a contrasting situation unfolds when a crack is present at the center of the detection core, as depicted in Figure 4.19(b). In such a scenario, the crack disturbs the regions of ECs that interact with the detection core, leading to a simultaneous reduction of EMF values within the core to zero. This disruption arises due to the alteration of the magnetic field and the perturbation in the flow of ECs due to the presence of the crack. Consequently, the output signal of the detection core also becomes nullified.

On the contrary, the unbalanced condition indicates the existence of cracks within the low carbon steel. In this context, cracks positioned below ε_1 (depicted in Figure 4.19(c)) or ε_2 (shown in Figure 4.19(d)) substantially disrupt the ECs within these respective regions. This disruption results in the loss of ε_1 or ε_2 values, leading to an asymmetry within the detection core. By comparing the extent of this imbalance in EMFs within the detection core, the properties of the

cracks, such as their sizes, can be ascertained.

4.3.2. Signal Processing Methods

4.3.2.1. Wavelet Filter

Wavelet filters are potent signal processing techniques employed to extract signal characteristics and mitigate noise. The wavelet transform engages in a correlation between a mother wavelet ($\psi(t)$) and the input signal ($v(t)$). As the mother wavelet undergoes shifts and scales during this correlation, the wavelet transform produces a multi-resolution signal, enabling a more exhaustive analysis. For our purposes, we denote the scaling factor as 'a' (where $a > 0$) and the shifting factor as 'b'. The computation of the wavelet transform follows Equation (4.2.2), where the * symbol denotes the complex conjugate.

$$W(a, b; v(t), \psi(t)) = \int_{-\infty}^{+\infty} v(t) \frac{1}{a} \psi^* \left(\frac{t-b}{a} \right) dt \quad (4.2.2)$$

The design of wavelet filters involves three primary steps:

Step 1 – Decomposition: The input signal undergoes a decomposition process, resulting in wavelet coefficients that represent the signal across various frequency bands.

Step 2 – Filtering: The wavelet coefficients are subjected to processing to remove unwanted noise. Two widely employed noise removal methods are thresholding (*Denoise*) and principal component analysis (PCA). In the thresholding method, coefficients are compared to a predefined threshold value, with smaller coefficients being set to zero while larger ones remain unchanged. This approach is realized in MATLAB as "*denoise2*". The second method employs PCA to project the coefficients onto an orthogonal space. The projected coefficients are then either thresholded or limited to a few pertinent components, facilitating noise removal. This approach is implemented in MATLAB as "*wmspca*".

Step 3 – Reconstruction: Following the filtration of wavelet coefficients, the original signal is reconstructed through an inverse wavelet transform process. This reconstruction effectively eliminates the noise component, retaining only the desired and relevant signals. Notably, in this study, the input signals encompass multivariate scan eddy current images, rather than univariate signals. This deliberate choice allows for the consideration of correlations among the entirety of crack signals, thereby enhancing the effectiveness of the filtering outcomes.

4.3.2.2. Multivariate Singular Spectral Analysis (MSSA) Filter

The MSSA method, an extension of the SSA method, is tailored for the analysis of multivariate signals. It involves five pivotal steps:

Step 1 - Embedding: In this initial step, each scan line signal from the RUEC probe, denoted as V_l , serves as the foundation for constructing an embedding matrix named H_l . This construction is accomplished by segmenting the signal and subsequently stacking these segments together, as outlined in Equation (4.2.3). Each segment possesses a length of N , and this stacking procedure is iterated M times, where $M = S - N + 1$, with S representing the scan length. It is crucial to select an appropriate segment length N that effectively captures the entirety of the crack signal. Subsequently, the complete embedding matrix H is formed by amalgamating all the embedding matrices, as depicted in Equation (4.2.4).

$$H_l = \begin{bmatrix} V_l(1) & V_l(2) & \dots & V_l(N) \\ V_l(2) & V_l(3) & \dots & V_l(N+1) \\ \vdots & \vdots & \vdots & \vdots \\ V_l(M) & V_l(M+1) & \dots & V_l(L) \end{bmatrix} \quad (4.2.3)$$

$$H = [H_1, H_2, \dots, H_L] \quad (4.2.4)$$

Step 2 - Decomposition: The subsequent phase involves the decomposition of the embedding matrix H into submatrices through the projection of its covariance matrix into an orthogonal space using the singular vector decomposition (SVD) technique. The SVD method is applied to the covariance matrix C of the embedding matrix H to determine its eigenvectors and eigenvalues. The covariance matrix C is calculated using Equation (4.2.5), and the SVD decomposition process is delineated by Equation (4.2.6). In this equation, the columns within U and V are referred to as left and right eigenvectors, while the diagonal elements of matrix S represent the eigenvalues (λ_i , $1 \leq i \leq M$), which are sorted in a descending order. Notably, a higher eigenvalue signifies a greater intensity of the ECT sensor signal. Subsequently, the decomposition of the embedding matrix H is carried out based on the eigenvalues and eigenvectors, as specified in Equation (4.2.7).

$$C = \frac{\mathbf{1}}{N-1} (H - \bar{H})(H - \bar{H})^T \quad (4.2.5)$$

$$C = U \Lambda U^{-1} = U \Lambda V^T \quad (4.2.6)$$

$$\begin{aligned} H &= H_1 + H_2 + \dots + H_M \\ &= U_1 \sqrt{\lambda_1} V_1^T + U_2 \sqrt{\lambda_2} V_2^T + \dots + U_M \sqrt{\lambda_M} V_M^T \end{aligned} \quad (4.2.7)$$

Step 3 - Group selection: In this phase, the focus shifts to the identification of suitable submatrices or groups of submatrices, denoted as H_i ($1 \leq i \leq M$). These submatrices encompass a mix of signals,

including random noise, background noise due to variations in permeability or lift-off, and the crack signal itself. Optimal group selection can be accomplished through techniques such as the weighted correlation matrix or empirical methodologies. This step is crucial for effectively isolating the crack signal from other interfering components within the submatrices.

Step 4 - Reconstruction: Moving on to the reconstruction phase, the submatrix \mathbf{H}_i ($1 \leq i \leq M$) from Equation (4.2.7) serves as the foundation for rebuilding the input signal. This reconstruction is achieved by straightforwardly conducting diagonal averaging of the submatrix elements. Let's introduce $M^* = \min(M, N)$ and $N^* = \max(M, N)$, where \mathbf{H}_i^i represents a submatrix of \mathbf{H}_i corresponding to the signal V_i (i.e. $\mathbf{H}^i = [\mathbf{H}_1^i, \mathbf{H}_2^i, \dots, \mathbf{H}_L^i] = \sqrt{\lambda_i} U_i V_i^T$). Consequently, the reconstructed signal (\tilde{V}_i) corresponding to the submatrix \mathbf{E}^i can be computed using Equation (4.2.8). This step is fundamental in extracting the crack signal from the selected submatrix and contributes to the overall signal enhancement process.

$$\hat{V}_i(p) = \begin{cases} \frac{1}{p} \sum_{i=1}^l \mathbf{H}_p^i(i, p - i + 1) & \text{for } 1 \leq p < M^* \\ \frac{1}{M^*} \sum_{i=1}^{M^*} \mathbf{H}_p^i(i, p - i + 1) & \text{for } M^* \leq p < N^* \\ \frac{1}{S - p + 1} \sum_{i=p-M^*+1}^{M^*} \mathbf{H}_p^i(i, l - i + 1) & \text{for } N^* \leq p \leq S \end{cases} \quad (4.2.8)$$

Step 5 - Thresholding: The reconstructed signal could contain additional noise spreading on the entire scan length due to the large crack signal in the MSSA. Thus, the thresholding is necessary to remove small noise due to this unwanted effect of the MSSA. In this study, we implemented a simple thresholding by reducing the signal smaller than the threshold by a factor while keeping the same the larger signal with only offset removal, as described in Equation (4.2.9).

$$\hat{V} = \begin{cases} q * \hat{V}, & \text{if } \hat{V} < \text{threshold} \\ \hat{V} - \text{threshold}, & \text{otherwise} \end{cases} \quad (4.2.9)$$

4.3.3. Experimental setup

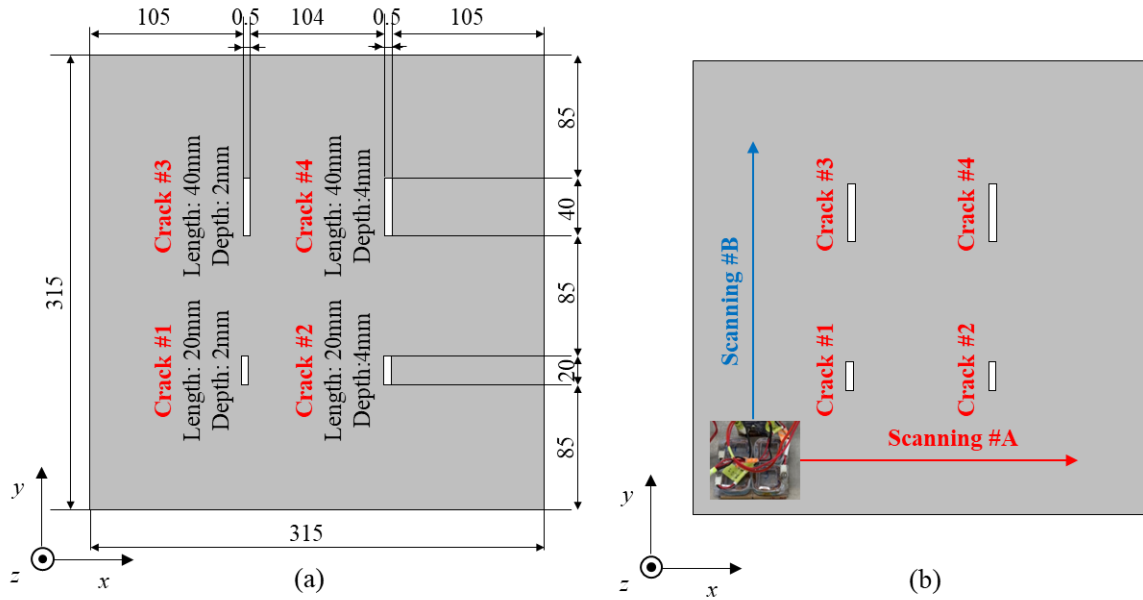


Figure 4.20. Specifications of low carbon steel plate with cracks (Unit in mm)

To conduct the experiment, a dedicated test specimen was crafted using a plate of SS400 low carbon steel. The manufacturing process employed electrical discharge machining, resulting in a plate that was intentionally outfitted with four artificial cracks boasting diverse lengths and depths. These fabricated cracks were deliberately introduced to serve as focal points for the assessment conducted with the RUEC probe, both in configurations featuring ferrite cores and those without. Detailed information regarding the dimensions of these artificial cracks, as well as the specifications of the low carbon steel plate, are provided in Figure 4.20(a). To streamline the scanning procedure, Figure 4.20(b) offers a visual representation of the trajectory followed by the RUEC probe across the surface of the low carbon steel plate.

The experiment was organized around the utilization of two distinct scanning patterns. The first pattern, referred to as Scanning #A, entailed the RUEC probe moving along the x-axis and then incrementally shifting in the y-axis direction. This scanning mode was strategically employed to scan the cracks that ran parallel to their respective lengths. On the other hand, Scanning #B involved the RUEC probe traversing the y-axis before undergoing shifts along the x-axis. By adopting this approach, the experiment aimed to scan the cracks that were positioned perpendicular to their lengths. Through a comprehensive analysis of the acquired crack signals from both scanning patterns, the experiment effectively demonstrated the probe's capability to generate eddy

currents within the low carbon steel plate, facilitating the detection and evaluation of the artificial cracks under various orientations.

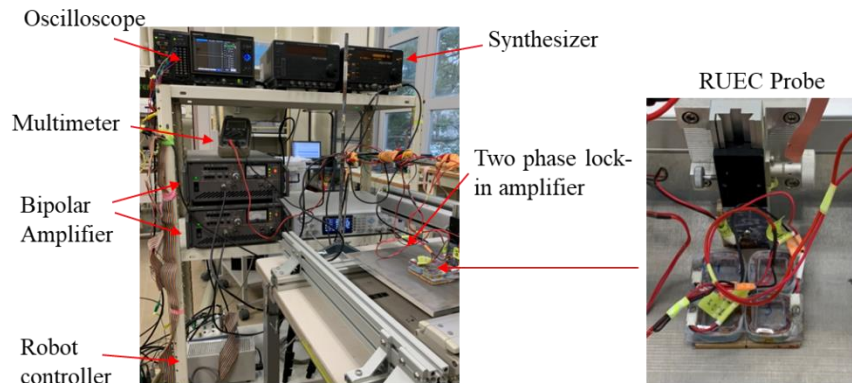


Figure 4.21. The prototype of the RUEC probe systems

Figure 4.21 provides an insight into the experimental setup of the prototype RUEC probe systems. These systems comprise RUEC probes, both equipped with and without ferrite cores, strategically positioned atop a higher-level low carbon steel plate. These probes are subjected to scanning by means of a computer-controlled positioning robot module, ensuring precise movements with a scanning interval of 1 mm in both the x-direction and y-direction. To carry out the experiments effectively, specialized signal processing units were employed. These units consisted of a two-phase lock-in amplifier (NF 5601 B) and a digital oscilloscope (Graphtec GL7000), boasting a data sampling capacity of 4 Hz. Their primary role was to meticulously process and analyze the signals captured by the probes during the experimental procedures. Within each RUEC probe, the excitation cores received an input of excitation current, with a magnitude set at 10 mA and a frequency of 10 kHz. This current was generated through the collaborative effort of a high-speed bipolar amplifier (NF HAS 4012, NF Co., Yokohama, Japan) and a function generator (WAVE FACTORY WF1946B, NF Co., Yokohama, Japan). These components were pivotal in delivering the requisite current to stimulate the excitation cores, thereby facilitating the generation of the RUECs vital for the experiment's success.

4.3.4. Experimental results and discussions

Figure 4.22 provides a comprehensive visual representation of the measurement outcomes derived from four distinct experimental scenarios: Scanning #A and Scanning #B conducted without the integration of ferrite cores, as well as Scanning #A and Scanning #B executed with the

presence of ferrite cores within each excitation core. These carefully designed scenarios aimed to meticulously explore the influence of ferrite cores on the efficacy of crack detection and characterization utilizing the RUEC probe.

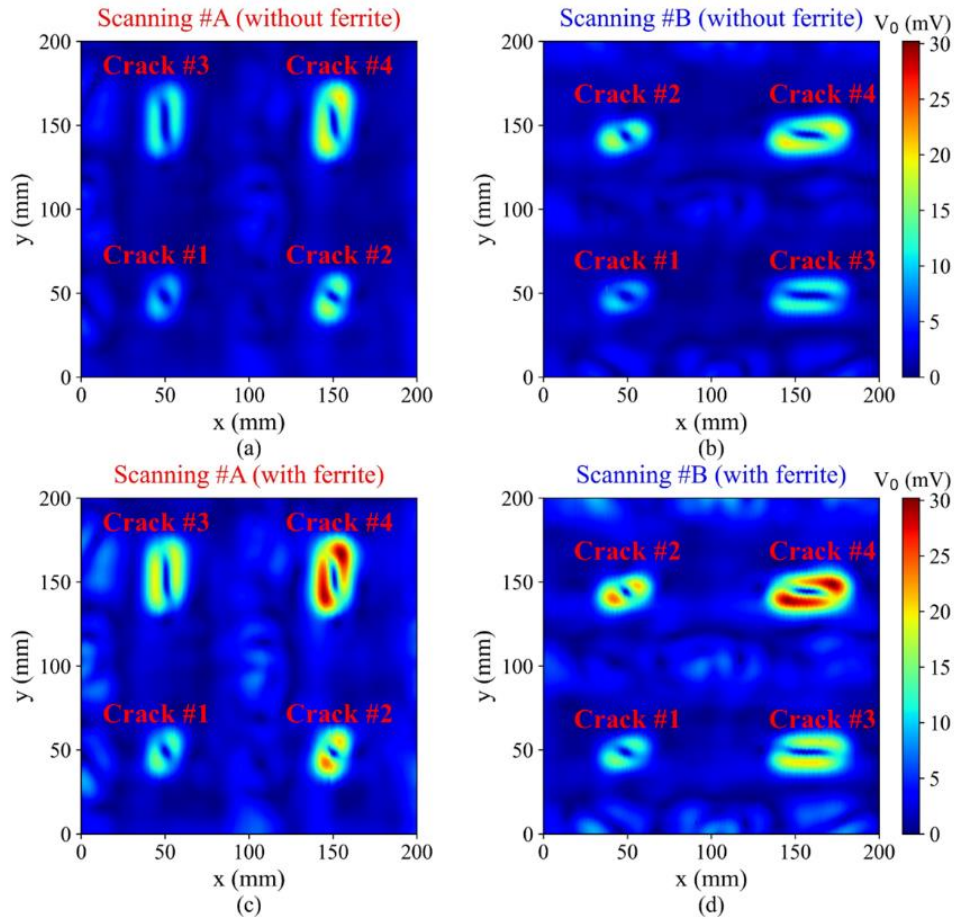


Figure 4.22. The measurement results of two scanning with RUEC probe: (a) Scanning #A without ferrite core, (b) Scanning #B without ferrite core, (c) Scanning #A with ferrite cores, (d) Scanning #B with ferrite cores

The obtained results deliver a clear and compelling illustration of the substantial enhancement in the quality of crack signals achieved through the incorporation of ferrite cores. Notably, Figures 4.22(c) and 4.22(d) correspond to Scanning #A and Scanning #B performed with the aid of ferrite cores, respectively. These figures distinctly showcase crack signals that exhibit heightened clarity and distinction, particularly when compared to the corresponding scans conducted in the absence of ferrite cores (depicted in Figures 4.22(a) and 4.22(b)). The strategic integration of ferrite cores plays a pivotal role in amplifying the magnetic fields generated by the RUEC probe. This augmentation directly contributes to the intensified generation of ECs within

the low carbon steel specimen. The consequence is a more robust signal response originating from the cracks, indicating an enhanced ability to detect and characterize them. Consequently, the utilization of ferrite cores stands out as a significant advancement that substantially elevates the overall performance and effectiveness of the RUEC probe in the realm of crack detection applications.

Moreover, the amplitudes of the crack signals remain consistent in both scenarios, irrespective of the presence or absence of ferrite cores. This uniformity underscores the rotational capability of the generated ECs within the low carbon steel specimen. In Figures 4.22(a) and 4.22(b), which depict cases without ferrite cores, the crack signals exhibit comparable magnitudes, emphasizing the inherent rotational behavior of the ECs. This rotational pattern of the ECs also persists in Figures 4.22(c) and 4.22(d), validating that the rotational nature of the ECs is upheld even with the integration of ferrite cores. However, it's important to address the significant issue of noise interference. When employing the RUEC probe on low carbon steel, a notable level of noise signals becomes evident. These noise signals arise in regions where the S/N ratio is unfavorably affected, potentially hindering accurate crack detection. Therefore, the implementation of supplementary signal processing techniques and meticulous analysis methods becomes imperative to effectively counteract and diminish the impact of noise interference. By doing so, these methods serve to ensure dependable crack detection and precise characterization, thereby elevating the overall reliability of the inspection process.

The experimental results show that the existence of residual stresses during the crack manufacturing process in low carbon steel exerts a significant influence on the detection of crack signals. This influence becomes particularly evident concerning the maximum amplitudes and orientations of the detected crack signals. These residual stresses introduce fluctuations in the amplitude of the crack signals, potentially leading to inaccuracies in evaluating the extent and dimensions of the cracks. These deviations from the anticipated amplitudes have the potential to undermine the dependability of crack detection and characterization. Furthermore, these residual stresses can also impact the orientation of the cracks, resulting in deviations from their intended directions. Consequently, the identified orientations of the cracks might not align precisely with their actual orientations, a phenomenon illustrated in Figure 4.22. This deviation can introduce uncertainties in crack orientation determination, affecting the overall accuracy of crack assessment.

4.3.5. MSSA results and discussions

The ECT signal used for scanning in this research has dimensions of 200×200 mm, and a segment length of 10 mm was deliberately chosen. This small segment length was selected to prevent overlap between adjacent cracks during the stacking process, ensuring the fidelity of the signal. In Figure 4.23, the distribution of eigenvalues acquired from the correlation matrix C for four distinct scanning outcomes is depicted. Upon careful examination, it becomes apparent that the eigenvalues exhibit consistent patterns for both scanning directions, labeled as A and B, irrespective of the presence or absence of a ferrite core within the RUEC probe.

Furthermore, a noticeable trend emerges in the eigenvalues when comparing the RUEC probe configurations with and without a ferrite core. Specifically, the eigenvalues associated with the RUEC probe equipped with a ferrite core consistently surpass those of the RUEC probe lacking a ferrite core. This divergence in eigenvalues strongly implies that the RUEC probe incorporating a ferrite core offers heightened sensitivity in the detection of cracks. The amplified eigenvalues indicate an elevated responsiveness to crack signals, underscoring the enhanced crack detection capabilities stemming from the integration of the ferrite core.

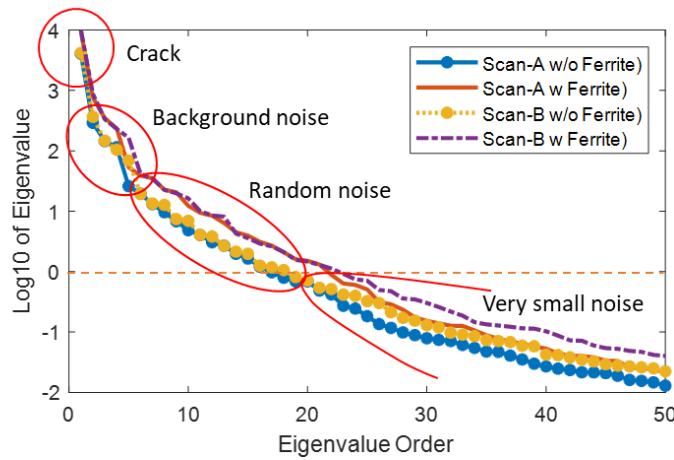


Figure 4.23. Eigenvalues distribution of the ECT scan results

The eigenvalues derived from the preceding analysis can be classified into three distinct categories, each characterizing different signal components: crack signals, background noise signals, and random noise signals. This classification offers a more comprehensive insight into the composition of the signal. Figure 4.24 visually presents the reconstructed signals associated with these three categories.

The signals categorized under group $k = 21-100$ (or potentially higher orders) represent

random noise signals. Signals belonging to group $k = 7-20$ correspond to minor variations in permeability. Those within group $k = 2-6$ denote significant alterations in permeability and variations in surface lift-off. Lastly, group $k = 1$ specifically comprises the crack signals. Reconstructing the signals from these discrete groups enables the analysis and interpretation of the distinct constituents within the scanned ECT signal.

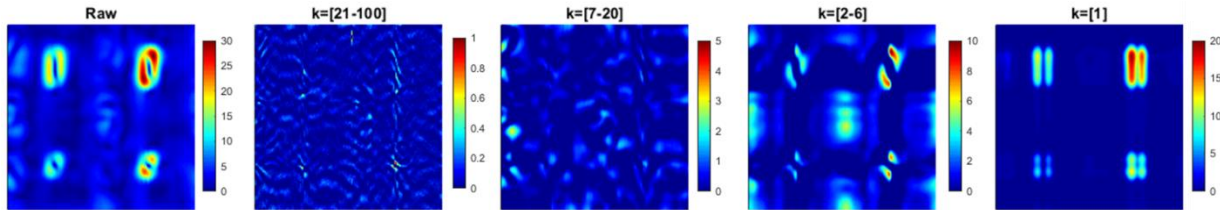


Figure 4.24. ECT scan signal reconstructed by MSSA method with different groups of submatrices.

Figure 4.25 presents a comprehensive comparison among the proposed MSSA filter, the wavelet-PCA filter, and the Denoise filter in processing the ECT-scanned signal acquired using the RUEC probe. The ECT signal is susceptible to significant noise interference due to the inherent structural and compositional heterogeneity in the low carbon steel material. Uneven permeability variations further contribute to intense fluctuations in signal intensity. Upon a thorough analysis of the filter results, it becomes apparent that the wavelet-PCA filter outperforms the Denoise filter. However, the efficacy of both filters in reducing noise in the signal's background regions and central areas is limited. In contrast, the MSSA filter demonstrates superior outcomes. It notably enhances the clarity of crack signals in comparison to the wavelet-PCA and Denoise filters. This effectiveness stems from the MSSA filter's adeptness in handling pronounced noise variations within the background and central sections of the signal. Consequently, it enhances both the identification and characterization of crack signals. The outcomes of this comparative analysis underscore the superior performance of the MSSA filter, particularly in its capability to mitigate substantial noise variations, especially in the background and central areas of the signal. This enhanced noise reduction contributes to improved precision in detecting and characterizing crack signals.

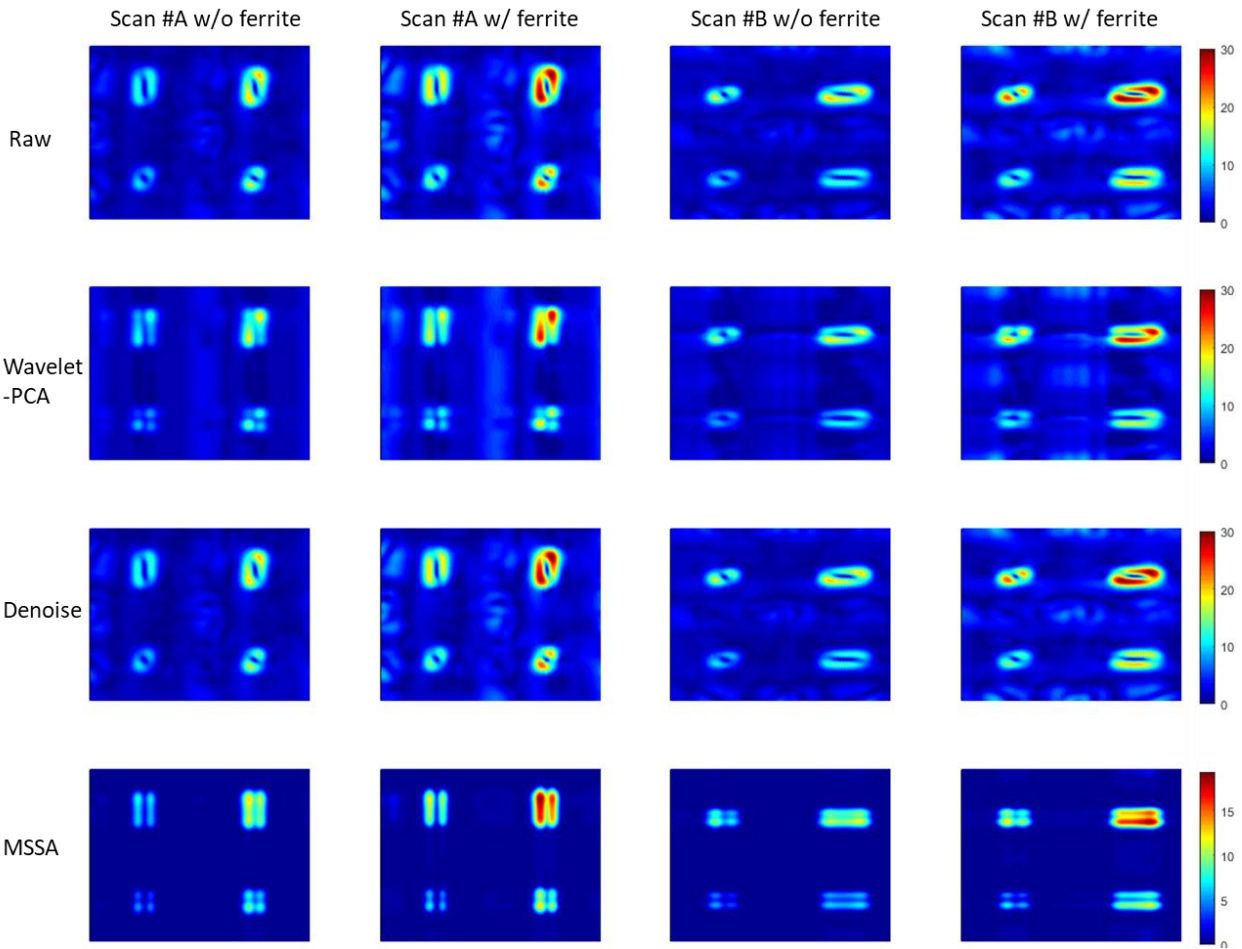


Figure 4.25. ECT scan signal filtered by wavelet-PCA, Denoise, and MSSA methods.

Moreover, the MSSA filter demonstrates its remarkable capability to handle peak signals associated with cracks, maintaining their accurate orientation even in the presence of variations introduced by the RUEC probe during the crack fabrication process in low carbon steel. Residual stresses during fabrication can lead to deviations in crack orientation, causing changes in the peak patterns of crack signals. However, the MSSA filter is tailored to address this challenge by precisely identifying and processing peak signals aligned with the actual crack direction. The MSSA filter's design is strategically aimed at tackling this issue. It effectively detects and enhances peak signals while maintaining their authentic orientation through the analysis of multivariate scan eddy current images. This strength proves pivotal in crack detection applications, ensuring that the extracted signals faithfully represent the existence and characteristics of cracks. By capturing the accurate crack direction and meticulously analyzing their peak patterns, the MSSA filter significantly elevates the accuracy and effectiveness of crack detection techniques in low carbon

steel.

4.4. Enhanced Film Eddy Current Probe with Interleaved Detection Coil and Amplification by Ferromagnetic Amorphous Alloy Particles

4.4.1. Methods and film EC probe design

4.4.1.1. Design of film EC probe and FAAP

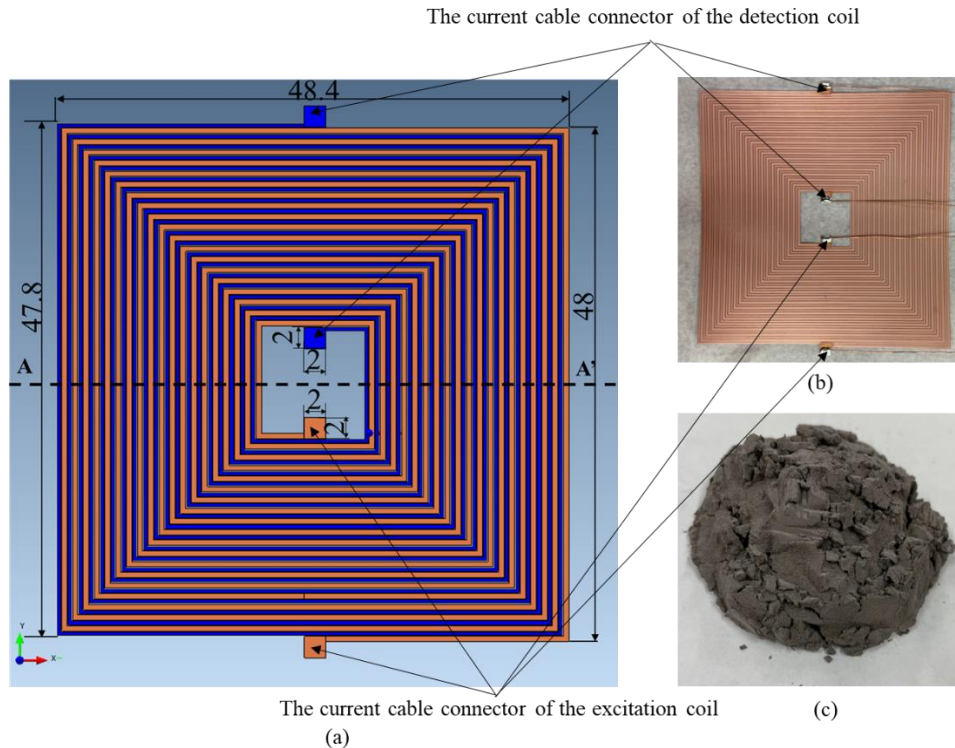


Figure 4.26 Structure of film EC probe (units are in mm). (a) structure of film EC probe, (b) actual film EC probe, and (c) FAAP.

Figure 4.26 depicts the structural configuration of the film EC probe. This innovative probe design involves a square-shaped detection coil interlaced with the excitation coil, each comprising 20 turns. The separation between adjacent coils is maintained at 0.1 mm, as illustrated in Figure 4.26. The wires utilized in the probe exhibit dimensions of 0.3 mm in width and 0.5 mm in thickness for the excitation coil (depicted by the blue coil in Figure 4.26(a)), and 0.5 mm in width and 0.5 mm in thickness for the detection coil (represented by the brown coil in Figure 4.26(a)). The actual film EC probe utilized in the experimental phase is displayed in Figure 4.26(b).

To enhance the magnetic flux density and induce more effective eddy currents on the test piece's surface, an iron-based ferromagnetic amorphous alloy particle (FAAP) was introduced onto

the film EC probe. This FAAP, illustrated in Figure 4.26(c) following an electrical insulation treatment, was chosen for its inherent attributes of high permeability. Additionally, the presence of FAAP contributes to an augmented interlinkage of magnetic flux with the detection coil. The particle size distribution of FAAP ranged from 5 to 100 μm , with the median diameter (D50) measuring 29.5 μm . Furthermore, the particle diameters corresponding to the 10th and 90th percentiles of the distribution, designated as D10 and D90, were recorded as 10.5 μm and 62.7 μm , respectively.

4.4.1.2. Model-based performance study

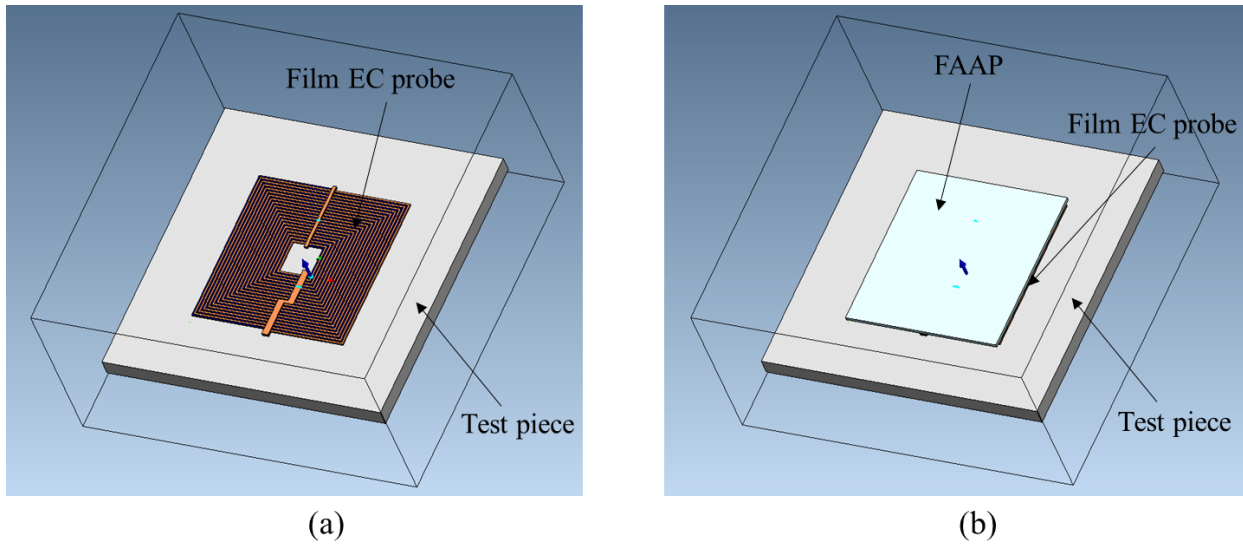


Figure 4.27 (a) Film EC probe models without FAAP and (b) with FAAP.

To conduct a comparative assessment of the induced EC amplitudes on the test piece's surface, two distinct models of the film EC probe were evaluated: one without the presence of the FAAP [depicted in Figure 4.27(a)], and the other incorporating FAAP [illustrated in Figure 4.27(b)]. This evaluation was carried out through a time-harmonic analysis utilizing finite element analysis software (Magnet 7 version 7.9.0.18, Mentor Graphics Corporation). The analysis employed an aluminum plate with dimensions of 90 mm in length, 90 mm in width, and 10 mm in thickness as the test piece. The electromagnetic properties of both the aluminum plate and the coils utilized in the models are detailed in Table 4.6. Furthermore, an excitation coil characterized by specific excitation currents and frequencies (300 kHz, 500 kHz, and 1 MHz) was employed for the analysis.

Table 4.6 Electromagnetic parameters used in analysis for Film EC probe.

Material	Electrical	Relative
----------	------------	----------

		conductivity, σ (MS/m)	permeability, μ_r
Wires of excitation coil and detection coil	Copper	57.7	1.0
Test piece	Aluminum	38.0	
FAAP	Fe-Si-B	0	100

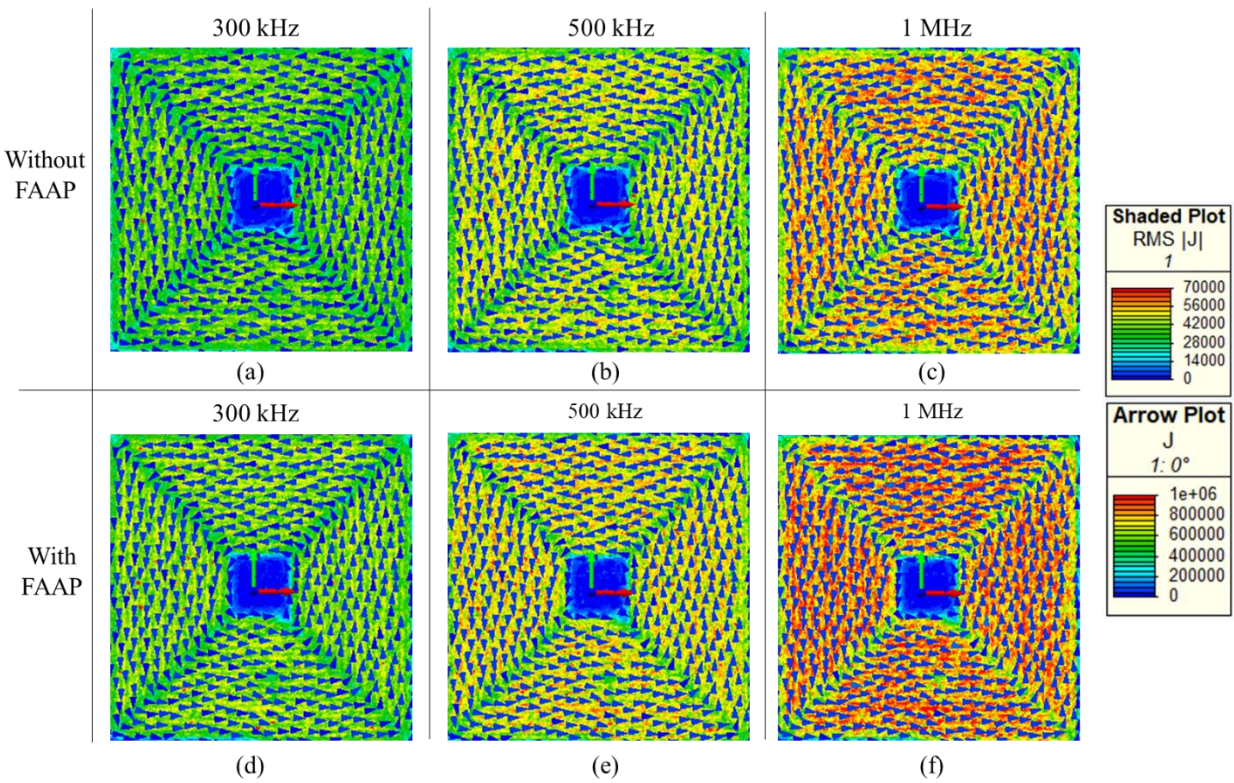


Figure 4.28 Contour plot of the EC distribution on the surface of the test piece with different excitation frequencies. (a) 300 kHz of frequency without FAAP, (b) 500 kHz of frequency without FAAP, (c) 1 MHz of frequency without FAAP, (d) 300 kHz of frequency with FAAP, (e) 500 kHz of frequency with FAAP, and (f) 1 MHz of frequency with FAAP.

Figure 4.28 depicts the outcomes of the finite element analysis showcasing contour plots of the EC distribution across the test piece's surface for various excitation frequencies: 300 kHz, 500 kHz, and 1 MHz. Specifically, Figures 4.28(a), 4.28(b), and 4.28(c) present the results obtained

without the presence of the FAAP, while Figures 4.28(d), 4.28(e), and 4.28(f) correspondingly illustrate the results achieved when FAAP is incorporated. These findings reveal that the film EC probe equipped with FAAP generates higher induced eddy currents on the surface of the aluminum plates as compared to the probe without FAAP.

Furthermore, considering the impact of the excitation frequencies, it's important to note that the utilization of high-frequency excitation currents results in the skin effect, which causes an increase in flux density on the test piece's surface. This effect becomes more prominent with higher excitation frequencies, further influencing the distribution of eddy currents and ultimately contributing to the observed differences between the results at different frequencies.

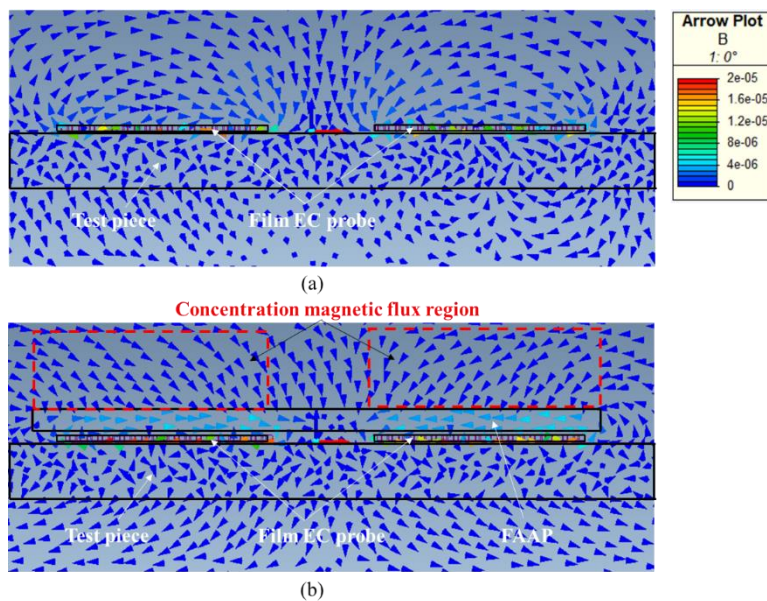


Figure 4.29 Shaded plot of magnetic flux distribution along the section A-A' (See Fig. 1(a)). (a) without FAAP, and (b) with FAAP

The elevation of induced EC on the surface of an aluminum plate, facilitated by the presence of FAAP, finds its elucidation in the magnetic flux distribution, as illustrated in Figure 4.29. When FAAP is absent, the magnetic flux passing through the film EC probe is limited, resulting in the generation of a relatively minor electromotive force (EMF) on the detection coil, as portrayed in Figure 4.29(a). Conversely, the inclusion of FAAP induces substantial magnetic fluxes within the film EC probe, consequently triggering a more pronounced EMF response on the detection coil, as demonstrated in Figure 4.29(b).

4.4.2. Experimental implementation

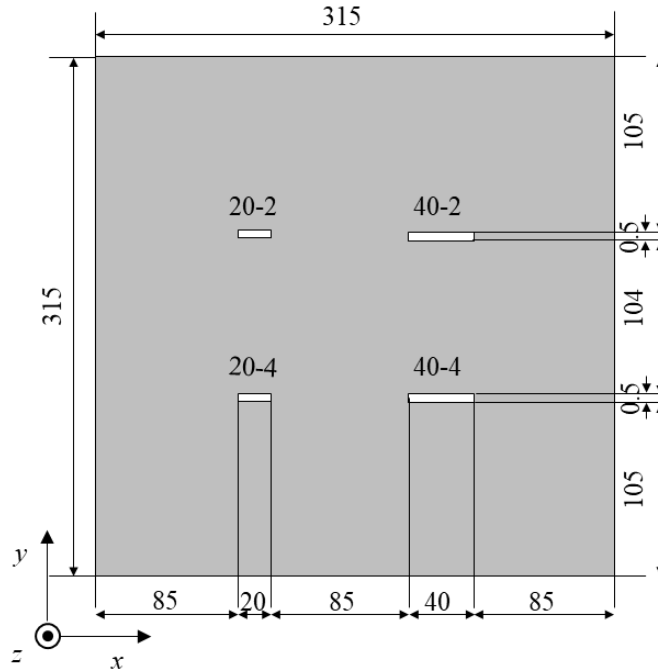


Figure 4.30 Four artificial cracks on the aluminum plate used for Film EC probe.

During the experimental investigation, a carefully selected aluminum plate was utilized as the primary test specimen. The distinct characteristics of this aluminum plate, such as its dimensions and composition, are meticulously depicted in the visual representation provided in Figure 4.30. To simulate real-world scenarios and assess the efficiency of the newly proposed film EC probe, the aluminum plate was intentionally subjected to the creation of artificial cracks. These cracks were fabricated using the electrical discharge machining method, ensuring consistency and precision in their dimensions and placements.

Table 4.7 Sizes of the four artificial cracks on the aluminum plate.

Test piece	Symbol of crack	Width (mm)	Length (mm)	Depth (mm)
Aluminum	20-2	0.5	20	2
	20-4			4
	40-2		40	2
	40-4			4

For the sake of comprehensive analysis, four artificial cracks were strategically positioned

within the aluminum plate. These artificial cracks exhibited a diverse range of lengths and depths, enabling a thorough examination of the film EC probe's capabilities in detecting defects of varying severity. The specific measurements outlining the lengths and depths of these artificial cracks are methodically tabulated in Table 4.7, offering a clear reference for the scope and extent of the experiment.

Table 4.8 Specifications of the Film EC probe's excitation and detection coils.

Excitation coil	Turns	20
	Wire diameter (mm)	0.3×0.5
	Inductance (mH)	0.01
	Resistance (Ω)	10.7
	Impedance (Ω)	10.7
Detection coil	Turns	20
	Wire diameter (mm)	0.5×0.5
	Inductance (mH)	0.01
	Resistance (Ω)	6.3
	Impedance (Ω)	6.3

To facilitate the detection process, the film EC probe incorporated distinct excitation and detection coils. These coils were engineered to fulfill the requirements of the experimental setup, with their precise specifications detailed in Table 4.8. These specifications, including coil dimensions, winding configurations, and other pertinent attributes, play a pivotal role in influencing the probe's performance during the experiment.

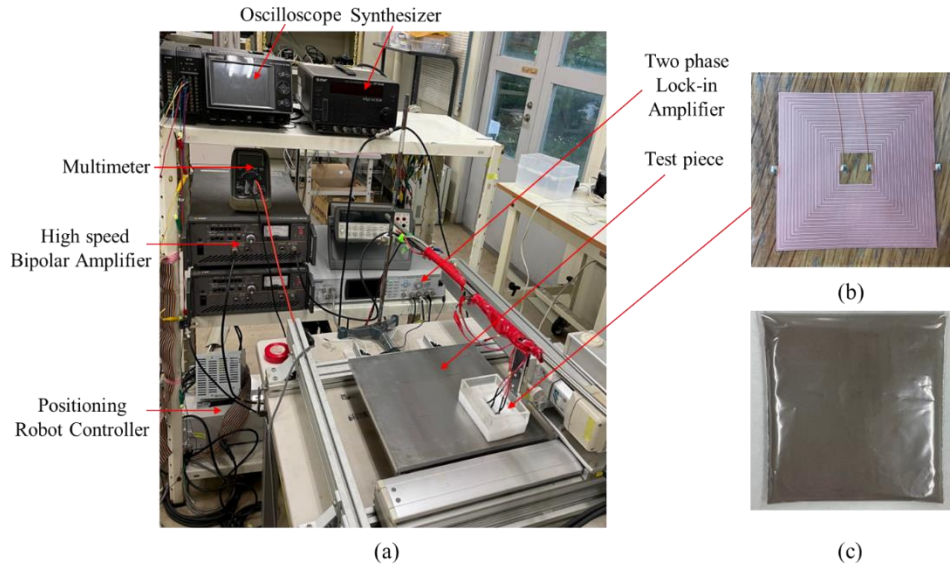


Figure 4.31. Experimental setup with the film EC probe. (a) experimental setup, (b) film EC probe, and (c) FAAP in a plastic bag.

Figure 4.31(a) presents the configuration of the experimental setup, illustrating how the various components were strategically arranged for effective execution. The focal point of this arrangement was the EC probe film, which played a central role in the experimental proceedings, as depicted in Figure 4.31(b). To generate the necessary excitation currents and frequencies, a signal generator (WAVE FACTORY WF1946B, NF Co., Yokohama, Japan) and a high-speed bipolar amplifier (NF HAS 4012, NF Co., Yokohama, Japan) were employed. These instruments ensured the consistent generation of an excitation current of 10 mA, accompanied by excitation frequencies spanning 300 kHz, 500 kHz, and 1 MHz.

The signal emanating from the detection coil underwent meticulous processing to extract meaningful data. This processing entailed the utilization of a two-phase lock-in amplifier (LI 5660, NF Co., Japan), after which the resultant data was securely stored in a digital oscilloscope (DATA PLATFORM GL7000, GRAPHTEC Co., Japan).

The dynamic movement of the EC probe over the scanning surface of the aluminum test piece was orchestrated by a computer-controlled positioning robot module. This module ensured precision in the scanning process, with a consistent speed of 10 mm/s maintained throughout. To capture comprehensive scan data, intervals of 1 mm were adhered to in both the x- and y-directions, allowing for detailed surface coverage.

To amplify the magnetic flux density and enhance the performance of the film EC probe,

a FAAP was incorporated into the setup. The FAAP, contained within a plastic bag measuring 60 mm in length and 60 mm in width (as shown in Fig. 8.6(c)), weighed approximately 50 g. This plastic bag, including the FAAP, possessed a total thickness of around 5 mm. Notably, the FAAP-laden plastic bag was directly affixed to the film EC probe using adhesive tape, ensuring proximity and effective interaction between the components.

4.4.3. Experimental results and discussion

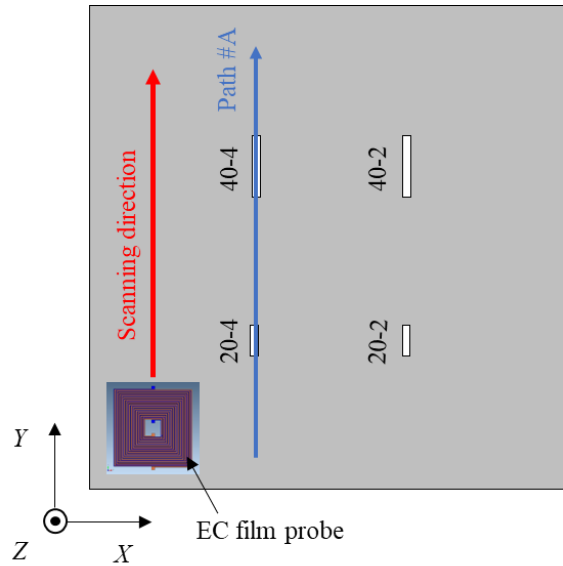


Figure 4.32. Scanning direction and a path on the test piece with Film EC probe.

Figure 4.32 provides a visual representation of the scanning strategy employed with the EC probe film across the test piece. In this arrangement, the EC probe film was directed to move along the y-axis, followed by incremental shifts along the x-axis direction. This meticulous scanning pattern was instrumental in capturing comprehensive data for analysis. The primary focus of the subsequent analysis was the assessment of crack detection signal amplitudes, specifically in relation to the film EC probe with and without the presence of the FAAP. To facilitate this assessment, a systematic approach was adopted. The measurement outcomes from the film EC probe were meticulously gathered by performing scans along a designated path, referred to as path #A. This path was deliberately chosen to traverse two distinct crack areas, namely 40-4 and 20-4, each marked by unique characteristics that held significance for the study. In essence, Figure 4.32 effectively visualizes the scan direction of the EC probe film, setting the stage for the subsequent analysis of crack detection signal amplitudes under varying conditions. The selected scanning path

ensured the collection of relevant data from specific crack areas, thus contributing to the comprehensive evaluation of the film EC probe's performance.

4.4.3.1. Experimental results with film EC probe

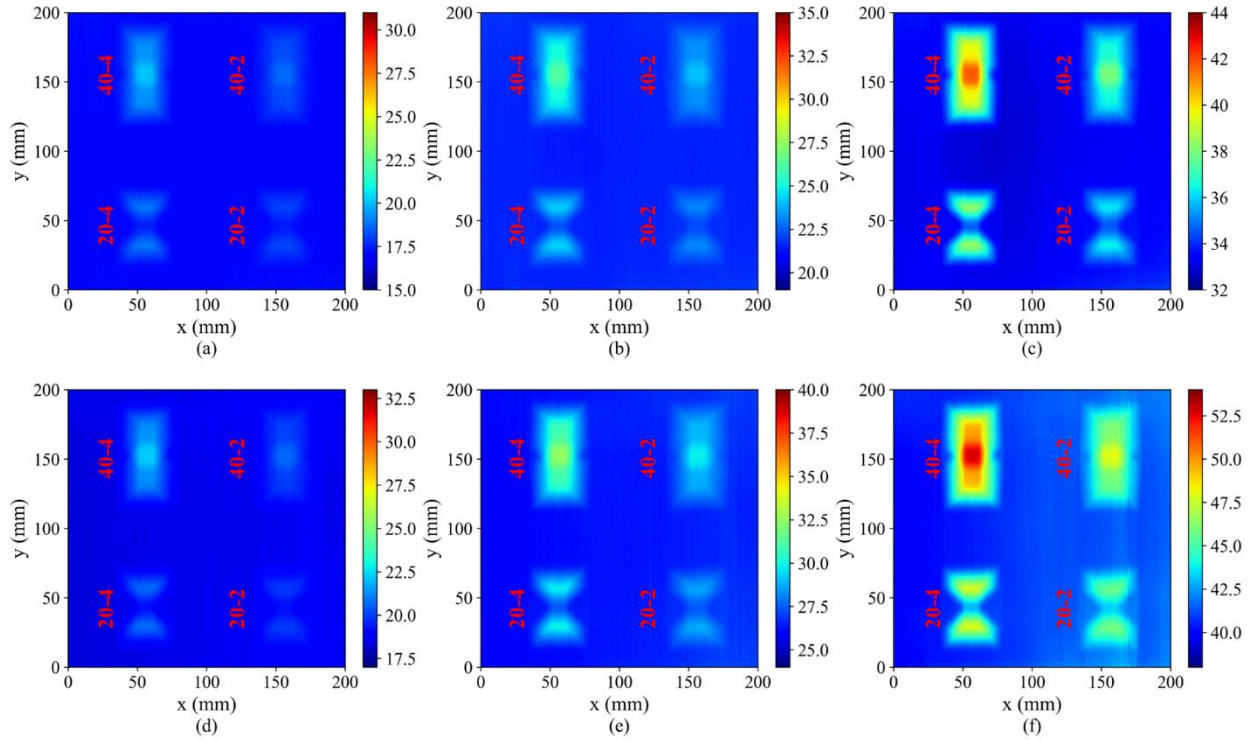


Figure 4.33. Measurement results of film EC probe. (a) 300 kHz of frequency without FAAP, (b) 500 kHz of frequency without FAAP, (c) 1 MHz of frequency without FAAP, (d) 300 kHz of frequency with FAAP, (e) 500 kHz of frequency with FAAP, and (f) 1 MHz of frequency with FAAP.

The measurement outcomes of the film EC probe under different excitation frequencies – 300 kHz, 500 kHz, and 1 MHz – both without and with the inclusion of FAAP, are vividly depicted in Figures 4.33(a), 4.33(b), 4.33(c), 4.33(d), 4.33(e), and 4.33(f), respectively. These figures effectively capture the detected response signals for each respective condition.

The analysis of these measurement results underscores the probe's effectiveness in detecting cracks, as indicated by the discernible presence of peak amplitudes for each crack. The capability of the film EC probe to successfully identify these cracks is evident. Nevertheless, an interesting observation emerges when comparing the peak amplitudes between cracks of differing lengths, specifically 40 mm and 20 mm. These differences are notable and offer valuable insights into the probe's ability to discern variations in crack sizes. Additionally, the introduction of FAAP

has a significant impact on the measurement results. This influence becomes apparent when assessing the amplitude of the crack peaks. The results unambiguously demonstrate a substantial increase in the crack peak amplitude signal due to the presence of FAAP. This outcome substantiates the efficacy of integrating FAAP into the film EC probe, contributing to the heightened sensitivity of crack detection.

In the film EC probe's configuration, the EMF of the detection coil (ε_t) is determined by subtracting the EMF generated by the eddy current's magnetic flux on the test piece's surface (ε_{EC}) from the EMF produced by the magnetic flux of the excitation current. It's crucial to note that these two eddy currents flow in opposing directions. When the film EC probe was positioned over a crack on the test piece, the presence of the crack led to a disruption in the eddy current flow on the test piece's surface. As a result, the magnetic flux generated by the eddy current on the test piece became diminished. Consequently, the value of ε_t increased, primarily due to the reduced impact of ε_{EC} , which was now diminished due to the disrupted eddy current caused by the crack. This behavior indicates that the presence of the crack resulted in a noticeable change in the electromotive force observed in the detection coil.

4.4.3.2. Measurement results of path #A

To examine the crack detection signal amplitude of the film EC probe in the presence of FAAP, we conducted measurements while the probe moved along path #A, covering two crack areas (40-4, 20-4), as depicted in Figure 4.32. For analysis, each signal was compared to the signal obtained from the region without any cracks. Generally, the signal amplitudes related to crack detection exhibited an increase due to the presence of FAAP. However, the increase in crack signal amplitude wasn't notably pronounced at 300 kHz (Figure 4.34(a)), while it displayed a significant increase as the excitation frequency advanced from 500 kHz to 1 MHz (Figures 4.34(b) and 4.34(c)).

The reason behind this phenomenon lies in the case where the excitation frequency was 1 MHz. In this scenario, the EC on the test piece's surface was the most substantial under our experimental conditions. Additionally, the EC was concentrated due to the presence of the cracks. Consequently, the magnetic flux stemming from this more concentrated EC around the cracks flowed towards the film EC probe. This effect was amplified by the low magnetic resistance in the magnetic circuit through the film EC probe, which was made possible by the FAAP. As a result, the signal amplitude for cracks detected by the film EC probe was notably enhanced. This indicates

that the FAAP had a significant impact on increasing the amplitude of crack signals detected by the film EC probe, particularly when operating at higher excitation frequencies.

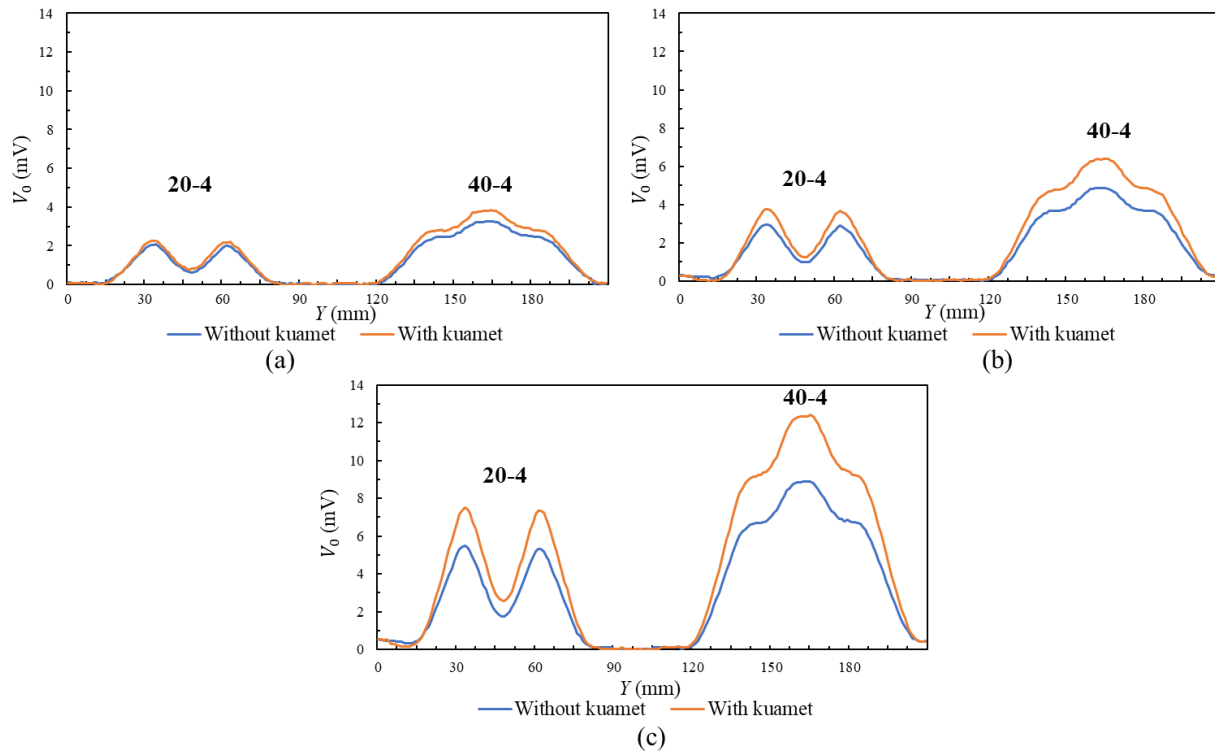


Figure 4.34 Measurement results of film EC probe along Path #A: (a) 300 kHz of frequency, (b) 500 kHz of frequency, and (c) 1 MHz of frequency.

The measurement outcomes reveal a notable distinction in the crack detection signals. Specifically, for the crack (20-4), two distinct peak signals were observed, whereas a single peak signal was evident for the crack (40-4). This observation underscores the notion that the configuration and shape of the detection signal are intrinsically influenced by the length of the crack.

Figure 4.35 illustrates the fundamental principle behind the crack signal detected by the film EC probe. In cases where the crack causes a disruption in the eddy current flow within the test piece (as depicted in Figure 4.35(a)), the total EMF (ε_t) registers a significant increase due to the corresponding reduction in ε_{EC} . On the other hand, when the crack is positioned beneath the central area of the film EC probe (as illustrated in Figure 4.35(b)), ε_t remains comparatively small. This is because the disruption of the eddy current in this scenario is minimal, resulting in minimal changes to ε_{EC} , as elucidated in Figure 4.34. Contrarily, for a crack with a length of 40 mm

positioned beneath the center of the film EC probe (as shown in Figure 4.35(c)), the disruption of the eddy current within the test piece becomes the most pronounced. Consequently, this leads to the emergence of a peak amplitude in the crack detection signal and the corresponding ε_{EC} reaches its lowest value. Hence, the observed occurrence of two amplitude peaks in the crack signal corresponds to cracks measuring 20 mm in length, while a single peak corresponds to cracks measuring 40 mm in length.

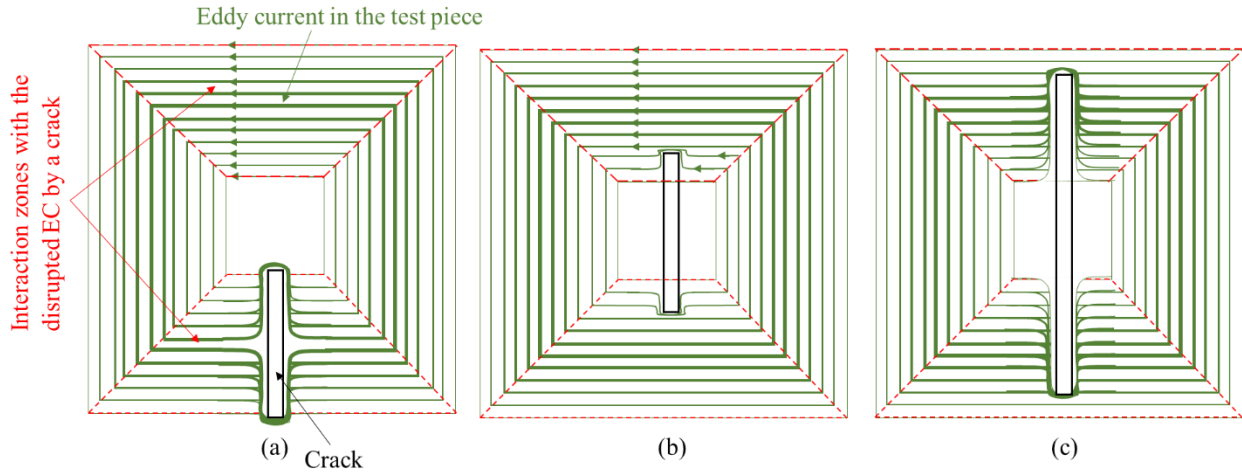


Figure 4.35 Principle of crack detection signal of the film EC probe: (a) the crack with 20 mm length under the center of the interaction zone; (b) crack with 20 mm length under the center of the film EC probe; and (c) crack with 40 mm length under the center of the film EC probe.

Table 4.9 Amount of crack peak signals amplitude increasing due to FAAP of the film EC probe (unit: mV).

		Frequency		
		300 kHz	500 kHz	1 MHz
Crack peak signal amplitude of film EC probe (mV)	Without FAAP	20.1	26.2	41.7
	With FAAP	22.3	32.5	52.7
Ratio between the crack peak signal amplitude of film EC probe with/without FAAP		1.10	1.24	1.26

The augmentation in crack peak signal amplitude due to the integration of Ferromagnetic

Amorphous Alloy Particles (FAAP) into the film EC probe has been comprehensively outlined in Table 4.9, drawing from empirical results obtained through experimentation. When juxtaposed with the outcomes derived from Finite Element Method (FEM) simulations, these findings underscore the inherent advantage of FAAP in enhancing magnetic flux density. However, it is imperative to underscore that the effectiveness of this augmentation in increasing the crack detection signal is subject to the specific excitation frequency employed. As a corollary, the experimental results align remarkably well with the simulated predictions, thus further corroborating the accuracy and robustness of the experimental methodology employed. This congruence between experimental and simulated outcomes not only bolsters the credibility of the research but also reaffirms the value of FAAP as an innovative and viable strategy for elevating the performance of the film EC probe in detecting defects.

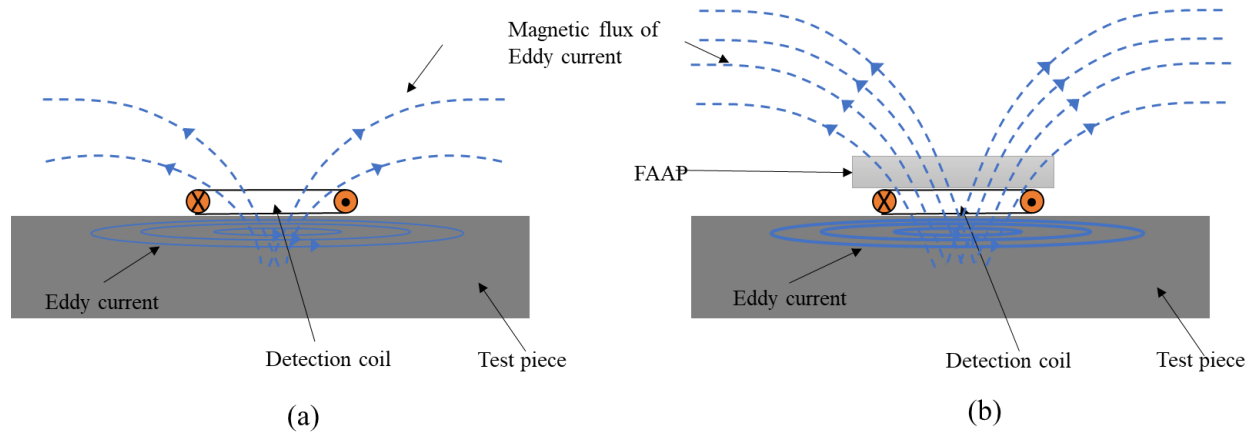


Figure 4.36 Principle of film EC probe: (a) without FAAP, (b) with FAAP

Figure 4.36 visually depicts the significant enhancement in the detection signal achieved through the strategic integration of Ferromagnetic Amorphous Alloy Particles (FAAP). The process involves the induction of eddy currents on the surface of the test piece, accomplished by harnessing the magnetic fluxes generated by the excitation coils. This intricate phenomenon is showcased in Figure 4.36(a), where the resultant EMF of the detection coil is a consequence of the secondary magnetic fluxes engendered by these eddy currents.

With the incorporation of FAAP, as illustrated in Figure 4.36(b), a notable augmentation occurs in the generation of magnetic fluxes. This surge is primarily attributed to the considerable contribution of FAAP, which acts as a magnetic flux amplifier. This augmentation significantly intensifies the generation of eddy currents on the surface of the test piece. Furthermore, FAAP's influence extends to enhancing the interlinkage of magnetic flux with the detection coil.

The net result of these interconnected effects is the amplification of signals captured by the detection coil. This amplification is particularly crucial in bolstering the system's overall detection sensitivity. By strategically leveraging FAAP, the system becomes adept at detecting even minute variations in the eddy current patterns induced on the test piece's surface.

4.4.3.3. Effect of crack size on signals

Figure 4.37 provides an in-depth insight into the relationship between the full width at half maximum (FWHM) value of the crack signals and the varying lengths of cracks. The FWHM value essentially represents the width of the crack signal at its half-maximum amplitude point. Upon analyzing the graph, a clear trend emerges as the length of cracks increases, regardless of their depths, the FWHM value of the corresponding crack signals also increases. This relationship suggests that longer cracks tend to exhibit broader signals with more gradual intensity variations.

Interestingly, when comparing the crack signal characteristics between scenarios with and without FAAP, a noteworthy observation can be made. The FWHM values of crack signals measured without the presence of FAAP (as seen in Figure 4.37(a)) are quite comparable to those obtained when FAAP is utilized (depicted in Figure 4.37(b)). This implies that the incorporation of FAAP does not significantly alter the FWHM values of the crack signals. In essence, the width of the crack signal remains relatively consistent whether FAAP is employed or not.

From the insights provided by Figure 4.37, a valuable inference can be drawn. The FWHM value of crack signals serves as a reliable indicator for evaluating the length of cracks. This assessment holds true for both scenarios, where the FAAP material is utilized and where it is not, showcasing the consistent applicability of this approach across different experimental conditions.

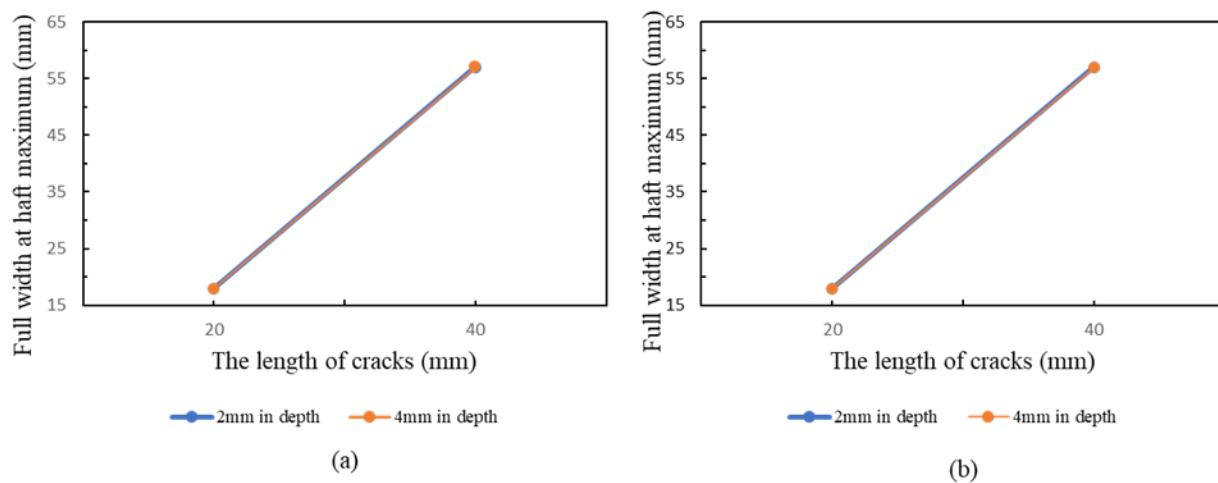


Figure 4.37 The relationship between the full width at half maximum value of the crack signals and the length of cracks. (a) without FAAP, (b) with FAAP

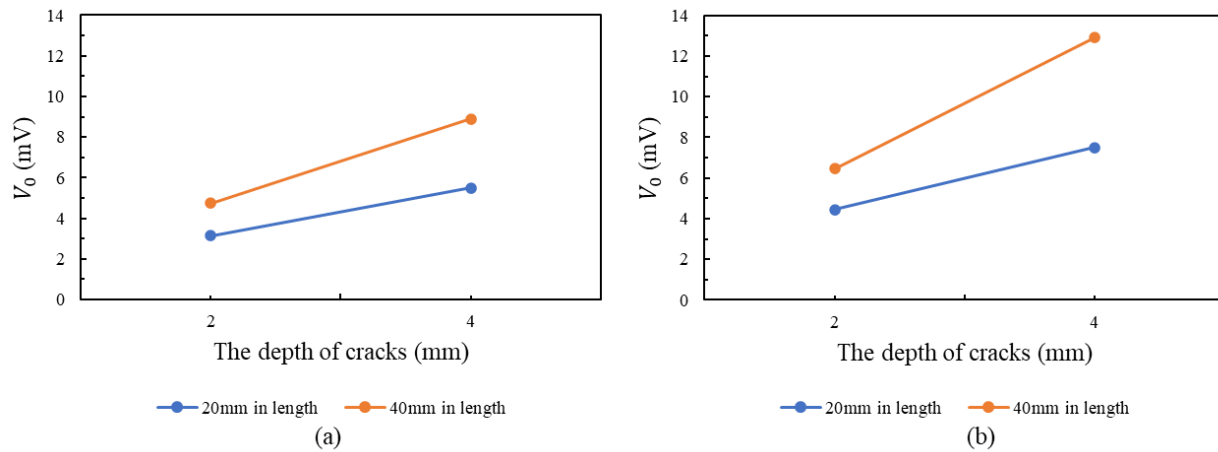


Figure 4.38 The relationship between the maximum value of V_0 and the depth of cracks. (a) without FAAP, (b) with FAAP

Figure 4.38 illustrates the correlation between the maximum amplitude value of V_0 and the varying depths of cracks. Evidently, the maximum V_0 value displays an upward trend as the depth of cracks increases. This observation indicates that deeper cracks tend to generate higher peak amplitudes in the V_0 signal, reflecting a stronger response from the detection system. It's worth noting that a pronounced distinction exists between scenarios with and without the implementation of FAAP, as depicted in Figure 4.38(a) and Figure 4.38(b) respectively. The utilization of FAAP introduces a notable difference in the amplitude of the signal in relation to crack depths.

Furthermore, a comparative analysis of the slopes of the graphs in Figure 4.38 provides additional insights. The slopes of Figure 4.38(b) (with FAAP) for both lengths of cracks appear to be steeper than those of Figure 4.38(a) (without FAAP) for the same crack lengths. This distinction implies that the presence of FAAP amplifies the sensitivity of the detection system to changes in crack depth. As a result, the signal amplitudes exhibit more significant variations for different crack depths when FAAP is applied.

Given the ability to assess crack length from the FWHM values of crack signals (as discussed in Figure 4.37), coupled with the evaluation of crack depth from the maximum V_0 amplitudes (as demonstrated in Figure 4.38), a comprehensive approach for characterizing cracks can be formulated. This two-fold analysis enables effective and accurate assessment of both crack

length and depth, thereby enhancing the precision and reliability of the crack detection process.

4.5. Summary

In summary, this chapter successfully showcased the effectiveness of the Rotating Uniform Eddy Current (RUEC) probe, particularly when equipped with ferrite cores, for crack detection in conductive materials. The incorporation of ferrite cores significantly amplified magnetic flux concentration, enhancing crack signal amplitudes and sensitivity. The probe demonstrated remarkable accuracy in detecting cracks of varying lengths and depths across diverse scenarios. Achieving self-nulling and self-differential characteristics in the detecting coil was identified as crucial, emphasizing the importance of calibration for optimal performance. The RUEC probe with ferrite cores holds promising prospects for non-destructive testing applications in industries such as aerospace, construction, and manufacturing, addressing the limitations of conventional methods.

Furthermore, the chapter introduced the utilization of Multivariate Singular Spectral Analysis (MSSA) filter for noise reduction and signal enhancement in crack detection. MSSA outperformed other filters in handling strong noise variations and preserving crack orientations, contributing significantly to the accuracy and reliability of crack detection methodologies, even in the presence of residual stresses and variations. The comprehensive experimental setup highlighted the potential of the RUEC probe and MSSA filter in non-destructive testing applications, emphasizing the need for advanced signal processing techniques and innovative probe designs.

In another chapter, a novel film eddy current (EC) probe enhanced by ferromagnetic amorphous alloy particles (FAAP) was proposed and investigated for crack detection. The probe's unique design and the use of FAAP significantly improved magnetic flux density and sensitivity, enhancing crack detection capabilities. Finite Element Method (FEM) simulations and experimental tests on aluminum plates validated the advantages of the FAAP-enhanced film EC probe, confirming its potential to boost sensitivity in crack detection.

Chapter 5: Influence of eddy current probe configurations on crack signal amplitude: exploring the impact of excitation coil orientation

5.1. Introduction

This research delves into an exploration of the performance of EC probes, achieved by analyzing three distinct configurations of excitation coils. This builds upon the prior investigations conducted by Ageng et al. [31]. The evaluation of ECs generated within the test specimen encompasses both computer simulations and practical experiments. To model the behavior of the three EC probes, simulation software was employed. These simulation results were then synthesized with physical tests carried out on an actual test specimen. The results of this chapter underscore that the sensitivity of the EC probe in detecting cracks is significantly enhanced when the excitation coils are oriented in the pancake direction. On the contrary, installing the excitation coils tangentially led to a diminished sensitivity and a marked reduction in the amplitude of crack signals. Furthermore, this research also explored EC probes equipped with self-nulling and self-differential features. These innovations prove effective in mitigating strong noise signals during the scanning process. The insights gleaned from this investigation offer promising avenues for optimizing the design and operation of EC probes across a wide array of applications. These applications encompass non-destructive testing of materials, crack detection, and quality control within manufacturing processes. As such, this study holds considerable potential for advancing various industrial practices.

5.2. The performance of previous EC probe

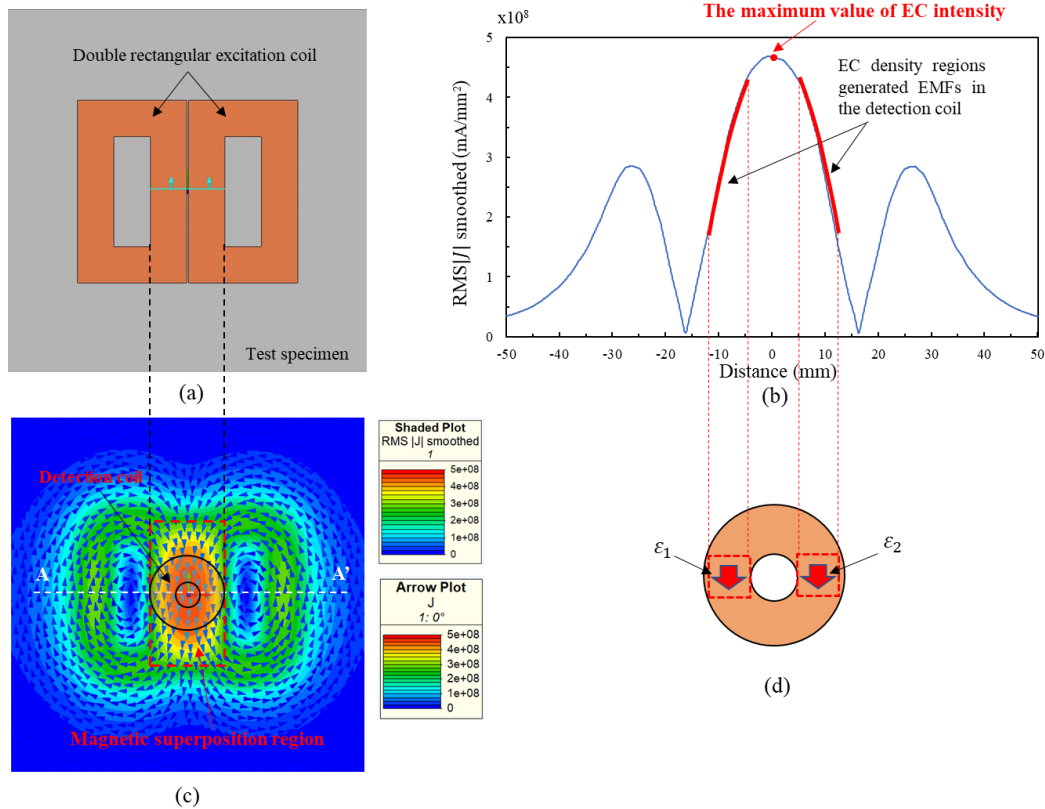


Figure 5.1 The principle of previous EC probe: (a) The structure of EC probe, (b) EC intensity along A-A' direction on the test specimen surface, (c) EC distribution on the test specimen surface, (d) Principle of EMFs generated on the circular detection coil.

This section delves into our earlier study on EC probes [31], shedding light on its inherent limitations. The previous iteration of the EC probe employed a double rectangular excitation coil configuration, aligned parallel to the surface of the test specimen, as depicted in Figure 5.1(a). The arrangement aimed to create a superposition magnetic field at the midpoint of the two excitation coils, resulting in the generation of robust ECs on the surface of the test specimen [refer to Figures 5.1(b) and 5.1(c)]. The objective was to harness the ECs produced within the region of the superposition magnetic field to enhance the strength of EMFs induced in the detection coil. This strategic enhancement sought to elevate the overall performance of the EC probe [see Figures 5.1(b) and 5.1(d)]. However, to satisfy the prerequisites of self-differential and self-nulling attributes essential for the EC probe, the positioning of the detection coil necessitated it to be situated beneath the excitation coil, precisely at the midpoint. Consequently, the EMFs generated in the detection coil, stemming from the ECs, emerged on opposing sides of the center of the test specimen, as illustrated in Figures 5.1(b) and 5.1(d). This arrangement leads to an underutilization

of regions where the ECs' magnitude is at its zenith. As a result, the performance of the EC probe faces limitations.

5.3. Materials and models for this study

5.3.1. Materials

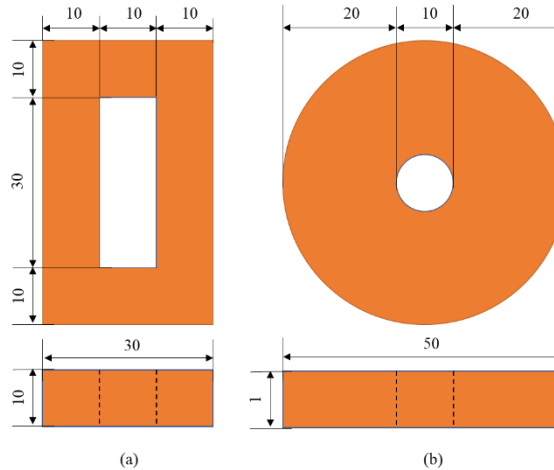


Figure 5.2 Structure of EC probe components (units in mm): (a) Each rectangular excitation coil, (b) Circular detection coil.

The components comprising the EC probe model are visually represented in Figure 5.2. In detail, each rectangular excitation coil and the circular detection coil were meticulously assembled, utilizing a total of 1300 turns of copper wire possessing a diameter measuring 0.2 mm. This assembly is depicted in Figures 5.2(a) and 5.2(b) correspondingly. The primary focus of our study centered around a meticulous comparison of the magnitude of ECs engendered on the surface of the test specimen. This comparison was undertaken with an intentional alteration in the orientations of the excitation coils. To ensure an optimal acquisition of the highest EC density value possible on the test specimen surface, our selection for the configuration of the detection coil was such that the zones of interaction responsible for generating EMFs within the detection coil maintained uniform areas. This specific choice facilitated a precise and accurate assessment of the ECs' intensity generated on the test sample through the EC probe models. By adopting this approach, our endeavor was to systematically explore the repercussions of varied EC probe configurations on the magnitude of crack signals. This strategy aimed to unravel the nuanced impact of the EC probe's layout on the amplitude of signals indicating the presence of cracks.

5.3.2. Finite element method (FEM) simulation

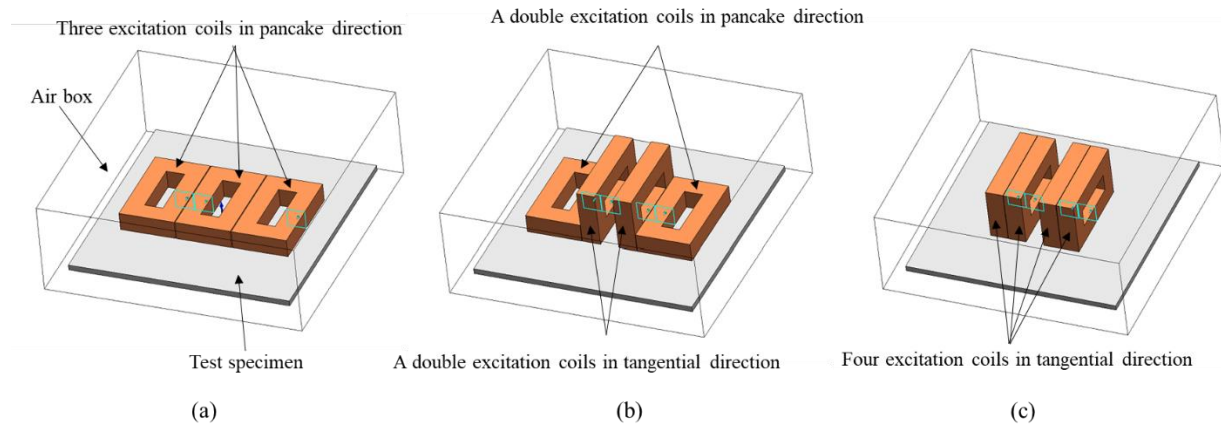


Figure 5.3 EC probe models for FEM simulation: (a) Three excitation coils in pancake direction (Type 1), (b) A double excitation coils in pancake and tangential directions (Type 2), (c) Four excitation coils in tangential direction (Type 3).

To delve into the influence of EC probe configuration on the magnitude of crack signals, our investigation encompasses the proposal of three distinctive EC probe models, as visually depicted in Figure 5.3. The initial model, designated as Type 1, showcases three rectangular excitation coils thoughtfully situated in proximity, oriented in a pancake direction. The second model, denoted as Type 2, integrates dual excitation coils, one in the pancake direction and the other in the tangential orientation. The final model, identified as Type 3, incorporates four excitation coils, all configured tangentially.

Each of these excitation coils, meticulously crafted with 1300 turns of copper wire boasting a diameter of 0.2 mm, is applied uniformly across the simulations. To facilitate an accurate assessment of the impact of excitation coil orientation on the Eddy Currents (ECs) engendered on the test specimen's surface, the zones of interaction responsible for generating EMFs in the detection coil are standardized across all three models.

A consistent excitation current of 10 mA and a frequency of 5 kHz are administered to the excitation coils. By subjecting the results derived from these three EC probe models to meticulous analysis, we gain the capacity to effectively evaluate the comprehensive effect of excitation coil direction on the ECs generated at the test specimen's surface. Moreover, this assessment allows us to comprehend the consequential repercussions on the magnitude of signals indicative of the presence of cracks. The electromagnetic parameters underpinning this rigorous analysis are itemized comprehensively within Table 5.1.

Table 5.1 Electromagnetic parameters used in analysis for EC probe models.

	Material	Electrical conductivity, σ (MS/m)	Relative permeability, μ_r
Wire of Excitation coil	Copper	57.7	1.0
Wire of Detection coil			
Test piece	Aluminum	38.0	

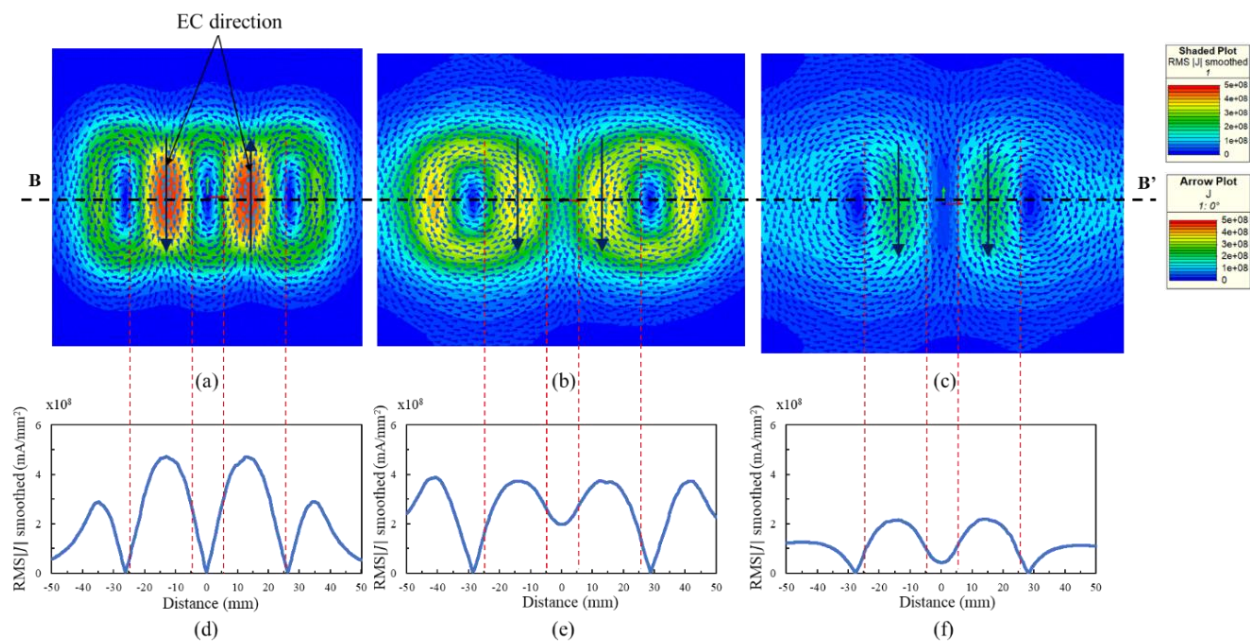


Figure 5.4 FEM simulation results with three EC probe models: (a) EC intensity distributed on the test specimen surface with Type 1, (b) EC intensity distributed on the test specimen surface with Type 2, (c) EC intensity distributed on the test specimen surface with Type 3, (d) EC intensity obtained along B-B' path of Type 1, (e) EC intensity obtained along B-B' path of Type 2, (f) EC intensity obtained along B-B' path of Type 3.

Figure 5.4 showcases the outcomes stemming from FEM simulations involving three distinct EC probe models. A thorough analysis of these simulation results distinctly illustrates that among the three types, Type 1 manifests the most heightened Eddy Current (EC) intensity on the surface of the test specimen. Directly following is Type 2, trailed by Type 3, as visually depicted in Figures 5.4(a), 5.4(b), and 5.4(c).

This observed trend gains further clarity when examining the EC intensity profiles along the B-B' trajectory. Within this context, the highest recorded value of EC intensity at the central

juncture of the excitation coils registers at 4.7 (mA/mm²) for Type 1 [Figure 5.4(d)]. This value gradually attenuates to 3.8 (mA/mm²) and subsequently to 2.2 (mA/mm²) for Type 2 [Figure 5.4(e)] and Type 3 [Figure 5.4(f)] respectively.

The significance of these findings lies in their decisive demonstration that excitation coils oriented in the pancake direction, sharing a common interaction region, can yield notably stronger EC intensity on the surface of the test specimen compared to their counterparts oriented in the tangential direction. Notably, when employing four excitation coils configured tangentially, as seen in Type 3, there is a remarkable reduction in the EC intensity generated on the test specimen's surface.

It's pertinent to highlight that while the magnitudes of ECs generated on the test specimen's surface exhibit uniformity across Type 1 [Figure 5.4(a)], Type 2 [Figure 5.4(b)], and Type 3 [Figure 5.4(c)], their orientations differ distinctly. Notably, ECs generated by Type 1 are oriented in opposing directions, whereas those produced by Type 2 and Type 3 are aligned in the same direction. This variance in the directional alignment of ECs bears the potential to significantly impact the configuration of EMFs within the detection coil.

The subtle dissimilarity in the ECs' directional alignment holds implications for the subsequent formation of EMFs within the detection coil. These resulting EMFs, in turn, can exert a substantial influence on the efficacy of crack detection on the test specimen. The forthcoming section will delve deeper into the discussion of how these variations in EC direction intricately interplay with the generation of EMFs and, consequently, their implications for accurate crack detection.

5.3.3. The principle of formation of EMFs in the detection coil and the crack signal

The section of the test specimen that has been strategically selected for generating the EMFs ε_1 and ε_2 from the ECs is thoughtfully delineated in Figure 5.5. This entails a pivotal focus on the area of interaction between the coils and the test specimen that culminates in the generation of these essential EMFs. It is noteworthy that the positioning of the detection coil assumes a central location, situated below the excitation coils of each variant of the probe.

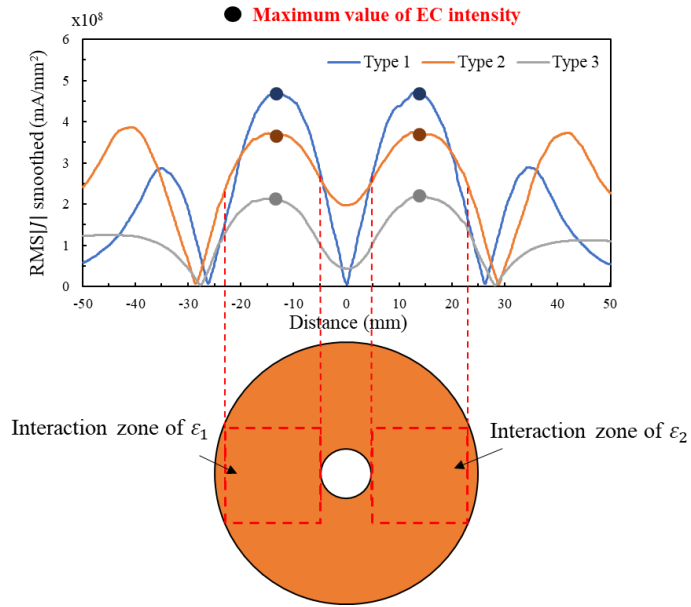


Figure 5.5 Region of EC on the test specimen used for generating EMFs ε_1 and ε_2 in the detection coil.

The configuration of the detection coil corresponds harmoniously to the design outlined in Figure 5.2(b). This design, in its careful orchestration, ensures that the EMFs are engendered within regions characterized by the utmost intensity of ECs. The strategic reasoning behind this specific configuration is to facilitate a meticulous comparison and appraisal of the performance exhibited by the three distinct probe types.

The deliberate alignment of EMF generation with the regions boasting the peak EC intensity facilitates a direct and equitable comparison of the EMF signals derived from the three different probe types. By this approach, a robust basis is established for the evaluation of sensitivity and accuracy across each probe type in the realm of crack detection. This intricate setup essentially offers a pathway to meticulously assess the capabilities and limitations of each probe type, particularly concerning their efficacy in detecting cracks.

5.3.3.1. The principle of crack detection signal with Type 1

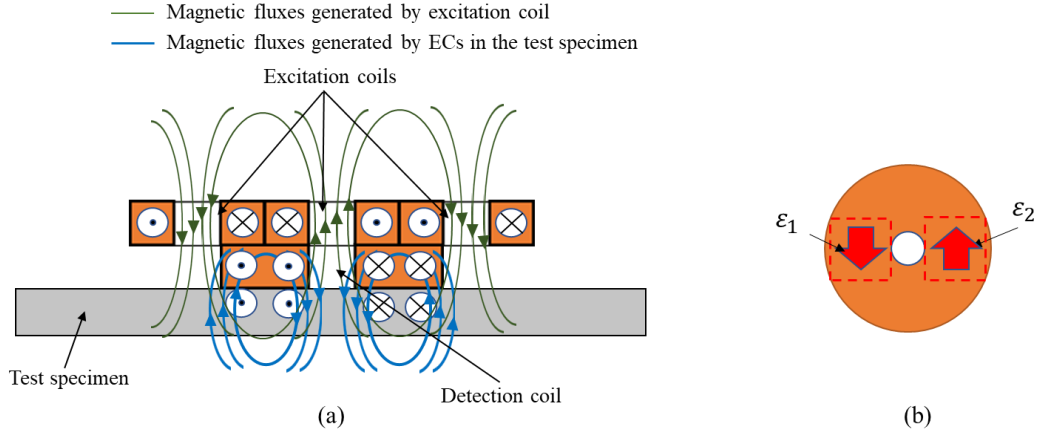


Figure 5.6 Principle of electromotive forces generated on detection coil for Type 1: (a) The signal generated on the detection coil, (b) The direction of EMFs on the detection coil.

In this segment, we delve into the fundamental mechanism underlying the generation of EMF within the detection coil for Type 1, as illustrated in Figure 5.6. The configuration of this detection coil gives rise to a distinctive interaction pattern with the ECs generated within the magnetic superposition regions of the test specimen, as evidenced in Figure 5.4(a).

This phenomenon is intricately linked to the polarity of the magnetic fluxes, as elucidated in Figure 5.6(a), which originate from the excitation coils. These magnetic fluxes engender magnetic superposition regions characterized by opposing directions. Consequently, the ECs generated within these regions also manifest opposite directions. The consequence of this contrasting EC directionality is reflected in the EMF values within the detection coil. Specifically, the EMFs within the detection coil arise from the intricate interplay between the EMFs generated by the magnetic fluxes originating from the excitation coils and the ECs present within the test specimen. Due to the opposing nature of the EC directions, the EMFs they generate within the detection coil tend to nullify each other. Importantly, despite the alignment of EMFs ε_1 and ε_2 in the same polarities yet opposing directions, as visualized in Figure 5.6(b), the cumulative EMF value of the detection coil remains the summation of ε_1 and ε_2 . This is primarily because both EMFs share a consistent direction aligned with the copper wire within the detection coil. This nuanced interplay within the detection coil intricately shapes the resulting EMF values and sets the foundation for the subsequent analyses.

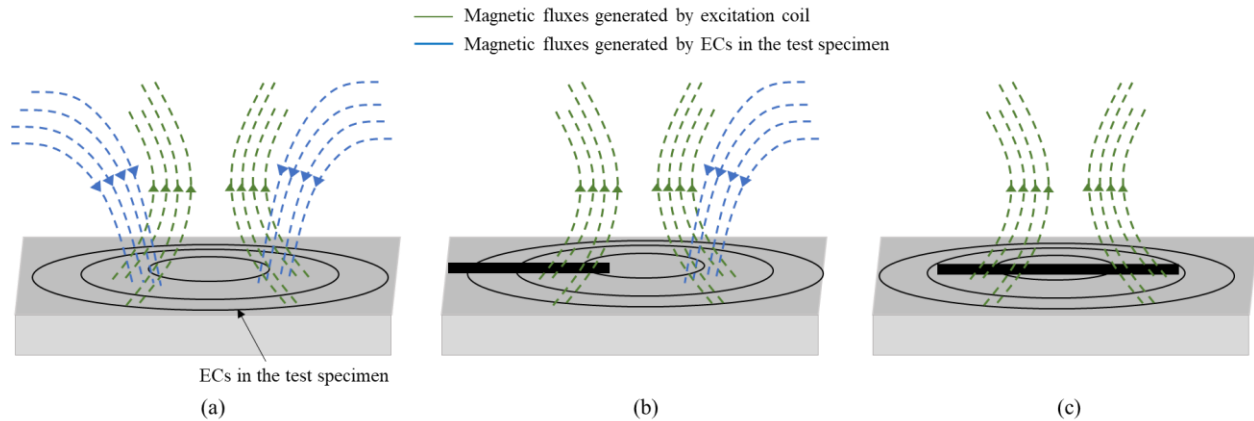


Figure 5.7 Principle of the output detection signal with the circular detection coil of Type 1: (a) Without a crack, (b) With a crack under the left side of the detection coil, (c) With a crack under the center of the detection coil.

Figure 5.7 serves as a visual representation of the operational principle governing the output detection signal of the circular detection coil within the Type 1 probe. In the absence of any cracks within the test specimen, as exemplified in Figure 5.7(a), the ECs generated on the test specimen give rise to a magnetic flux. This magnetic flux is counteracted and nullified by the magnetic flux stemming from the excitation coils. Consequently, the EMF values observed within the detection coil emerge because of the mutual cancellation of EMFs originating from the magnetic fluxes of both the excitation coils and the ECs present within the test specimen, mirroring the scenario depicted in Figure 5.6(a).

However, when a crack is introduced into the test piece, a disruptive element enters the equation. This disruption triggers a deviation in the generation of ECs on the test specimen's surface. This deviation translates into a diminution of the magnetic flux that would have been otherwise induced by the ECs. This alteration allows for the magnetic flux engendered by the excitation coils to gain prominence and dominance. This transition becomes evident in Figures 5.7(b) and 5.7(c).

Consequently, a more substantial magnetic flux traverses through the detection coil, thereby resulting in an amplification of the signal generated within the detection coil. In essence, the presence of a crack in the test specimen tips the equilibrium of magnetic fluxes within the probe. This shift in balance manifests as a measurable alteration in the output signal of the circular detection coil. The interplay between the magnetic fluxes and the detection coil's responsiveness unveils the probe's ability to detect cracks through observable signal variations.

5.3.3.2. The principle of crack detection signal with Type 2 and Type 3

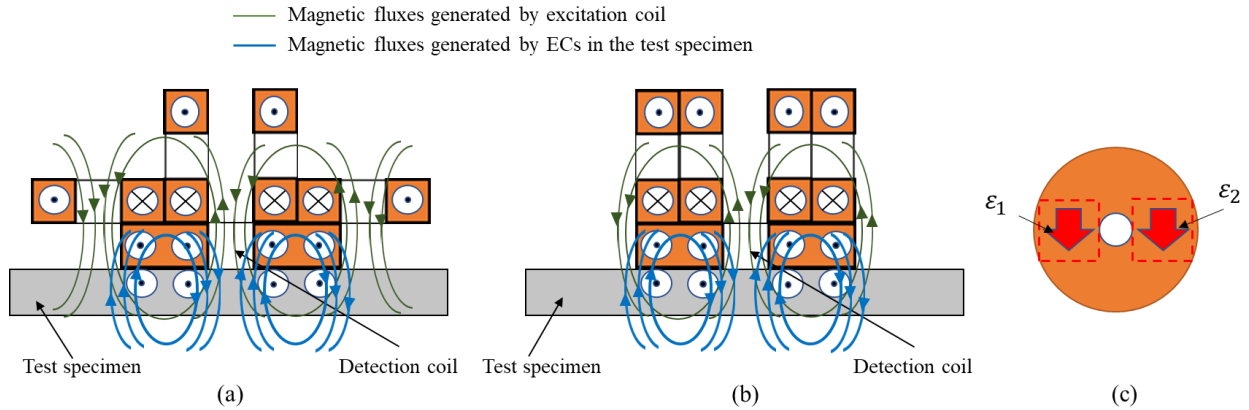


Figure 5.8 Principle of electromotive forces generated on detection coil for Type 2 and Type 3: (a) The signal generated on the detection coil of Type 2, (b) The signal generated on the detection coil of Type 3, (c) The direction of EMFs on the detection coil.

This paragraph delves into the underlying principle governing the generation of EMF within the detection coil for both Type 2 and Type 3 probes. The detailed explanation is accompanied by illustrative content in Figure 5.8. The ECs produced within the magnetic superposition zones on the test specimen surface manifest identical polarities and directions. This alignment is attributed to the congruence in the directions of the magnetic superposition regions arising from the magnetic fluxes generated by the excitation coils, as visibly portrayed in Figures 5.4(b) and 5.4(c).

However, it is pivotal to note that while the EMFs ϵ_1 and ϵ_2 generated within the detection coil share consistent directions, the cumulative EMF value within the detection coil equates to the disparity between ϵ_1 and ϵ_2 . This variance arises due to the opposing direction taken by one of the EMFs concerning the copper wire orientation within the detection coil. Because of this alignment, positioning the detection coil at the center of the EC probes culminates in a consistent output signal of zero in instances where no crack is present on the test specimen's surface.

This specific setup ensures that the detected signals remain neutral in the absence of any cracks, providing a robust baseline for signal evaluation and subsequently enhancing the accuracy of crack detection through signal deviation.

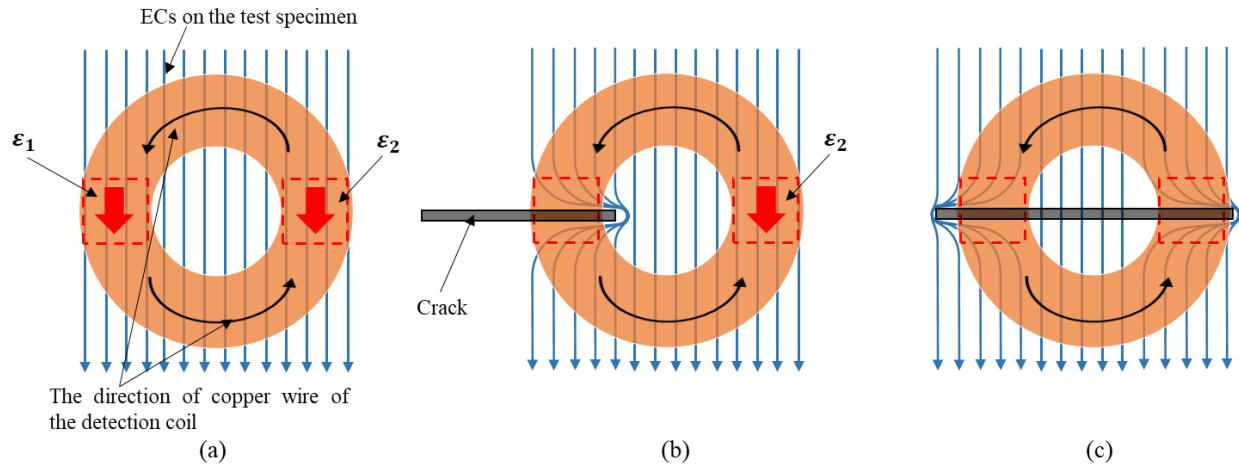


Figure 5.9 Principle of the output detection signal with the circular detection coil of Type 2 and Type 3: (a) Without a crack, (b) With a crack under the left side of the detection coil, (c) With a crack under the center of the detection coil.

The operational principle governing the output detection signal, particularly concerning the circular detection coil for both Type 2 and Type 3 probes, is visually expounded in Figure 5.9. This principle draws parallels with the conceptual framework outlined in Reference [31], establishing a coherent foundation for comprehension. The dynamics of the output detection signal pivot on the influence exerted by the EMFs engendered within the detection coil by the ECs present on the test specimen's surface. This process encompasses two distinctive scenarios: the balanced condition and the unbalanced condition.

The balanced condition emerges in situations devoid of cracks on the test specimen's surface. In this scenario, the EMFs ε_1 and ε_2 , harnessed within the detection coil, mirror each other in magnitude yet adopt opposing polarities, vividly portrayed in Figure 5.9(a). This meticulous arrangement results in the mutual negation of these EMFs, embodying what is termed the self-differential characteristic. The culmination of this alignment is a nullification of the output detection signal, characterizing the self-nulling characteristic.

In stark contrast, the unbalanced condition unfolds when a crack is present beneath the detection coil of the EC probes. This presence disrupts the harmonious pattern of ECs ordinarily generated on the test specimen's surface. Consequently, the intensity value of ε_1 and ε_2 undergoes modification, depicted explicitly in Figures 5.9(b) and 5.9(c). This disruption breaks the self-nulling nature that characterizes the balanced condition, paving the way for the generation of a discernible crack detection signal. This intricate interplay between the conditions of balance and

imbalance encapsulates the core principle governing the sensitivity of the probe's signal generation with respect to crack detection.

5.4. Experimental setup

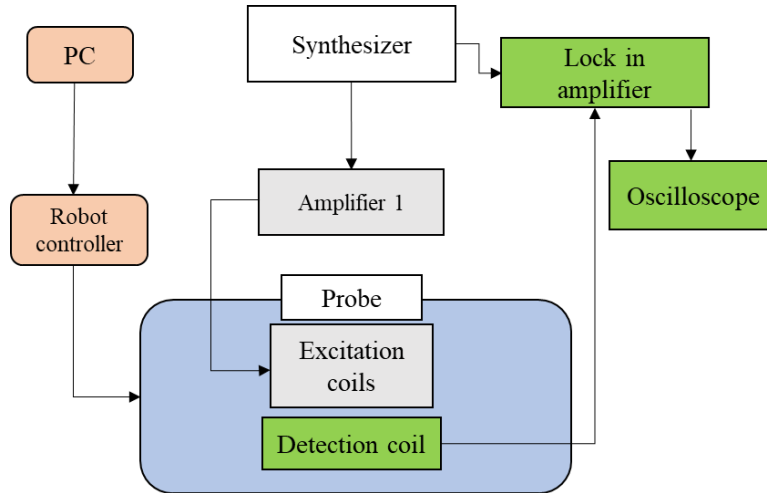


Figure 5.10 Diagram of the experimental setup

Table 5.2 The sizes of four artificial cracks in the aluminum plate used for EC probe models.

Symbol of cracks	Width (mm)	Length (mm)	Depth (mm)
20-2	0.5	20	2
20-4			4
40-2		40	2
40-4			4

The diagram depicting the experimental setup is featured in Figure 5.10, while its practical implementation is illustrated in Figure 5.12. This setup necessitated the utilization of a function generator (WAVE FACTORY WF1946B, NF Co., Yokohama, Japan) alongside high-speed bipolar amplifiers (NF HAS 4012, NF Co., Yokohama, Japan). These components functioned in tandem to generate an alternating excitation current boasting a frequency of 5 kHz and a magnitude of 10 mA.

To execute the experimental trials, a test specimen was meticulously crafted from 5052 aluminum plates. This specimen was carefully equipped with artificially induced cracks of varying dimensions, as discernible in Figure 5.11. The creation of these cracks was achieved through the process of electrical discharge machining. Their respective dimensions and sizes have been

meticulously documented and are comprehensively presented within Table 5.2.

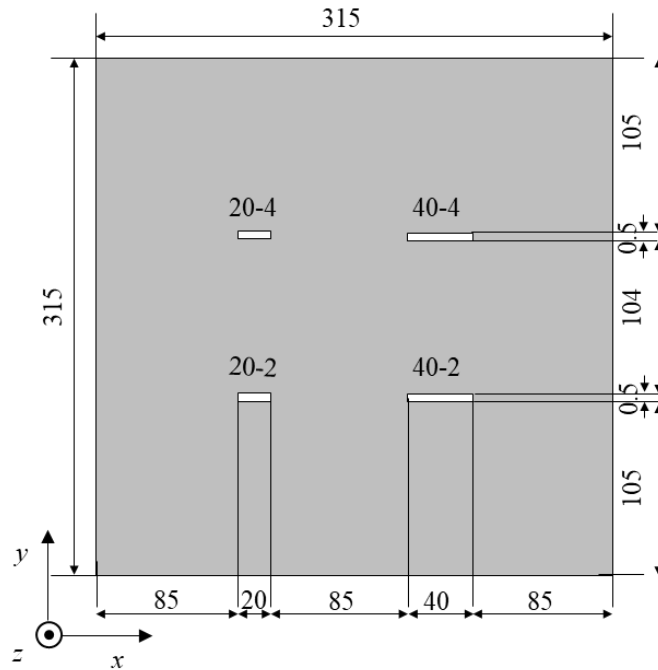


Figure 5.11. Specifications of aluminum plate

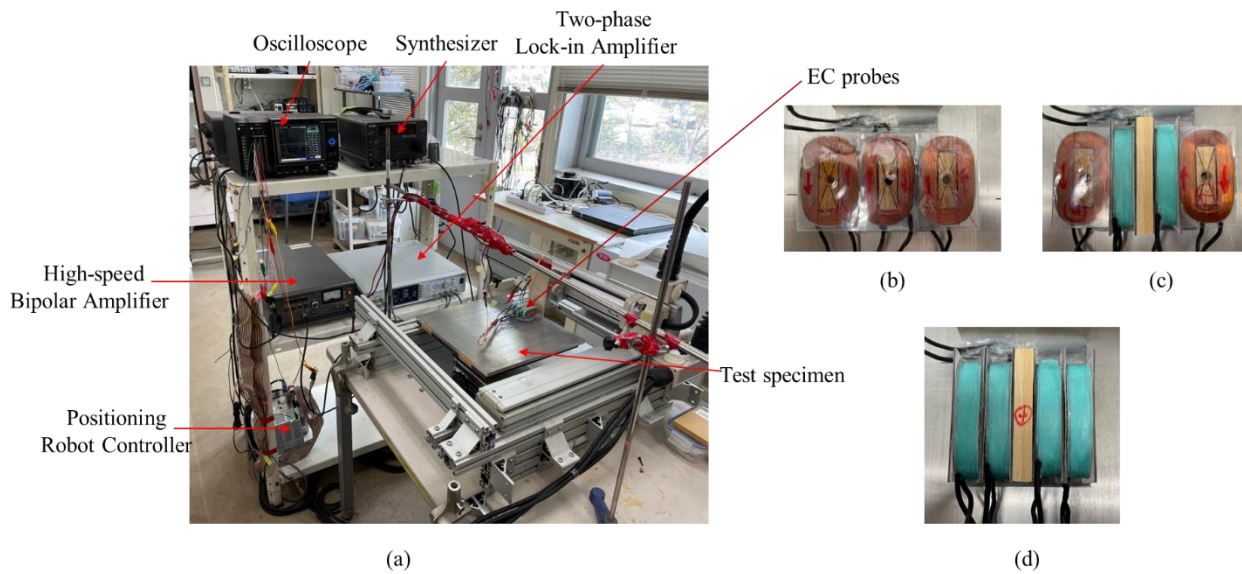


Figure 5.12. Experimental implementation: (a) Experimental setup, (b) Actual shape of Type 1, (c) Actual shape of Type 2, (d) Actual shape of Type 3

For the duration of the experiments, a scanning interval of 1 mm was consistently maintained. The acquisition of output amplitude signals was facilitated by a singular detection coil. These acquired signals underwent processing through a two-phase lock-in amplifier (NF 5601B)

before being archived in a digital oscilloscope (Graphtec GL7000).

The distinct configurations of the three EC probe Types are vividly portrayed in Figures 5.12(b), 5.12(c), and 5.12(d), each with its corresponding parameters documented in Table 5.3. This meticulous outline encapsulates the comprehensive apparatus and methodology employed throughout the experimental trials.

Table 5.3 The parameters of each excitation coil and the detection coil used for EC probe models.

Parameters	Each excitation coil	Detection coil
Turns	1300	1300
Wire diameter (mm)	0.2	0.2
Resistance (k Ω)	0.471	0.691
Impedance (k Ω)	3.117	2.774
Inductance (mH)	50.19	45.57

5.5. Results and discussions

5.5.1. Measurement results of three EC probe models

To comprehensively evaluate the proficiency of crack detection through varying EC probe configurations, a meticulous procedure was adopted. The EC probes were systematically scanned along the y-axis, conducting a thorough scan for the presence of cracks. This procedure was subsequently repeated, with the EC probes being systematically shifted along the x-axis, as visually depicted in Figure 5.13(a). The attainment of accurate and precise scanning was largely facilitated through the utilization of a computer-controlled positioning robot module. This technological component seamlessly enabled the movement of the EC probes across the scanning surface of the test specimen, maintaining a consistent velocity of 10 mm/s. In pursuit of obtaining high-resolution scans, a scan pitch of 0.5 mm, along with a scan distance of 1 mm, was meticulously selected. These specific parameters ensured a meticulous and detailed assessment of the scanning surface, capturing intricate nuances that could potentially signify the presence of cracks. This elaborate approach underscores the commitment to achieving accurate and reliable results throughout the scanning process.

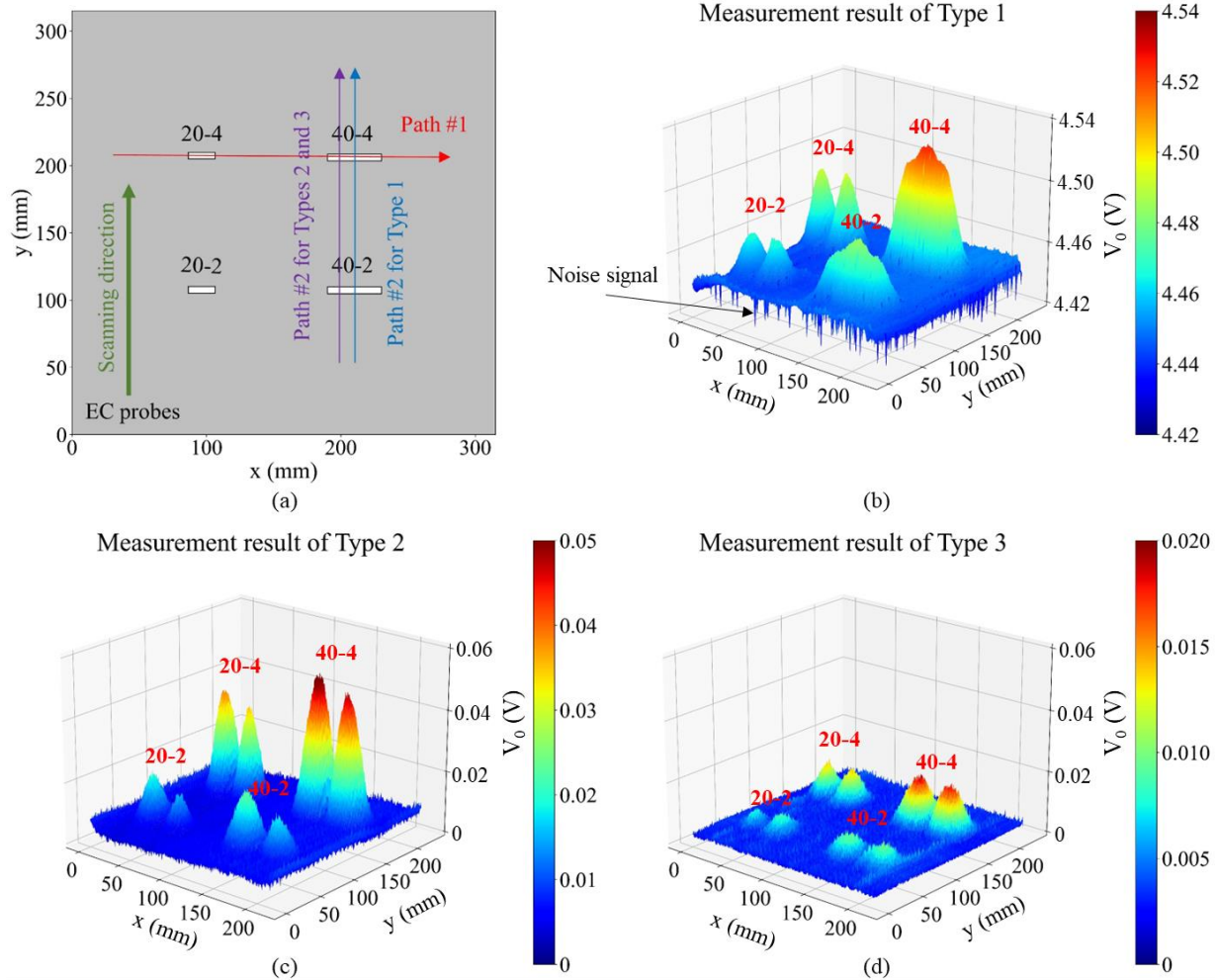


Figure 5.13. Measurement results of three EC probe Types through the scanning process: (a) Scanning direction and Paths of EC probes for experiments, (b) Measurement result of Type 1, (c) Measurement result of Type 2, (d) Measurement result of Type 3.

The outcomes derived from the measurements conducted using the three distinct EC probe configurations are eloquently presented in Figures 5.13(b), 5.13(c), and 5.13(d). These findings unequivocally showcase the ability of all three probe types to distinctly discern signals emanating from cracks of varying dimensions. To enhance clarity, 3D representations were crafted to visually portray the measurement outcomes. This approach notably accentuates the occurrence of noise signals encountered during the scanning procedure of Type 1.

Upon analysis, it becomes apparent that when the area of the crack isn't positioned directly beneath the detection coil, the output signal of Type 1 approximates 4.43 V [Figure 5.13(b)], while the corresponding output signals for Type 2 and Type 3 converge towards zero [Figures 5.13(c)

and 5.13(d)]. This stark distinction corroborates the self-nulling and self-differential attributes inherent to Type 2 and Type 3 probes. These attributes, as evidenced by these experimental findings, validate the earlier discovery gleaned from simulation results that the output signal remains null in the absence of a crack on the test specimen.

Furthermore, the data deduced from the experimental trials brings to the forefront a noteworthy observation: noise signals are considerably prevalent during the scanning process involving Type 1, whereas they exhibit near-absence in the cases of Type 2 and Type 3. This pronounced contrast underscores the considerable potential harnessed by the self-nulling and self-differential traits, particularly in the context of noise cancellation. This inherent noise mitigation capability presents a promising avenue for refining the accuracy and reliability of crack detection procedures.

It's important to highlight that for cracks labeled as 40-4 and 40-2, distinct patterns emerged during the scanning process. When utilizing Type 1 probe configuration, a solitary peak manifested within the crack signal. Conversely, scanning with Type 2 and Type 3 probes yielded the observation of two distinct peaks. This intriguing phenomenon can be elucidated through the recognition that when the crack is positioned at the center of the detection coil, a nullification of EMF values arises due to the perturbation of ECs on the test specimen's surface.

During this specific alignment, the magnetic fluxes originating from the excitation coils gain prominence, thus leading to the attainment of maximum crack output signal amplitude for Type 1. In stark contrast, the crack output signal remains stationary at zero for both Type 2 and Type 3 probes, owing to their inherently balanced conditions. This notable observation substantiates the notion that the crack detection principle governing Type 1 probes can yield a more substantial crack signal magnitude when compared to its counterparts, Type 2 and Type 3. The intricate interplay between crack location and probe configuration unveiled through these experimental results underscores the intricacies that dictate signal behavior and sensitivity in crack detection scenarios.

5.5.2. Measurement results of path #1 and path #2

To dissect and comprehensively understand the captured crack signals across the three distinct EC probe Types, an analytical approach was undertaken. The evaluation encompassed measurements conducted along Path #1, which traversed through two specific crack zones (designated as 20-4 and 40-4). This was subsequently complemented by measurements along Path

#2, which in turn encompassed two additional distinct crack regions (identified as 40-2 and 40-4).

It's noteworthy that the distinctive positioning of the maximum crack signal amplitude played a pivotal role in shaping the approach to analysis. For Type 1 probe, the peak signal amplitude was centered, whereas for Type 2 and Type 3 probes, it was lateral. Due to this variation, a judicious decision was made to exclusively showcase the measurement outcomes for Path #2 across all three EC probe Types. This decision was rooted in the intent to provide a coherent and illustrative representation, accentuating the nuances that differentiate the probes in a consistent setting. Following this strategic approach, the gathered measurement results were adeptly arranged and showcased in Figure 5.14. This meticulous selection and arrangement of data ensures a focused and insightful presentation of the obtained outcomes, thereby facilitating a more streamlined interpretation and comparison across the three EC probe Types.

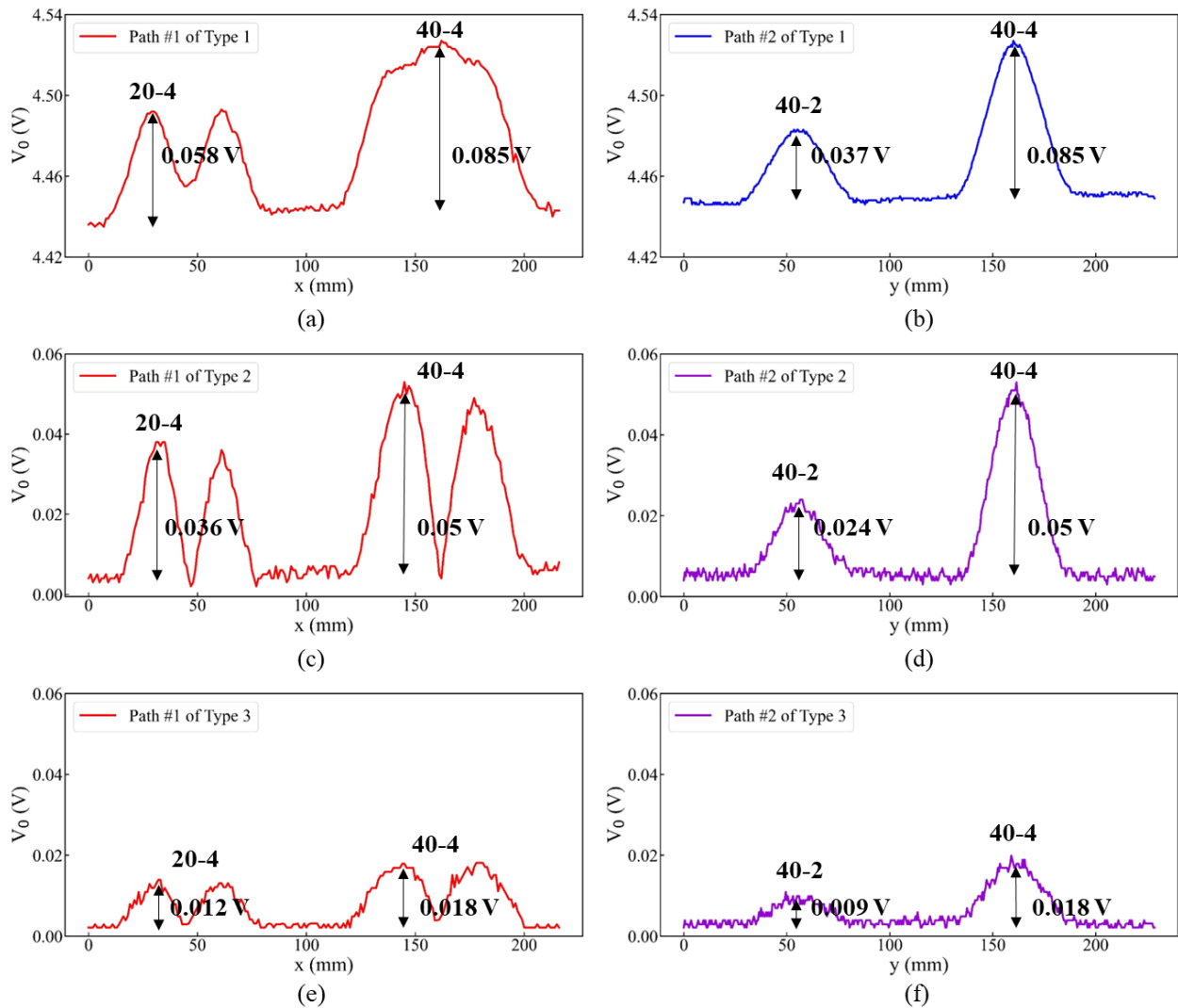


Figure 5.14. Measurement results of three EC probe Types through two Paths: (a) Path #1 of Type 1, (b) Path #2 of Type 1, (c) Path #1 of Type 2, (d) Path #2 of Type 2, (e) Path #1 of Type 3, (f) Path #2 of Type 3.

Despite the apparent presence of noise signals within the measurement outcomes associated with Type 1 during the scanning procedure, a more nuanced observation emerges when considering the measurement results along two distinct Paths of Type 1. Surprisingly, these results indicate a noteworthy absence of noise signals. This observation implies that the noise signal linked to Type 1 predominantly emerges at the initiation or conclusion of the scan, a scenario that arises due to the abrupt halt in the process during movement transitions. This peculiar concern, however, becomes inconsequential when the EC probe sustains a uniform and unvarying velocity during movement.

In addition, Figure 5.14(a) effectively captures a unique phenomenon wherein the crack signal for crack (20-4) exhibits a bifurcation into two distinctive peaks. This phenomenon's genesis can be attributed to the relatively shorter length of the crack, a characteristic that leads to a subtle disruption of the ECs on the test specimen's surface. Consequently, the prevailing dominance of the magnetic fluxes originating from the excitation coils is diminished within the signal, thereby resulting in a diminution of the crack signal. A parallel pattern is discernible within Type 2 and Type 3 probes, particularly in cases where the two cracks, 40-4 and 20-4, share identical depths. In these scenarios, the crack signal intensity for crack (20-4) experiences notable attenuation owing to the crack length's deficiency vis-à-vis the detection coil's radius. This pattern is vividly illustrated in Figures 5.14(c) and 5.14(e).

Furthermore, an intriguing observation is discerned when comparing cracks (40-4 and 40-2) of equivalent length. Here, the peak signal intensity corresponding to crack (40-4) is twice that of crack (40-2), offering a direct indicator of the crack's depth. This distinctive pattern is cogently presented in Figures 5.14(b), 5.14(d), and 5.14(f). These discerning findings underscore the pivotal importance of meticulously harmonizing the detection coil's configuration with the dimensions of the crack. This judicious matching is an essential component in unlocking the optimal performance potential of the EC probe.

While the EC probe Types inherently vary in their approaches to crack detection, the amplitude value of the crack signal serves as a quantifiable indicator of the alterations occurring in the Eddy Currents (ECs) across the test specimen's surface due to the presence of cracks. To

meticulously scrutinize and assess the crack signal dynamics, we concentrated on the measurement results stemming from an identical superposition region. These outcomes unfurl a vivid depiction of the interplay between crack detection principles and signal amplitudes, particularly in the context of a representative crack (40-4). The examination of these results underlines a salient observation: the maximum crack signal amplitude registers at 0.085 V for Type 1, exhibiting a substantial reduction to 0.05 V for Type 2, before ultimately descending to 0.018 V for Type 3. This intriguing trend delineates that the ECs engendered on the test specimen's surface witness attenuation when the excitation coils are oriented in a tangential direction relative to the test specimen's surface. This aligned pattern of diminishing signal amplitudes across the three probe Types resonates seamlessly with the findings garnered from the simulation process. In essence, these empirical results provide a coherent validation of the simulation-derived results, cementing the understanding that the configuration of excitation coils significantly influences the ECs' vigor, consequently influencing the amplitude of the generated crack signal.

5.6. Summary

This chapter delves into the enhancement of EC probe performance by investigating the impact of three distinct excitation coil configurations on the evaluation of ECs generated within the test specimen. The performance evaluation involves simulations and experimental measurements conducted on three models of EC probes. The study's findings shed light on the distinctive attributes of each EC probe type.

Type 1 EC probe, owing to its pancake direction installation of excitation coils, demonstrates heightened sensitivity in detecting cracks. However, a noteworthy limitation surfaces in the form of susceptibility to noise signals at the scan's commencement and conclusion due to abrupt movement changes. On the other hand, Type 2 and Type 3 EC probes, designed with self-nulling and self-differential features, effectively suppress potent noise signals during scanning. Regrettably, this advantage comes at the expense of reduced amplitude values in crack signals, leading to a compromise in crack detection sensitivity when compared to Type 1. Remarkably, among the three variants, Type 3 showcases the lowest sensitivity due to its excitation coil's tangential installation, which significantly diminishes the amplitude of crack signals.

In essence, each EC probe type presents its distinct merits and drawbacks. The selection of the appropriate EC probe hinges on the specific requirements of the inspection task at hand. For applications necessitating surface crack detection, a thoughtful consideration of crack attributes

and the operational environment is crucial. The study's outcomes furnish valuable insights into the diverse performance profiles of distinct EC probe types, thereby contributing to the refinement of crack detection methodologies across an array of applications.

Chapter 6: Conclusions

Reviewing all the studies that have been described in all chapters, the following are the conclusions of this dissertation.

This comprehensive study has explored various advancements in eddy current (EC) probe technology for crack detection in conductive materials. The study aims to improve EC probe performance by enhancing crack detection ability through various core shapes and materials.

1. Using copper core material to create a specially designed copper core aimed at converging eddy currents at the tip of the copper core

➤ Advantages:

- High electrical conductivity: Allows the generation of eddy currents within the copper core and controls the convergence of eddy currents.
- Ease of machine and repair: Copper is easily machinable and repairable, facilitating customization of cores for specific testing needs.

➤ Disadvantage:

- The generation of ECs within the copper core from the excitation coil before inducing ECs on the surface of the test specimen results in significant current loss compared to traditional EC probes. However, this issue is addressed by the strong convergence of EC intensity at the tip of copper core.

Based on the characteristics of the copper core, the study has showcased the efficacy of the eddy current convergence (ECC) probe featuring a copper core (as known with high electrical conductivity and non-magnetic properties), emphasizing its robust ability to identify defects. This is particularly notable in a design incorporating a pair of copper cores for the ECC probe, which effectively controls the eddy current generated in the test specimen in a uniform direction. This design adheres to the self-nulling and self-differential characteristics, effectively mitigating noise during the scanning process caused by the probe's movements. However, proposed models of ECC probes with a copper core exhibit a drawback in scenarios where cracks align parallel to the EC current line. This alignment results in a noteworthy reduction in the intensity of the acquired crack signal. Consequently, there is a pressing need to develop an innovative ECC probe capable of discerning cracks in all directions.

To address the limitations of prior research, the subsequent study introduced the Uniform Rotating Eddy Current Convergence (RUECC) probe. The probe not only inherited the strengths

of its predecessors, such as the capability to converge eddy currents and manifest self-nulling and self-differencing characteristics found in earlier ECC probes, but also, through enhanced design, engendered rotating uniform eddy currents. This innovation significantly bolstered the adaptability of the RUECC probe in identifying cracks of all sizes and directions. This represents a substantial stride forward in enhancing crack detection sensitivity, positioning the RUECC probe as a promising instrument in the continuous evolution of non-destructive testing methodologies.

2. Using support material including ferrite core and ferromagnetic amorphous alloy particles (FAAP) for enhancing crack signal amplitude.

2.1 Ferrite core

➤ Advantages:

- High magnetic permeability: Ferrite cores efficiently amplified magnetic flux, enhancing the sensitivity of eddy current probes.
- Non-electrical conductivity: Ferrite cores do not conduct electricity, reducing eddy current losses within the core and directing induced currents primarily into the test specimen.

➤ Disadvantage:

- For the convergence condition, when the magnetic permeability changes from high to low, the magnetic flux generated in the ferrite core flows outward, resulting in difficulties in achieving convergence condition.

2.2 Ferromagnetic amorphous alloy particles (FAAP)

Including the advantages and disadvantages of ferrite cores in section 2.1, FAAP has additional advantages and disadvantages as follows:

➤ Advantages:

- High permeability even at high frequencies: Due to amorphous condition, they maintain high permeability at high frequencies.

➤ Disadvantage:

- High cost: Amorphous ferromagnetic alloy particles may be pricier than other materials used in magnetic applications.

Based on the characteristics of the ferrite core, the integration of ferrite cores in the RUEC probe has been explored, demonstrating enhanced crack detection capabilities through improved magnetic flux concentration. The study's results suggest promising prospects for the RUEC probe,

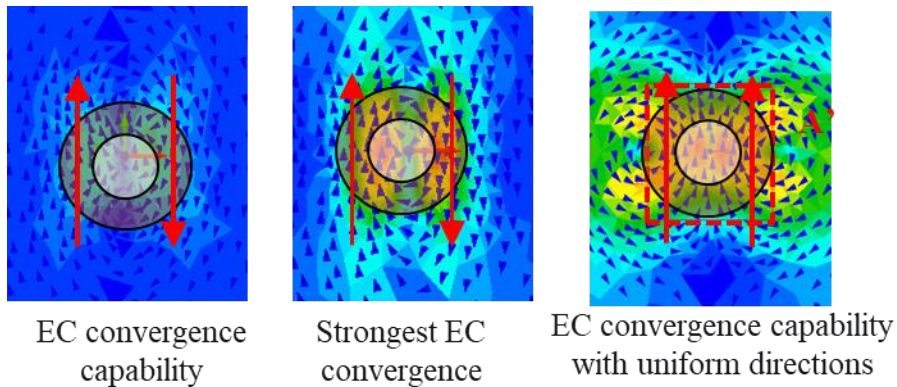
with potential applications in industries such as aerospace, construction, and manufacturing.

Furthermore, based on the characteristics of the FAAP, the investigation into film EC probes enhanced by FAAP has shown improved crack detection capabilities. The correlation between crack characteristics and signal parameters provides a comprehensive basis for accurate crack evaluation, contributing to the refinement of non-destructive testing methodologies.

The study has also delved into the impact of different excitation coil configurations on EC probe performance, highlighting the distinct merits and drawbacks of each type. The results offer valuable insights into selecting the appropriate EC probe based on specific inspection requirements.

In summary, this study contributes significantly to the field of crack detection in conductive materials, presenting innovative probe designs, exploring diverse materials, and providing insights into signal processing techniques. The study's outcomes pave the way for further refinements, applications, and advancements in non-destructive testing methodologies.

The basis for the design of a single detection coil for ECC probes



When determining the optimal size for the detection coil in eddy current (EC) probes, it's crucial to guarantee its efficacy in detecting variations in EC signals during scanning, particularly in regions exhibiting the most intense EC activity (as shown in the figure above).

References

- [1] S. Xie, Z. Duan, J. Li, Z. Tong, M. Tian, and Z. Chen, “A novel magnetic force transmission eddy current array probe and its application for nondestructive testing of defects in pipeline structures,” *Sensors Actuators, A Phys.*, vol. 309, 2020, doi: 10.1016/j.sna.2020.112030.
- [2] Q. Yang *et al.*, “A novel circumferential eccentric eddy current probe and its application for defect detection of small-diameter tubes,” *Sensors Actuators A Phys.*, vol. 331, p. 113023, 2021, doi: <https://doi.org/10.1016/j.sna.2021.113023>.
- [3] W. Li, X. Yuan, G. Chen, X. Yin, and J. Ge, “A feed-through ACFM probe with sensor array for pipe string cracks inspection,” *NDT E Int.*, vol. 67, pp. 17–23, 2014, doi: <https://doi.org/10.1016/j.ndteint.2014.06.006>.
- [4] R. Hamia, C. Cordier, and C. Dolabdjian, “Eddy-current non-destructive testing system for the determination of crack orientation,” *NDT E Int.*, vol. 61, pp. 24–28, 2014, doi: <https://doi.org/10.1016/j.ndteint.2013.09.005>.
- [5] E. Mohseni, H. Habibzadeh Boukani, D. Ramos França, and M. Viens, “A Study of the Automated Eddy Current Detection of Cracks in Steel Plates,” *J. Nondestruct. Eval.*, vol. 39, no. 1, pp. 1–12, 2020, doi: 10.1007/s10921-019-0647-9.
- [6] L. Q. Trung, N. Kasai, K. Sekino, and A. Kasahara, “A novel film eddy current probe having a detection coil interleaved to the excitation coil and the amplified effect by ferromagnetic amorphous alloys particles,” *Sensors Actuators A Phys.*, vol. 347, no. September, p. 113913, 2022, doi: 10.1016/j.sna.2022.113913.
- [7] Z. Liu, J. Yao, C. He, Z. Li, X. Liu, and B. Wu, “Development of a bidirectional-excitation eddy-current sensor with magnetic shielding: Detection of subsurface defects in stainless steel,” *IEEE Sens. J.*, vol. 18, no. 15, pp. 6203–6216, 2018, doi: 10.1109/JSEN.2018.2844957.
- [8] Z. Liu, A. D. Koffman, B. C. Waltrip, and Y. Wang, “Eddy Current Rail Inspection Using AC Bridge Techniques,” *J. Res. Natl. Inst. Stand. Technol.*, vol. 118, no. March 2017, p. 140, 2013, doi: 10.6028/jres.118.007.
- [9] M. Grosso *et al.*, “Eddy current and inspection of coatings for storage tanks,” *J. Mater. Res. Technol.*, vol. 7, no. 3, pp. 356–360, 2018, doi: 10.1016/j.jmrt.2018.05.006.
- [10] N. Alatawneh, P. R. Underhill, and T. W. Krause, “Low-Frequency Eddy-Current Testing

- for Detection of Subsurface Cracks in CF-188 Stub Flange,” *IEEE Sens. J.*, vol. 18, no. 4, pp. 1568–1575, 2018, doi: 10.1109/JSEN.2017.2782799.
- [11] Z. Song, T. Yamada, H. Shitara, and Y. Takemura, “Detection of Damage and Crack in Railhead by Using Eddy Current Testing,” *J. Electromagn. Anal. Appl.*, vol. 03, no. 12, pp. 546–550, 2011, doi: 10.4236/jemaa.2011.312082.
- [12] R. Yang, Y. He, B. Gao, G. Yun Tian, and J. Peng, “Lateral heat conduction based eddy current thermography for detection of parallel cracks and rail tread oblique cracks,” *Meas. J. Int. Meas. Confed.*, vol. 66, pp. 54–61, 2015, doi: 10.1016/j.measurement.2015.01.024.
- [13] L. H. Ichinose, Y. Kohno, T. Kitada, and M. Matsumura, “Applications of Eddy Current Test to Fatigue Crack Inspection of Steel Bridges,” *Mem. Fac. Eng. Osaka City Univ.*, vol. 48, no. May, pp. 57–62, 2007.
- [14] C. C. H. Lo and N. Nakagawa, “Evaluation of eddy current and magnetic techniques for inspecting rebars in bridge barrier rails,” *AIP Conf. Proc.*, vol. 1511, pp. 1371–1377, 2013, doi: 10.1063/1.4789202.
- [15] N. Yusa, Y. Sakai, and H. Hashizume, “An eddy current probe suitable to gain information about the depth of near-side flaws much deeper than the depth of penetration,” *NDT E Int.*, vol. 44, no. 1, pp. 121–130, 2011, doi: <https://doi.org/10.1016/j.ndteint.2010.10.003>.
- [16] N. Yusa, H. Hashizume, R. Urayama, T. Uchimoto, T. Takagi, and K. Sato, “An arrayed uniform eddy current probe design for crack monitoring and sizing of surface breaking cracks with the aid of a computational inversion technique,” *NDT E Int.*, vol. 61, pp. 29–34, 2014, doi: <https://doi.org/10.1016/j.ndteint.2013.09.004>.
- [17] L. Q. Trung, N. Kasai, K. Sekino, and S. Miyazaki, “Eddy current convergence probes with self-differential and self-nulling characteristics for detecting cracks in conductive materials,” *Sensors Actuators A Phys.*, vol. 349, no. October 2022, p. 114084, 2023, doi: 10.1016/j.sna.2022.114084.
- [18] M. Fan, B. Cao, P. Yang, W. Li, and G. Tian, “Elimination of liftoff effect using a model-based method for eddy current characterization of a plate,” *NDT E Int.*, vol. 74, pp. 66–71, 2015, doi: 10.1016/j.ndteint.2015.05.007.
- [19] N. O. Romero-Arismendi, J. A. Pérez-Benítez, E. Ramírez-Pacheco, and J. H. Espina-Hernández, “Design method for a GMR-based eddy current sensor with optimal sensitivity,” *Sensors Actuators, A Phys.*, vol. 314, 2020, doi: 10.1016/j.sna.2020.112348.

- [20] H. Hoshikawa and K. Koyama, "Uniform Eddy Current Probe with Little Disrupting Noise," *Rev. Prog. Quant. Nondestruct. Eval.*, vol. 17, pp. 1059–1066, 1998, doi: 10.1007/978-1-4615-5339-7_137.
- [21] H. Hoshikawa and K. Koyama, "A New ECT Probe with Rotating Direction Eddy Current," *Rev. Prog. Quant. Nondestruct. Eval.*, vol. 15, pp. 1091–1098, 1996, doi: 10.1007/978-1-4613-0383-1_142.
- [22] K. Koyama and H. Hoshikawa, "Basic Study of a New ECT Probe Using Uniform Rotating Direction Eddy Current BT - Review of Progress in Quantitative Nondestructive Evaluation: Volume 16A," D. O. Thompson and D. E. Chimenti, Eds., Boston, MA: Springer US, 1997, pp. 1067–1074. doi: 10.1007/978-1-4615-5947-4_139.
- [23] H. Hoshikawa, "Signal phase indication of flaw depth by a lift-off noise free eddy current probe," vol. 430, pp. 430–437, 2003, doi: 10.1063/1.1472830.
- [24] H. Hoshikawa, "A New Eddy Current Surface Probe for Short Flaws with Minimal Lift-Off Noise," vol. 413, no. April, pp. 413–418, 2003, doi: 10.1063/1.1570165.
- [25] H. Hoshikawa, "A new ECT surface probe without lift-off noise and with phase information on flaw depth," vol. 969, pp. 969–976, 2003, doi: 10.1063/1.1373861.
- [26] H. Hoshikawa, K. Koyama, and Y. Naruse, "Detecting weld zone over anticorrosion painting by rotating uniform eddy current probe," *AIP Conf. Proc.*, vol. 760, pp. 502–508, 2005, doi: 10.1063/1.1916717.
- [27] H. Hoshikawa, K. Koyama, and K. Mizoguchi, "Surface flaw testing of weld zone by a new eddy current probe," *AIP Conf. Proc.*, vol. 820 I, pp. 353–360, 2006, doi: 10.1063/1.2184550.
- [28] K. Koyama, H. Hoshikawa, and G. Kojima, "Eddy current nondestructive testing for carbon fiber-reinforced composites," *J. Press. Vessel Technol. Trans. ASME*, vol. 135, no. 4, pp. 1–2, 2013, doi: 10.1115/1.4023253.
- [29] A. Lopes Ribeiro, H. Geirinhas Ramos, and O. Postolache, "A simple forward direct problem solver for eddy current non-destructive inspection of aluminum plates using uniform field probes," *Meas. J. Int. Meas. Confed.*, vol. 45, no. 2, pp. 213–217, 2012, doi: 10.1016/j.measurement.2011.03.029.
- [30] A. S. Repelianto and N. Kasai, "The improvement of flaw detection by the configuration of uniform eddy current probes," *Sensors (Switzerland)*, vol. 19, no. 2, 2019, doi:

- 10.3390/s19020397.
- [31] A. S. Repelianto, N. Kasai, K. Sekino, and M. Matsunaga, "A uniform eddy current probe with a double-excitation coil for flaw detection on aluminium plates," *Metals (Basel)*, vol. 9, no. 10, 2019, doi: 10.3390/met9101116.
- [32] A. Bernieri, L. Ferrigno, M. Laracca, and A. Rasile, "Eddy Current Testing Probe Based on Double-Coil Excitation and GMR Sensor," *IEEE Trans. Instrum. Meas.*, vol. 68, no. 5, pp. 1533–1542, 2019, doi: 10.1109/TIM.2018.2890757.
- [33] J. Ge, C. Yang, F. Yu, and N. Yusa, "Transformation of the rotating eddy current testing signal at the desired eddy current orientation," *NDT E Int.*, vol. 125, no. October 2021, p. 102551, 2022, doi: 10.1016/j.ndteint.2021.102551.
- [34] A. S. Repelianto, N. Kasai, K. Sekino, M. Matsunaga, and L. Q. Trung, "Flaw detection in aluminum plates using a rotating uniform eddy current probe with two pairs of excitation coils," *Metals (Basel)*, vol. 9, no. 10, 2019, doi: 10.3390/met9101069.
- [35] W. Li, X. Yuan, G. Chen, J. Ge, X. Yin, and K. Li, "High sensitivity rotating alternating current field measurement for arbitrary-angle underwater cracks," *NDT E Int.*, vol. 79, pp. 123–131, 2016, doi: <https://doi.org/10.1016/j.ndteint.2016.01.003>.
- [36] Z. Xu, X. Wang, and Y. Deng, "Rotating Focused Field Eddy-Current Sensing for Arbitrary Orientation Defects Detection in Carbon Steel," *Sensors*, vol. 20, no. 8. 2020. doi: 10.3390/s20082345.
- [37] T. Matsumoto *et al.*, "Investigation of electromagnetic nondestructive evaluation of residual strain in low carbon steels using the eddy current magnetic signature (EC-MS) method," *J. Magn. Magn. Mater.*, vol. 479, no. November 2018, pp. 212–221, 2019, doi: 10.1016/j.jmmm.2019.01.103.
- [38] S. Takeda, T. Uchimoto, A. Kita, T. Matsumoto, and T. Sasaki, "Mechanism study of the residual stress evaluation of low-carbon steels using the eddy current magnetic signature method," *J. Magn. Magn. Mater.*, vol. 538, no. July, p. 168268, 2021, doi: 10.1016/j.jmmm.2021.168268.
- [39] R. Zu, Y. Yang, X. Huang, D. Jiao, J. Zhao, and Z. Liu, "A stress detection method for metal components based on eddy current thermography," *NDT E Int.*, vol. 133, no. March 2022, p. 102762, 2023, doi: 10.1016/j.ndteint.2022.102762.
- [40] T. Vijayachandrika, S. Thirunavukkarasu, and B. P. C. Rao, "Comprehensive study on

- radial coil influence in designing segmented remote field eddy current probe for defect detection in ferromagnetic tubes,” *Nondestruct. Test. Eval.*, vol. 37, no. 3, pp. 346–365, May 2022, doi: 10.1080/10589759.2021.1998488.
- [41] Z. Chu, Z. Jiang, Z. Mao, Y. Shen, J. Gao, and S. Dong, “Low-power eddy current detection with 1-1 type magnetoelectric sensor for pipeline cracks monitoring,” *Sensors Actuators, A Phys.*, vol. 318, p. 112496, 2021, doi: 10.1016/j.sna.2020.112496.
- [42] A. A. Yahya *et al.*, *BM3D image denoising algorithm based on an adaptive filtering*, vol. 79, no. 27–28. Multimedia Tools and Applications, 2020. doi: 10.1007/s11042-020-08815-8.
- [43] P. Wang, H. Zhu, D. Li, H. He, and C. Qin, “Crack Detection under Coating of Flow Passage Parts based on Adaptive Second Generation Wavelet,” *J. Phys. Conf. Ser.*, vol. 1744, no. 4, p. 42151, 2021, doi: 10.1088/1742-6596/1744/4/042151.
- [44] K. Ji, P. Wang, Y. Jia, Y. Ye, and S. Ding, “Adaptive Filtering Method of MFL Signal on Rail Top Surface Defect Detection,” *IEEE Access*, vol. 9, pp. 87351–87359, 2021, doi: 10.1109/ACCESS.2021.3065044.
- [45] S. Zhao, J. Zhou, Y. Liu, J. Zhang, and J. Cui, “Application of Adaptive Filtering Based on Variational Mode Decomposition for High-Temperature Electromagnetic Acoustic Transducer Denoising,” *Sensors*, vol. 22, no. 18, 2022, doi: 10.3390/s22187042.
- [46] D. Vasić, I. Rep, D. Špikić, and M. Kekelj, “Model of magnetically shielded ferrite-cored eddy current sensor,” *Sensors*, vol. 22, no. 1, 2022, doi: 10.3390/s22010326.
- [47] S. Zhang and C. Ye, “Model of Ferrite-cored Driver-pickup Coil Probe Application of TREE Method for Eddy Current Nondestructive Evaluation,” *Appl. Comput. Electromagn. Soc. J.*, vol. 37, no. 05 SE-Articles, pp. 632–638, Nov. 2022, doi: 10.13052/2022.ACES.J.370513.
- [48] A. K. Soni, R. Kumar, S. K. Patel, and A. Soni, “Non-destructive Fusion Method for Image Enhancement of Eddy Current Sub-surface Defect Images BT - Machine Vision and Augmented Intelligence—Theory and Applications,” M. K. Bajpai, K. Kumar Singh, and G. Giakos, Eds., Singapore: Springer Singapore, 2021, pp. 613–621.
- [49] L. Shu, H. Songling, and Z. Wei, “Development of differential probes in pulsed eddy current testing for noise suppression,” *Sensors Actuators, A Phys.*, vol. 135, no. 2, pp. 675–679, 2007, doi: 10.1016/j.sna.2006.10.013.

- [50] R. Keshwani and S. Bhattacharya, "Ferrite cores as back yoke for enhancing hall sensor sensitivity in caliper tool for pipeline inspection," *Sens. Rev.*, vol. 29, no. 4, pp. 355–360, 2009, doi: 10.1108/02602280910986610.
- [51] M. Mirzaei, P. Ripka, and V. Grim, "A novel eddy current speed sensor with a ferrite E-core," *IEEE Magn. Lett.*, vol. 11, no. c, pp. 1–5, 2020, doi: 10.1109/LMAG.2020.2993501.
- [52] V. Arjun, B. Sasi, B. P. C. Rao, C. K. Mukhopadhyay, and T. Jayakumar, "Optimisation of pulsed eddy current probe for detection of sub-surface defects in stainless steel plates," *Sensors Actuators, A Phys.*, vol. 226, pp. 69–75, 2015, doi: 10.1016/j.sna.2015.02.018.
- [53] P. May, E. Zhou, and D. Morton, "The design of a ferrite-cored probe," *Sensors Actuators, A Phys.*, vol. 136, no. 1, pp. 221–228, 2007, doi: 10.1016/j.sna.2006.11.031.
- [54] N. Kasai, S. Matsuzaki, and T. Sakamoto, "Experimental and analytical study for detectability of the back-side flaws of flat ferromagnetic plates by RFECT," *NDT E Int.*, vol. 44, no. 8, pp. 703–707, 2011, doi: <https://doi.org/10.1016/j.ndteint.2011.08.002>.
- [55] N. Kasai, Y. Fujiwara, K. Sekine, and T. Sakamoto, "Evaluation of back-side flaws of the bottom plates of an oil-storage tank by the RFECT," *NDT E Int.*, vol. 41, no. 7, pp. 525–529, 2008, doi: <https://doi.org/10.1016/j.ndteint.2008.05.002>.
- [56] P. May, E. Zhou, and D. Morton, "Numerical modelling and implementation of ferrite cored eddy current probes," *NDT E Int.*, vol. 40, no. 8, pp. 566–576, 2007, doi: 10.1016/j.ndteint.2007.06.003.
- [57] M. K. Ghosh *et al.*, "Numerical modelling of magnetic characteristics of ferrite core taking account of both eddy current and displacement current," *Heliyon*, vol. 5, no. 8, p. e02229, 2019, doi: 10.1016/j.heliyon.2019.e02229.
- [58] N. Kasai, S. Ogawa, T. Oikawa, K. Sekine, and K. Hasegawa, "Detection of Carburization in Ethylene Pyrolysis Furnace Tubes by a C Core Probe with Magnetization," *J. Nondestruct. Eval.*, vol. 29, no. 3, pp. 175–180, 2010, doi: 10.1007/s10921-010-0075-3.
- [59] K. Hasegawa, T. Oikawa, and N. Kasai, "Development of an Eddy Current Inspection Technique with Surface Magnetization to Evaluate the Carburization Thickness of Ethylene Pyrolysis Furnace Tubes," *J. Nondestruct. Eval.*, vol. 31, no. 4, pp. 349–356, 2012, doi: 10.1007/s10921-012-0146-8.
- [60] Z. Zeng, L. Udpa, and S. S. Udpa, "Finite-element model for simulation of ferrite-core eddy-current probe," *IEEE Trans. Magn.*, vol. 46, no. 3 PART 2, pp. 905–909, 2010, doi:

10.1109/TMAG.2009.2034651.

- [61] H. Sabbagh, J. Bowler, and D. Sabbagh, “A model of eddy-current probes with ferrite cores,” *Nondestruct. Test. Eval.*, vol. 5, no. 1, pp. 67–79, 1989, doi: 10.1080/02780898908952955.
- [62] Y. Lu and J. R. Bowler, “An analytical model of eddy current ferrite-core probes,” *AIP Conf. Proc.*, vol. 1430, no. 31, pp. 387–392, 2012, doi: 10.1063/1.4716254.
- [63] Z. Chen and K. Miya, “A new approach for optimal design of Eddy Current Testing probes,” *J. Nondestruct. Eval.*, vol. 17, no. 3, pp. 105–116, 1998, doi: 10.1007/BF02446114.
- [64] T. G. Santos, P. Vilaca, L. Quintino, J. dos Santos, and L. Rosado, “INNOVATIVE EDDY CURRENT PROBE FOR MICRO DEFECTS,” *AIP Conf. Proc.*, vol. 1211, no. 1, pp. 377–384, doi: DOI:101063/13362418.
- [65] Q. P. Ma, B. Gao, G. Y. Tian, C. R. Yang, and K. Chen, “Complexed Shape Micro Defects Inspection By High Sensitivity Flexible TRT Eddy Current Array,” in *2019 Far East NDT New Technology & Application Forum (FENDT)*, 2019, pp. 110–114. doi: 10.1109/FENDT47723.2019.8962592.
- [66] Q. Ma, B. Gao, G. Y. Tian, C. Yang, L. Xie, and K. Chen, “High sensitivity flexible double square winding eddy current array for surface micro-defects inspection,” *Sensors Actuators A Phys.*, vol. 309, p. 111844, 2020, doi: <https://doi.org/10.1016/j.sna.2020.111844>.
- [67] D. Wu, S. Lin, H. Chen, and X. Wang, “Mutual inductance model of double printed circuit board-based coplanar rectangular spiral coils for eddy-current testing,” *Int. J. Numer. Model. Electron. Networks, Devices Fields*, vol. 36, no. 1, pp. 1–15, 2023, doi: 10.1002/jnm.3038.
- [68] X. Fan, Y. He, T. Chen, and C. Hou, “Research on crack monitoring technology of flexible eddy current array sensor based on TMR sensors,” *Measurement*, vol. 192, p. 110926, 2022, doi: <https://doi.org/10.1016/j.measurement.2022.110926>.
- [69] H. Zhang, L. Ma, and F. Xie, “A method of steel ball surface quality inspection based on flexible arrayed eddy current sensor,” *Measurement*, vol. 144, pp. 192–202, 2019, doi: <https://doi.org/10.1016/j.measurement.2019.05.056>.
- [70] W. Zhang, C. Wang, F. Xie, and H. Zhang, “Defect imaging curved surface based on flexible eddy current array sensor,” *Measurement*, vol. 151, p. 107280, 2020, doi: <https://doi.org/10.1016/j.measurement.2019.107280>.
- [71] J. Petzold, “Advantages of softmagnetic nanocrystalline materials for modern electronic applications,” *J. Magn. Magn. Mater.*, vol. 242–245, pp. 84–89, 2002, doi:

- [https://doi.org/10.1016/S0304-8853\(01\)01206-9](https://doi.org/10.1016/S0304-8853(01)01206-9).
- [72] R. Hasegawa, “Advances in amorphous and nanocrystalline magnetic materials,” *J. Magn. Magn. Mater.*, vol. 304, no. 2, pp. 187–191, 2006, doi: <https://doi.org/10.1016/j.jmmm.2006.02.119>.
- [73] L. K. Varga, L. Novák, and F. Mazaleyrat, “Effective magnetic anisotropy and internal demagnetization investigations in soft magnetic nanocrystalline alloys,” *J. Magn. Magn. Mater.*, vol. 210, no. 1, pp. 25–30, 2000, doi: [https://doi.org/10.1016/S0304-8853\(99\)00600-9](https://doi.org/10.1016/S0304-8853(99)00600-9).
- [74] “Notice No.93 of the Office of Hazardous Materials Regulation,” pp. 1–8, [Online]. Available: https://www.fdma.go.jp/laws/tutatsu/assets/120824kisei_93.pdf
- [75] B. A. Auld and J. C. Moulder, “Review of advances in quantitative eddy current nondestructive evaluation,” *J. Nondestruct. Eval.*, vol. 18, no. 1, pp. 3–36, 1999, doi: [10.1023/A:1021898520626](https://doi.org/10.1023/A:1021898520626).
- [76] L. S. Obrutsky, V. S. Cecco, S. P. Sullivan, and D. Humphrey, “Transmit-receive eddy current probes for circumferential cracks in heat exchanger tubes,” vol. 54, 1996, [Online]. Available: <https://www.osti.gov/biblio/197662>
- [77] S. P. Sullivan, V. S. Cecco, L. S. Obrutsky, D. Humphrey, S. P. Smith, and K. A. Emde, “Computer Modeling of Eddy Current Transmit-Receive Probes for Tube Inspection BT - Review of Progress in Quantitative Nondestructive Evaluation: Volume 17A,” D. O. Thompson and D. E. Chimenti, Eds., Boston, MA: Springer US, 1998, pp. 283–289. doi: [10.1007/978-1-4615-5339-7_36](https://doi.org/10.1007/978-1-4615-5339-7_36).
- [78] S. Couture, X. Wang, A. Goncharov, and V. Lomakin, “A coupled micromagnetic-Maxwell equations solver based on the finite element method,” *J. Magn. Magn. Mater.*, vol. 493, p. 165672, 2020, doi: <https://doi.org/10.1016/j.jmmm.2019.165672>.
- [79] X. Yuan *et al.*, “Novel phase reversal feature for inspection of cracks using multi-frequency alternating current field measurement technique,” *Mech. Syst. Signal Process.*, vol. 186, p. 109857, 2023, doi: <https://doi.org/10.1016/j.ymsp.2022.109857>.
- [80] M. E. Hiroyasu SHIMOJI, Shigeru AIHARA, Takashi TODAKAKA, Minoru FUJIKI, “Development of transcranial magnetic stimulation coil by using the eddy current concentration method.” p. Vol. 20, No.1, 2012.
- [81] L. Q. Trung, N. Kasai, K. Sekino, and S. Miyazaki, “An eddy current convergence probe

with copper core and single detection coil to detect flaws on aluminum plates,” *NDT E Int.*, vol. 132, no. October 2021, p. 102707, 2022, doi: 10.1016/j.ndteint.2022.102707.

International publications and conferences

✦ International Journal Publication (7 Published)

[1] **L.Q. Trung**, N. Kasai, K. Sekino, S. Miyazaki, “An eddy current convergence probe with copper core and single detection coil to detect flaws on aluminum plates”, *NDT and E International (Elsevier)* 132 (2022) 102707.

<https://doi.org/10.1016/j.ndteint.2022.102707>.

[2] **L.Q. Trung**, N. Kasai, K. Sekino, S. Miyazaki, “Eddy current convergence probes with self-differential and self-nulling characteristics for detecting cracks in conductive materials”, *Sensors and Actuators A: Physical (Elsevier)* 349 (2023) 114084.

<https://doi.org/10.1016/j.sna.2022.114084>.

[3] **L.Q. Trung**, N. Kasai, K. Sekino, S. Miyazaki, “A sophisticated design of copper core to converge rotating eddy current control for detecting cracks in conductive materials”, *Scientific Reports (Nature)* (2023) 1–10.

<https://doi.org/10.1038/s41598-023-32319-8>.

[4] **L.Q. Trung**, N. Kasai, K. Sekino, A. Kasahara, “A novel film eddy current probe having a detection coil interleaved to the excitation coil and the amplified effect by ferromagnetic amorphous alloys particles”, *Sensors and Actuators A: Physical (Elsevier)* 347 (2022) 113913.

<https://doi.org/10.1016/j.sna.2022.113913>.

[5] **L.Q. Trung**, N. Kasai, K. Sekino, N.C. Hanh, “The effect of eddy current probe configurations on crack signal magnitude: Consideration of excitation coil direction”, *Sensors and Actuators A: Physical (Elsevier)* 358 (2023) 114437.

<https://doi.org/10.1016/j.sna.2023.114437>.

[6] **L.Q. Trung**, S. Miyazaki, N. Kasai, K. Sekino, “Rotating uniform eddy current probe using four rectangular excitation coils with ferrite cores for cracks detection in conductive materials”, *IOP Conf. Ser. Mater. Sci. Eng. (IOP science)* 1289 (2023) 12032.

<https://doi.org/10.1088/1757-899X/1289/1/012032>.

[7] **L.Q. Trung**, N. Kasai, M. Le, K. Sekino, “Crack detection in low carbon steel using Rotating Uniform Eddy Current probe and noise signal filtering based on Multivariate Singular Spectrum Analysis”, *Sensors and Actuators A: Physical (Elsevier)* 362 (2023) 114628.

<https://doi.org/10.1016/j.sna.2023.114628>.

Technical Report (1)

[1] | **L.Q. Trung**, N. Kasai, K. Sekino, “Uniform Eddy Current Testing and Alternating Current Field Measurement”, *Journal of The Japanese Society for Non-Destructive Inspection* 71 (10) 441 – 444.

Domestic Conference (4)

[1] **L.Q. Trung**, N. Kasai, K. Sekino, S. Miyazaki, “A new uniform eddy current probe with two pair of excitation coil to detect flaws on aluminum plates”, *YNU Science and Engineering Joint Research Symposium, a participation event to commemorate the 100th anniversary of the founding of engineering*, Yokohama National University, 2021/11/20, Yokohama.

[2] **L.Q. Trung**, N. Kasai, K. Sekino, S. Miyazaki, “Study on detecting the artificial flaws on aluminum plates using rotating uniform eddy current probes”, *The Japan Society for Non-Destructive Inspection, “Maintenance Inspection Mini Symposium*, 2021/11/26, Tokyo.

[3] **L.Q. Trung**, N. Kasai, K. Sekino, S. Miyazaki, “Study on an eddy current convergence probe with a copper core to detect flaws on conductive plates”, *Kanagawa NDT Exchange Meeting: 27th Autumn Technology Presentation*, October 21, 2022, Kanagawa.

[4] **L.Q. Trung**, N. Kasai, K. Sekino, S. Miyazaki, “Study on an eddy current convergence probe with a copper core to detect flaws on conductive materials”, *The Japan Society for Non-Destructive Inspection, 2022 Maintenance Inspection Mini Symposium*, November 1, 2022, Tokyo.

International Conference (2)

[1] **L.Q. Trung**, N. Kasai, K. Sekino, S. Miyazaki, “Flaws detectability on an aluminum surface using a pancake uniform eddy current probe and an eddy current convergence probe”, *7th US-JAPAN NDT symposium*, 2022/08/23-2022/08/26, Marriott Waikoloa Beach Resort & Spa Waikoloa, Hawaii, USA.

[2] **L.Q. Trung**, S. Miyazaki, N. Kasai, K. Sekino, “Rotating uniform eddy current probe using four rectangular excitation coils with ferrite cores for cracks detection in conductive materials”, *The 4th International Conference on Transportation Infrastructure and Sustainable Development TISDIC 2023*, 2023/08/26-2023/08/28, Da Nang, Viet Nam.

 **Best Paper Award (1)**

[1] **L.Q. Trung**, S. Miyazaki, N. Kasai, K. Sekino, “Rotating uniform eddy current probe using four rectangular excitation coils with ferrite cores for detecting cracks in conductive materials”, *4th International Conference on Transportation Infrastructure and Sustainable Development (TISDIC 2023)*, 2023/08/26-2023/08/28, Da Nang, Vietnam.

 **Awards (1)**

[1] The funding support of the 2022 Research Grant Program for Doctor Student of the Japanese Society for Non-Destructive Inspection (4/2022-3/2023).